Volume 98, Number 1, January–February 1993
Journal of Research of the National Institute of Standards and Technology

Contents

Articles

News Briefs

Volume 98, Number 1, January–February 1993
Journal of Research of the National Institute of Standards and Technology

Volume 98, Number 1, January–February 1993
Journal of Research of the National Institute of Standards and Technology

Volume 98, Number 1, January–February 1993
Journal of Research of the National Institute of Standards and Technology

Foreword

Since 1967 when the National Institute of Standards and Technology Reactor (NBSR) achieved criticality, reactor-based research programs have increased enormously both in scope and in number of research participants (over 600 in FY 91). Currently operating at 20 MW power and a peak thermal core flux of 4×10^{14} n/(cm^2 s), the NBSR is one of the top three research reactors in the country, with a broad range of research programs which utilize thermal beams.

In recent years, there has been an increasing interest in the use of "cold" neutrons (energy < 0.005 eV) for a variety of studies. As a result of their longer wavelengths, total reflection at interfaces makes it possible to build neutron guides, which can be used to transport intense beams over many tens of meters, and to focus beams down onto smaller spots. This, in turn, has opened up many new instrumentation possibilities and research opportunities, which are best characterized in terms of increased resolution in energy (by up to five orders of magnitude) and in the size of structures which can be determined.

Western Europe has not only been the site of the initial development of neutron guides and cold sources, it has been the unquestioned leader in the utilization of these devices in advanced neutron scattering facilities employing new instrumentation. In 1984 the United States had one operating cold source at Brookhaven National Laboratory, one under development [at the then National Bureau of Standards (now NIST)], and no guide halls. In contrast, at the Institut Laue-Langevin (ILL)—the most extensively used research reactor in the world—16 of 27 instruments were on cold neutron guides. Since then a second cold source and second guide hall have been added to the ILL complex.

The growing impact of cold neutrons in chemistry, physics, materials science, and biology was recognized in 1984 by the Seitz-Eastman Committee, commissioned by the National Academy of Sciences at the request of the President's science advisor. This study was instrumental in focusing attention on the need for cold neutron capabilities in this country. In 1987, NBS and the Department of Commerce responded to the national need for cold neutron capability by initiating the development of the Cold Neutron Research Facility (CNRF). As of December 1992, nine experimental stations had been developed and installed, two more were ready for installation and commissioning, and the balance (for 15 total) were at various stages of design and construction. A second generation cold source that will greatly increase the intensity of all stations has been designed and is being built for installation in 1993. The external user program has been initiated, with excellent response from the community, both inside and outside NIST. This therefore is an appropriate time to produce a detailed, technical description of the facility and of the research that it will enable. For this special issue of the Journal of Research a number of review papers have been prepared which describe research activities which employ cold neutrons, and the NIST instruments with which such activities can be pursued.

J. Michael Rowe
Chief,
Reactor Radiation Division,
National Institute of Standards and Technology

Volume 98, Number 1, January–February 1993
Journal of Research of the National Institute of Standards and Technology

[J. Res. Natl. Inst. Stand. Technol. 98, 1 (1993)]

The NIST Cold Neutron Research Facility

Volume 98 Number 1 January–February 1993

H. J. Prask, J. M. Rowe, J. J. Rush, and I. G. Schröder

National Institute of Standards and Technology,
Gaithersburg, MD 20899

The Cold Neutron Research Facility (CNRF) at the National Institute of Standards and Technology (NIST) Research Reactor (NBSR) is now coming on line, with the first seven experimental stations operational, and more stations scheduled to be installed during 1992. The present article provides an introduction to the facility, and to other articles in the current issue that give more details on some of the research opportunities that the facility will bring to NIST.

Key words: cold neutrons; guide hall; neutron facilities; neutron guides; neutron instrumentation; neutron properties; neutrons; research reactors.

Accepted: July 8, 1992

1. Introduction

Since the advent of nuclear reactors with reasonably high fluence rates (fluxes) in the 1950s, the use of the thermal neutrons produced by these sources to study a wide range of problems has grown rapidly. This growth has resulted from the properties of neutrons as probes, which include:

- absorption with subsequent radioactive decay (used as an analytical tool)
- high penetration as a result of the lack of an electrical charge
- scattering by nuclear interactions (which leads to a *non*monotonic variation of scattering with atomic number)
- special sensitivity to hydrogen and hydrogenous materials along with strong difference in scattering by hydrogen and deuterium
- scattering by magnetic interactions (as a result of the magnetic dipole of the neutron)
- simple interpretation of results (as a result of the weak interaction)
- the nondestructive nature of low energy neutrons
- the fact that neutrons with wavelengths comparable to interatomic spacings in condensed matter have energies comparable to the energies of atomic vibrations.

The potential of this research was realized early, and the Atomic Energy Commission built a succession of research reactors with increasing fluence rates throughout the 1950s and 1960s.

This potential was also perceived by three physicists at the National Bureau of Standards (NBS, now NIST)—R. S. Carter, H. Landon, and C. Muelhause—who proposed, designed, and built the 20 MW research reactor, NBSR, on the new NBS site in Gaithersburg. The original proposal was justified on the importance of the contributions that the NBSR would provide to the NBS mission in analytic chemistry, standards, solid state physics, and nuclear physics, and was intended to serve NBS and other government agencies in the

Washington area. The reactor design emphasized versatility, incorporating a large number of experimental facilities with different capabilities, rather than concentrating on any one specific area of research. The success of this philosophy can be seen both in the increasing utilization of the reactor by NIST and other researchers, and in the changing emphasis in programs over the years. The design also included many advanced features that have since been incorporated into other designs, including a completely passive emergency cooling system, a novel split core fuel design (recently adopted into designs for the Advanced Neutron Source and the spallation source at Los Alamos National Laboratory), helium and carbon dioxide blankets around high flux regions to reduce radioactive emissions, and the use of large radial penetrations into the high flux regions to maximize intensity for beam research.

Since the reactor first achieved continuous operation in 1969, the use of the facilities has grown steadily in both the number of researchers served (over 450 research participants the last year before the CNRF was operational) and in the breadth of the community served (the 450 participants came from 15 NIST divisions or offices, 25 other government agencies, 50 universities and 25 industrial laboratories). The NBSR has gone from a local resource to a truly national facility, with researchers from all over the country. A diagram of the current layout of facilities around the reactor is shown in Fig. 1.

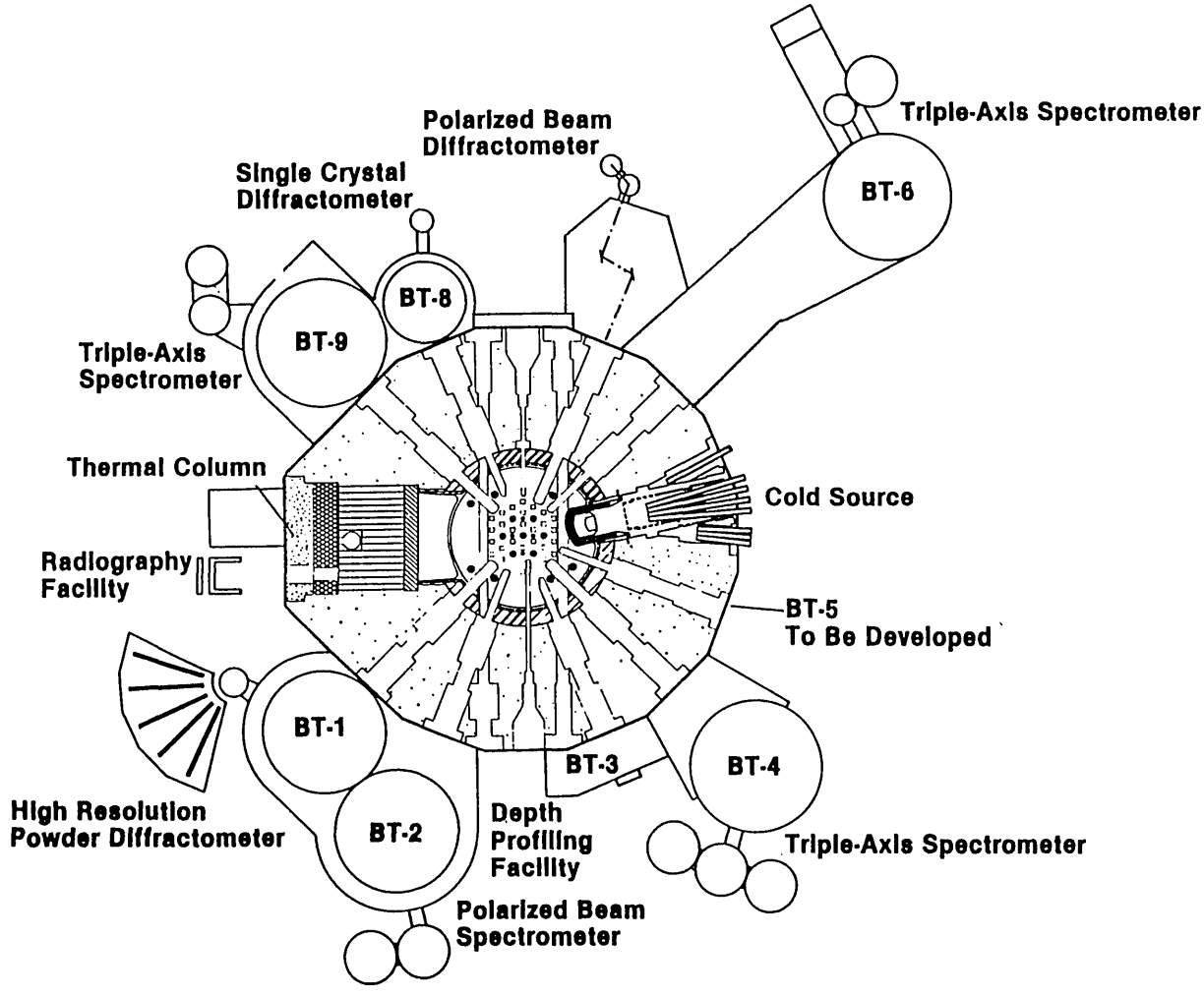

Fig. 1. Principal experimental facilities in the reactor hall.

One of the features incorporated into the design was the large penetration for a "cold neutron source" shown in Fig. 1. From the beginning, the designers intended that this penetration would one day be used to provide an intense source of neutrons with lower energies than those typical of other ports by installation of a cryogenically cooled block of neutron moderator. A moderator for neutrons is a material which scatters the neutrons produced by fission so that their energy is reduced from the MeV energies typical of nuclear reactions down to the meV energies typical of atomic motions in thermal equilibrium at approximately room temperature. The energy spectrum produced by such moderators is a Maxwellian distribution with a characteristic temperature close to that of the moderator itself—hence the name thermal neutrons. An example of such a spectrum is shown in Fig. 2, with temperature chosen to represent the spectrum seen by the thermal beam tubes at the

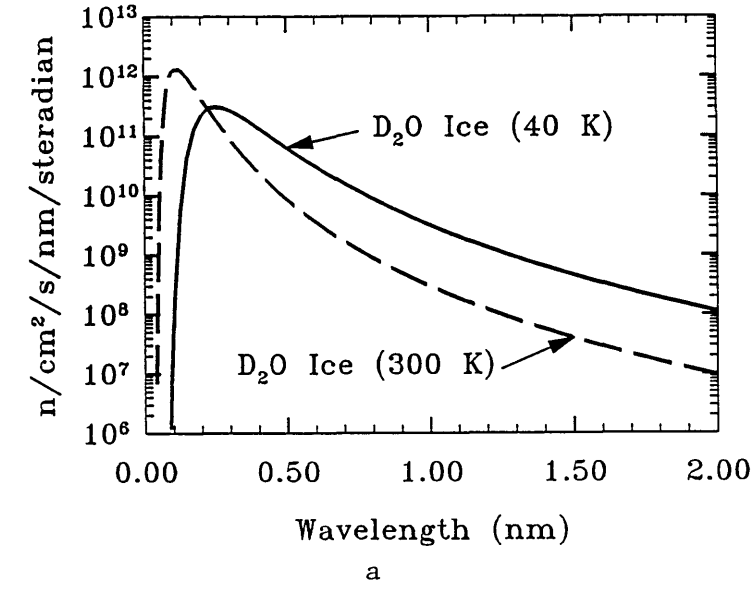

a

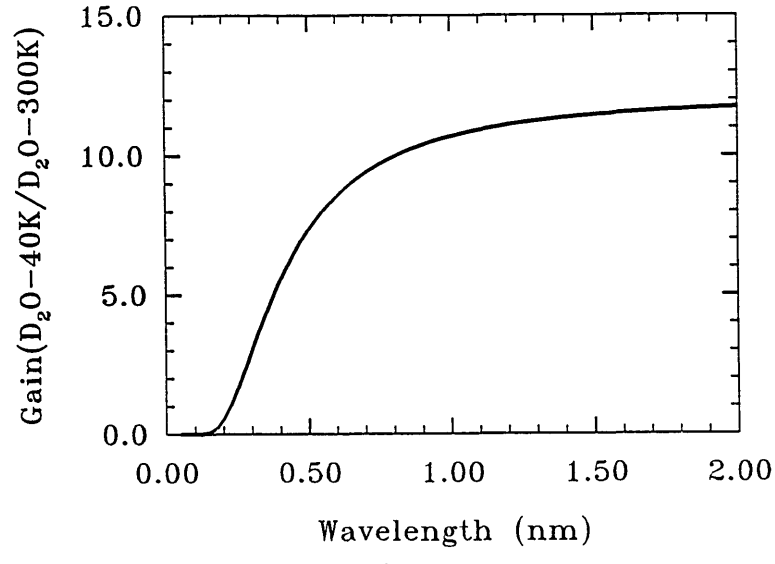

b

Fig. 2. (a) Neutron fluxes for the cold moderator cavity filled with liquid D_2O and D_2O ice. (b) Flux gain, D_2O(ice)/D_2O(liquid), from the data of (a). The moderator temperature of 40 K produces a Maxwellian distribution with an "effective" temperature of 60 K.

NBSR. Cold neutrons are defined as those with energies less than 5 meV, corresponding to 60 K and velocities less than 1000 m/s. However, this cold neutron port was not utilized at the beginning, and the development concentrated on the thermal neutron beams and facilities. In 1985, the development of the cryogenic port began in earnest with funding of a cold neutron initiative (made possible by preliminary funding from the NBS director in 1984). As discussed below, events have shown that the large area allowed for a cold source in the NBSR design and the very wide range of angular access (over 30°) was a key to providing a unique opportunity to create the only fully internationally competitive cold neutron research capability in the United States.

The interest in applications of cold neutron techniques was stimulated by the success of the Western European research reactors, most notably the Institut Laue Langevin (ILL) in Grenoble, France. Among the many successes of these facilities was the demonstration of the power of a technique called Small Angle Neutron Scattering (SANS) as applied to a wide variety of problems in polymers, biology, metallurgy, and other areas in which structures with distance scales in the 1–100 nm range were critical. The United States was highly competitive in atomic and molecular scale measurements with thermal neutrons, but was far behind in utilization of longer wavelength neutrons, and the SANS technique was the area addressed first. In 1979 one of the first competence proposals funded by the NBS director was to develop a SANS spectrometer and research program at the NBSR, which led to the 8 m SANS on a beam from the cold source port (but without a cold source installed). This facility was a success, and the use of the instrument for a wide variety of studies grew rapidly, with users from many parts of NBS and outside organizations. It was clear that the productivity and capability of this instrument could be dramatically increased by completion of the cold source itself, since the instrument used neutrons with velocities below 1000 m/s, and was therefore working with the tail of the 350 K Maxwellian spectrum characteristic of the NBSR moderator. At the same time, it was evident that many other measurements could be greatly improved by the use of cold neutrons, if the cold source were developed and space were available to develop the proper instruments.

Another of the developments that had been demonstrated at the ILL was the use of long neutron "guides" to conduct intense beams of neutrons 10's of meters away from the reactor into large experimental halls (generally called guide halls). These guides are based on the total internal reflection of neutrons below a critical angle that is a function of the reflecting material and neutron energy. This reflection is exactly analogous to optical reflection, and the critical angle depends on the deBroglie wavelength of the neutron, which is inversely proportional to neutron velocity and equal to 0.4 nm at 1000 m/s. Thus, guides work best at long wavelengths and therefore for cold neutrons. The guides themselves consist of pipes which are made of optically flat glass coated with materials of high scattering power (generally an isotope of nickel) and which are evacuated in order to reduce losses due to air scattering. Using these devices, it is possible to transport intense beams of cold neutrons out of the reactor building with losses of less than 1%/m, thus opening up the possibility of creating many new types of measurement capability in a large new experimental hall.

Based on these considerations, NBS proposed a cold neutron facility for the FY1985 budget, and it was included in the budget submission to the Department of Commerce and OMB for that year. However, many proposals for new facilities were submitted at that time from different agencies, so the Office of Science and Technology Policy requested a national study to set priorities for these facilities. As a result, the National Academy of Sciences commissioned a study by a panel of the National Research Council on "Major Facilities for Materials Sciences and Related Disciplines" chaired by Professor F. Seitz and Dr. D. Eastman to set national priorities. At the same time, a smaller initiative to develop the cold neutron source at the NBSR and to conduct research using two prototype instruments was funded in the FY1985 budget at the $1.5M level. With this funding, work on the cold source accelerated, and by 1987, the present cold source was installed and operating with the two prototype instruments—an improved 8 m SANS spectrometer and a time-of-flight spectrometer for studying dynamical processes. At the same time, the full NBS proposal for a Cold Neutron Research Facility was presented to the Seitz-Eastman committee.

In 1985, the committee reported its findings as a list of priorities divided into two different categories—new facilities, and new capabilities at existing facilities. In the last category, the proposals for cold neutron capabilities were given the highest priority for immediate funding. This priority was a recognition of the large contributions of cold neu-

tron measurement to many areas of research, and of the fact that the United States was seriously behind in these techniques, at a time that Western Europe had invested over $150M in such facilities, and Japan was about to build a new reactor largely driven by cold neutron research needs.

In response, NBS and the Department of Commerce submitted the CNRF proposal for the FY1986 budget, and it was included in the President's budget submission to Congress. Although the need for the facility was accepted and no technical faults were seen, this initiative was not funded for FY1986, and was resubmitted for FY1987. The original proposal was for a short project of 3 years, with a total construction budget of $25M. In FY1987, a proposal for the CNRF with the same budget, but stretched over 1987–1992 was approved by the Congress, and in the late fall of 1986, detailed design of the facility began. This approval gave NBS the mission of building a national facility for shared use by researchers from all over the nation that would make available the cold neutron measurement techniques that did not exist anywhere else in the United States. The CNRF that is now becoming operational is the result.

2. Cold Neutron Source

A research reactor operates by the fissioning of uranium, a nuclear reaction which produces neutrons of energies in the range of 1–2 MeV. However, the fission process itself requires neutrons of 8–9 orders of magnitude lower energies (25 meV) to proceed efficiently. For this reason, all thermal reactors require that the fuel be surrounded by "moderators", which slow to thermal energies the neutrons produced by the fission process. These moderators are usually water—in the case of the NBSR, heavy water or D_2O at approximately room temperature. Heavy water has a lower neutron capture cross-section than normal water (H_2O) and so is often used in research reactors, where the goal is to produce the maximum number of neutrons possible for use in beams. At the same time, the moderator also provides neutrons which are the right energy for use in most neutron research, with a typical energy of 25 meV, corresponding to a velocity of 2200 m/s, and a deBroglie wavelength of 0.18 nm. The neutrons are used for experiments either by inserting samples into the reactor itself or by extracting beams through holes (beam tubes) which penetrate the shielding.

As shown in Fig. 2, even for the normal D_2O moderator ($T \sim 40$ °C) there are some neutrons with energy below 5 meV (cold neutrons), but the number is small because they come from the tail of the spectrum. The number of these neutrons could obviously be increased by lowering the temperature of the moderator, and this is the basis for the idea of a cold neutron "source." Of course, a cold neutron source does not generate cold neutrons—rather, it further moderates existing neutrons to lower effective temperatures. As a result, cold moderators or sources are never as efficient as might be expected on the naive idea of simply reducing the effective temperature. There are additional losses which reduce the gain by varying amounts, depending on the details of the reactor, moderator geometry, moderator properties, etc., and in any given case, different compromises must be made. Also, there are stringent safety requirements which impose additional constraints.

A schematic diagram of the existing cold neutron source is shown in Fig. 3, with the neutron guides (see description below) installed. The main components are the lead/bismuth shield lining the beam port (required to reduce γ-ray heating in the moderator), a cryostat containing the D_2O ice (which is surrounded by an insulating vacuum and a helium blanket), and the cooling tubes (which carry helium gas at 30–40 K to cool the source). The other main component (not shown) is a helium gas refrigerator which supplies 1.0 KW of cooling at a helium mass flow rate of 28 g/s. The cryostat is fabricated of a magnesium alloy, in order to reduce the heat load on the system and increase the neutron efficiency. With the reactor operating at 20 MW, the helium gas enters the cryostat at 37 K and exits at 43 K, giving an average temperature in the ice (as a result of thermal conductivity) of approximately 45 K. This moderator was chosen for the first cold source in the NBSR on the basis of good neutron properties and safety considerations. The spectrum which this moderator produces is shown in Fig. 2, and the measured gain which it provides for cold neutrons is of the order of 10. (Gain is defined as the measured ratio of the number of cold neutrons produced with the moderator filled with D_2O ice at low temperature to the number produced with the moderator filled with D_2O at 300 K.) By direct experiment (as well as calculation), we have determined that this ratio is maximized by the addition of 7% H_2O. The moderator is, in fact, operated this way. This moderator has been in service since 1987, and system reliability is now quite good (>98%

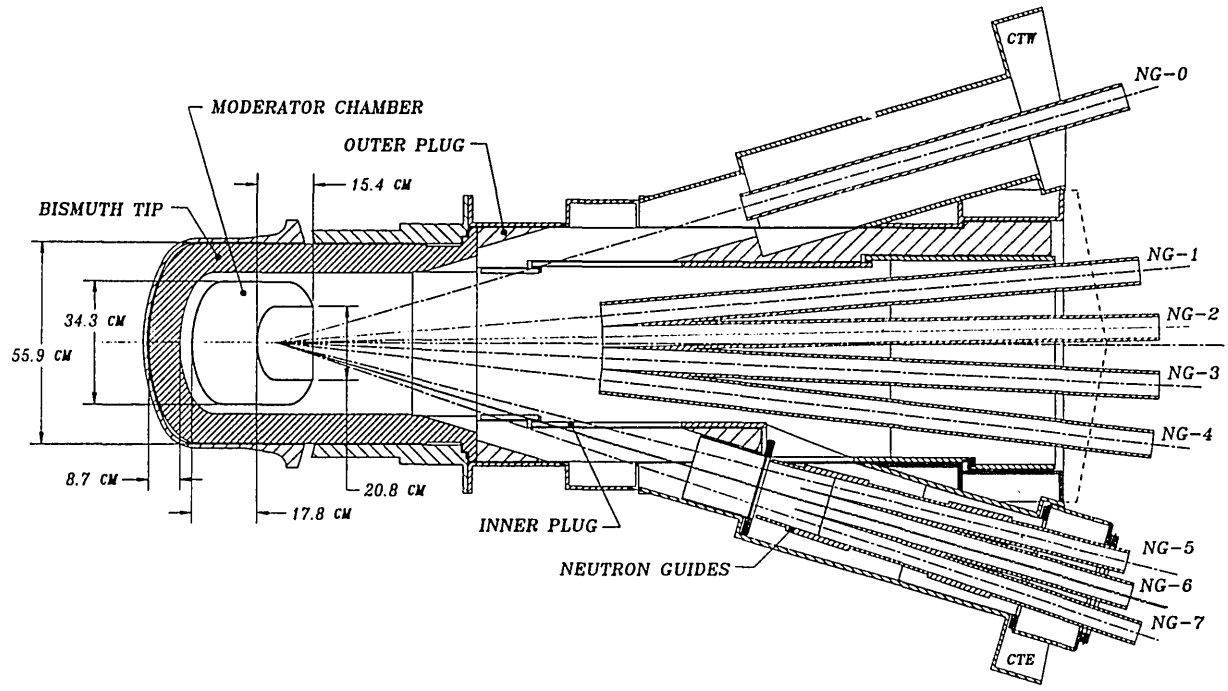

Fig. 3. The D_2O cold source at the NBSR.

availability). As a result of radiation damage of the solid ice, the moderator is warmed up to ~80–100 K every 2 days to allow recombination of the constituents produced by radiolysis.

With this source in operation, we have turned our attention to a second generation source which will utilize liquid hydrogen. Such a source offers several advantages over the ice source, but also imposes several new constraints and safety issues. The primary gain comes from the fact that hydrogen remains liquid down to 14 K, and liquids, because of their diffusional motions, are—in general—better neutron moderators for low energies (the relatively low energy rotational levels of the hydrogen molecule are also extremely beneficial). The liquid source is also easier to operate, since the moderating material can be cooled outside the reactor, and flowed into the source. This simplifies the associated plumbing, since fewer lines must be maintained in high radiation fields. The main drawback comes from the necessity to handle relatively large volumes of hydrogen, with the potential safety problems that this implies. However, it should be noted that the entire inventory is the equivalent of less than one standard gas bottle.

A schematic drawing of the proposed hydrogen source is shown in Fig. 4, from which several features should be noted. First, as a result of the lower density of hydrogen, the lead/bismuth shield can be left out, with a resultant gain in intensity and simplicity. Second, the source itself is much thinner, as

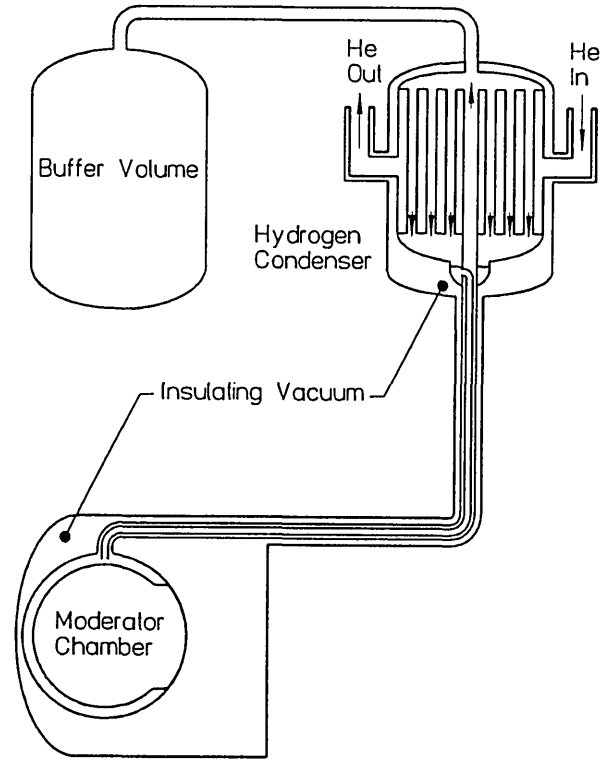

Fig. 4. The H_2 cold source to be installed at the NBSR.

a result of the high scattering power of hydrogen. The moderator chamber is a 2 cm thick, spherical shell with an outside diameter of 32 cm, containing about 5 L of liquid hydrogen. A 20 cm diameter reentrant hole fully illuminates the guides with cold neutrons from the flux-trap in the interior of the sphere. Safety and simplicity are the dominant design considerations of the source, shown schematically in Fig. 4. A large buffer volume is open to the moderator chamber so that the entire liquid hydrogen inventory can vaporize and expand into the buffer without over-pressurizing the system. The cooling mechanism is a gravity fed flow of liquid into the moderator chamber, where evaporation removes the heat produced by the radiation. The hydrogen is in a cooled loop, reliquified outside the beam port, completing the naturally circulating thermosyphon requiring no pumps or moving parts. The entire hydrogen system is surrounded by an insulating vacuum, which is in turn surrounded by gaseous helium (not shown in Fig. 4) in order to prevent the entry of oxygen into any volume containing hydrogen. This is a central part of the safety philosophy—namely, to limit the oxygen available for combination with hydrogen. The liquefaction is done in the hydrogen condenser, with cooling provided by a 3.5 KW helium gas refrigerator. The first engineering tests of the proposed new source will take place this summer, and a full safety analysis is being prepared for submission to the Nuclear Regulatory Commission this year. Calculations of the performance of this source (performed both by analytical and Monte Carlo methods) indicate a further gain of cold neutrons available for experiments of at least a factor of two over the existing source, with somewhat larger gains at the lower energies.

3. The Neutron Guides

Because of the wave properties of the neutron, it is necessary to consider an index of refraction for different materials in which neutrons propagate, and to take account of differences in these indices as the neutrons cross surfaces between materials of different properties. As originally shown by Fermi (see following paper by N. F. Berk), the index of refraction, n, of a material is given by

$$n^2 = 1 - \lambda^2 \cdot N \cdot a_c / \pi \qquad (1)$$

where λ is the neutron wavelength, N is the number of atoms per unit volume, and a_c is the coherent neutron scattering length (scattering cross-section $= 4\pi a_c^2$). Just as is the case for visible light, the difference in indices of refraction of two media can lead to total reflection at a surface. For the case of neutrons, this leads to an expression for the critical angle γ_c in terms of the neutron wavelength and materials properties (assuming a vacuum-material interface) as

$$\gamma_c = \lambda \cdot (N \cdot a_c / \pi)^{1/2} \qquad (2)$$

with γ_c in radians. In contrast to visible light, typical values in the neutron case for n and γ_c are 10^{-5} and 1°, respectively. In principle, the reflectivity is unity for angles less than the critical one, but in practice the reflectivity is less than this for various reasons, such as surface roughness and variations in coating thickness. This phenomenon is the basis for the manufacture of "neutron guides," which are used in the CNRF.

The actual neutron guides are long tubes of rectangular cross section (either 120×50 or 150×60 mm^2), made from boron containing glass, polished on the inside to an rms surface roughness of 2 nm and a flatness equivalent to 10^{-4} rad, coated with approximately 80 nm of ^{58}Ni (this isotope of nickel has the best neutron properties of any material readily available), and evacuated most of their length. The guides are manufactured commercially in 1500 mm lengths (which are in turn fabricated from 500 mm length components), and then aligned to the requisite 10^{-4} rad over the entire length (up to 70 m) by optical techniques after being mounted on I-beam supports. When aligned, the 1500 mm lengths are joined together by a silicone based sealant (the gaps are less than 0.25 mm), sealed at the ends by windows of Al or Mg, and helium leak tested. They are then evacuated by turbo-molecular pumps, and surrounded by neutron and γ-ray shielding. These guides conduct the neutrons from the cold source described above (see Fig. 3) out through the reactor confinement building walls into the experimental hall described below. In order to maintain the integrity of the reactor building containment, a "shutter" is inserted at the wall which closes automatically by gravity whenever the reactor is shut down, providing a complete seal of the building. These shutters also serve to interrupt the neutron beams when desired, so that work can be performed in the experimental hall while the reactor is operating.

Four guides, NG-3, NG-5, NG-6, and NG-7, have now been installed, and their performance has been measured, showing that the losses (due primarily to reflectivity losses resulting from surface roughness) are less than 0.7%/m. Thus, beams

can be transported over several tens of meters (the longest guide is 71 m), with low loss. As a result, many new experimental stations can be built, increasing the utilization of a unique facility. In addition, since guides transport cold neutrons preferentially, unwanted radiation is reduced in inverse proportion to the square of the distance from the source.

The actual number of neutrons transmitted by the guides depends on the solid angle accepted, which is determined by the critical angle for total reflection, as defined above. For ^{58}Ni, $\gamma_c = 0.02\ \lambda$, where λ is the neutron wavelength in nm, and γ_c is the angle of reflection in radians. Since both senses of angle are transmitted, the total divergence accepted is $2\gamma_c$., in both the horizontal and vertical directions, giving a solid angle of $4\gamma_c^2$ sterad. While this is quite adequate for many experiments using cold neutrons, larger divergences would be useful in some cases, and for shorter wavelength (thermal) neutrons, the transmission is almost too small to be useful.

For several years, coatings with larger critical angles have been sought, and in fact so-called supermirrors have been developed which consist of many layers of materials with different neutron properties, arranged in a particular sequence. These devices can double, triple, or even quadruple the critical angle, but until recently, the reflectivities were too low for use in guides, where many reflections take place before a neutron reaches the end of the guide (the average number of reflections is directly proportional to the critical angle, and inversely proportional to the guide dimensions perpendicular to the beam direction). Researchers at NIST, in collaboration with Oak Ridge and Brookhaven National Laboratories, and with two small industrial firms, have recently demonstrated that these devices can be made with the requisite reflectivity for use in guides, at least on the laboratory scale. We are planning to use these coatings for at least the tops and bottoms of the three remaining guides.

4. The Experimental Hall and Associated Facilities

The new experimental hall, often referred to as the guide hall, is a slab on grade structure 61 m long × 30 m wide × 13.7 m high built adjacent to the north wall of the original reactor building. The design floor loading is ~96000 N/m^2 (2000 lb/ft^2) in order to support the massive instruments and shielding associated with neutron beams. The walls, roof supports, and rails for a 20 ton crane are supported on augured cast-in-place piles, which are independent of the floor structure for vibration isolation. In addition, reinforced concrete beams, independently supported on their own piles, are laid out along the individual guide tube directions, providing a stable, vibration-free platform that allows the guides to retain their precision alignment to 10^{-4} rad even when heavy loads are moved on the experimental floor.

For radiation protection, the guides are surrounded along their entire length by specially constructed shielding consisting of welded steel tanks filled with either steel shot and paraffin or a paraffin-borax mixture. The shielding is divided into modular pieces with specially designed overlap so that at any point, the shielding can be removed in order to insert instruments as required. In Fig. 5, which is taken facing away from the reactor looking towards the wall, the first three guides (with top shielding removed) and the beam shutters can be seen.

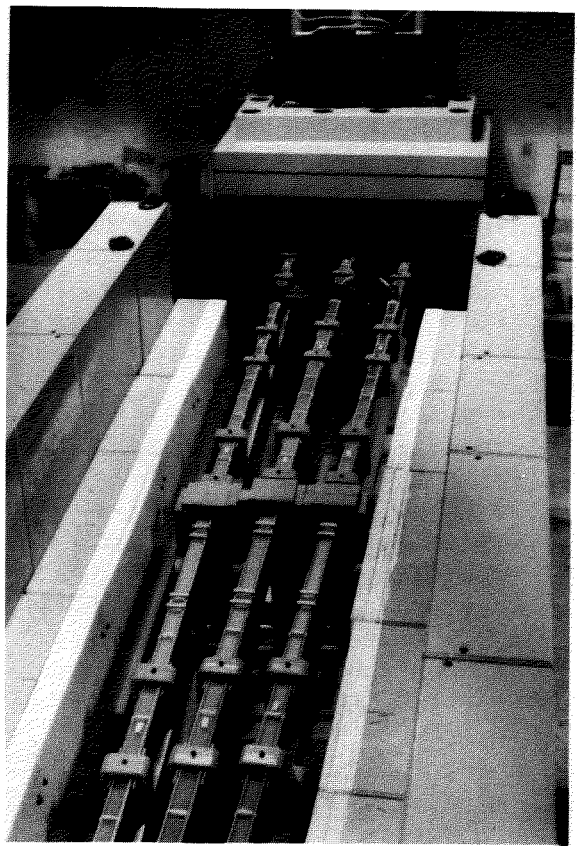

Fig. 5. Neutron guides, NG-5, NG-6, and NG-7, in the NBSR reactor hall.

In order to get the beams into the guide hall, it was first necessary to core-bore seven large diameter holes through the ~8 m thick reinforced concrete wall, after which a stainless steel liner was inserted and grouted into place. The guides were inserted into a 9 m long steel casing, aligned optically, and the entire casing-guide assembly was then aligned onto the guide direction. The ends of the casings are sealed to the reactor building walls, and the empty space between the casing and liners is filled with mineral oil, which is a good neutron shielding material. Outside the wall, the guides are individually assembled from 1.5 m sections supported on I-beams, aligned optically, and joined together with a silicone sealant to form a continuous vacuum tight assembly. The vacuum required for neutron economy is low ($\lesssim$0.1 Pa); but, in order to prevent accumulation of material on the guide surfaces which would reduce the reflectivity, the actual vacuum is substantially better ($\simeq$1 mPa).

Each neutron guide serves several different experimental stations, and the system must allow all stations to operate simultaneously. Therefore, care must be taken in designing the methods used for beam extraction. This is accomplished in one of two different ways—either by dividing the height of the beams, so that a station uses a particular portion of the beam, or by inserting a device (usually a crystal monochromator) in the beam which removes a small fraction of the entire beam allowing the rest to continue for use further downstream. Experimental stations which must use the entire beam, or which must be directly in the beam line, are put at the end positions (which are in great demand). Examples of the latter type of instruments are the Small Angle Neutron Scattering (SANS) instruments, and the neutron lifetime experiment. Several of the instruments at various experimental stations are described in companion papers, which provide more details on the particular arrangements. Figure 6 shows two photographs taken in March 1992 showing the overall layout of the guide hall. Figure 7 shows a schematic drawing of the guide hall and associated instrumentation as it will exist when the facility is finished. As of March 1992, seven stations have been commissioned: an 8 m small-angle neutron scattering (SANS) spectrometer, a cold-neutron depth profiling facility, a neutron-optics test bench, a prompt gamma activation analysis station, a medium resolution time-of-flight spectrometer, a fundamental neutron physics station, and a high-resolution 30 m SANS spectrometer.

In addition to the guide hall, a new office/laboratory wing was built to support the hundreds of research participants that will utilize the CNRF for a broad range of different investigations. Space is provided therein for sample preparation, controlled temperature sample environmental assembly, and simple chemical preparation. A computer terminal room is also provided for simple data reduction and plotting, with terminals connected to a local area network that allows data transfer from the instruments to a local computer. From there, the data can be transferred to various media for transfer to the guest researchers' home institutions for subsequent data analysis.

5. Neutron Instrumentation: An Overview

Neutron instrumentation at the CNRF encompasses a number of experimental techniques which include: those designed to determine the intrinsic properties of the neutron, neutron absorption for chemical analysis, and a range of neutron scattering instruments. In the case of neutron scattering it is appropriate to place in context the detailed discussions of instruments and applications that are described in the following articles.

Neutron scattering comprises a series of related techniques the object of which is to measure either of two cross sections (the details of which are elucidated in the following paper by N. F. Berk)

$d\sigma(Q)/d\Omega$ = the angle-dependent differential cross section integrated over energies.

$d^2\sigma(Q,\omega)/d\Omega d\omega$ = the energy- and angle-dependent double differential cross section.

The power of neutron scattering techniques stems from the enormous range over which Q, the wavevector transfer, and $\hbar\omega$, the energy transfer, can be varied, and the relevant cross sections evaluated. Of particular interest for our purposes here is the extension of range that cold neutrons provide.

In Fig. 8 are shown the size regimes probed by the various techniques by which $d\sigma(Q)/d\Omega$ is measured. It is clear that cold neutrons provide an extremely important enhancement of the SANS technique. This has been utilized for a number of materials science applications such as the evolution of pore size in ceramics and precipitates in metals.

a

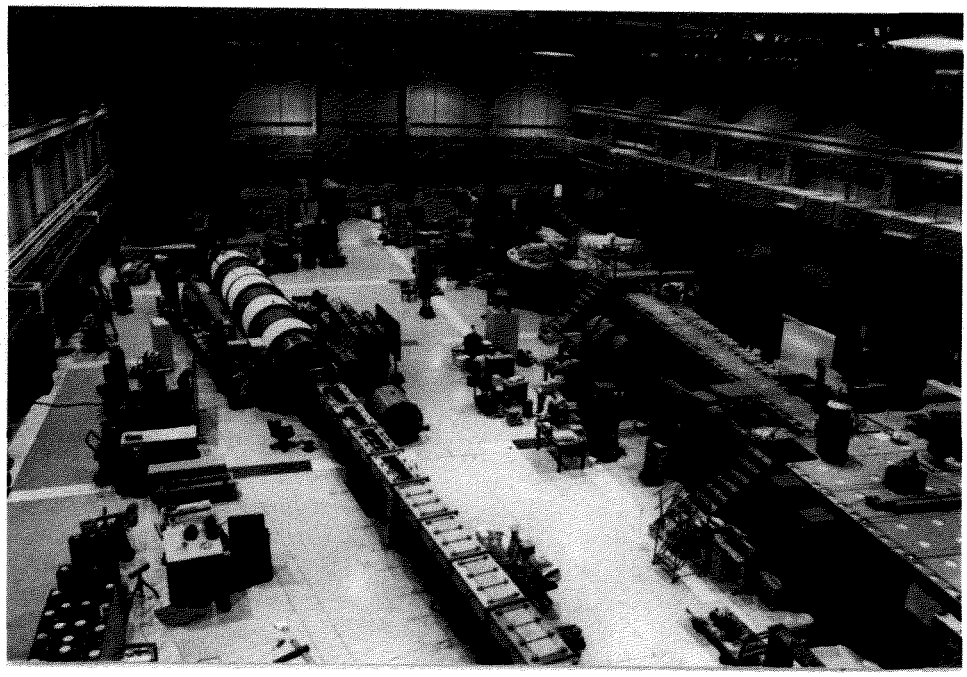

b

Fig. 6. The guide hall (a) looking toward the confinement building; (b) looking away from the confinement building.

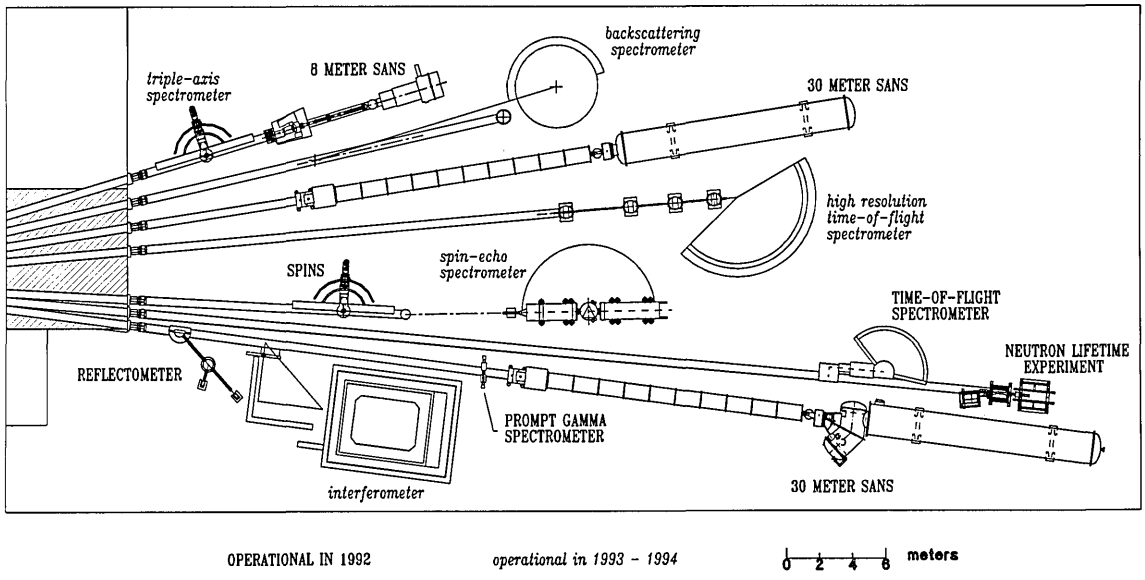

Fig. 7. Floor plan of the CNRF on completion.

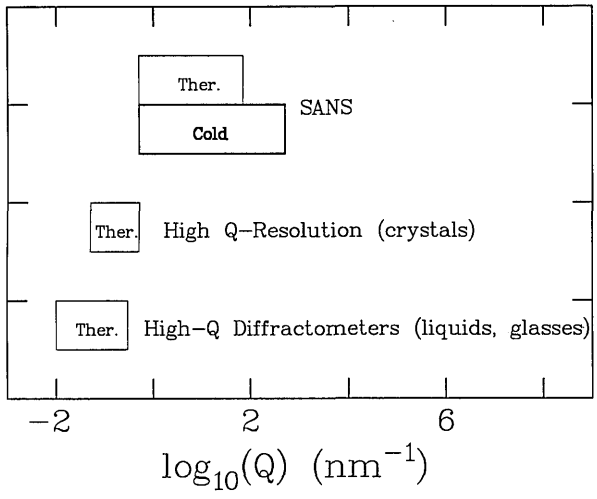

Fig. 8. The wave-vector transfer ranges for neutron instruments which measure $d\sigma/d\Omega$.

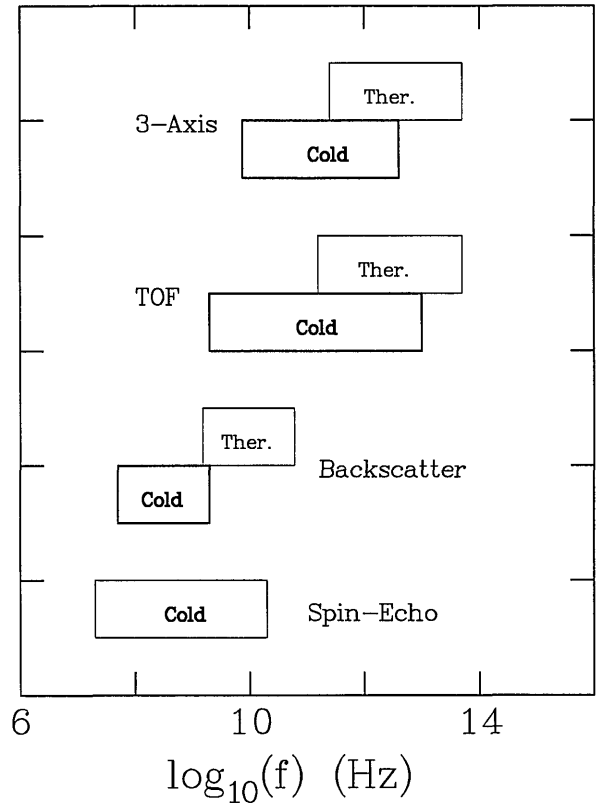

Fig. 9. The accessible vibrational frequency ranges for neutron instruments which measure $d^2\sigma/d\omega d\Omega$.

In Fig. 9 the techniques used to measure $d^2\sigma(Q,\omega)/d\Omega d\omega$ are indicated according to the approximate range of frequency of motion which each probes. It is clear that for a given instrument type, the availability of cold neutrons extends the accessible range of dynamics to significantly lower frequencies.

In Table 1 some representative bound-atom scattering lengths and cross sections are given to illustrate the randomly varying sensitivity of neutrons to various elements. As described in detail in the following paper by N. F. Berk, the scattering length relates to the details of the neutron-nucleus interaction, whereas the cross section is a measure of the probability for scattering.

6. Outside Participation

It is planned that on completion the number of research stations associated with the CNRF will

Table 1. Neutron and x-ray scattering characteristics[a,b,c]

Element/isotope	b_{coh}(fm)	σ_{coh}(fm^2)	σ_{tot}(fm^2)	$f_{x\text{-}ray}$(fm)
^{1}H	−3.74	1.76	81.7	0.2
^{2}H	6.67	5.59	7.6	0.2
C	6.65	5.55	5.55	4.8
N	9.36	11.01	11.50	5.3
O	5.80	4.23	4.23	6.2
Al	3.45	1.50	1.50	15.5
Fe	9.54	11.44	11.83	33.0
W	4.77	2.86	4.86	114.0
U	8.42	8.90	8.91	148.0

[a] Neutron characteristics from V. F. Sears, in Methods of Experimental Physics: Neutron Scattering, Vol. 23A, eds. K. Sköld and D. L. Price, Academic Press, Inc. (1986) pp. 521–550.
[b] b_{coh} = coherent scattering length, σ_{coh} = bound-atom coherent scattering cross section, σ_{tot} = coherent + incoherent scattering cross sections.
[c] Atomic scattering factors for x rays ($\sin\theta/\lambda = 5$ nm^{-1}) from G. E. Bacon, Neutron Diffraction, 3rd Edition, Clarendon Press, Oxford (1975) pp. 38–41.

number 15 (capacity for two or three additional experimental stations will exist at the end of the funded project) and will be of two types. NIST will develop nine experimental stations for the use of the general United States science community. Two-thirds of the available time on these stations will be allocated by a Program Advisory Committee (PAC) on the basis of scientific merit of written proposals. The PAC has been appointed by NIST with a majority of members chosen from outside NIST. The other mode of operation will involve Participating Research Teams (PRTs), which develop and provide continuing support for the additional stations. These PRTs may include NIST although this is not necessary. Proposals from prospective PRTs are selected by the facility manager with the advice of the PAC.

The PRTs are responsible for the design, construction, maintenance, and up-grading of the facilities, in return for which they receive 3/4 of the available time. The remaining time is allocated by the PAC in the usual manner according to the proposal review system. For all instrumental stations, instrument-responsible scientists will be designated to assist users in the performance of their experiments. As of May 1992 PRT agreements include the following:

- Exxon Engineering and Research Corporation has participated in the design and construction of the CNRF's first 30 m high-resolution small-angle neutron scattering (SANS) spectrometer, now operational. The University of Minnesota, through its Center for Interfacial Engineering (a collaboration among academia, government, and some 30 affiliate companies) is also a member of the PRT for this instrument.
- In a special form of PRT, NIST and the National Science Foundation (NSF) are developing a Center for High Resolution Neutron Scattering (CHRNS) for research in chemistry, physics, biology, and materials science at the CNRF. The center, comprising two state-of-the-art neutron research instruments being constructed by NIST with funding from NSF, is open to use by U.S. universities, industries, and government agencies. Approximately 75 percent of the NSF-funded portion of CHRNS will be scheduled entirely by the PAC, with about 25 percent of time set aside for instrument improvement, "breakthrough" experiments, and a small allotment of time for instrument-responsible scientists. The CHRNS instruments are the (second) 30 m SANS spectrometer and one-half of the spin-polarized inelastic neutron scattering (SPINS) spectrometer.
- A cold-neutron reflectometer is being developed by NIST in a PRT with IBM and the University of Minnesota.
- The Organic and Electronic Materials Department of Sandia National Laboratories (SNL) has also entered into a long-term cooperative research agreement with the CNRF. SNL will provide partial funding for development and support costs of the new ultra-high-resolution time-of-flight spectrometer and the new back-reflection spectrometer.
- Additional outside support and cooperation, already in place, includes a grant from Kodak for the chemical-analysis facilities, along with some equipment funding for Fundamental Physics applications by NSF—through the University of Missouri—and Department of Energy, and for cold-neutron crystal spectrometry by Johns Hopkins University. Further participation by outside groups is anticipated before the project is complete in 1993.

7. Outlook

In partnership with industry and government, NIST's mission includes providing services based on science and technology to enhance the competitive posture of the United States in global markets. To underpin the technology programs, NIST has a broad range of scientific programs which are motivated by NIST's charter to provide technical services to the scientific and engineering communities.

The CNRF is an outstanding example of the realization of NIST's new mission in the context of its original charter. In addition to programs of fundamental scientific importance, it provides academic, industrial, and government scientists and engineers with advanced measurement technologies for research directly relevant to the materials, information and communication, chemical, electronics, and biotechnology industries.

Efforts to educate the scientific and engineering communities in the use of neutron techniques have met with dramatic success as evidenced by the increase in research participants over the last several years (even without the CNRF). Since the initiation of the CNRF a number of workshops have been held which have focussed on the broad range of cold neutron applications: from fundamental studies of the neutron, to macromolecules and microstructure studies, to cold neutron spectroscopy, to chemical analysis of advanced materials.

In the following papers some of the instruments of the CNRF are described in detail. Within each paper an attempt is made to illustrate the variety of applications possible for that instrument type, and insofar as possible, how CNRF capabilities compare with or extend the state-of-the-art of cold neutron research worldwide.

About the authors: Henry J. Prask is a Scientific Assistant in the Reactor Radiation Division of the NIST Materials Science and Engineering Laboratory. J. Michael Rowe is Chief of the Reactor Radiation Division and Manager, Cold Neutron Project. John J. Rush is a Group Leader, Neutron Condensed Matter Science Group, and Ivan G. Schröder is a Technical Leader, Cold Neutron Project in the Reactor Radiation Division. The National Institute of Standards and Technology is an agency of the Technology Administration, U.S. Department of Commerce.

Volume 98, Number 1, January–February 1993
Journal of Research of the National Institute of Standards and Technology

[J. Res. Natl. Inst. Stand. Technol. 98, 15 (1993)]

Outline of Neutron Scattering Formalism

Volume 98 | Number 1 | January–February 1993

N. F. Berk

National Institute of Standards and Technology,
Gaithersburg, MD 20899

Neutron scattering formalism is briefly surveyed. Topics touched upon include coherent and incoherent scattering, bound and free cross-sections, the Van Hove formalism, magnetic scattering, elastic scattering, the static approximation, sum rules, small angle scattering, inelastic scattering, thermal diffuse scattering, quasielastic scattering, and neutron optics.

Key words: elastic scattering; inelastic scattering; neutron scattering; neutron scattering theory; quasielastic scattering; small angle scattering.

Accepted: July 10, 1992

1. Introduction

Neutron scattering provides a direct measure of spatial and temporal correlations of atomic positions and magnetic states of the target system. Thus, to a considerable extent the theory of neutron scattering is aimed at calculating physical quantities that are of interest beyond the scattering technique itself. This outline is a short and highly selective tour through the basic mathematics and concepts of the canonical neutron scattering formalism, which may provide useful preparation for the more focused contributions that follow in this collection. Our approach is didactic but also takes much for granted. We start abruptly, for example, with the general formula for the differential cross section and along the way leave out a great deal that could be said; important topics are ignored, and some of the discussions may seem to end prematurely. If terse, however, the outline also strives to be logical and cohesive and to set out a digestable overview of what is, after all, a far-ranging discipline.

Fortunately for the reader, excellent and well-known introductory articles and texts are available, as well as advanced treatments of both general and specialized interest. References [1-18] of this article serve as a list of some of these. Scherm's [13] succinct and lively tutorial on the mathematical formalism of neutron scattering was the inspiration for the present treatment, which borrows liberally from it. The opening chapters of Bée's book [4] also give a thorough and readable survey of the formalism. The introductory review by Price and Sköld [10] has broad scope and provides a balanced development of both theoretical and practical material, while the authoritative collection of articles edited by Sköld and Price [17] reaches into many areas of application. Squires' clear and efficient textbook [18] is a standard and helpfully incorporates mathematical preparation that other sources often leave out. The treatise by Marshall and Lovesey [8] is a classic presentation of the formalism.

The author is indebted to colleagues who perused drafts of this article at various stages of preparation. Even in its brevity it tries to convey their insightful comments.

2. Basic Formulas

2.1 The Born Approximation

Our starting point for this outline of neutron scattering formalism is the definition of the double-differential scattering cross-section per particle, as obtained from the Born approximation:

$$\left(\frac{\mathrm{d}^2\sigma}{\mathrm{d}\Omega \mathrm{d}\omega}\right)_{s_0\to s} = \frac{1}{N}\left(\frac{m}{2\pi\hbar}\right)^2 \frac{k}{k_0} \sum_{n_0,n} p(n_0)$$

$$|\langle \boldsymbol{k}, s, n, |V|\boldsymbol{k}_0, s_0, n_0\rangle|^2 \, \delta\left(\frac{E_n - E_{n_0}}{\hbar} - \omega\right) , \quad (1)$$

where Ω denotes the scattering solid angle, ω, the angular frequency corresponding to energy transfer $\hbar\omega$, m, the neutron mass and N, the number of nuclei in the scattering system. Note that in some treatments, the differential cross-section is defined with respect to an energy differential, which introduces a dimensional factor of $\hbar^{-1}$ on the right-hand side of Eq. (1). The incident neutron beam is in the plane-wave state $|\boldsymbol{k}_0, s_0\rangle$, where $\boldsymbol{k}_0$ is the incident wavevector and s_0 is the incident spin. The scattered beam is in the state $|\boldsymbol{k}, s\rangle$, where $\boldsymbol{k}$ and s refer to the outgoing beam. The fundamental formula in Eq. (1) effectively is the product of a kinematical factor, k/k_0, with the transition rate from Fermi's golden rule. The matrix element of the neutron-scatterer interaction V is taken in the product representation

$$|\boldsymbol{k}, s, n\rangle = |\boldsymbol{k}, s\rangle |n\rangle ,$$

where

$$H|n\rangle = E_n|n\rangle$$

and H is the Hamiltonian of the scatterer. The summation over the initial states of the scatterer is weighted by a probability density, $p(n_0)$. The momentum transferred *to* the scatterer by the neutron beam is $\hbar\boldsymbol{Q}$, where

$$\boldsymbol{Q} = \boldsymbol{k}_0 - \boldsymbol{k} \quad (2)$$

is called the scattering wavevector, or, more often than not, simply the scattering "vector." We designate the energies of an incident and scattered neutron as E_0 and E, respectively. Then, consistent with the right hand side of Eq. (1), the angular frequency ω is determined by the neutron energy, $E_0 - E$, transferred *to* the scatterer:

$$\hbar\omega = \frac{\hbar^2}{2m}(k_0^2 - k^2) . \quad (3)$$

Thus positive ω corresponds to excitation of the target, which is convenient in calculations which focus on the properties of the scatterer rather than on the analysis and configuration of the measuring instrument. Indeed, with respect to the probing neutron, $\omega > 0$ means energy *loss* or "down" scattering, while $\omega < 0$ represents energy *gain* or "up" scattering.

2.2 Nuclear Scattering in Homogeneous Systems

For nuclear scattering the interaction potential is well-approximated by the Fermi pseudopotential

$$V(\boldsymbol{r}) = \frac{2\pi\hbar^2}{m} \sum_j b_j \, \delta(\boldsymbol{r} - \boldsymbol{R}_j) , \quad (4)$$

where b_j is the isotope- and spin-dependent scattering length of the neutron-nuclear interaction, and the summation is over all of the nuclei in the system. The scattering lengths in Eq. (4) are defined for fixed nuclei in the laboratory frame, and are generally referred to as "bound " (or "bound-atom") scattering lengths. For unbound nuclei, the bound scattering lengths are replaced by "free" scattering lengths,

$$a_i = \frac{A_i}{A_i + 1} b_i , \quad (5)$$

where the A_i are the nuclear atomic weights. The prefactor in Eq. (5) stems from the reduced mass of the interacting neutron-nucleus pair. The bound scattering lengths, in fact, are always the correct choice, provided the scattering is calculated correctly, as illustrated below by the case of the ideal gas. Thus tabulations of scattering lengths (e.g., the comprehensive table by Sears [14]) give the bound values. For most nuclei, of course, the differences between the bound and free scattering lengths are relatively small, but hydrogen and deuterium are notable exceptions.

For a neutron beam of arbitrary spin polarization, the scattered intensity is determined by

$$\frac{d^2\sigma}{d\Omega\, d\omega} = \sum_{s_0,s} p(s_0)\left(\frac{d^2\sigma}{d\Omega\, d\omega}\right)_{s_0\to s} \tag{6}$$

where $p(\frac{1}{2})-p(-\frac{1}{2})$ is the polarization state of the beam. For an unpolarized beam, $p(\pm\frac{1}{2})=\frac{1}{2}$, while for nonmagnetic interactions the cross-section is independent of s_0. When there is no knowledge connecting the internal (isotopic and spin) states of the scattering nuclei to their positions, the observed cross-section is an average over the nuclear degrees of freedom:

$$\frac{d^2\sigma}{d\Omega\, d\omega} = \left\langle \frac{d^2\sigma}{d\Omega\, d\omega} \right\rangle_{\text{nuc}} . \tag{7}$$

It is generally an excellent approximation to assume that there are no correlations between the internal states of different nuclei. As a consequence,

$$\overline{b_i b_j} = \overline{b}_i\, \overline{b}_j, \quad i \neq j,$$

where the overbar denotes the average over nuclear internal degrees of freedom. Then

$$\overline{b_i b_j} = b_{\text{inc}}^2 \delta_{ij} + b_{\text{coh}}^2 , \tag{8}$$

where

$$\begin{aligned} b_{\text{coh}} &= \overline{b}, \quad \text{and} \\ b_{\text{inc}}^2 &= \overline{b^2} - \overline{b}^2 , \end{aligned} \tag{9}$$

define the interactions for nuclear *coherent* and *incoherent* scattering. The effective scattering lengths, b_{inc} and b_{coh}, are often expressed in terms of bound cross-sections as,

$$\sigma_\alpha = 4\pi b_\alpha^2 , \tag{10}$$

where

$$\alpha = \begin{cases} \text{"coh"}, \\ \text{"inc"}. \end{cases} \tag{11}$$

Therefore,

$$\sigma_{\text{inc}} + \sigma_{\text{coh}} = 4\pi \overline{b^2} . \tag{12}$$

Equation (8) can be rewritten even more compactly as

$$\overline{b_i b_j} = \sum_\alpha \xi_{i,j}^\alpha b_\alpha^2 , \tag{13}$$

where

$$\xi_{i,j}^\alpha = \begin{cases} 1 & \text{for } \alpha = \text{"coh"}, \\ \delta_{i,j} & \text{for } \alpha = \text{"inc"}. \end{cases} \tag{14}$$

The combination of Eqs. (1), (4), (7), (13) and (14) then gives

$$\frac{d^2\sigma}{d\Omega\, d\omega} = \frac{k}{4\pi k_0} \sum_\alpha \sigma_\alpha S_\alpha(\mathbf{Q},\omega) , \tag{15}$$

where

$$S_\alpha(\mathbf{Q},\omega) = \frac{1}{N} \sum_{n_0,n} p(n_0) \sum_{i,j} \xi_{i,j}^\alpha \langle n_0 | e^{-i\mathbf{Q}\cdot\mathbf{R}_j} | n \rangle \langle n | e^{i\mathbf{Q}\cdot\mathbf{R}_i} | n_0 \rangle \delta\left(\frac{E_n - E_{n_0}}{\hbar} - \omega\right) . \tag{16}$$

Explicitly, these are:

$$S_{\text{coh}}(\mathbf{Q},\omega) = \frac{1}{N} \sum_{n_0,n} p(n_0) \sum_{i,j} \langle n_0 | e^{-i\mathbf{Q}\cdot\mathbf{R}_j} | n \rangle \langle n | e^{i\mathbf{Q}\cdot\mathbf{R}_i} | n_0 \rangle \delta\left(\frac{E_n - E_{n_0}}{\hbar} - \omega\right) , \tag{17}$$

and

$$S_{\text{inc}}(\mathbf{Q},\omega) = \frac{1}{N} \sum_{n_0,n} p(n_0) \sum_{i} |\langle n | e^{i\mathbf{Q}\cdot\mathbf{R}_j} | n_0 \rangle|^2 \delta\left(\frac{E_n - E_{n_0}}{\hbar} - \omega\right) . \tag{18}$$

Notice that the site summation in $S_{coh}(\mathbf{Q},\omega)$ is unrestricted and thus includes the summation in $S_{inc}(\mathbf{Q},\omega)$. The total cross-section is obtained from

$$\sigma_{total} = \int\int_{-\infty}^{E_0/\hbar} \frac{d^2\sigma}{d\Omega\, d\omega}\, d\Omega\, d\omega\,. \qquad (19)$$

In the upper limit, $E_0 = \hbar^2 k_0^2/2m$ is the incident energy, the largest possible neutron energy loss. Often, however, ω-integral is well-approximated by taking the upper limit to ∞. The quantity

$$\Sigma = \frac{N}{V}\sigma_{total}\,, \qquad (20)$$

for N scattering nuclei in sample volume V, is called the *macroscopic* cross-section and is just the inverse of the scattering mean free path.

The total cross-section, Eq. (19), depends on the incident neutron energy; note, for example, the factor $k_0 = \sqrt{2mE_0}/\hbar$ in Eq. (1). The E_0-dependence of total cross-section can be obtained analytically for the case of neutron scattering by an ideal gas. The result shows that $\sigma_{total} \propto E_0^{-1/2}$ for $E_0 \to 0$, as expected from the kinematics, while for $E_0 \gg k_B T/A$, the asymptotic scattering is

$$\sigma_{total} = \left(\frac{A}{A+1}\right)^2 (\sigma_{inc} + \sigma_{coh})\,,$$

which is just the free cross-section. This renormalization of the bound cross-sections at high incident energy is brought about by the recoil kinetic energy of the impulsive neutron-atom collisions and is observed in condensed matter.

The relation in Eq. (15) is the basic law of nonmagnetic neutron scattering from homogeneous systems. Generalizations to heterogeneous nuclear scattering and magnetic scattering, described below, depart only slightly from this archetype. Thus (nuclear) neutron scattering is a sum of *coherent* and *incoherent* contributions, each of which conveys different kinds of information about the scattering system. Only $S_{coh}(\mathbf{Q},\omega)$ expressly depends on the relative positions and motions of the nuclei and thus provides explicit knowledge of structure and collective dynamics. In contrast, $S_{inc}(\mathbf{Q},\omega)$ discloses no spatial structure and only reveals the motions of individual particles. For example, while coherent scattering can measure a phonon dispersion curve, ω vs $\mathbf{Q}$, incoherent scattering can only measure a phonon density of states, $N(\omega)$. Needless to say, a density of states is often just the information desired.

The weights of coherent and incoherent scattering in the measurement are determined—for a homogeneous system—by σ_{coh} and σ_{inc}, which vary randomly from one nuclear species to another. Most nuclei are stronger coherent scatterers than incoherent scatters, and a few even scatter *only* coherently. For example, if we define

$$f_\alpha = \frac{\sigma_\alpha}{\sigma_{total}}\,, \qquad (21)$$

then $f_{coh} = 1$ for the abundant isotopes of Al, C, and O, while $f_{coh} \geq 0.97$ for Mg and Fe. Some nuclei scatter mostly *incoherently*. For example, $f_{inc}(V) = 0.995$ and $f_{inc}(Co) = 0.84$. Hydrogen, $f_{inc}(H) = 0.98$, is a singular example of an incoherent scatterer. Its total cross-section, $\sigma_{total}(H) = 82$ barns (1 barn $= 10^{-28} m^2$), is by far the largest among the elements and, of course, it is abundant in many materials. Hydrogen in hydrated compounds and in hydrocarbons causes significant incoherent scattering, which often masks the desired coherent scattering in structure determinations. Indeed, in small angle neutron scattering, water scattering, which is virtually independent of $\mathbf{Q}$ in the range of interest, is used to calibrate area detectors for spatial nonuniformity. Deuterium scatters incoherently, as well, but actually is a stronger coherent scatterer, with $f_{coh}(D) = 0.74$. Hydrogen and deuterium also are readily dissolved in many metals as a highly mobile interstitial impurity. Incoherent neutron scattering thus probes hydrogen vibrations and transport in these metals: in $S_{inc}(\mathbf{Q},\omega)$, the position operator, $\mathbf{R}_i(t)$, then refers to only to H if the host metal is a coherent scatterer.

In heterogeneous nuclear systems, Eq. (15) is replaced by

$$\frac{d^2\sigma}{d\Omega\, d\omega} = \frac{k}{k_0}\sum_\alpha S_\alpha^{het}(\mathbf{Q},\omega)\,, \qquad (22)$$

where

$$S_\alpha^{het}(\mathbf{Q},\omega) = \frac{1}{N}\sum_{n_0,n} p(n_0)\sum_{i,j} \Xi_{i,j}^{\alpha}$$

$$\langle n_0|e^{-i\mathbf{Q}\cdot\mathbf{R}_j}|n\rangle\langle n|e^{i\mathbf{Q}\cdot\mathbf{R}_i}|n_0\rangle\,\delta\left(\frac{E_n - E_{n_0}}{\hbar} - \omega\right), \qquad (23)$$

and where the ξ-function defined in Eq. (14) has been extended to the Ξ-function,

$$\Xi_{i,j}^{\alpha} = \begin{cases} b_{\mathrm{coh},i}\, b_{\mathrm{coh},j} & \text{for } \alpha = \text{"coh"}, \\ \delta_{i,j}\, b_{\mathrm{inc},i}^2 & \text{for } \alpha = \text{"inc"}. \end{cases} \quad (24)$$

Thus, in heterogeneous systems, including crystals with bases, the coherent scattering is also sensitive to the *signs* of the constituent b_{coh}-values, which also vary randomly with species, although $b_{\mathrm{coh}} > 0$ in most cases. For example $b_{\mathrm{coh}}(\mathrm{H}) = -0.37$, while $b_{\mathrm{coh}}(\mathrm{D}) = 0.65$. This sign difference is exploited in a wide variety of neutron scattering experiments, in which deuteration is used to label molecular sites or adjust overall coherent scattering contrasts to enhance the contributions from various components of the structure.

2.3 Van Hove Formalism

The Van Hove formalism recasts the Born approximation formula for $S_{\alpha}(\boldsymbol{Q},\omega)$ into the Heisenberg representation and introduces quantum generalizations of classical correlation functions. Begin with the identity,

$$\langle m|A_{\mathrm{op}}\delta\left(\frac{E_n - E_m}{\hbar} - \omega\right)|n\rangle =$$

$$\frac{1}{2\pi}\int_{-\infty}^{\infty} e^{i\omega t}\langle m|A_{op}(t)|n\rangle \mathrm{d}t\,, \quad (25)$$

where

$$A_{\mathrm{op}}(t) = e^{i\frac{\mathrm{H}}{\hbar}t} A_{\mathrm{op}} e^{-i\frac{\mathrm{H}}{\hbar}t}\,. \quad (26)$$

Then Eq. (16) becomes

$$S_{\alpha}(\boldsymbol{Q},\omega) = \frac{1}{2\pi}\int_{-\infty}^{\infty} e^{-i\omega t} I_{\alpha}(\boldsymbol{Q},t)\mathrm{d}t\,, \quad (27)$$

with the introduction of

$$I_{\alpha}(\boldsymbol{Q},t) = \frac{1}{N}\sum_{i,j}\xi_{i,j}^{\alpha}\left\langle e^{-i\boldsymbol{Q}\cdot\boldsymbol{R}_i(0)}\, e^{-i\boldsymbol{Q}\cdot\boldsymbol{R}_j(t)}\right\rangle\,. \quad (28)$$

Two additional steps were also needed to reach Eq. (28). First

$$e^{i\frac{\mathrm{H}}{\hbar}t} e^{i\boldsymbol{Q}\cdot\boldsymbol{R}} e^{-i\frac{\mathrm{H}}{\hbar}t} = e^{-i\boldsymbol{Q}\cdot\boldsymbol{R}(t)}$$

and

$$\sum_{n_0} p(n_0)\langle n_0|A_{\mathrm{op}}|n_0\rangle = \langle A_{\mathrm{op}}\rangle\,.$$

Finally, with the use of the obvious identity,

$$e^{i\boldsymbol{Q}\cdot\boldsymbol{R}_j} = \int e^{i\boldsymbol{Q}\cdot\boldsymbol{r}_j}\,\delta(\boldsymbol{r} - \boldsymbol{R}_j)\mathrm{d}^3 r\,,$$

Eq. (28) takes the form

$$I_{\alpha}(\boldsymbol{Q},t) = \int e^{i\boldsymbol{Q}\cdot\boldsymbol{r}_j} G_{\alpha}(\boldsymbol{r},t)\mathrm{d}^3 r\,. \quad (29)$$

where

$$G_{\alpha}(\boldsymbol{r},t) = \frac{1}{N}\sum_{i,j}\xi_{i,j}^{\alpha}\int$$

$$\langle\delta(\boldsymbol{r}' - \boldsymbol{R}_i(0))\,\delta(\boldsymbol{r}' + \boldsymbol{r} - \boldsymbol{R}_j(t))\rangle\mathrm{d}^3 r'\,. \quad (30)$$

Then $S_{\alpha}(\boldsymbol{Q},\omega)$ and $G_{\alpha}(\boldsymbol{r},t)$ are connected by the Fourier transform

$$S_{\alpha}(\boldsymbol{Q},\omega) = \frac{1}{2\pi}\int\int_{-\infty}^{\infty}$$

$$e^{i(\boldsymbol{Q}\cdot\boldsymbol{r} - \omega t)}\, G_{\alpha}(\boldsymbol{r},t)\mathrm{d}^3 r\mathrm{d}t\,, \quad (31)$$

and its inverse,

$$G_{\alpha}(\boldsymbol{r},t) = \int\int_{-\infty}^{\infty}$$

$$e^{-i(\boldsymbol{Q}\cdot\boldsymbol{r} - \omega t)}\, S_{\alpha}(\boldsymbol{Q},\omega)\frac{\mathrm{d}^3 Q}{(2\pi)^3}\mathrm{d}\omega\,. \quad (32)$$

The asymmetric placement of the 2π in these Fourier integrals is unfortunate, perhaps, but conventional. It could be avoided, say, by multiplying

the right-hand-side of Eq. (28) by 2π, but this is never done. The relationships among the quantities

$S_\alpha(\boldsymbol{Q},\omega) \rightarrow$ "scattering function",
$I_\alpha(\boldsymbol{Q},t) \rightarrow$ "intermediate scattering function",
$G_\alpha(\boldsymbol{r},t) \rightarrow$ "correlation function",

comprise the Van Hove representation of the Born approximation. Now the nuclear position operators, $\boldsymbol{R}_i(t)$, are not constants of motion, so that

$$[\boldsymbol{R}_i(t),\boldsymbol{R}_j(t')] \neq 0 \ ,$$

and the substitutions implied by the the δ-functions can not be made in Eq. (30), except in a classical approximation. However, the correlation function in the coherent case can be exactly represented by the form

$$G_{\text{coh}}(\boldsymbol{r},t) = \frac{1}{N}\int \langle \rho(\boldsymbol{r}',0)\rho(\boldsymbol{r}'+\boldsymbol{r},t)\rangle \mathrm{d}^3r' \ , \quad (33)$$

where

$$\rho(\boldsymbol{r},t) = \sum_i \delta(\boldsymbol{r}-\boldsymbol{R}_i(t)) \quad (34)$$

is the nuclear particle density operator. Also, with

$$\rho(\boldsymbol{Q},t) = \int \mathrm{e}^{i\boldsymbol{Q}\cdot\boldsymbol{r}}\rho(\boldsymbol{r},t)\mathrm{d}^3r \ , \quad (35)$$

the coherent intermediate scattering function is also represented by

$$I_{\text{coh}}(\boldsymbol{Q},t) = \frac{1}{N}\langle \rho(-\boldsymbol{Q},0)\rho(\boldsymbol{Q},t)\rangle \ . \quad (36)$$

In materials applications, the meaning of $\langle\cdots\rangle$ is generalized to include configurational averaging, as well as the implied thermal average. For a heterogeneous scattering population, $b_{\text{coh}}\rho(\boldsymbol{r},t)$ becomes the *scattering-length density* field,

$$\eta(\boldsymbol{r},t) = \sum_i b_{\text{coh},i}\delta(\boldsymbol{r}-\boldsymbol{R}_i(t)) \ , \quad (37)$$

and $S^{\text{het}}_{\text{coh}}(\boldsymbol{Q},\omega)$ is a sum of contributions depending on self- and cross-correlations among the various nuclear populations.

The Van Hove formulation was a signal advance in non-relativistic scattering theory and a major stimulus to condensed matter applications beyond crystallography. Although rooted in Fermi's golden rule, it manages, with the introduction of the correlation function, to "hide" its overt quantum mechanical origins and bring forth a classical looking representation that is a powerful guide to intuition, while also providing the path to relationships with statistical mechanics and linear response theory.

In thermal equilibrium, the statistical weight $p(n_0)$ of the initial states is the Boltzmann factor

$$p(n_0) = \frac{\mathrm{e}^{-\beta En0}}{Z}$$

where

$$\beta = \frac{1}{k_{\text{B}}T} \ , \quad \text{and} \quad Z = \sum_n \mathrm{e}^{-\beta En} \ .$$

The energy conservation explicit in Eq. (1) means that

$$p(n_0) \rightarrow p(n)\mathrm{e}^{\beta\hbar\omega} \ .$$

within the sums over states. This leads eventually to the *principal of detailed balance*:

$$S_\alpha(-\boldsymbol{Q},-\omega) = \mathrm{e}^{-\beta\hbar\omega}S_\alpha(\boldsymbol{Q},\omega) \ . \quad (38)$$

In applications to inelastic scattering, Eq. (38) predicts that "down" scattering ($\omega > 0$) is always stronger than "up" scattering ($\omega < 0$). For centrosymmetric systems, the scattering function is an even function of $\boldsymbol{Q}$,

$$S_\alpha(-\boldsymbol{Q},\omega) = S_\alpha(\boldsymbol{Q},\omega) \ . \quad (39)$$

Actually, this is also true for systems without a center of symmetry if the inverted equililbrium structure differs from the original by a constant displacement.

The scattering function, $S_\alpha(\boldsymbol{Q},\omega)$, is defined to be real, but the derived correlation function, $G_\alpha(\boldsymbol{r},t)$, is complex:

$$G(\boldsymbol{r},t) = G'(\boldsymbol{r},t) + iG''(\boldsymbol{r},t) \ .$$

This can be seen from the integral in Eq. (32), since $S_\alpha(\boldsymbol{Q},\omega)$ is not an even function of ω—the constraint of detailed balance. Thus a general relationship exists between the real and imaginary parts of the correlation function, which ultimately leads to:

$$S_\alpha(\boldsymbol{Q},\omega) = \frac{2i}{1-\mathrm{e}^{-\beta\hbar\omega}} \int \mathrm{e}^{(i\boldsymbol{Q}\cdot\boldsymbol{r}-\omega t)}G''_\alpha(\boldsymbol{r},t)\mathrm{d}^3r\,\mathrm{d}t \ . \quad (40)$$

This leads in turn to a concise connection between the scattering theory and linear response theory:

$$S_{\mathrm{coh}}(\boldsymbol{Q},\omega)=\frac{-2\hbar}{1-\mathrm{e}^{-\beta\hbar\omega}}\chi''(\boldsymbol{Q},\omega)\,, \tag{41}$$

where $\chi(\boldsymbol{Q},\omega)$ is the generalized susceptibility function for the density operator in Eq. (34).

2.4 Magnetic Scattering of Unpolarized Neutrons

Since the neutron has a magnetic moment, incident neutrons interact not only with the nuclei of the atoms in the scatterer but also with the magnetic moments of their unpaired electrons. For unpolarized beams, the magnetic interaction with the nuclear spins is already incorporated into the distinction between b_{coh} and b_{inc} in Eq. (9). The potential for the neutron-electron interaction is

$$V_{\mathrm{mag}}(r)=-\boldsymbol{\mu}\cdot\boldsymbol{B}(r)\,, \tag{42}$$

where $\boldsymbol{\mu}=\gamma\mu_{\mathrm{N}}\boldsymbol{\sigma}$ is the neutron magnetic moment operator, in terms of the neutron gyromagnetic ration, $\gamma=1.9132$, the nuclear magneton, μ_{N}, and the Pauli operator, $\boldsymbol{\sigma}$. The internal magnetic field operator, $\boldsymbol{B}(r)$, is

$$\boldsymbol{B}(r)=2\mu_{\mathrm{B}}\sum_i\left[\nabla\times\left(\frac{\boldsymbol{s}_i\times\hat{\boldsymbol{r}}}{r^2}\right)+\frac{\boldsymbol{p}_i\times\hat{\boldsymbol{r}}}{r^2}\right], \tag{43}$$

where μ_{B} is the Bohr magneton, $\boldsymbol{s}_i$ and $\boldsymbol{p}_i$ are the electron spin and momentum operators, respectively, and the summation is over all unpaired electrons. The (^) symbol denotes a unit vector. For the Born approximation the required matrix element of $\boldsymbol{B}(r)$ is

$$\langle k|\boldsymbol{B}(r)|k_0\rangle=2\mu_{\mathrm{B}}\sum_i\left[\hat{\boldsymbol{Q}}\times(\boldsymbol{s}_i\times\hat{\boldsymbol{Q}})+\frac{i(\boldsymbol{p}_i\times\hat{\boldsymbol{Q}})}{\hbar Q}\right]\mathrm{e}^{i\boldsymbol{Q}\cdot\boldsymbol{r}} \tag{44}$$

$$=\mu_0\boldsymbol{M}(\boldsymbol{Q})\,, \tag{45}$$

where μ_0 is the vacuum magnetic permeablity and $\boldsymbol{M}$ is the magnetization operator. For an unpolarized beam, the differential cross-section can be expressed as in Eq. (15) with the identifier α taking on the additional value "mag", and with the definition

$$\sigma_{\mathrm{mag}}=4\pi(\gamma r_0)^2\,, \tag{46}$$

where r_0 is the classical electron radius. Note that this usage of the symbol, σ_{mag}, is not universal. The generalization of the Van Hove representation to the magnetic case gives,

$$S_{\mathrm{mag}}(\boldsymbol{Q},\omega)=\sum_{\mu,\nu}\frac{\delta_{\mu\nu}-\hat{\boldsymbol{Q}}_\mu\hat{\boldsymbol{Q}}_\nu}{(2\mu_{\mathrm{B}}\mu_0)^2}\frac{1}{2\pi}\int_{-\infty}^{\infty}I_{\mu\nu}^{\mathrm{mag}}(\boldsymbol{Q},t)\,\mathrm{d}t\,, \tag{47}$$

where μ and ν are coordinate labels. The intermediate scattering function $I_{\mu\nu}^{\mathrm{mag}}(\boldsymbol{Q},t)$ extends the definition in Eq. (36),

$$I_{\mu\nu}^{\mathrm{mag}}(\boldsymbol{Q},t)=\frac{1}{N_{\mathrm{m}}}\langle\boldsymbol{M}_\mu(-\boldsymbol{Q},0)\boldsymbol{M}_\nu(\boldsymbol{Q},t)\rangle\,, \tag{48}$$

for N_{m} magnetic ions, while the corresponding magnetization correlation function, from Eq. (33), is

$$G_{\mu\nu}^{\mathrm{mag}}(\boldsymbol{r},t)=\frac{1}{N_{\mathrm{m}}}\int\langle\boldsymbol{M}_\mu(\boldsymbol{r}',0)\boldsymbol{M}_\nu(\boldsymbol{r}'+\boldsymbol{r},t)\rangle\mathrm{d}^3r'. \tag{49}$$

Thus, except for the appearance of the quantity known as the Halpern tensor,

$$\delta_{\mu\nu}-\hat{\boldsymbol{Q}}_\mu\hat{\boldsymbol{Q}}_\nu\,, \tag{50}$$

in Eq. (47), the formal extension of nuclear scattering to magnetic scattering of unpolarized beams simply entails replacing the scalar nuclear density, ρ, by the components of the magnetization, $\boldsymbol{M}_\mu$. The Halpern factor, however, is responsible for the special, anisotropic character of magnetic neutron scattering. For example, for a single-domain ferromagnetic sample,

$$\delta_{\mu\nu}-\hat{\boldsymbol{Q}}_\mu\hat{\boldsymbol{Q}}_\nu\rightarrow 1-(\hat{\boldsymbol{Q}}\cdot\hat{\boldsymbol{M}})^2 \tag{51}$$

where $\hat{\boldsymbol{M}}$ is the direction of the domain magnetization. Thus, in the Born approximation, there is no magnetic scattering for $\boldsymbol{Q}\parallel\boldsymbol{M}$. As indicated by the scattering law, Eq. (15), now with

$$\alpha=\begin{cases}\text{"coh"},\\ \text{"inc"},\\ \text{"mag"},\end{cases} \tag{52}$$

nuclear and magnetic scattering coexist, in general, in magnetic materials and can have comparable weight. The anisotropy of magnetic scattering offers one means of separating these contributions by choosing directions of $\boldsymbol{Q}$ along which the magnetic component is suppressed. Squires [18] introduces basic elements of magnetic scattering, while Balcar and Lovesey [3] provide a thorough exposition.

3. Generic Applications

3.1 Elastic Scattering

The scattering function can be analyzed into distinct ω-dependent contributions according to:

$$S_\alpha(\mathbf{Q},\omega) = I_\alpha(\mathbf{Q},\infty)\delta(\omega) + S_\alpha^{\mathrm{ne}}(\mathbf{Q},\omega)\,. \quad (53)$$

The first part is called the *elastic* scattering, which, by convention, means scattering with no change in the neutron energy, so that $k = k_0$. The isolation of the elastic contribution is the result of writing

$$I_\alpha(\mathbf{Q},t) = I_\alpha(\mathbf{Q},\infty) + [I_\alpha(\mathbf{Q},t) - I_\alpha(\mathbf{Q},\infty)]\,, \quad (54)$$

in the integrand of Eq. (27) and assuming that the limit,

$$I_\alpha(\mathbf{Q},\infty) = \lim_{t\to\infty}[I_\alpha(\mathbf{Q},t)]\,,$$

exists. The first term in Eq. (54) is independent of t and thus produces the scattering proportional to $\delta(\omega)$. The *non*-elastic part $S_\alpha^{\mathrm{ne}}(\mathbf{Q},\omega)$ stems from the Fourier transform of the t-dependent remainder and comprises both *in*elastic and *quasi*elastic contributions. Furthermore, for $|t-t'|\to\infty$,

$$\begin{aligned}\langle A(t)B(t')\rangle &= \langle A(t)\rangle\langle B(t')\rangle \\ &= A^{\mathrm{eq}}B^{\mathrm{eq}}\,, \end{aligned} \quad (55)$$

where the A^{eq} is equilibrium average of the operator A. Therefore, in Eq. (53)

$$I_{\mathrm{coh}}(\mathbf{Q},\infty) = \frac{1}{N}\,|\rho^{\mathrm{eq}}(\mathbf{Q})|^2\,, \quad (56)$$

which is the basis of structure determinations in solids. Various aspects of this extensive field are elucidated in [1], [7], [8], [11], and [18]. For liquids, on the other hand, $\rho^{\mathrm{eq}}(\mathbf{r}) = N/V$, so that

$$I_{\mathrm{coh}}(\mathbf{Q},\infty) = \frac{1}{N}\left(\frac{N}{V}\right)^2\delta(\mathbf{Q})\,,$$

leading to the dictum that liquids scatter elastically only in the forward direction. The weight of incoherent elastic scattering is given by

$$I_{\mathrm{inc}}(\mathbf{Q},\infty) = \int e^{i\mathbf{Q}\cdot\mathbf{r}}\,P_{\mathrm{self}}(\mathbf{r},\infty)\,d\mathbf{r}\,, \quad (57)$$

where

$$P_{\mathrm{self}}(\mathbf{r}) = \int \langle\delta(\mathbf{r}')\rangle\langle\delta(\mathbf{r}'+\mathbf{r})\rangle\,d^3r' \quad (58)$$

can be interpreted as the conditional probability density for nuclear position $\mathbf{r}$ at time $t\to\infty$, given that $\mathbf{r} = \mathbf{0}$ at $t = 0$. These expressions for the elastic scattering are easily extended to heterogeneous systems.

3.2 Energy-Integrated Scattering: The Static Approximation

Coherent elastic scattering, which reveals equilibrium structure, must be measured by energy-resolved techniques. Often, however, structure is studied using methods that do not discriminate the scattered neutron energy; these experiments observe the energy-integrated cross-section

$$\frac{d\sigma}{d\Omega} = \int_{-\infty}^{\frac{E_0}{\hbar}} \frac{d^2\sigma}{d\Omega\,d\omega}\,d\omega\,. \quad (59)$$

In the *static approximation*, this is represented as

$$\left(\frac{d\sigma}{d\Omega}\right)_{\mathrm{static}} = \frac{\sigma_{\mathrm{inc}}}{4\pi}S_{\mathrm{inc}}(\mathbf{Q}) + \frac{\sigma_{\mathrm{coh}}}{4\pi}S_{\mathrm{coh}}(\mathbf{Q})\,, \quad (60)$$

where

$$S_\alpha(\mathbf{Q}) = \int_{-\infty}^{\infty} S_\alpha(\mathbf{Q},\omega)\,d\omega\,. \quad (61)$$

Since $\mathbf{Q}$ is held fixed in the ω-integration, this approximation entails neglecting the $\mathbf{Q}$-dependence of the final neutron wavenumber,

$$k = |k_0 - \mathbf{Q}|\,,$$

and setting $k = k_0$, as in elastic scattering. Then from Eq. (27),

$$S_\alpha(\mathbf{Q}) = I_\alpha(\mathbf{Q},0)\,. \quad (62)$$

Since $[\mathbf{R}_i(t), \mathbf{R}_j(t)] = 0$, this can be analyzed as

$$S_\alpha(\mathbf{Q}) = \int e^{-i\mathbf{Q}\cdot\mathbf{r}}\,G_\alpha(\mathbf{r},0)\,d^3r\,, \quad (63)$$

where

$$G_\alpha(\mathbf{r},0) = \frac{1}{N}\sum_{i,j}\xi_{i,j}^{\alpha}\,\langle\delta(\mathbf{r}+\mathbf{R}_i(0)-\mathbf{R}_j(0))\rangle\,. \quad (64)$$

Therefore, for the incoherent contribution,

$$G_{\rm inc}(r,0)=\delta(r)\,, \tag{65}$$

so that

$$S_{\rm inc}(Q)=1\,. \tag{66}$$

For the more interesting coherent component,

$$S_{\rm coh}(Q)=\delta(r)+{\rm g}(r)\,, \tag{67}$$

where

$${\rm g}(r)=\sum_{j\neq 0}\langle\delta(r+R_0(0)-R_j(0))\rangle \tag{68}$$

is the static pair-correlation function. Thus energy-integrated coherent scattering measures an average of instantaneous "snapshots" of the time-dependent structure, while elastic coherent scattering measures the equilibrium averaged structure. In harmonic crystalline solids, where the atoms more-or-less "stay put," both methods yield the equilibrium positions and mean-square thermal displacements, but the two forms of measurement differ in important ways. Indeed, from Eq. (53), one has

$$S_{\rm coh}(Q)=S^{\rm el}_{\rm coh}(Q)+S^{\rm ne}_{\rm coh}(Q)\,, \tag{69}$$

where we have defined

$$S^{\rm el}_{\rm coh}(Q)=I_{\rm coh}(Q,\infty)\,, \tag{70}$$

and

$$S^{\rm ne}_{\rm coh}(Q)=\int_{-\infty}^{\infty}S^{\rm ne}_{\rm coh}(Q,\omega)\,{\rm d}\omega\,. \tag{71}$$

For monatomic harmonic crystals, in particular,

$$S^{\rm el}_{\rm coh}(Q)=\frac{(2\pi)^3}{\Omega_0}\,{\rm e}^{-2W}\sum_{K}\delta(Q-K)\,, \tag{72}$$

where Ω_0 is the volume of the unit cell, the K are wavevectors of the reciprocal lattice, and $\exp(-2W)$ is the Debye-Waller factor, which depends on the thermal displacements and is defined below at Eq. (107). The δ-functions in Eq. (72) are the Bragg peaks from which the equilibrium structure is deduced. In this context the integrated nonelastic scattering in Eq. (69) is referred to as *thermal diffuse scattering*. For the special case of an Einstein solid (dispersionless vibrations), the thermal diffuse scattering varies monotonically with Q. In general, however, for dispersive vibrations (acoustic phonons), the thermal diffuse scattering is a structured background, including temperature-dependent "wings" centered on the Bragg peaks. Thermal diffuse scattering is discussed again in Sec. 3.5.2.

In strongly anharmonic solids and systems where structure changes on the time scale of the measurements, elastic and energy-integrated scattering probe substantially different correlations, and only the latter provides the short-time information usually of interest in such cases.

3.3 Sum Rules

Taken in a larger context, the formula in Eq. (61) is the zeroth-order member of a set of frequency moments of the scattering function, $S_\alpha(Q,\omega)$, which in normalized form is defined by

$$\langle\omega^n\rangle_\alpha(Q)=\frac{1}{S_\alpha(Q)}\int_{-\infty}^{\infty}\omega^n\,S_\alpha(Q,\omega)\,{\rm d}\omega\,. \tag{73}$$

In particular,

$$\langle\omega^0\rangle_\alpha(Q)=1\,. \tag{74}$$

While seeming trivial, in practice Eq. (74) actually constrains physically distinct measurements and thus provides a means of checking their mutual consistency. The higher-order rules are formally generated starting with Eq. (27):

$$\frac{d^n}{{\rm d}t^n}I_\alpha(Q,t)\big|_{t=0}=i^n\int_{-\infty}^{\infty}S_\alpha(Q,\omega)\omega^n\,{\rm d}\omega\,. \tag{75}$$

Then it is easy to get

$$\langle\omega^n\rangle_\alpha(Q)=\frac{(-i)^n}{NS_\alpha(Q)}\sum_{i,j}\xi^\alpha_{i,j}$$

$$\left\langle{\rm e}^{-iQ\cdot R_i(0)}\frac{{\rm d}^n}{{\rm d}t^n}\,{\rm e}^{iQ\cdot R_j(t)}\right\rangle_{t=0}\,, \tag{76}$$

where, following Eq. (26), the derivatives with respect to t are determined by

$$\frac{\mathrm{d}}{\mathrm{d}t}\, e^{iQ\cdot R_j(t)} = \frac{i}{\hbar}\left[H, e^{iQ\cdot R_j(t)}\right]. \tag{77}$$

For velocity-independent interactions, the commutator is independent of the atom-atom interaction potential and gives

$$\left[H, e^{iQ\cdot R_j(t)}\right] = \left[-\frac{\hbar^2\nabla_j^2}{2M}\,,\, e^{iQ\cdot R_j(t)}\right] =$$

$$e^{iQ\cdot R_j(t)}\left(\frac{\hbar^2 Q^2}{2M} + \hbar Q\cdot \dot{R}_j(t)\right), \tag{78}$$

where M is the atomic mass. The contribution from the second term averages to zero in Eq. (76), and, recalling the normalization in Eq. (73), it follows easily that

$$\hbar\langle\omega\rangle_\alpha(Q) = \frac{\hbar^2 Q^2}{2M}\,, \tag{79}$$

which can be interpreted as the average recoil kinetic energy at fixed scattering vector Q. Note that if the t-derivative is treated classically, the result is equivalent to keeping only the second term in Eq. (78), which gives $\langle\omega\rangle_\alpha(Q) = 0$. This is inconsistent with the asymmetry of $S_\alpha(Q,\omega)$ required by detailed balance, Eq. (38), except in the high-temperature limit.

Higher moments are increasingly system-dependent and more difficult to calculate. For a classical liquid, the second moments are

$$\langle\omega^2\rangle_\alpha(Q) = \frac{Q^2 k_B T}{M S_\alpha(Q)}\,. \tag{80}$$

The coherent case,

$$\langle\omega^2\rangle_{\mathrm{coh}}(Q) = \frac{Q^2 k_B T}{M S_{\mathrm{coh}}(Q)}\,, \tag{81}$$

and its analogues come into play in the analysis of quasielastic scattering (Sec. 3.6) in liquids and lattice fluids, where $\langle\omega^2\rangle_{\mathrm{coh}}(Q)$ is used as a measure of the width of the coherent contribution to the quasielastic line. Then Eq. (81) predicts that the width has a minimum near the maximum of $S_{\mathrm{coh}}(Q)$, the effect known as *de Gennes narrowing*, which physically expresses the relative stability of density fluctuations that are consonant with the dominant short-ranged liquid order at $Q_{\max}$.

3.4 Small Angle Neutron Scattering (SANS)

Small angle scattering is the discipline of studying microstructure of materials by investigating scattering in the immediate neighborhood of the incident beam. For neutrons with wavelengths larger than the *Bragg cutoff*—i.e., $\lambda_0 > a$, where a is the largest unit cell dimension—Bragg scattering from the atomic-scale structure is suppressed, and all scattering is near the forward direction. The Q-dependence of small angle scattering thus arises from structural variations over length scales usually much larger than the atomic scale. An informal but helpful rule is that microstructure on length scale L produces scattering in the Q-range

$$Q \leq 2\pi L^{-1}\,. \tag{82}$$

In other words, the more homogeneous the microstructure, the smaller the Q-range in which it is observable. To a good approximation in SANS, the scattering angle is given by $2\theta = \lambda_0 Q/2\pi$. Combining this with the criterion in Eq. (82), gives

$$2\theta \leq \frac{\lambda_0}{L}\,. \tag{83}$$

This shows that increasing the neutron wavelength magnifies the observable scale of microstructure; i.e., at a given scattering angle (position on the detector relative to the incident beam), larger homogeneous regions contribute to the scattering at larger incident wavelengths. Small angle scattering also occurs for neutron wavelengths below the Bragg cutoff, but then intensity at small angles is reduced by Bragg scattering into large angles. In thick specimens, especially, multiple Bragg scattering can contaminate scattering in the small angle regime, a bane of the early history of the field.

As with other methods of structure determination, small angle scattering can be implemented as elastic scattering, following Eqs. (53) and (56), or as energy-integrated scattering, as defined in the preceding section. Most SANS instruments, in fact, integrate the scattered energy transfer, and the static approximation usually is appropriate. Thus, for heterogeneous systems Eqs. (84) and (63) are generalized as

$$\left(\frac{\mathrm{d}\sigma}{\mathrm{d}\Omega}\right)_{\mathrm{static}} = \sum_\alpha S_\alpha^{\mathrm{het}}(Q)\,, \tag{84}$$

and

$$S_\alpha^{\text{het}}(\boldsymbol{Q}) = \int e^{i\boldsymbol{Q}\cdot\boldsymbol{r}} G_\alpha^{\text{het}}(\boldsymbol{r},0)\,d^3r\,. \tag{85}$$

Since the notation is getting cumbersome, for the remainder of this section the superscript "het" will be omitted, and the specification, $t=0$, will become implicit. Also, recalling Eq. (9), b_{coh} will be denoted by the more compact $\bar{b}$. Now, in order to make contact with conventional SANS terminology, introduce the function $\Gamma(\boldsymbol{r})$,

$$G_{\text{coh}}(\boldsymbol{r}) = \frac{V}{N}\Gamma(\boldsymbol{r})\,. \tag{86}$$

Then, from Eqs. (33) and (37),

$$\Gamma(\boldsymbol{r}) = \frac{1}{V}\int \langle \eta(\boldsymbol{r}')\eta(\boldsymbol{r}'+\boldsymbol{r})\rangle d^3r'\,. \tag{87}$$

For the incoherent contribution, Eq. (30) easily gives

$$G_{\text{inc}}(\boldsymbol{r}) = \langle b_{\text{inc}}^2\rangle \delta(\boldsymbol{r})\,, \tag{88}$$

where

$$\langle b_{\text{inc}}^2\rangle = \frac{1}{N}\sum_i b_{\text{inc},i}^2\,. \tag{89}$$

This is just the extension of Eq. (65) to heterogeneous systems. Small angle scattering usually is analyzed in terms of the Porod-Debye correlation function, as defined by

$$\gamma(\boldsymbol{r}) = \frac{\Gamma(\boldsymbol{r})-\Gamma(\infty)}{\Gamma(0)-\Gamma(\infty)}\,. \tag{90}$$

By construction, it follows immediately that

$$\begin{aligned}\gamma(0) &= 1, \quad \text{and}\\ \gamma(\infty) &= 0\,.\end{aligned} \tag{91}$$

Using Eq. (87), the limits of $\gamma(\boldsymbol{r})$ are

$$\begin{aligned}\gamma(0) &= \langle \eta^2\rangle_V, \quad \text{and}\\ \gamma(\infty) &= \langle \eta\rangle_V^2\,,\end{aligned} \tag{92}$$

where

$$\langle \cdots\rangle_V = \frac{1}{V}\int \langle \cdots\rangle\, d^3r, \tag{93}$$

means a combined thermal-configurational-volume average. In most theoretical SANS treatments these averages are treated as being redundant, and the choice of which one to do "first" is usually a matter of mathematical convenience. The Porod-Debye correlation function can then be written as

$$\gamma(\boldsymbol{r}) = \frac{\frac{1}{V}\int \langle \Delta\eta(\boldsymbol{r}')\Delta\eta(\boldsymbol{r}'+\boldsymbol{r})\rangle d^3r'}{\langle(\Delta\eta)^2\rangle_V}\,, \tag{94}$$

where

$$\Delta\eta(\boldsymbol{r}) = \eta(\boldsymbol{r}) - \langle\eta\rangle_V\,, \tag{95}$$

is the fluctuating part of the scattering-length density field. The combination of these results gives

$$N\left(\frac{d\sigma}{d\Omega}\right)_{\text{static}} = N\langle b_{\text{inc}}^2\rangle + (2\pi)^3 V\langle(\Delta\eta)^2\rangle_V \delta(\boldsymbol{Q}) + V\langle(\Delta\eta)^2\rangle_V \int e^{i\boldsymbol{Q}\cdot\boldsymbol{r}}\,\gamma(\boldsymbol{r})\,d^3r\,. \tag{96}$$

The first term is a Q-independent background, and the second is the forward coherent scattering, which usually is masked by a beam stop. The Fourier transform of $\gamma(\boldsymbol{r})$ in the last term describes the scattering caused by the spatial variation of the microstructure. Equation (96) is the basic law of small angle neutron scattering.

A typical class of materials in SANS studies consists of two or more homogeneous phases separated by sharp interfaces and partitioned into multiply-connected volume compartments. For such systems the scattering-length density can be represented as

$$\eta(\boldsymbol{r}) = \sum_n \bar{b}_n \rho_n(\boldsymbol{r})\,, \tag{97}$$

where

$$\rho_n(\boldsymbol{r}) = \sum_{i\in n} \delta(\boldsymbol{r}-\boldsymbol{R}_i)\,, \tag{98}$$

and $\bar{b}_n$ is its coherent scattering-length, which can be computed as a cellular average for polyatomic phases. The component densities satisfy

$$\langle \rho_n\rangle_V = \frac{N}{V}\phi_n\,, \tag{99}$$

where ϕ_n is the volume fraction of the n-th phase, and also have the properties,

$$\rho_n(\boldsymbol{r})\rho_m(\boldsymbol{r}) = \begin{cases} 0 & \text{for } m \neq n\,,\\ \frac{N}{V}\rho_n(\boldsymbol{r}) & \text{for } m = n\,.\end{cases} \tag{100}$$

The first expresses the spatial partitioning of the phases, while the second is the normalized idempotency condition. It then follows that

$$\langle(\Delta\eta)^2\rangle_V = \left(\frac{N}{V}\right)^2 [\langle b_{\rm coh}^2\rangle - \langle b_{\rm coh}\rangle^2], \qquad (101)$$

where

$$b_{\rm coh} = \sum_n \phi_n \bar{b}_n . \qquad (102)$$

For the special but important case of two phases, this reduces to the symmetrical formula

$$\langle(\Delta\eta)^2\rangle_V = \phi(1-\phi)(\eta_1-\eta_2)^2, \qquad (103)$$

where ϕ is the volume fraction of either one of the phases, and η_1 and η_2 are the scattering-length densities.

3.5 Inelastic Scattering

In Eq. (53) the non-elastic contribution, $S_\alpha^{\rm ne}(\boldsymbol{Q},\omega)$, may describe *in*elastic scattering, *quasi* elastic scattering, Sec. 3.6, or both, depending on the system being studied. Inelastic scattering means energy-resolved scattering *not* centered on $\omega = 0$. Coherent inelastic scattering typically consists of well-defined lines riding on a diffuse, or structureless, ω-dependent background. The lines result from resonant scattering of the neutron by long-lived elementary excitations of the system, such as phonons and magnons (in magnetic materials) and impurity atom vibrations in host-guest systems. Diffuse coherent inelastic scattering is produced by scattering from multiple, or non-elementary, excitations. Energy-integrated inelastic scattering is usually the main source of the thermal diffuse background in structure determinations using energy-insensitive detection methods. Incoherent inelastic scattering measures excitation densities of states, to a first approximation.

3.5.1 Scattering by Phonons

Scattering by phonons provides the prototype for neutron inelastic scattering. Squires [18] gives a lucid treatment. To calculate the intermediate scattering function, Eq. (27), resolve the nuclear position operator into the equilibrium coordinate and a time-dependent small displacement,

$$\boldsymbol{R}_j(t) = \boldsymbol{R}_j^{\rm eq} + \boldsymbol{u}_j(t) . \qquad (104)$$

Then, using the phonon representation of the displacement operator, one can derive (with some tedium) the basic identity of the harmonic approximation,

$$\left\langle e^{-i\boldsymbol{Q}\cdot\boldsymbol{R}_i(0)}\, e^{i\boldsymbol{Q}\cdot\boldsymbol{R}_j(t)} \right\rangle = e^{-i\boldsymbol{Q}\cdot(\boldsymbol{R}_i^{\rm eq}-\boldsymbol{R}_j^{\rm eq})} e^{-2W} e^{2W_{ij}(\boldsymbol{Q},t)}, \qquad (105)$$

where

$$W_{ij}(\boldsymbol{Q},t) = \frac{1}{2}\langle \boldsymbol{Q}\cdot\boldsymbol{u}_i(0)\boldsymbol{Q}\cdot\boldsymbol{u}_j(t)\rangle , \qquad (106)$$

and

$$W = W_{ii}(\boldsymbol{Q},0) . \qquad (107)$$

The ubiquitous exponential, $\exp(-2W)$, is the *Debye-Waller factor*. It is a long-standing convention to leave the $\boldsymbol{Q}$-dependence of the W function implicit. A concrete formula for W follows from Eq. (113) in the next section. Although correct quantum mechanically, the result in Eq. (105) actually can be obtained more directly by treating $\boldsymbol{Q}\cdot\boldsymbol{u}_j(t)$ as a classical Gaussian random variable, ζ, with zero mean, and by using the concommitant rule:

$$\langle e^{\zeta}\rangle = e^{1/2\langle\zeta^2\rangle} .$$

The Taylor expansion of the final exponential in Eq. (105) leads to a systematic development of the inelastic scattering function, $S_\alpha^{\rm inel}(\boldsymbol{Q},\omega)$. The first term (unity) gives the elastic scattering from the equilibrium structure, as in Eq. (56). The next term—the first t-dependent one—describes *one-phonon* scattering, while the remainder produces *multi-phonon* scattering. For a Bravais lattice the result for coherent one-phonon scattering turns out to be:

$$S_{\rm coh}^{\rm 1-ph}(\boldsymbol{Q},\omega) = \frac{(2\pi)^3}{\Omega_0}\frac{\hbar e^{-2W}}{2M}\sum_{q,s,K}\frac{[\boldsymbol{Q}\cdot\epsilon_s(\boldsymbol{q})]^2}{\omega_s(\boldsymbol{q})}$$
$$\{[n_s(\boldsymbol{q})+1]\delta(\omega-\omega_s(\boldsymbol{q}))\delta(\boldsymbol{Q}-\boldsymbol{q}-\boldsymbol{K})$$
$$+[n_s(\boldsymbol{q})]\delta(\omega+\omega_s(\boldsymbol{q}))\delta(\boldsymbol{Q}+\boldsymbol{q}+\boldsymbol{K})\} . \qquad (108)$$

In this formula M is the nuclear mass, Ω_0 is the volume of the lattice unit cell, and $\boldsymbol{K}$ is a reciprocal lattice wavevector (often denoted as $2\pi\boldsymbol{\tau}$, where $\boldsymbol{\tau}$ is a reciprocal lattice vector). The phonon modes of wavevector $\boldsymbol{q}$ and polarization s have frequencies $\omega_s(\boldsymbol{q})$, polarization vectors $\boldsymbol{\epsilon}_s(\boldsymbol{q})$ and thermal occupations $n_s(\boldsymbol{q})$. The two terms in Eq. (108) describe, respectively, scattering with the emission of a phonon—the neutron is *down*-scattered by energy $\hbar\omega_s(\boldsymbol{q})$—and scattering with the absorption of a phonon—the neutron is *up*-scattered by energy $\hbar\omega_s(\boldsymbol{q})$. In each case the scattering satisfies the kinematical constraints

$$\frac{\hbar^2}{2m}(k_0^2-k^2)=\pm\hbar\omega_s(\boldsymbol{q}) \tag{109}$$

and

$$\boldsymbol{k}_0-\boldsymbol{k}=\boldsymbol{K}\pm\boldsymbol{Q}\,. \tag{110}$$

For *incoherent* one-phonon scattering, the scattering function can be obtained from Eq. (108) by making the formal replacement,

$$\frac{(2\pi)^3}{\Omega_0}\delta(\boldsymbol{Q}\mp\boldsymbol{q}-\boldsymbol{K})\overset{\text{inc}}{\rightarrow}1.$$

This leads to

$$S_{\text{inc}}^{1-\text{ph}}(\boldsymbol{Q},\omega)=$$

$$\frac{3N\hbar e^{-2W}}{2M}\,\frac{\langle[\boldsymbol{Q}\cdot\boldsymbol{\epsilon}_s(\boldsymbol{q})]^2 n_s(\boldsymbol{q})\rangle_\omega}{\omega}\mathcal{N}(\omega)\,, \tag{111}$$

where $\mathcal{N}(\omega)$ is the one-phonon density of states and $\langle\cdots\rangle_\omega$ denotes the average over the surface in reciprocal space on which $\omega_s(\boldsymbol{q})=\omega$.

For multi-phonon processes the corresonding kinematical relations are not mode-specific, and diffuse ω-dependent scattering generally is the result. Often the multi-phonon background must be estimated in order to achieve a reliable analysis of one-phonon scattering. Occasionally multi-phonon scattering may even appear in the guise of "broadened" one-phonon scattering in complicated spectra.

Inelastic scattering is also used to measure spin-wave spectra in magnetic materials. The kinematical constraints for 1-*magnon* scattering are the same as in Eq. (110). Determination of local vibrations in host-guest systems is another important application of inelastic scattering. For example, in hydrogen in metals, the point symmetry of occupied interstitial sites usually is revealed simply by assignment of the intensities produced by vibrational modes having signature degeneracies.

3.5.2 Thermal Diffuse Scattering

With the material now at hand, we continue the description of thermal diffuse scattering begun in Sec. 3.2. In general the energy-integrated nonelastic scattering that constitutes thermal diffuse scattering incorporates both quasielastic and inelastic scattering. Here, however, we only consider the inelastic contribution from phonon scattering. Thus using Eq. (105) in Eqs. (28) and (62), and recalling Eq. (71), one gets

$$S_{\text{coh}}^{\text{nc}}(\boldsymbol{Q})=1-e^{-2W}+\frac{e^{-2W}}{N}$$

$$\sum_{i\neq j}e^{-i\boldsymbol{Q}\cdot(\boldsymbol{R}_i^{\text{eq}}-\boldsymbol{R}_j^{\text{eq}})}(e^{2W_{ij}(\boldsymbol{Q},0)}-1)\,, \tag{112}$$

where $W_{ij}(\boldsymbol{Q},t)$ was defined in Eq. (106). Explicitly, for $t=0$,

$$W_{ij}(\boldsymbol{Q},0)=\frac{\hbar}{4MN}\sum_{\boldsymbol{q},s}\frac{[\boldsymbol{Q}\cdot\boldsymbol{\epsilon}_s(\boldsymbol{q})]^2}{\omega_s(\boldsymbol{q})}$$

$$[2n_s(\boldsymbol{q})+1]\cos[\boldsymbol{q}\cdot(\boldsymbol{R}_i^{\text{eq}}-\boldsymbol{R}_j^{\text{eq}})]\,. \tag{113}$$

The formula for W, Eq. (107), is obtained by setting $i=j$ here. For an Einstein model the thermal displacements on different sites are uncorrelated, so that $W_{ij}(\boldsymbol{Q},0)=0$ for $i\neq j$. In this case, therefore, the term in Eq. (112) with the sum over sites vanishes identically, and the thermal diffuse background is 1-exp$(-2W)$. Notice that in the opposite extreme, if $W_{ij}(\boldsymbol{Q},0)$ were independent of the distance between sites, the summation in Eq. (112) would produce Bragg peaks, as in $S_{\text{coh}}^{\text{el}}(\boldsymbol{Q})$. Instead, $W_{ij}(\boldsymbol{Q},0)\rightarrow 0$ as $|\boldsymbol{R}_i^{\text{eq}}-\boldsymbol{R}_j^{\text{eq}}|\rightarrow\infty$, and this fall-off moderates the site summation. However, $W_{ij}(\boldsymbol{Q},0)$ decays slowly with distance, which leads to a weakened expression of the reciprocal lattice structure in the thermal diffuse scattering. This is seen by expanding $\exp[2W_{ij}(\boldsymbol{Q},0)]$, in analogy to the phonon expansion of $S_{\text{coh}}^{\text{inel}}(\boldsymbol{Q},\omega)$. Indeed, one can obtain the 1-phonon thermal diffuse scattering directly by integrating Eq. (108) with respect to ω.

This gives

$$S_{\text{coh}}^{1-\text{ph}}(\mathbf{Q}) = \frac{(2\pi)^3}{\Omega_0}\frac{\hbar e^{-2W}}{2M} \sum_{s,\mathbf{K}} [\mathbf{Q}\cdot\epsilon_s(\tilde{\mathbf{q}})]^2 \frac{[2n_s(\tilde{\mathbf{q}})+1]}{\omega_s(\tilde{\mathbf{q}})} , \quad (114)$$

where

$$\tilde{\mathbf{q}} = \mathbf{Q} - \mathbf{K}$$

for each $\mathbf{K}$ in the sum. Thus the acoustic phonon branches give rise to algebraic singularities coincident with the Bragg peaks, since $\omega_s(\tilde{\mathbf{q}}) = c_s\tilde{\mathbf{q}}$ for small $|\tilde{\mathbf{q}}|$. Specifically, for $\tilde{\mathbf{q}}\to 0$ near a particular $\mathbf{K}$ and at temperatures such that $\hbar\omega(\tilde{\mathbf{q}}) \ll k_B T$, then

$$S_{\text{coh}}^{1-\text{ph}}(\mathbf{Q}) \propto |\mathbf{Q}-\mathbf{K}|^{-2} , \quad (115)$$

since $n_s(\tilde{\mathbf{q}}) \sim k_B T/\hbar\omega_s(\tilde{\mathbf{q}})$. On the other hand, if $\hbar\omega_s(\tilde{\mathbf{q}}) \gg k_B T$, then

$$S_{\text{coh}}^{1-\text{ph}}(\mathbf{Q}) \propto |\mathbf{Q}-\mathbf{K}|^{-1} , \quad (116)$$

Although these results are derived in the harmonic approximation, they correctly imply that soft modes in plastic crystals also produce significant thermal diffuse scattering near $\mathbf{Q} = \mathbf{K} + \mathbf{q}_c$, where $\omega_s(\mathbf{q}_c) = 0$ at the softening temperature.

Historically, before the ascendancy of inelastic neutron scattering, x-ray thermal diffuse scattering was the chief means of measuring phonon dispersion in solids by fitting lineshapes with expressions like Eq. (114).

3.6 Quasielastic Scattering

Quasielastic scattering is energy-resolved scattering centered on $\omega = 0$ and is the result of neutrons interacting with purely dissipative excitations, which can be viewed as motions at imaginary frequencies. Usually this means scattering by diffusing nuclei. Typically, quasielastic and inelastic scattering are well-separated from each other, since vibrational angular frequencies tend to be much larger than diffusive jump rates. Sometimes, however, analysis of the scattering near $\omega = 0$ into its elastic, quasielastic and inelastic components is not easy.

A prototype for quasielastic neutron scattering is incoherent quasielastic scattering from hydrogen in metals. At high temperatures the correlation function, $G_{\text{inc}}(\mathbf{r},t)$ in Eq. (30), is well-approximated by the classical limit,

$$G_{\text{inc}}^{\text{class}}(\mathbf{r},t) = P_{\text{self}}(\mathbf{r},t) = \langle \delta(\mathbf{r} + \mathbf{R}_0(0) - \mathbf{R}_0(t)) \rangle , \quad (117)$$

which is the finite-t generalization of Eq. (58). Application of jump diffusion theory to the calculation of $P_{\text{self}}(\mathbf{r},t)$ then leads to the Lorentzian quasielastic lineshape,

$$S_{\text{inc}}(\mathbf{Q},\omega) = \frac{\Gamma(\mathbf{Q})/\pi}{\omega^2 + \Gamma(\mathbf{Q})^2} , \quad (118)$$

where $\Gamma(\mathbf{Q})$ depends on the diffusion constant and on the structure visited by the diffusing particle. Incoherent quasielastic scattering coexists with incoherent elastic scattering given by Eq. (57), which is called the *elastic incoherent structure factor* in the concerned literature. This "EISF" is proportional to the reciprocal of Ω_{self}, the volume accessible to the diffusing particle. Thus, the less localized the self-diffusion, the smaller the weight of incoherent elastic scattering.

Coherent quasielastic scattering, which was alluded to in Sec. 3.3, is important in fluid systems, indeed wherever diffusive transport of coherently scattering nuclei occurs. Quasielastic scattering also is produced by diffusive rotational modes in plastic crystals and caged systems. See [4] for an extensive treatment of quasielastic scattering.

4. Neutron Refraction and Reflection

The Born approximation neglects interference between the incident and scattered waves. This usually is justified in standard beam-target geometries for scattering at wide angles from small samples. These interactions become important, however, as scattering becomes concentrated into the forward direction. Then the sharp distinction between incident and scattered beams within the scattering medium is lost, and it is necessary to solve the Schrödinger equation ("dynamical" scattering) without resort to the Born approximation ("kinematical" scattering).

An important problem where dynamical scattering theory is required is a neutron beam incident on a semi-infinite scattering medium having a smooth, planar boundary, say at $z = 0$. The Schrödinger equation for this case is

$$\frac{-\hbar^2}{2m}\nabla^2\psi(\mathbf{r}) + V(\mathbf{r})\psi(\mathbf{r}) = E_0\psi(\mathbf{r}) , \quad (119)$$

where $E_0=\hbar^2k_0^2/2m$, and the potential is the step function,

$$V(r)=\begin{cases}0, & z>0\\ \langle V\rangle_{\text{cell}}, & z\leq 0\end{cases}\cdot \tag{120}$$

The effective scattering potential in the medium is the average of $V(r)$ over the crystalline unit cell. This is a good approximation for neutrons beyond the Bragg cutoff. In detail,

$$\langle V\rangle_{\text{cell}}=\frac{2\pi\hbar^2}{m}\rho\,\langle b_{\text{coh}}\rangle_{\text{cell}}\ , \tag{121}$$

where $\rho=N/V$, and b_{coh} is arithmetically averaged over the cell. The trial solution is

$$\psi(r)=\begin{cases}e^{ik_0\cdot r}+u_r\,e^{ik_r\cdot r}, & z>0\\ u_m\,e^{ik_m\cdot r}, & z\leq 0\end{cases}\cdot \tag{122}$$

where $k_r=k_0$. The subscript "r" denotes the reflected beam, while "m" refers to the wave within the scattering medium. The angle of incidence ϕ and the angles of the reflected and refracted waves ϕ_r and ϕ_m, respectively, are conventionally measured from the flat in neutron optics. Since the model potential is everywhere independent of x and y, the wavevectors k_0, k_r and k_m have equal components parallel to the surface. Thus the reflection is specular, $\phi_r=\phi$. The boundary conditions at $z=0$ are

$$\begin{aligned}1+u_r&=u_m\ ,\quad\text{and}\\ (1-u_r)k_0\sin\phi&=u_mk_m\sin\phi_m\ .\end{aligned} \tag{123}$$

It follows easily from Eq. (122) in Eq. (119) that

$$\frac{\hbar^2k_0^2}{2m}=\frac{\hbar^2k_m^2}{2m}+\langle V\rangle_{\text{cell}}\ . \tag{124}$$

This gives the index of refraction of the scattering medium,

$$n=\frac{k_m}{k_0}=\sqrt{1-\frac{\langle V\rangle_{\text{cell}}}{E_0}}\ . \tag{125}$$

The amplitude of the reflected wave works out to

$$u_r=\frac{\sin\phi-\sqrt{\sin^2\phi-\sin^2\phi_c}}{\sin\phi+\sqrt{\sin^2\phi-\sin^2\phi_c}}\ , \tag{126}$$

where ϕ_c is the critical angle,

$$\phi_c=\arcsin\sqrt{1-n^2}\ . \tag{127}$$

For $\phi\leq\phi_c$, Eq. (126) shows that $|u_r|=1$, which indicates that the incident wave is totally reflected. In this case the normal component of k_m is imaginary, and the wave in the medium is evanescent. When $\phi>\phi_c$, k_m is real, and its direction is given by Snell's law. The index of refraction in Eq. (125) can be written as

$$n\approx 1-\frac{\lambda_0^2}{2\pi}\eta\ , \tag{128}$$

where $\eta=\rho\langle b_{\text{coh}}\rangle_{\text{cell}}$ is the average scattering length density of the medium and generally is positive. Typically $n=1-O(10^{-5})$ for thermal neutrons, which gives critical angles

$$\phi_c\approx\lambda_0\sqrt{\frac{\eta}{\pi}} \tag{129}$$

of only fractions of a degree. The longer wavelengths of cold neutrons give substantially larger critical angles, which are required for practical applications of neutron guides. For media in which $\eta<0$, the index of refraction is greater than unity, ϕ_c is imaginary, and the incident wave is never totally reflected (except at $\phi=0$).

The scattering wavevector for neutron reflection is defined as

$$Q=k_0-k_r\ , \tag{130}$$

so that $Q=2k_0\sin\phi$. The neutron reflectivity, $R=|u_r|^2$, then is obtained from Eq. (126) as

$$R(Q)=\left[\frac{Q-\sqrt{Q^2-Q_c^2}}{Q+\sqrt{Q^2-Q_c^2}}\right]^2, \tag{131}$$

where $Q_c=2k_0\sin\phi_c$. This is equivalent to the Fresnel formula for reflectivity in optics. Thus,

$R(Q)=1$ for $Q \leq Q_c$, while for $Q \gg Q_c$, the reflectivity falls as

$$R(Q) \sim \frac{16\pi^2\eta^2}{Q^4} . \quad (132)$$

The asymptotic behavior in Eq. (132) is identical to that derived from the Born approximation for the potential in Eq. (120) when $d\sigma/d\Omega$, Eq. (60), is converted to the reflectivity, an observation made only recently by Sinha, et al. [16]. The reflection laws from heterogeneous and nonuniform surfaces and films depart significantly from Eq. (131) and are sensitive to model details. For expositions of neutron reflectometry and optics, see [9], [12], and [15].

5. References

[1] G. E. Bacon, Neutron Diffraction, 3rd ed., Oxford University Press, Oxford (1975).
[2] G. E. Bacon, Neutron Scattering in Chemistry, Butterworths, London and Boston (1977).
[3] E. Balcar, and S W. Lovesey, Theory of Magnetic Neutron and Photon Scattering, Oxford University Press, New York (1989).
[4] M. Bée, Quasielastic Neutron Scattering, Adam Hilger, Bristol and Philadelphia (1988).
[5] P. A. Egelstaff, ed., Thermal Neutron Scattering, Academic Press, New York (1965).
[6] G. Kostorz, ed., Neutron Scattering, Treatise on Materials Science and Technology, Volume 15, Academic Press, New York (1979).
[7] M. A. Krivoglaz, Theory of X-Ray and Thermal-Neutron Scattering by Real Crystals, Plenum Press, New York (1969).
[8] W. Marshall and S. W. Lovesey, Theory of Thermal Neutron Scattering, Clarendon Press, Oxford (1971).
[9] J. Penfold and R. K. Thomas, The Application of the Specular Reflection of Neutrons to the Study of Surfaces and Interfaces, J. Phys. Cond. Matt. **2**, 1369 (1990).
[10] D. L. Price and K. Sköld, Introduction to Neutron Scattering, in Methods of Experimental Physics, Volume 23, Neutron Scattering, K. Sköld and D. L. Price, eds., Academic Press, Orlando (1986) p. 1.
[11] E. Prince, Mathematical Techniques in Crystallography and Materials Science, Springer-Verlag, New York (1982).
[12] T. P. Russell, X-ray and Neutron Reflectivity for the Investigation of Polymers, Materials Science Reports **5** (1990) p. 171.
[13] R. Scherm, Fundamentals of Neutron Scattering by Condensed Matter, Ann. Phys. **7**, 349 (1972).
[14] V. F. Sears, Neutron Scattering Lengths and Cross Sections, in Methods of Experimental Physics, Volume 23, Neutron Scattering, K. Sköld and D. L. Price, eds, Academic Press, Orlando (1986) p. 521.
[15] V. F. Sears, Neutron Optics, Oxford University Press, New York (1989).
[16] S. K. Sinha, E. B. Sirota, S. Garoff, and H. B. Stanley, X-ray and Neutron Scattering from Rough Surfaces, Phys. Rev. **B38**, 2297 (1988).
[17] K. Sköld and D. L. Price, eds., Methods of Experimental Physics, Volume 23, Neutron Scattering Academic Press, Orlando (1986).
[18] G. L. Squires, Introduction to the Theory of Thermal Neutron Scattering, Cambridge University Press, Cambridge (1978).

About the author: *Norman F. Berk is a theoretical physicist in the Reactor Radiation Division of the NIST Materials Science and Engineering Laboratory. The National Institute of Standards and Technology is an agency of the Technology Administration, U.S. Department of Commerce.*

Volume 98, Number 1, January–February 1993
Journal of Research of the National Institute of Standards and Technology

[J. Res. Natl. Inst. Stand. Technol. 98, 31 (1993)]

Small Angle Neutron Scattering at the National Institute of Standards and Technology

Volume 98 Number 1 January–February 1993

B. Hammouda, S. Krueger, and C. J. Glinka

National Institute of Standards and Technology,
Gaithersburg, MD 20899

The small angle neutron scattering technique is a valuable method for the characterization of morphology of various materials. It can probe inhomogeneities in the sample (whether occurring naturally or introduced through isotopic substitution) at a length scale from the atomic size (nanometers) to the macroscopic (micrometers) size. This work provides an overview of the small angle neutron scattering facilities at the National Institute of Standards and Technology and a review of the technique as it has been applied to polymer systems, biological macromolecules, ceramic, and metallic materials. Specific examples have been included.

Key words: ceramic morphology; macromolecules in solution; metal alloys; microstructure; polymer structure; protein-DNA complexes; sintering; small-angle neutron scattering.

Accepted: July 8, 1992

1. Introduction

Small angle neutron scattering (SANS) instruments are very useful for the investigation of microstructures of 1 to nearly 500 nm in size in various materials such as porous media, polymers, ceramics, metals, etc. The very low energies of thermal neutrons make them an excellent non-destructive probe of microstructure since neutrons are very penetrating in most materials. The ability to substitute deuterium (D) for hydrogen (H) in macromolecular complexes makes SANS a unique technique for probing macromolecular conformations in synthetic and biological polymers.

Examples of research areas well-suited to the SANS technique include the determination of void sizes and their distributions in porous media such as metals, coals, shales, gels, etc. as well as the investigation of particle agglomeration in unsintered ceramic bodies and evolution of pore populations during sintering. SANS is also useful for the investigation of the morphology of polymer ("plastic") materials and of the relationship between their structures and properties. Structural changes of synthetic and biological macromolecules in solution with changing environment can be monitored and the internal structure of aggregated systems such as membranes, micelles (water-oil-soap), microphase segregated copolymers, etc. can be determined. SANS can also provide structural information that is helpful in the understanding of the thermodynamics of two-phase systems such as polymer blends, metal alloys, composites, etc.

Since neutrons have a magnetic moment, the magnetic scattering from magnetic materials can also be studied. SANS is useful for the determination of the range and degree of order in magnetic structures and for the measurement of critical properties of magnetic systems.

The National Institute of Standards and Technology has been operating an 8 m SANS instrument since the early 1980s. By the summer of 1992,

two 30 m high resolution SANS instruments were fully operational. This work describes the three SANS instruments at NIST and gives an overview of SANS research opportunities in the areas of polymer science, biology, ceramics, and metals.

2. The NIST SANS Instruments

The 8 m NIST SANS instrument benefited from the installation of a cold source at the NIST reactor in 1987, which resulted in substantial increases in intensity for that instrument. After the construction of a guide hall, completed in 1990 as part of the Cold Neutron Research Facility (CNRF), the 8 m SANS instrument was moved to the end of one of the newly installed neutron guides. The first 30 m SANS instrument (the Exxon/Univ. of Minn. SANS), also installed in the guide hall, began operation in the Spring of 1991 while the second 30 m instrument (the CHRNS-SANS) began operation in the summer of 1992.

2.1 The 8 m SANS Instrument

The 8 m SANS spectrometer [1] is a general purpose instrument with a broad range of accessible scattering vectors (i.e., scale lengths probed), continuously variable wavelength and a number of possible sample environments. The instrument characteristics are listed in Table 1. The instrument components include a helical velocity selector with 25% wavelength resolution (which means high intensity on sample), a 4.5 m evacuated flight tube preceding the sample and a 3.5 m scattering flight path that can be rotated about the sample position to reach larger scattering angles. A computer-controlled sample chamber that houses up to six positions is available for measurements at near ambient temperatures. The sample chamber can be removed to accommodate bulkier sample environments such as a cryostat or displex. Neutrons are detected with an area detector with an active area of 64×64 cm. The low-Q limit on the instrument is achieved with multibeam converging pinhole collimation.

2.2 The Two 30 m SANS Instruments

The two 30 m SANS spectrometers are high resolution, wide scattering vector range instruments that combine and improve upon some of the best features of existing long flight path instruments in the world. The characteristics for the two instruments are listed in Table 2 and a schematic of the NIST/EXXON/Univ. of Minn. 30 m SANS is shown in Fig. 1. The neutron intensity at the sample position of that instrument (for a 1.5 cm diameter sample) is shown in Fig. 2 which also shows the intensity at the sample position for the 8 m SANS instrument.

Table 1. 8 m SANS instrument characteristics

Source size:	5×5 cm
Wavelength range:	0.48–2.0 nm (velocity selector)
Wavelength resolution:	25% (fixed)
Collimation:	Single pair of circular irises or 7-channel converging beam collimation
Q_{min}:	0.06 nm^{-1} at 0.6 nm wavelength 0.035 nm^{-1} at 0.9 nm wavelength
Q range:	0.03 to 5.0 nm^{-1}
Sample size:	0.4–2.0 cm with pinhole collimation 1.5 cm with converging collimation
Flux at sample:	10^3 to 5×10^5 n/cm^2·s depending on slit size and wavelength.

Table 2. 30 m SANS instrument characteristics

Source size:	5×5 cm
Wavelength range:	0.4–2.0 nm (velocity selector)
Wavelength resolution:	7%–30% (continuously tunable)
Q-Range:	0.01–6 nm^{-1} (CHRNS-SANS) 0.01–10 nm^{-1} (NIST/EXXON/Univ. of Minn. SANS)
Sample size:	0.5–2.5 cm
Expected flux at sample:	10^3 to 10^6 n/cm^2·s depending on slit size, wavelength, and source to sample distance

The design characteristics of these two 30 m SANS instruments have many similar features including a computer-controlled multidisk velocity selector, an adjustable incident flight path with neutron guide sections that can be moved into the beam in order to bring the effective neutron source closer to the sample therefore enhancing the intensity, and a beam polarizing device (supermirror transmission polarizer) to be developed. The scattering flight path can be varied between 2 and 16 m by changing the detector position. Both instruments provide two different sample positions. The first position features a multi-position sample chamber which can accommodate up to nine sample positions. Upstream, the second sample position consists of an adjustable sample table for bulky sample environments. A number of sample environments are available for the SANS users. These include heating blocks and circulating baths for measurements at temperatures ranging from -20 to 200 °C, a closed cycle He^3 cryostat for measurements in the 30 mK to 300 K range and

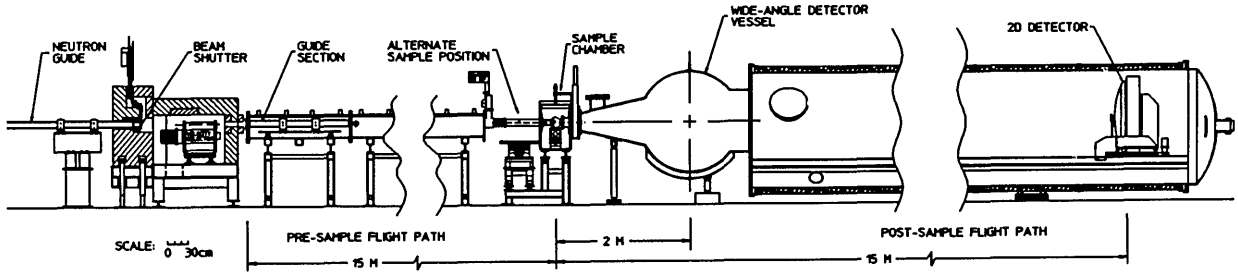

Fig. 1. Schematic drawing of the NIST/EXXON/Univ. of Minn. 30 m SANS instrument.

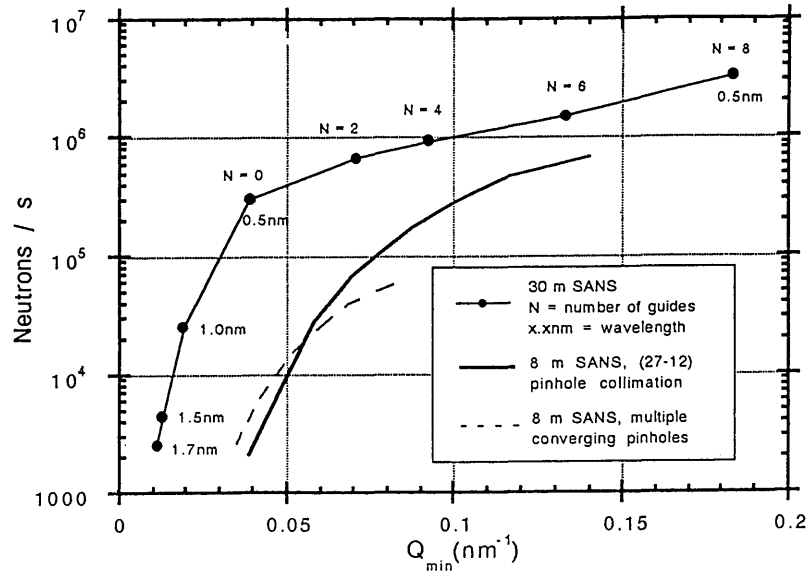

Fig. 2. Intensity at the sample position for the NIST/EXXON/Univ. of Minn. 30 m SANS instrument and for the 8 m SANS instrument.

furnaces for measurements at temperatures up to 2000 °C. Shearing cells are available for measuring liquids and gels under shear. In addition, measurements can be made in magnetic fields up to 7 T.

A set of user friendly software packages for data acquisition, reduction and analysis as well as instrument control have been written. A microvax 4000[1] computer is used for data acquisition and reduction while Macintosh computers are used for on-line color imaging of the data. The ability to take reduced data away on IBM PC or Macintosh floppy disks is also provided.

[1] Certain commercial equipment, instruments, or materials are identified in this paper to specify adequately the experimental procedure. Such identification does not imply recommendation or endorsement by the National Institute of Standards and Technology, nor does it imply that the materials or equipment identified are necessarily the best available for the purpose.

3. Small Angle Neutron Scattering from Polymers

3.1 Introduction

Small angle neutron scattering is a unique diagnostic technique to probe the morphology of polymer materials. Due to the ability to replace hydrogen atoms by deuterium, this technique can monitor specific macromolecular conformations in polymer solutions as well as in bulk polymer systems. It can also monitor concentration fluctuations in phase decomposing binary mixtures such as homopolymer and/or copolymer blends. Contrast variation methods (mixing deuterated and non-deuterated polymers or solvents) are used to change the "color" of polymer chains making them more or less visible to neutrons similarly to the staining method in electron microscopy.

Due to the fact that SANS spectra are not abundant in prominent features (as for example diffraction or NMR spectra are), the SANS technique relies heavily on modeling of the scattering intensity. Macromolecular systems can be modelled fairly well owing to the pioneering work of many scientists such as P. Flory (Gaussian chains, theta temperature, etc.), H. Kuhn (polymer chain stiffness, etc.), W. Stockmayer (geiation, etc.), B. Zimm (dilute solutions, etc.), P.G. de Gennes (random phase approximation, scaling ideas, etc.) to name only a few. The SANS technique has shown with no ambiguity, for instance, that polymer coils follow random walk trajectories when they are in the bulk state [2–4]. This means that correlations between monomers along the chain backbone are screened by other surrounding chains, so that the chain "forgets" quickly (after one or two steps) about where its other parts are. This screening is less effective in polymer solutions and self avoiding walk statistics are more appropriate making coils more swollen or more collapsed depending on whether the constraints on the walk are repulsive or attractive (i.e., depending on the nature of the monomer-solvent interactions). Flory introduced a characteristic transition temperature (called the theta temperature) for which the monomer-solvent interactions are equivalent making the chain appear "ideal" (as if it were in a bulk environment). Below this temperature, the solvent cannot dissolve the polymer, while above it, it becomes a good solvent.

Blending of polymers is necessary for better controlled physical properties of polymeric materials. Unfortunately, most polymer alloys are incompatible (i.e., most polymers do not like to mix). The binary mixtures that are known to mix have been very precious systems for studying the thermodynamics of phase separation. For example, polystyrene and polyvinylmethylether (PS/PVME) show [5] a lower critical solution temperature (LCST) since they are miscible at room temperature but phase separate with a spinodal decomposition temperature around 140 °C when the fractions are about 30/70 and molecular weights 435,000/188,000. The mixing of low molecular weight polystyrene and polybutadiene (PS/PB), on the other hand, has an upper critical solution temperature (UCST) phase diagram [6] and shows mixing upon heating from ambient temperature (spinodal temperature is around 37 °C for a mixture of 77/23 dPS/hPB with $M_w = 900/4{,}500$). Conformations in the miscible region, concentration fluctuations close to the immiscible region as well as the delimitation of the spinodal line have been well understood for a number of polymer blend systems [5–14] using the SANS technique with deuterium labeling of one of the components.

A method of forcing different polymers to mix is to chemically copolymerize them at the small block level. Most copolymers can therefore mix at the macroscopic level but show microphase separation. Here also, the SANS technique supplemented with specific deuteration of one of the blocks has been valuable [15–18] in mapping out chain conformations in each of the various possible morphologies (lamellar, rod-like, spherical).

In cases where detailed models of polymer systems are not available, generic SANS methods such as Guinier plots are used to extract characteristic sizes. Other direct methods based on linear fits of combinations if $I(Q)$ and Q vs powers of Q are used to extract scaling laws which are signatures of various kinds of morphologies. $I(Q)$ is the measured scattered intensity and Q is the scattering wavenumber. For instance a slope of -2 in a plot $\log[I(Q)]$ vs $\log(Q)$ hints that chains are in ideal (Gaussian) conformations.

3.2 SANS from Polymer Solutions

Polymer solutions constitute a bench-mark for understanding basic interactions between monomers and solvent molecules. Effects of temperature, concentration and chain stiffness have been thoroughly investigated [19–23] using the SANS technique.

Temperature effects are investigated using Flory's swollen chain approach. Variation of the radius of gyration, R_g, of a single chain (i.e., its effective statistical size) with the number of monomers N in the chain (representative of the molecular weight M_w) follows the simple mean field scaling law: $R_g = N^{\nu} a^2/6$, where a is the monomer size and ν is the Flory excluded volume parameter ($\nu = 1/2$ for ideal chains, $\nu = 1/3$ for collapsed chains and $\nu = 0.6$ for fully swollen chains). Of course scattering data contains contributions from inter-chain contributions which are accounted for through concentration effects on the scattered intensity $I(Q)$ or on the structure factor $S(Q)$. These two quantities are related to each other by the coherent scattering cross section $\{b\}^2$, monomer volume fraction ϕ_p, and machine constant C:

$$I(Q) = C\{b\}^2 \phi_p S(Q). \qquad (1)$$

In dilute solutions, only binary chain interactions contribute to the interaction energy, making the second virial coefficient the dominant term in a virial expansion. Such interactions occur mainly through single contacts (as pointed out by Zimm [24]) making the static structure factor, $S(Q)$, a simple two-term expansion in terms of the monomer volume fraction:

$$S(Q)=S_0(Q)[1-v\phi_p S_0(Q)]. \quad (2)$$

Here, $S_0(Q)$ is the single-chain structure factor and v is the excluded volume during the interaction between monomers and solvent molecules which is related to the monomer-solvent Flory interaction parameter K as:

$$v=(1/\phi_s-2K). \quad (3)$$

Moreover, $\phi_s=1-\phi_p$ is the solvent volume fraction. The reciprocal form of Zimm's expansion can be derived directly [25,26] using the random phase approximation (RPA) and was a major tool (Zimm plot) for extracting single chain properties from dilute polymer solutions. This method of obtaining single chain properties is hampered by low scattering signals due to the low polymer concentrations involved. Another method allowing the use of concentrated polymer solutions was introduced in 1980 [27,28].

The high concentration method of extracting single chain properties such as the radius of gyration, the monomer size or the persistence length (which is a measure of chain stiffness) consists in using mixtures of deuterated and non-deuterated polymers of the same molecular weight in semidilute or concentrated solutions. The single chain structure factor can be obtained from the scattering data by varying the fraction of deuterated chains while keeping the total polymer concentration constant.

A representative example [29] of this method is included here. Figure 3 shows the single-chain and the total scattering structure factors for dPS in hPS of $M_w=65{,}000$ as shown in Ref. 29. More than two (for redundancy) relative concentrations ($\phi_{dPS}/\phi_{hPS}=20\%,40\%,60\%,85\%$) were measured in toluene solutions with fixed concentration ($\phi_p=22\%$). The total scattering structure factor is seen to be flat (as expected) owing to the fact that all monomers contribute to that term equally.

The use of high concentrations increases the signal-to-noise ratio making it much easier to monitor single chain properties. This high concentration method made Zimm plots less preferable in SANS data analysis.

3.3 SANS from Blends of Homopolymers

In the case where polymers are homogeneously mixed (blended), the RPA is also very useful. A two-component blend (called A and B for convenience) and shown in Fig. 4 can be looked at as a polymer component (say A) in solution in the other component (B). The partial structure factors, such as $S_{AA}(Q)$, can be related to the bare structure

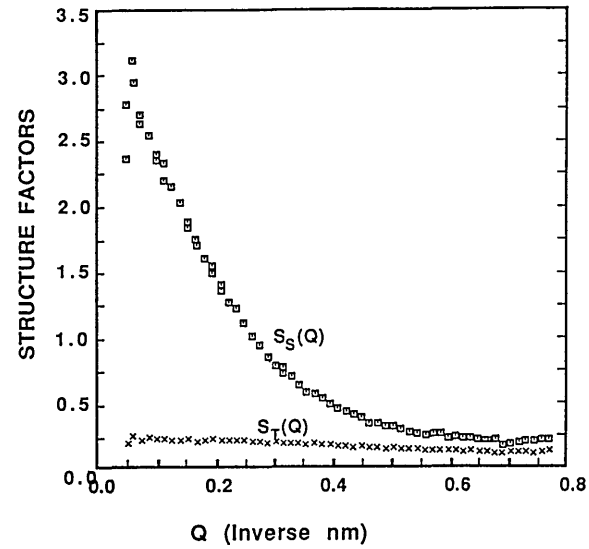

Fig. 3. Single-chain and total structure factors for a concentrated solution of mixtures of deuterated and nondeuterated polystyrene (dPS, hPS) in toluene. The total polymer concentration was 22% and the relative deuterated fractions were varied from 0% to 85%.

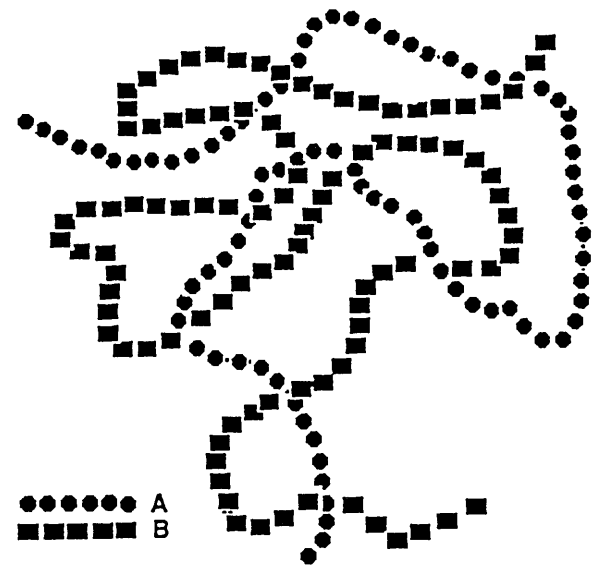

Fig. 4. Schematic representation of a two-component polymer blend. Only two macromolecules are represented for simplicity.

factors $S_{0AA}(Q)$ and $S_{0BB}(Q)$ (when no interactions are present) for AA and BB correlations as:

$$1/\phi_A S_{AA}(Q) = [1/\phi_A S_{0AA}(Q)] + [1/\phi_A S_{0BB}(Q)] - 2K_{AB} \quad (4)$$

where ϕ_A and ϕ_B are the partial volume fractions ($\phi_A + \phi_B = 1$). The bare structure factors are usually replaced by a Debye function (Gaussian coils) which is a good representation of ideal non-interacting chains.

This RPA result for the structure factors is an extension [30,31] of Eq. (2) in which the solvent volume fraction ϕ_s is replaced by $\phi_B S_{0BB}(Q)$. This result was first introduced by de Gennes [25] and is applicable to situations where a mean field approach is valid such as in dilute solutions, concentrated solutions, melts and blends. It does not give good results in semidilute solutions where chains start overlapping (multiple contacts are not accounted for in the RPA) but do not overlap enough to begin screening intrachain correlations.

The scattered intensity for an incompressible blend is given by:

$$I(Q) = C\{b_A - b_B\}^2 S_{AA}(Q), \quad (5)$$

where b_A and b_B are the scattering lengths of monomers A and B, respectively. A correlation length ξ can be extracted from a fit of the data (taken at different sample temperatures T) to the Ornstein-Zernike form:

$$I(Q) = C\{b_A - b_B\}^2 N_A \phi_A / (1 + Q^2 \xi^2) \quad (6)$$

in the Guinier region. Plots of $I^{-1}(Q)$ vs T^{-1} or of the extracted ξ^2 vs T^{-1} show a linear behavior which deviates sharply close to the spinodal temperature (where concentration fluctuations start becoming large, signaling the onset of phase separation). Extrapolation of this linear behavior gives the spinodal temperature T_s (for which both $I(Q)$ and ξ blow up). This method, when repeated for different volume fractions, has allowed a precise mapping of the spinodal line for many compatible polymer blend mixtures.

As an example, scattering SANS data and the resulting phase diagram [5] for a dPS/PVME blend are shown in Figs. 5 and 6. The molecular weight were $M_w = 435{,}000$ and 188,000 and the volume fractions were 30/70 for the two components (dPS and PVME), respectively. The Flory interaction parameter $K_{dPS/PVME}$ was found to vary inversely with temperature away from the spinodal temperature as the mean field theory predicts.

3.4 SANS from Copolymers and Copolymer/ Homopolymer Mixtures

The RPA approach for a blend of two homopolymers can be extended to include an arbitrary number of homopolymers and/or copolymers using a matrix notation formalism:

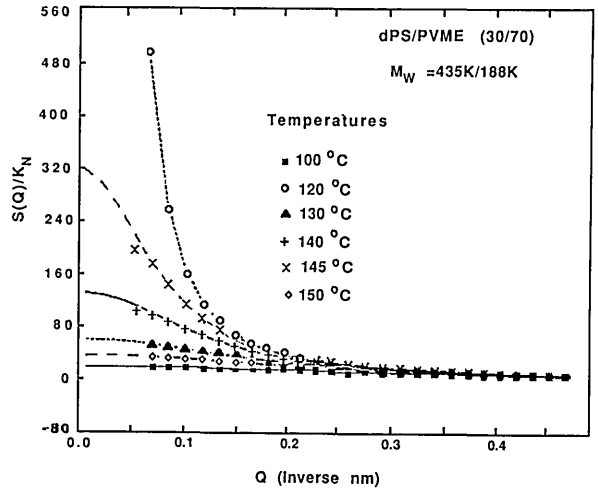

Fig. 5. Corrected SANS intensity for a blend of 30/70 dPS/PVME taken at various temperatures from the one-phase region to the two-phase region.

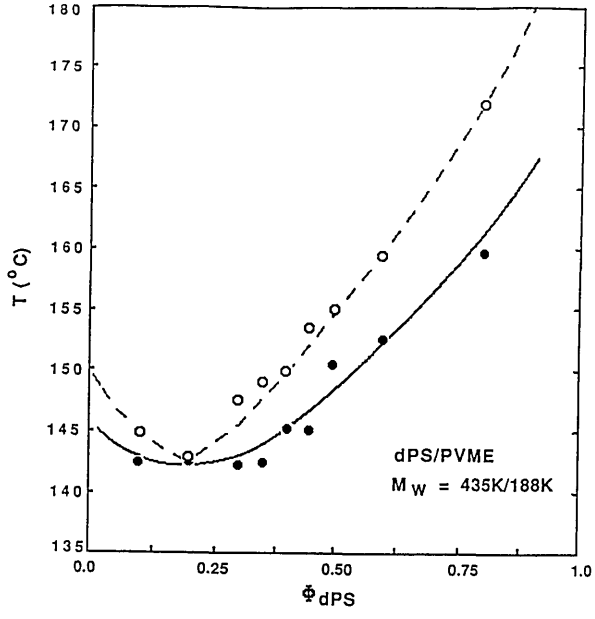

Fig. 6. Phase decomposition diagram as obtained from SANS measurements for the 30/70 dPS/PVME blend system.

$$X^{-1}(Q)=X_0^{-1}(Q)+v \quad (7)$$

where the matrices X and X_0 represent the interacting and bare structure factors respectively and the matrix v contains the various excluded volumes v_{AA}, v_{BB} and v_{AB}. The various structure factors for the interacting system are obtained from the inverse of Eq. (7). In the case of block copolymers, the off-diagonal elements of the bare structure factors matrix $X_0(Q)$ are non-zero and represent cross correlations between different blocks. These results were derived by Benoit and coworkers [31]. Sakurai et al. [32] used a similar approach to sort out the effects of microstructure and deuterium labeling in random copolymers of 3,4 polyisoprene (hPI) with 1,4 hPI in 1,2 dPB with 1,4 dPB (copolymer A-B in copolymer C-D). The effective Flory interaction parameter K_{eff} shows an LCST phase separation behavior while the individual interaction parameters K_{AB}, K_{AC}, etc., all clearly show a UCST behavior. The overall behavior results from an interplay among all of these partial interaction parameters.

3.5 Other SANS Applications from Polymers

The SANS technique has been very successfully used in many other polymer problems. For example, SANS has been instrumental in the understanding of polymer conformations in semicrystalline polymers. For instance, it was found that the radius of gyration of deuterated chains in crystalline polyethylene is comparable to that in the disordered phase [33–38] (before crystallization). This points to the fact that only local conformational changes are required during crystallization. SANS has also found extensive applications in understanding polymer adsorption on micron size latex particles [39–43], in charged polymer systems [44–45], and in gels and interpenetrating networks [46–54], etc.

One of the goals of materials science is to seek structure/property relationships. SANS has contributed [55–58] to materials science by providing conformational changes when polymer materials have been subject to various treatments. For instance, the degree of anisotropy of polymer chains has been investigated in partially deuterated (5%) polystyrene (M_w=250,000) samples that were hot stretched above the glass-rubber transition temperature (110 °C) and then quenched back to ambient temperature. It was found [55–56] that macromolecules follow the external (mechanical) stretching affinely up to elongations that double the sample length. Beyond that elongation, plastic deformations take over and the chains start slipping past each other in order to release the externally applied stress. Similar methods were also used [57–58] to monitor macromolecular orientation along a shear band that developed after notching and compressing partially deuterated PS samples.

3.6 Future Research Horizons

Since its introduction in the early 1970s, the SANS technique has found a great deal of applications in the field of polymer research covering applications all the way from cutting edge science to applied routine characterization. Newly introduced methods (such as the high concentration method or the random phase approximation) have brought renewed interest in the SANS technique making it an ever growing research tool for polymer scientists. A recent literature search of the Chemical Abstracts database based on the two keywords "neutron" and "polymer" came up with 480 articles that were published between 1980 and 1990, 424 of which used the SANS technique.

The two 30 m SANS instruments that have been constructed at NIST will certainly help alleviate such an unsatiable demand for beam time. These two long flight path instruments have resolutions from the near atomic (1 nm) to the near micrometer (500 nm) length scales. This, combined with good intensity on sample, is opening up a wide range of experiments in the area of polymers. One such experiment will consist in the investigation of shear induced phase separation of polymer solutions. Solutions of high molecular weight ($M_w=10^6$) dPS in DOP solvent show a UCST phase diagram with a spinodal temperature around 13 °C. They are also known to phase separate at room temperature when under high shear rates. Monitoring of the chain conformations will yield a better understanding of the thermodynamic phase diagram and of its shifting under shear. Because of the large R_g's involved, such an experiment requires the use of a low-Q instrument such as a 30 m instrument.

Another experiment will use a time slicing feature that is being included in the data acquisition software of the 30 m SANS instruments at NIST. This feature allows the recording of sequential time spectra with small time mesh increments. A dPS/hPB blend is in the two-phase region at room temperature and goes to the one-phase region either by heating over 40 °C or by shearing the mixture. We intend to investigate the conformational changes that are associated with the return to the

two-phase region after quenching back down to room temperature or after cessation of the shear flow.

4. Small Angle Neutron Scattering from Biological Macromolecules

4.1 Introduction

SANS is an important complement to techniques such as electron microscopy, hydrodynamic measurements and biochemical assays in the study of biological structures since macromolecules are measured in solution without further preparation. The main advantage of neutrons for the study of biological macromolecules is that the lighter elements such as carbon, hydrogen, nitrogen, and oxygen all have similar neutron scattering lengths. In addition, the large difference in the scattering lengths of hydrogen and deuterium makes it possible to study different components of a macromolecular complex *in situ* by substituting D_2O for H_2O in the solution and/or D for H in the complex. This makes SANS useful for the study of two-component systems such as protein-nucleic acid or lipid-protein complexes and even more complex systems such as cells and vesicles. If deuterium labelling is used, individual subunits can be located within multi-subunit proteins. In addition, conditions can be manipulated to highlight interactions between macromolecule and solvent. Several reviews on the applications of SANS have been published in the last several years [59–62].

4.2 Method

A macromolecule will only scatter neutrons when its scattering length density, ρ, is different from that of the surrounding solution. Since SANS is a low resolution technique, the solvent is assumed to be infinite and homogeneous, with a scattering length density, ρ_s. The difference between the scattering length density of the macromolecule and that of the solvent, $\Delta\rho = \rho - \rho_s$, is known as the contrast. The intensity of the scattered neutrons, can be written as [63]

$$I(Q) = n(\Delta\rho)^2 < \left| \int_V \exp(iQ\cdot r) d^3r \right|^2 >, \qquad (8)$$

where $n = N/V$ is the number of macromolecules per unit volume and $< >$ denotes an average over all possible orientations of the macromolecule. Q is the momentum transfer of the neutron, with a magnitude of

$$Q = 4\pi(\sin\theta)/\lambda, \qquad (9)$$

where 2θ is the scattering angle. At zero scattering angle,

$$I(0) = n(\Delta\rho V_p)^2, \qquad (10)$$

where V_p is the particle volume which is inaccessible to the solvent [60].

By manipulating the contrast by changing either ρ or ρ_s, the intensity of the scattered neutrons at $Q = 0$ can be increased or decreased, depending upon the value of $\Delta\rho$. If ρ_s is changed by adjusting the ratio of H_2O to D_2O in the solvent, then $\Delta\rho$ varies linearly with the concentration of D_2O ($\%D_2O$) in the solvent [60]. Thus, a plot of $\sqrt{I(0)}$ vs. $\%D_2O$ yields a straight line which crosses the x-axis at the point where the neutron intensity vanishes. This is the match point of the molecule. This match point is especially useful for composite systems, such as protein-DNA or lipid-protein complexes. Using the method of "contrast variation" [64], the scattering from one component can be minimized by adjusting the H_2O/D_2O ratio in the solvent, thus allowing the scattering from the other component to dominate the total scattering. Figure 7 shows the scattering length density from several components of biological complexes as a function of $\%D_2O$ in the solvent. Note that the scattering density from water varies from -0.562×10^{10} cm^{-2} for H_2O to 6.4×10^{10} cm^{-2} for D_2O.

In the small angle limit, the Guinier approximation for the scattered intensity,

$$I(Q) \sim I(0)\exp(-Q^2R_g^2/3), \qquad (11)$$

where R_g is the radius of gyration of the macromolecule, applies in the range $QR_g \lesssim 1$. Both $I(0)$ and R_g may be determined from a plot of $\ln[I(Q)]$ vs Q^2. $I(0)$ is related to the molecular weight of the molecule and R_g to the shape. Beyond the Q region where Eq. (11) is valid, $I(Q)$ must be compared to model curves in order to gain further information about the macromolecular structure. SANS has been useful for rapid measurements of the radius of gyration and molecular weight of macromolecules in solution [65]. Rapid characterization can be provided in solution in a non-"invasive" manner. More extensive studies aiming to further characterize biological macromolecules are described below.

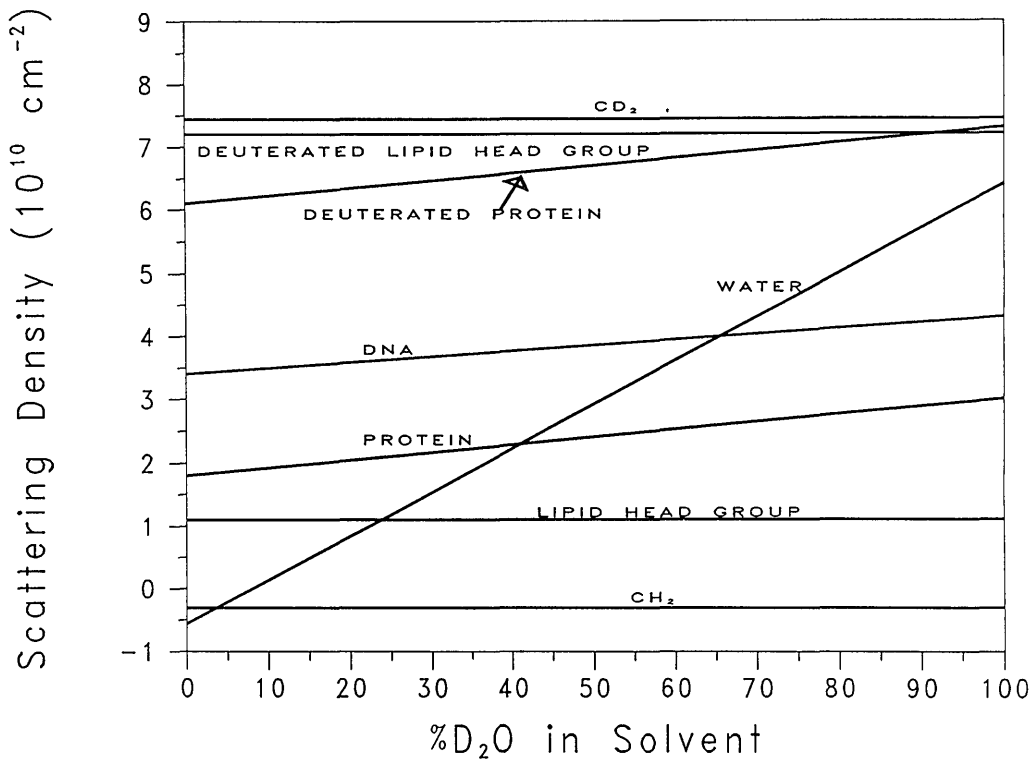

Fig. 7. Scattering density vs %D_2O in the solvent for various biological components.

4.3 Multi-Component Systems

Systems such as protein-nucleic acid complexes are well suited to SANS studies since there is a large difference in scattering length densities between protein and that of nucleic acid. Thus, the location of the nucleic acid component relative to the protein component can be ascertained. Conformational changes in the protein upon nucleic acid binding can also be quantified. This technique has been applied successfully to a number of systems of which the nucleosome [66], DNA-gyrase [67] and amino-actyl tRNA synthetase systems [68,69] are just a few examples.

The prokaryotic ribosome has been the subject of extensive SANS studies. SANS has been used not only to locate the RNA component in the 30S and 50S ribosomal subunits [70–73], but also to map the location of the constituent proteins with respect to one another using the label triangulation technique [70,74–76]. This method can only be successful if pairs of deuterated proteins are incorporated into the ribosome so that the distance between them could be measured. The shapes of these proteins have also been determined from measurements of isolated proteins in solution [77] and from measurement of the proteins *in situ* using specific deuteration [70]. Deuterium labelling has proven successful for the measurement of distances between subunits in the DNA-dependent RNA polymerase [78–80] and from tryptophan synthase [81].

4.4 Membrane Proteins

Membrane proteins are an integral part of biological membranes. The complexity of the membrane composition makes them difficult to study *in situ*. Yet, the hydrophobic nature of membrane proteins also can pose a problem for solution studies. The development of detergents which allow the extraction of active membrane proteins [82] has helped to alleviate this problem. Since a membrane protein is soluble in detergent, its radius of gyration and molecular weight can be obtained using the contrast variation technique. The method was applied successfully to the ATP/ADP transport protein [83].

4.5 Cells and Vesicles

The cores of cells and vesicles can be studied *in situ* using the method of contrast variation, provided that the scattering length density of the core

constituents is sufficiently different from that of the surrounding membrane. The protein cores of red blood cells [84] and neurosecretory vesicles [85] have been studied by using contrast variation to minimize the scattering from the cell membrane. Figure 8 shows the scattered intensity from red blood cells in 100% D_2O, where the membrane scattering dominates the total intensity, and in H_2O, where the protein (hemoglobin) scattering dominates. The sharply-rising portion of the curve at low-Q values corresponds to the cell membrane whereas the peak in the intensity at approximately $Q = 0.85$ nm^{-1} is due to interacting hemoglobin molecules. While the overall intensity is smaller in the H_2O case, the ratio of hemoglobin to membrane intensity is much larger under the same conditions. Similarly, the magnetic scattering from magnetite particles in magnetotactic bacteria was measured in 30% D_2O, where the scattering from the bacterium was minimized with respect to that of the magnetite particles [86].

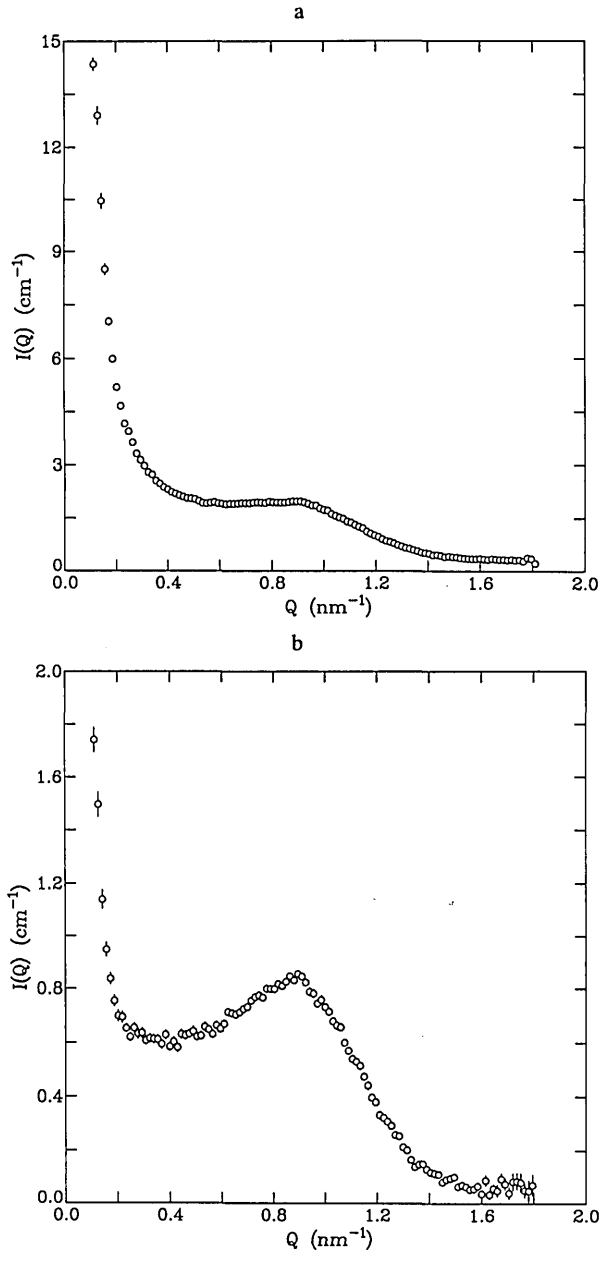

Fig. 8. Scattered intensity from blood cells in a) 100% D_2O and b) H_2O (0% D_2O). The scattering a low Q values is due to the cell membranes whereas the peak at $Q \approx 0.85$ nm^{-1} is due to interacting hemoglobin molecules.

4.6 Interaction with Solvent

A hydration shell around a macromolecule can be measured directly with SANS if its scattering length density differs from that of the bulk solvent. Using deuterated glycerol and alcohol aqueous solvents, the hydration shell around ribonuclease A was measured [87]. Charged macromolecules can be surrounded by a volume of dense solvent due to the exclusion of salts in their immediate vicinity. In an H_2O/D_2O contrast variation experiment, such a region surrounding tRNA was studied under different salt conditions [88].

4.7 Future Directions

The development of cold neutron beams has made the SANS technique more useful for the study of biological macromolecules in dilute solutions. However, even at dilute concentrations, purified material is needed in milligram quantities. Improved biochemical techniques for producing molecules and complexes in these quantities will allow many more systems to be examined. Specific deuteration could also be fully exploited if the investment in sample preparation is reduced.

5. Small Angle Neutron Scattering from Ceramic Materials

5.1 Introduction

The SANS technique is an important tool for measuring residual porosity in sintered ceramics since other techniques such as mercury porosimetry and gas adsorption are not available for measurement when the pores are closed. However, conventional SANS measurements will only detect residual pores smaller than 100 nm. Additionally,

many ceramic materials contain microstructural fractures that are larger than 100 nm, including initial porosity, particle agglomeration, and impurity effects in the compacted powder and during the early sintering stages [89]. Finally, conventional SANS cannot be used readily to study the porosity of green or partially-sintered ceramics due to the high porosity of these materials.

The range of sizes applicable to neutron scattering has been extended to 10 μm using multiple small angle scattering (MSANS) techniques [90,91]. The MSANS formalism can be used to measure thicker as well as denser systems in which the coherent elastic neutron scattering cross-section is dominated by multiple scattering. Consequently, powder samples with large particle agglomerates can be measured at densities approaching 50% of theoretical density (TD). In addition, large pores in green compacts (50–60% TD) can be measured with MSANS even though the porosity is very high (40–50%). Together, conventional SANS and MSANS can effectively be used to cover the full range of relevant microstructure sizes in ceramic systems.

Using the MSANS formalism to extend the range of sizes measurable with small angle neutron scattering to between 0.08–10 μm, the evolution of microstructure as a function of thermal processing, which is important for the development of process models in ceramics, has been addressed [92,93]. In addition, the processing/microstructure relationships in ceramic materials as a function of green body density and sintering aids such as MgO [94] have been investigated.

5.2 MSANS Theory

Unlike conventional SANS, the scattering in the MSANS regime is dominated by multiple neutron scattering. The radii of the scattering pores, or particle agglomerates, are the same order of magnitude as the mean distance a neutron can travel through the material before being scattered or absorbed. This means that the neutrons scatter from only one pore, or particle agglomerate, at a time even though they may scatter many times before leaving the sample. Thus, there is no contribution to the measured scattering from interference between scatterers.

The interaction of neutrons with matter is characterized by the phase shift v that a plane wave undergoes in traversing a particle of radius R. This phase shift determines the shape of the single-particle differential scattering cross section, $d\Sigma(Q)/d\Omega$), as a function of the scattering wavevector Q, where $|Q|=2\pi\epsilon/\lambda$ and $\epsilon << 1$ is the scattering angle and λ is the neutron wavelength. v depends upon $\Delta\rho$, the contrast of the particle or void relative to the scattering matrix such that

$$v = 2\Delta\rho R\lambda. \tag{12}$$

In the SANS diffraction regime, $v << 1$, whereas in the MSANS regime, $0.1 \leq v \leq 2.0$.

In conventional SANS, the scattered intensity as a function of Q is independent of neutron wavelength and its shape near $Q=0$ depends only on the particle dimensions. Figure 9a represents a typical SANS scattering curve. The scattered intensity around $Q=0$ cannot be measured directly because it lies in the same region as the transmitted beam, which is 10^3 to 10^7 times more intense than the scattered beam. Therefore, a beamstop is usually employed to prevent the transmitted beam from reaching, and thus damaging, the neutron detector. For any particle shape, the particle size can be described by its radius of gyration R_g, or Guinier radius [95], which applies at the small Q portion of the scattering intensity curve.

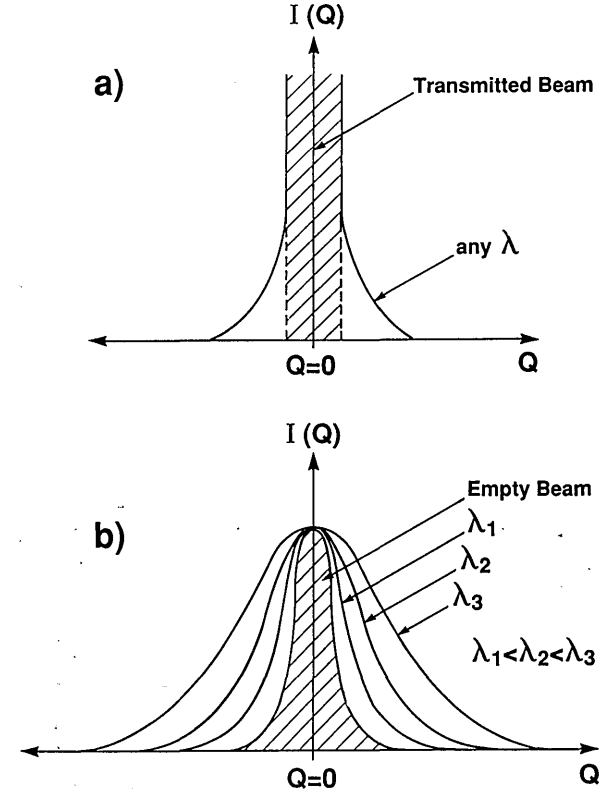

Fig. 9. Representation of a typical SANS scattering curve for a) conventional SANS and b) multiple SANS.

In MSANS, the intensity of the transmitted beam is immeasurably small and the width of the scattered intensity curve near $Q=0$ is broadened far beyond the broadening due to instrumental resolution. The amount of beam broadening is dependent upon the incident neutron wavelength as illustrated in Fig. 9b, where representative MSANS curves are shown for different wavelengths incident on a single sample. The intensities have been normalized such that $I(0)=1.0$. In each case, the scattered intensities, $I(Q)$, have a curvature, r_c, near $Q=0$ and can be approximately described as a Gaussian with a width proportional to λ^2. An effective radius, $R_{eff}(0)$, where the 0 refers to the small Q region near $Q=0$, can be determined for the scatterers from the wavelength dependence of r_c using the MSANS formalism represented in Eqs. (2.12–2.15) of Berk and Hardman-Rhyne [90,91]. The MSANS formalism in effect replaces the standard Guinier analysis in the small Q region of $I(Q)$ where $R_{eff}(0)$, rather than R_g, defines the size of the scatterers. However, both R_g and $R_{eff}(0)$ are volume-weighted measures of pore radius.

Even under conditions where the low Q portion of the scattering curve is dominated by multiple scattering, the large Q portion of the scattering curve, where $QR \leq 10$, follows [90] single particle Porod [95] behavior where the scattered intensity is proportional to Q^{-4}. Thus the standard Porod analysis [95] can be applied to the large Q region of $I(Q)$ independent of the existence of MSANS at low Q.

In the Porod region, the scattered intensity can be written as

$$I(Q)=PQ^{-4}+B, \tag{13}$$

where B is a background term and P is Porod's constant defined as

$$P=2\pi(\Delta\rho)^2(S/V), \tag{14}$$

where S/V is the normalized total surface scattering area per unit volume. Obtained in this manner, S/V is independent of the shape of the scattering pores or particle agglomerates. If a spherical shape is assumed, an effective radius, $R_{eff}(\infty)$, where (∞) refers to the large Q portion of the scattering curve, can be obtained since $R_{eff}(\infty)=3\phi(V/S)$ where ϕ is the volume fraction of scatterers. The number density can be obtained from $N_p=(S/V)/(4\pi R_{eff}(\infty))^2$. Unlike R_g and $R_{eff}(0)$, $R_{eff}(\infty)$ is a surface area-weighted measure of pore radius.

5.3 Creep Cavitation

The failure of ceramics at elevated temperatures often involves the evolution of cavitated grain boundaries. Subsequently, the cavities coalesce to form cracks which then can grow, ultimately causing creep failure. SANS has been used to study the nucleation and growth of creep cavities in sintered alumina [96,97] as well as to characterize the shape of creep cavities in hot-pressed silicon carbide [98,99]. By combining Guinier and Porod results, size distributions for the cavities as a function of creep strain were derived for both materials. SANS was also used to study the materials after post-creep thermal treatment [100] to determine the best way to remove prior creep damage in the form of grain boundary cavitation.

5.4 Powders, Compacts, and Sintered Ceramics

The first studies which tested the MSANS formalism involved the characterization of alumina powder [101] and sintered and green compacts of yttrium chromite [102]. The alumina (Al_2O_3) powder samples ranged in thickness from 2 to 10 mm and in density from 28% TD to 33% TD. By analyzing the broadening of the scattered intensity curve as a function of neutron wavelength an effective radius of $R_{eff}(0)=265$ nm [101] was determined for the alumina particles. The versatility of MSANS is demonstrated in an experiment [102] in which pressed powder samples of yttrium chromite were measured in the green state (57% TD) and after sintering (94% TD). The green compact showed much more beam broadening than the sintered compact due to the larger pore volume fraction in the green case. However, the fitted $R_{eff}(0)$ values for both samples were nearly identical, with $R_{eff}(0)=0.17$ μm for the green compact and $R_{eff}(0)=0.18$ μm for the sintered sample.

5.5 Pore Evolution and Processing/ Microstructure Relationships

Knowledge of the microstructure evolution as a function of thermal processing is important for the development of process models in ceramics. The pore evolution of crystalline alumina [93] and porous glassy silica [92] have been measured by MSANS as a function of sintering. Figure 10 shows the scattered intensity as a function of wavelength for an 85% TD alumina sample. The beam broadening effect, which is the signature of copious multiple scattering, is easily seen. Using the MSANS

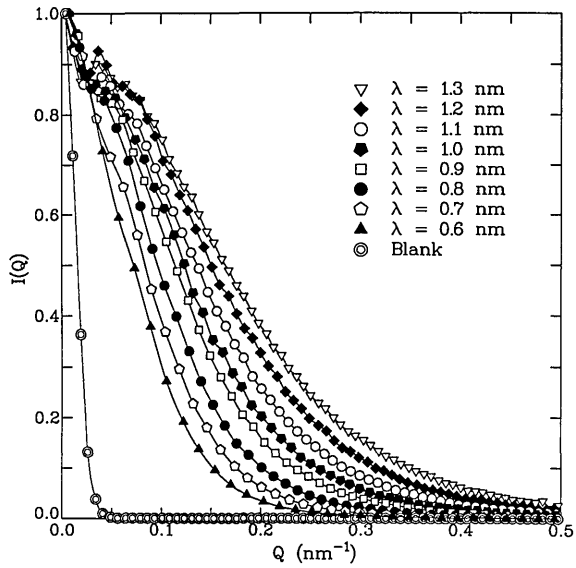

Fig. 10. Scattered intensity as a function of neutron wavelength for an 85% TD alumina.

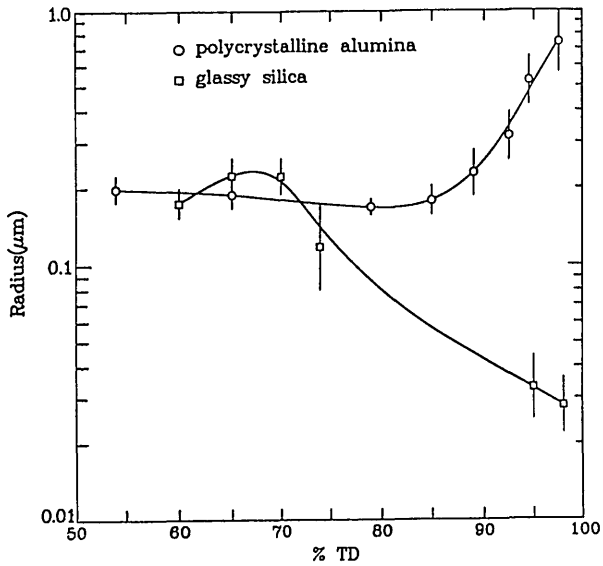

Fig. 11. A comparison of the effective pore radius, determined from MSANS measurements, as a function of % TD for a glassy silica system and a polycrystalline alumina system.

formalism, an effective radius, $R_{eff}(0) = 0.18$ μm, was determined. Similarly, effective radii were determined for samples ranging in densities from 54% to 97.5% TD for the alumina samples and from 60% to 98% TD for the silica samples. In addition, the effect of green body density and the addition of a sintering aid, MgO, on the pore evolution was examined for the alumina system [94].

By combining the results from the silica and alumina studies, the processing/microstructure relationships in both systems were examined in order to gain a quantitative measure of the structural evolution which takes place when different sintering mechanisms dominate [103]. Figure 11 shows the effective pore radius, determined from the MSANS measurements, as a function of %TD for both silica and alumina. Glassy silica sinters by means of viscous flow whereas crystalline alumina sinters by means of surface and volume diffusion. Figure 11 shows the effective pore sizes as a function of density. Clearly, these two major sintering mechanisms lead to very different microstructure evolution signatures.

5.6 Future Directions

MSANS measurements typically require on the order of a few minutes to 1 h, which is much more rapid than conventional SANS measurements. If measurements are made at the minimum number of three suitable wavelengths, the time per pore size determination can be quite short. Thus, the MSANS technique makes possible *in situ* studies of the pore evolution in ceramic materials as they are being sintered.

6. Small Angle Neutron Scattering from Metallic Materials

6.1 Introduction

The same SANS techniques used to study ceramics can be applied to metallic materials as well. These materials also contain microstructure such as precipitates, cavities, phase domains, density fluctuations, magnetic domains, microcracks, and dislocations [104] which can be measured with SANS. The technique is important in developing process models since it provides a quantitative characterization of microstructure.

6.2 Precipitate Distribution

Precipitates are important in alloys since relatively small changes in precipitate distribution can cause large changes in yield strength or fracture toughness [104]. SANS has been used at NIST to study the precipitate concentration and size distribution in HSLA steel as a function of different heat treatments [105]. HSLA steel is a Cu-Fe system whose strength is developed by the precipitation of a copper-rich phase. Since Fe has a magnetic moment and Cu does not, the scattering

contrast between the two components is enhanced, making SANS a unique tool for studying precipitates in this material. Figure 12 shows the 2-D scattering pattern from HSLA steel in a horizontal magnetic field. The magnetic field serves to align the magnetic domains in the Fe matrix to eliminate scattering from domain walls [104]. Thus, the scattering pattern is due to the precipitates and the anisotropy arises because the magnetic scattering is enhanced only in the direction perpendicular to the external magnetic field.

6.3 Deformation

SANS has been used to study the effects of plastic deformation on metallic systems. For example, the relationship between microstructure and the permanent volume expansion associated with plastic deformation in maraging steel and aluminum alloys was studied by measuring the scattered intensities before and after straining [104]. Because the intensity increased after straining, the volume expansion could not be caused by an increase of scattering centers such as microcracks or dislocations [104]. Rather, deformation-induced dissolution of precipitates would best explain the SANS results. On the other hand, SANS studies of deformed and annealed Cu and α-phase Cu Al single crystals [106] found that the measured intensities resulted from dislocation scattering rather than from bulk segregation of Al in the alloys.

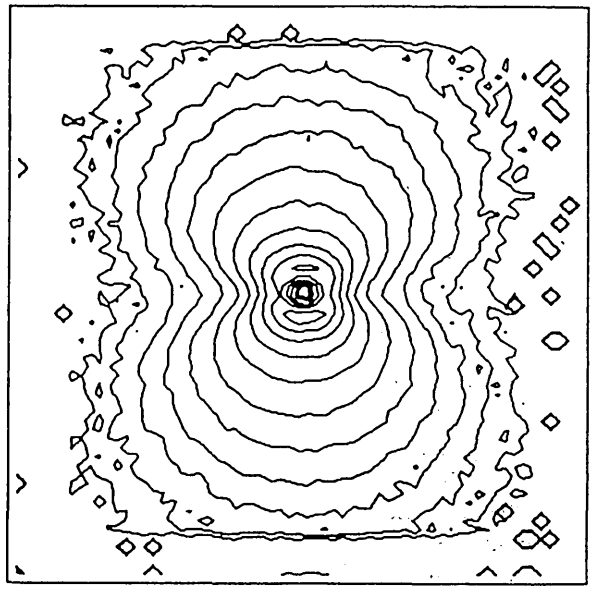

Fig. 12. Two-dimensional SANS pattern from an HSLA steel in a horizontal magnetic field.

6.4 Grain Boundary Cavitation

High temperature failure of alloys is often due to slow nucleation and growth of grain boundary cavities. SANS has been used to study both creep cavitation [107,108] and fatigue-induced cavitation [109,110,111]. In particular, SANS was used to study void growth in alloy 800 during creep [107] by measuring the scattered intensity as a function of creep time for six different samples. More recently, growth rates of grain boundary cavities in Cu during high temperature fatigue [111] have been studied and compared with those resulting from creep. The SANS measurements were combined with precision density measurements to accurately measure cavity surface area and cavity size.

Acknowledgments

We thank Drs. Charles Han, Gabrielle Long, and John Barker for reading portions of this manuscript and making suggestions for improvement. Some of the material in this article is based upon activities supported by the National Science Foundation (under Agreement No. DMR-8805794).

7. References

[1] C. J. Glinka, J. M. Rowe, and J. G. LaRock, J. Appl. Cryst. **19**, 427 (1986).
[2] P. J. Flory, Principles of Polymer Chemistry, Cornell University Press, Ithaca, NY (1953).
[3] P. G. De Gennes, Scaling Concepts in Polymer Physics, Cornell University Press, NY (1979).
[4] R. G. Kirste, W. A. Kruse, and J. Schelten, Makromol. Chem. **162**, 299 (1973).
[5] C. C. Han, B. J. Bauer, J. C. Clark, Y. Muroga, Y. Matsushita, M. Okada, Q. Tran-Cong, and T. Chang, Polymer **29**, 2002 (1988).
[6] A. Nakatani, H. Kim, Y. Takahashi, and C. C. Han, J. Chem. Phys. **93**, 795 (1990).
[7] G. D. Wignall, H. R. Child, and F. Li-Aravena, Polymer **21**, 131 (1980).
[8] J. Koberstein, J. Polym. Sci., Polym. Phys. Ed. **20**, 593 (1982).
[9] H. Yang, G. Hadziioannou, and R. S. Stein, J. Polym. Sci., Polym. Phys. Ed. **21**, 159 (1983).
[10] C. T. Murray, J. W. Gilmer, and R. S. Stein, Macromolecules **18**, 996 (1985).
[11] M. Shibayama, R. S. Stein, and C. C. Han, Macromolecules **18**, 2179 (1985).
[12] D. J. Lohse, Polym. Eng. Sci. **26**, 1500 (1986).
[13] D. Schwahn and H. Yee-Madeira, Colloid Polym. Sci. **265**, 867 (1987).
[14] M. G. Brereton, E. W. Fisher, C. Herkt-Maetzky, and K. Mortensen, J. Chem. Phys. **87**, 6144 (1987).
[15] R. Duplessix, J. P. Cotton, H. Benoit, and C. Picot, Polymer **20**, 1181 (1979).

[16] R. W. Richards and J. L. Thomason, Polymer **22**, 581 (1981).
[17] F. S. Bates, Macromolecules **18**, 525 (1985).
[18] B. Hammouda, W. Yelon, A. C. Lind, and F. Y. Hansen, Macromolecules **22**, 418 (1989).
[19] R. W. Richards, A. Maconnachie, and G. Allen, Polymer **22**, 147 (1981); **22**, 158 (1981); **22**, 153 (1981).
[20] K. Okano, K. Kurita, S. Nakajima, E. Wada, M. Furusaka, and Y. Ishikawa, Physica B+C **120**, 413 (1983).
[21] R. Ullman, H. Benoit, and J. S. King, Macromolecules **19**, 183 (1986).
[22] J. S. Higgins and A. Maconnachie, Polymer Solution, W. C. Forsman, ed., Plenum, N.Y. (1986) pp. 83-238.
[23] A. T. Boothroyd, G. L. Squires, L. J. Fetters, A. R. Rennie, J. C. Horton, and A. M. de Vallera, Macromolecules **22**, 3130 (1989).
[24] B. Zimm, J. Chem. Phys. **14**, 164 (1946); **16**, 1093 (1948).
[25] P. G. de Gennes, J. Phys. **31**, 235 (1970).
[26] K. Binder, J. Chem. Phys. **79**, 6387 (1983).
[27] C. E. Williams, M. Nierlich, J. P. Cotton, G. Jannink, F. Boue, M. Daoud, B. Farnoux, C. Picot, P. G. de Gennes, M. Rinaudo, and M. Moan, J. Polym. Sci., Polym. Phys. Lett. **17**, 379 (1979).
[28] A. Z. Akcasu, G. C. Summerfield, S. N. Jahshan, C. C. Han, C. Y. Kim, and H. Yu, J. Polym. Sci., Polym. Phys. Ed. **18**, 863 (1980).
[29] J. S. King, W. Boyer, G. D. Wignall, and R. Ullman, Macromol. **18**, 709 (1985).
[30] H. Benoit and M. Benmouna, Polymer **25**, 1059 (1984).
[31] M. Duval, C. Picot, M. Benmouna, and H. Benoit, J. Phys. **49**, 1963 (1988).
[32] S. Sakurai, H. Jinnai, H. Hasegawa, T. Hashimoto, and C. C. Han, Macromolecules **23**, 451 (1990).
[33] J. M. Guenet and C. Picot, Polymer **20**, 1473 (1979); **20**, 1483 (1979).
[34] G. D. Ballard and J. Schelten, J. Cryst. Growth **48**, 169 (1980).
[35] D. Y. Yoon and P. J. Flory, Polym. Bull. **4**, 693 (1981).
[36] M. Stamm, J. Hocker, and A. Axmann, Mol. Cryst. Liq. **77**, 125 (1981).
[37] D. M. Sadler and P. J. Barham, J. Polym. Sci., Polym. Phys. Ed. **21**, 309 (1983).
[38] E. W. Fisher, Polym. J. **17**, 307 (1985).
[39] K. J. Barnett, T. Cosgrove, B. Vincent, A. N. Burgess, T. L. Crowley, T. King, J. D. Turner, and T. F. Tadros, Polymer **22**, 283 (1981).
[40] L. Auvray and P. G. de Gennes, Europhys. Lett. **2**, 647 (1986).
[41] T. Cosgrove, T. G. Heath, K. Ryan, and T. L. Crowley, Macromolecules **20**, 2879 (1987).
[42] L. Auvray, J. P. Cotton, B. Farnoux, D. Ausserre, I. Caucheteux, H. Hervet, and F. Rondelez, Polym. Prep. **29**, 383 (1988).
[43] J. S. Higgins, P. E. Tomlins, J. V. Dawkins, G. G. Maghami, and S. A. Shakir, Polym. Comm. **29**, 122 (1988).
[44] T. R. Earnest, J. S. Higgins, and W. J. MacKnight, Macromolecules **15**, 1390 (1982).
[45] J. P. Aime, F. Bargain, M. Schott, H. Eckhardt, R. Elsenbaumer, G. G. Miller, M. E. McDonnell, and K. Zero, Synth. Meth. **28**, C407 (1989).
[46] C. Picot, Polymer **20**, 1316 (1979).
[47] R. Ullman, Macromolecules **15**, 1395 (1982).
[48] A. M. Fernandez, J. M. Widmaier, L. H. Sperling, and G. D. Wignall, Polymer **25**, 1718 (1984).
[49] J. Bastide, R. Dupessix, C. Picot, and S. Candau, Macromolecules **17**, 83 (1984).
[50] N. S. Davidson, R. W. Richards, and A. Maconnachie, Macromolecules **19**, 434 (1986).
[51] R. M. Briber and B. J. Bauer, Macromolecules **21**, 3296 (1988).
[52] P. G. Higgs and R. C. Ball, J. Phys. **49**, 1785 (1988).
[53] M. Daoud, Physica B **156-157**, 405 (1989).
[54] W. L. Wu, L. Jong, A. Hanyu, L. Coyne, and R. S. Stein, Macromolecules **23**, 351 (1990).
[55] F. Boue, M. Nierlich, G. Jannink, and R. Ball, J. Phys. **43**, 137 (1982).
[56] B. Hammouda, R. A. Bubeck, and D. F. R. Mildner, Polymer **27**, 393 (1986).
[57] J. M. Lefebvre, B. Escaig, and C. Picot, Polymer **23**, 1751 (1982).
[58] R. A. Bubeck, B. Hammouda, and H. Kaiser, Polymer Comm. **27**, 354 (1986).
[59] D. M. Engelman and P. B. Moore, Annu. Rev. Biophys. Bioeng. **4**, 219–239 (1975).
[60] B. Jacrot, Rep. Prog. Phys. **39**, 911–953 (1976).
[61] G. Zaccai and B. Jacrot, Annu. Rev. Biophys. Bioeng. **12**, 139–157 (1983).
[62] P. A. Timmins and G. Zaccai, Eur. J. Biophys. **15**, 257–268 (1988).
[63] G. Porod, in Small Angle X-ray Scattering, O. Glatter, and O. Kratky, eds., New York, Academic Press (1982) pp. 17–51.
[64] H. B. Stuhrmann and A. Miller, J. Appl. Cryst. **11**, 325–345 (1978).
[65] B. Jacrot and G. Zaccai, Biopolymers **20**, 2413–2426 (1981).
[66] J. F. Pardon, D. L. Worcester, J. C. Wooley, K. Tatchell, K. E. Van Holde, and B. M. Richards, Nucleic Acids Res. **2**(11), 2163–2176 (1975).
[67] S. Krueger, G. Zaccai, A. Wlodawer, J. Langowski, M. O'Dea, A. Maxwell, and M. Gellert, J. Mol. Biol. **211**, 211–220 (1990).
[68] P. Dessen, S. Blanquet, G. Zaccai, and B. Jacrot, J. Mol. Biol. **126**, 293–313 (1978).
[69] D. Moras, B. Lorber, P. Romby, J. P. Ibel, R. Giégé, A. Lewit-Bentley, and M. Roth, J. Biomol. Struct. Dynamics **1**, 209–223 (1983).
[70] P. B. Moore, D. M. Engelman, J. A. Langer, V. R. Ramakrishnan, D. G. Schindler, B. P. Scheonborn, Y. Sillers, and S. Yakubi, in Neutrons in Biology, B. P. Scheonborn, ed., Plenum Press, New York (1984) pp. 73–91.
[71] P. B. Moore, D. M. Engelman, and B. P. Schoenborn, J. Mol. Biol. **91**, 101–120 (1975).
[72] P. Beaudry, H. U. Petersen, M. Grunberg-Manago, and B. Jacrot, Biochem. Biophys. Res. Commun. **72**, 391 (1976).
[73] V. Ramakrishnan, Science **231**, 1562–1564 (1986).
[74] D. M. Engelman and P. B. Moore, Proc. Natl. Acad. Sci. **69**, 1997–1999 (1972).
[75] W. Hoppe, J. Mol. Biol. **78**, 581–585 (1973).
[76] R. P. May, H. B. Stuhrmann, and K. H. Hierhaus, in Neutrons in Biology, B. P. Scheonborn, ed., Plenum Press, New York (1984) pp. 25–45.
[77] I. N. Serdyuk, G. Zaccai, and A. S. Spirin, FEBS Lett. **94**, 349–352 (1978).
[78] P. Stöckel, R. May, I. Strell, Z. Cejka, W. Hoppe, H. Heumann, W. Zillig, H. L. Crespi, J. J. Katz, and K. Ibel, J. Appl. Cryst. **12**, 176–185 (1979).

[79] P. Stöckel, R. May, I. Strell, Z. Cejka, W. Hoppe, H. Heumann, W. Zillig, and H. L. Crespi, Eur. J. Biochem. **112**, 411–417 (1980).
[80] P. Stöckel, R. May, I. Strell, Z. Cejka, W. Hoppe, H. Heumann, W. Zillig, and H. L. Crespi, Eur. J. Biochem. **112**, 419–423 (1980).
[81] K. Ibel, R. P. May, K. Kirschner, A. H. Lane, H. Szadkowski, M. T. Dauvergne, and M. Zulauf, Eur. J. Biophys. **151**, 505–514 (1985).
[82] M. LeMaire, J. V. Moller, and C. Tanford, Biochemistry **15**, 2336–2342 (1976).
[83] M. R. Block, G. Zaccai, G. J. M. Lauquin, and P. V. Vignais, Biochem. Biophys. Res. Commun. **78**, 471–477 (1982).
[84] S. Krueger and R. Nossal, Biophys. J. **53**, 97–105 (1988).
[85] S. Krueger, J. W. Lynn, J. T. Russell, and R. Nossal, J. Appl. Cryst. **23**, 546–555 (1989).
[86] S. Krueger, G. J. Olson, J. J. Rhyne, R. B. Blakemore, Y. A. Gorby, and N. Blakemore, J. Magnet. Magn. Mater. **82**, 17–28 (1989).
[87] M. S. Lehmann and G. Zaccai, Methods Enzymol. **127**, 619–629 (1986).
[88] Z. Q. Li, R. Giégé, B. Jacrot, R. Oberthur, J. C. Thierry, and G. Zaccai, Biochemistry **22**, 4380–4388 (1983).
[89] K. A. Hardman-Rhyne, K. G. Frase, and N. F. Berk, Physica **136b**, 223–225 (1986).
[90] N. F. Berk and K. A. Hardman-Rhyne, J. Appl. Cryst. **18**, 467–472 (1985).
[91] N. F. Berk and K. A. Hardman-Rhyne, J. Appl. Cryst. **21**, 645–651.
[92] G. G. Long and S. Krueger, J. Appl. Cryst. **22**, 539–545 (1989).
[93] S. Krueger, G. G. Long, and R. A. Page, Acta Cryst. **A47**, 282–290 (1991).
[94] G. G. Long, S. Krueger, and R. A. Page, J. Am. Ceram. Soc. **74**(7), 1578–1584 (1991).
[95] G. Kostorz, A Treatise on Materials Science, and Technology, H. Herman, ed., Vol. 15, New York, Academic Press (1979) pp. 227–289 (1979).
[96] R. A. Page, J. Lankford, and S. Spooner, J. Mater. Sci. **19**, 3360–3374 (1984).
[97] R. A. Page, J. Lankford, K. S. Chan, K. A. Hardman-Rhyne, and S. Spooner, J. Am. Ceram. Soc. **70**(3), 137–145 (1987).
[98] R. A. Page, J. Lankford, and S. Spooner, Acta Metall. **32**(9), 1275–1286 (1984).
[99] R. A. Page and S. Spooner, J. Mater. Sci. **21**, 1417–1422 (1986).
[100] R. A. Page and J. Lankford, Int. J. High Technol. Ceramics **2**, 179–193 (1986).
[101] K. A. Hardman-Rhyne and N. F. Berk, J. Appl. Cryst. **18**, 473–479 (1985).
[102] K. A. Hardman-Rhyne, N. F. Berk, and E. R. Fuller, Jr., J. Res. Natl. Bur. Stand. (U.S.) **89**(1), 17–34 (1984).
[103] G. G. Long, S. Krueger, R. A. Gerhardt, and R. A. Page, J. Mater. Res. **6**(12), 2706–2715 (1991).
[104] R. J. Fields, R. C. Dobbyn, and C. J. Glinka in NDE of Microstructure for Process Control, H. N. G. Wadley, ed., Proc. Symp. Am. Soc. for Metals, ASM Metals Congress, Detroit, MI, 123–131 (1984).
[105] G. E. Hicho, L. C. Smith, S. Singhal, and R. J. Fields, J. Heat Treating **3**(3), 205–212 (1984).
[106] J. E. Epperson, G. Kostorz, C. Ortiz, P. Fürnrohr, and K. W. Gerstenberg, Acta Metall. **27**, 1363–1372 (1979).
[107] G. G. Nilsson and M. Roth, Mater. Sci. Eng. **50**, 101–108 (1981).
[108] E. R. Fuller Jr., R. J. Fields, T.-J. Chuang, and S. Singhal, J. Res. Natl. Bur. Stand. (U.S.) **89**(1), 35–45 (1984).
[109] M. H. Yoo, J. C. Ogle, B. S. Borie, E. H. Lee, and R. W. Hendricks, Acta. Metall. **30**, 1733–1743 (1982).
[110] R. Page and J. R. Weertman, Scripta Metall. **14**, 773–777 (1980).
[111] J. G. Barker and J. R. Weertman, Scripta Metall. **24**, 227–232 (1990).

About the authors: *Boualem Hammouda, Susan Krueger, and Charles J. Glinka are research physicists in the Reactor Radiation Division of the National Institute of Standards and Technology. The National Institute of Standards and Technology is an agency of the Technology Administration, U.S. Department of Commerce.*

Volume 98, Number 1, January-February 1993
Journal of Research of the National Institute of Standards and Technology

[J. Res. Natl. Inst. Stand. Technol. 98, 47 (1993)]

Neutron Reflectivity and Grazing Angle Diffraction

Volume 98 Number 1 January-February 1993

J. F. Ankner, C. F. Majkrzak, and S. K. Satija

National Institute of Standards and Technology,
Gaithersburg, MD 20899

Over the last 10 years, neutron reflectivity has emerged as a powerful technique for the investigation of surface and interfacial phenomena in many different fields. In this paper, a short review of some of the work on neutron reflectivity and grazing-angle diffraction as well as a description of the current and planned neutron reflectometers at NIST is presented. Specific examples of the characterization of magnetic, superconducting, and polymeric surfaces and interfaces are included.

Key words: diffraction; interfaces; neutron reflectivity; polymer interfaces; surfaces; thin films.

Accepted: July 10, 1992

1. Introduction

Total reflection of neutrons was first observed by Fermi and Zinn [1] in 1944 and was used to determine the neutron scattering lengths of various elements. Since then, the neutron's optical properties have been used in a variety of studies in physics, chemistry, metallurgy, and biology. Over the last ten years, neutron reflectivity has emerged as a powerful technique for the investigation of surface and interfacial phenomena in many different fields. Although similar studies on surfaces can be performed with x-ray reflectivity, neutrons provide a unique advantage because isotopic substitution can be used to achieve large contrasts in the scattering density. Most notably, the isotopic labeling of hydrogen and deuterium has been used extensively to study polymer thin films [2]. Neutrons also couple to atomic magnetic moments and hence specular reflection of polarized neutrons is a sensitive probe of surface magnetic phenomena [3].

In this paper, we will present a short review of some of the work on neutron reflectivity and grazing-angle diffraction as well as a description of the current and planned neutron reflectometers at NIST. Specific examples of the characterization of magnetic, superconducting, and polymeric surfaces and interfaces will be included. This will not be an exhaustive review of the field—for some recent reviews on the subject, see Refs. [2] and [4].

2. Basic Principles

In neutron reflectivity experiments an incident beam of neutrons strikes the surface of a flat sample at an angle ϕ (Fig. 1). Neutrons striking the surface undergo refraction and reflection if the refractive indices on the opposite sides of the interface are different. The refractive index for neutrons can be defined as

$$n_1 = \frac{k_1}{k_0} = \sqrt{1 - \frac{V_1}{E}}$$

$$= \sqrt{1 - \frac{4\pi N_1 (b_1 \pm p_1)}{k_0^2}}, \quad (1)$$

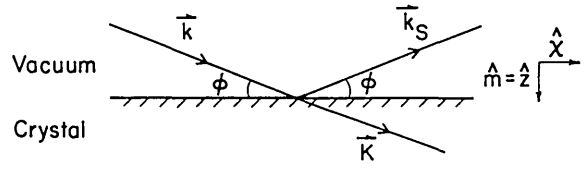

Fig. 1. Diffraction geometry for specular reflectivity. The incident beam k strikes the surface at angle ϕ and the reflected beam k_s exits at the same angle.

where k_1 and k_0 are the neutron wavevectors in a medium corresponding to a potential energy V_1 and in the vacuum, respectively; E is the vacuum neutron kinetic energy, N_1 the number of atoms per unit volume, and b_1 and p_1 the average nuclear and magnetic scattering lengths. The magnetic term describes the special case of a ferromagnetic medium so we see that a ferromagnetic material is birefringent, with the scattering length being proportional to the magnitude of the average ordered atomic magnetic moment. In the case where absorption in nonnegligible, b_1 is a complex quantity. With a few exceptions, the nuclear scattering length b_1 for neutrons is a positive quantity, meaning that the refractive index is less than one. Therefore, below a critical angle given by

$$\phi_{1c}=\left(\frac{4\pi N_1 b_1}{k_0^2}\right)^{1/2}, \tag{2}$$

the neutrons are totally reflected and only an exponentially damped evanescent wave penetrates into the sample. For typical materials, n_1 is such that the critical angle for total external reflection is on the order of $(1°/\text{nm})\lambda$, where λ is the de Broglie wavelength of the incident neutrons. Beyond the critical angle, the reflectivity decreases rapidly.

For specular reflection of neutrons the angle of reflection is the same as the angle of incidence. The wavevector corresponding to the specular scattering process is $Q=|k_{0s}-k_0|=2k_0\sin\phi$, where k_0 and k_{0s} are the incident and specular wavevectors. The reflectivity measured as a function of Q is related to the neutron refractive index profile normal to the surface. A number of different methods exist for calculating the reflectivity from a given scattering density (Nb) profile.

Since the momentum transfer in specular reflectivity is only in the direction normal to the surface, this scattering can be described in terms of the solution of the one-dimensional wave equation (derived from the Schrödinger equation),

$$\psi''(z)+\left(\frac{Q^2}{4}-4\pi N_1 b_1\right)\psi(z)=0, \tag{3}$$

where $\psi(z)=e^{ik_{0z}z}$) is the neutron wave function and $\hat{z}$ is the unit normal to the surface. For a stratified medium where b and/or N are functions of the depth z, the reflectivity can be calculated by imposing continuity on the wave function and its first derivative sequentially at each boundary between layers of constant potential in piece-wise continuous fashion using well-known matrix methods. Then, by modelling the refractive index profile as a function of depth z, an attempt to fit an observed reflectivity profile can be made. The reflectivity can also be calculated from the refractive index profile using methods developed in classical optics [5]. These methods are completely equivalent.

In the kinematical limit (when the reflectivity is much less than 1), one can write this reflectivity as

$$R(Q)=|r(Q)|^2\approx\left|\frac{4\pi Nb}{Q}\int_{-\infty}^{\infty}\rho(z)e^{iQz}dz\right|^2, \tag{4}$$

where Nb is the average scattering density of the sample and $\rho(z)$ is the deviation from that average density as a function of depth z. Integrating this expression by parts, we can then express the reflectivity as

$$R(Q)\approx\frac{(4\pi Nb)^2}{Q^4}\left|\int_{-\infty}^{\infty}\frac{\partial\rho(z)}{\partial z}\,e^{iQz}dz\right|^2. \tag{5}$$

This expression shows that scattering density gradients determine the specular reflectivity. Hence, the reflectivity will be most sensitive to those portions of the density profile with the largest gradients. For a more detailed general discussion on reflectivity, see Refs. [6–8] (for polarized beams, see Refs. [9, 10]).

3. Instruments

Two basic methods of measuring neutron reflectivity have been developed. A wide range of wavevectors Q can be achieved by sending a broad-spectrum beam onto a sample at a fixed angle of incidence. Time-of-flight (TOF) is used to measure the wavelengths of the reflected neutrons. The TOF method has been utilized very successfully at pulsed neutron sources, originally by G. P. Felcher at Argonne National Laboratory. In addition to the pioneering instrument at Argonne, TOF reflectometers have been built at several different

laboratories around the world, including the ISIS pulsed source at Rutherford Lab in the U.K. [11], the Los Alamos National Lab pulsed source [12], and the instrument at the Orphee reactor at Saclay [13]. The TOF method possesses the advantage of constant sample illumination for all wavevectors. The relative resolution $\delta Q/Q$ is dominated by the angular divergence of the beam $\delta\theta$ and is, therefore, constant over the reflectivity profile. However, the actual resolution δQ varies widely over the whole Q range. For a review of TOF instruments, see Refs. [9] and [11].

On a reactor-based reflectometer, one has the option of using a monochromatic beam and a conventional θ–2θ scan for varying Q. In this method the illuminated area of the sample varies with angle, which requires that samples be large enough to intercept a substantial fraction of the beam at low angles. A general assumption in the field has been that long-wavelength neutrons are required for a reactor-based, fixed-wavelength reflectometer. However, we have shown that 0.235 nm neutrons can be used very effectively to measure profiles down to the range of $2\text{–}3 \times 10^{-7}$ absolute reflectivity. A schematic of the BT-7 reflectometer at NIST is shown in Fig. 2. A filtered and collimated monochromatic (0.235 nm) beam of neutrons is incident on the sample. The collimation of the slits before the sample is continuously variable. In a typical scan, the slit just before the sample varies from 50 μm to about 1 mm with increasing Q, yielding angular divergences in the range of 0.3–1 mrad. The wavelength spread is mainly determined by the collimation before the monochromator and is $\delta\lambda/\lambda \sim 0.01$. The Q resolution at small momentum transfers ($Q \approx 0.2$ nm^{-1}) is about 0.02 nm^{-1} and at large transfers ($Q \approx 2$ nm^{-1}) is of order 0.05 nm^{-1}. A resolution of 0.02 nm^{-1} means that one can resolve Kiessig fringes from a film 200–300 nm thick. Reflectivities down to the $2\text{–}3 \times 10^{-7}$ can be measured on this instrument. The present arrangement requires samples to be in the vertical geometry. It is also worth pointing out that this instrument can be used in polarized-beam mode, by means of polarizing supermirrors. Both incident and exit polarization analyses are available.

Another reflectometer to be located in the NIST guide hall is presently under construction. This instrument will allow the sample to be in the horizontal position, thereby facilitating the study of liquid-vapor interfaces. Figure 3 shows both the elevation and plan views of the reflectometer. A neutron beam from the guide tube is monochromated and deflected down onto the sample by a graphite crystal. The angle of incidence is changed by raising or lowering the sample table and changing the tilt of the monochromator. Two detectors will be available—one for reflectivity and the other for grazing-angle diffraction, either or both of which will be position-sensitive detectors. Four different wavelengths, from 0.235 to 0.55 nm will be available. This instrument will be able to measure reflectivities in the 10^{-7} range.

Other reactor-based fixed-wavelength reflectometers around the world include ones at HFBR at Brookhaven National Lab, Jülich in Germany,

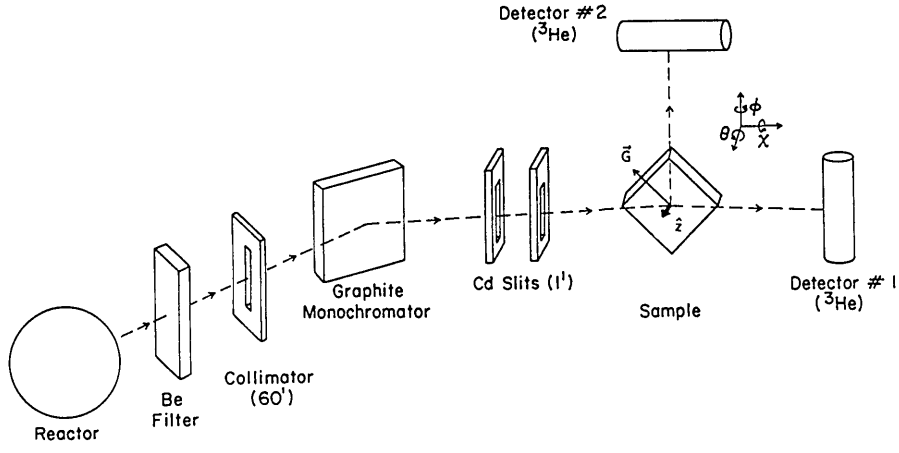

Fig. 2. Schematic of neutron reflectometer BT-7 at NIST. The specularly reflected beam enters detector 1. Detector 2 is used for grazing-angle diffraction.

and a new reflectometer/grazing-angle diffractometer at the Institut Laue-Langevin in Grenoble. We will now review some of the scientific studies being presently done or reported in the literature using neutron reflectometers. Parts of this review have already appeared in a recent paper by Majkrzak and Felcher [15].

3.1 Superconducting and Magnetic Layers

The interaction between the neutron's dipole moment μ and an atomic magnetic moment as characterized above by the scattering length p can also be expressed in a more general form as the potential energy $V = -\mu \cdot B$ where B is the local magnetic induction. One of the first magnetic profiles examined by neutron reflection was that of the penetration of an externally applied magnetic field into a superconducting material [16]. In superconducting materials the Meissner effect requires that $B = 0$ even in the presence of an external field (below a critical value). The shielding is provided by the onset of supercurrents in proximity to the surface. The penetration depth of the magnetic field is inversely proportional to the ability of the material to magnetically shield itself. Using a polarized neutron beam, spin-dependent reflectivity profiles can be measured because of the diamagnetic response of the superconductor to the applied magnetic field. The superconducting penetration depth in niobium, for example, has been directly measured by neutron reflectivity [16] to be 41 ± 4 nm, in reasonable agreement with theory.

In ferromagnetic materials, the magnetic contribution to the reflectivity can be much stronger than that observed in the case of a superconductor. It was predicted [17] and subsequently demonstrated [18] that a magnetic monolayer could be detected by neutron reflectivity. The effects of reduced dimensionality on interfacial magnetic states and corresponding critical behavior are of considerable current interest [19].

3.2 Magnetic Multilayers

By depositing a coherent superposition of a number of identical bilayers, the neutron reflectivity can be appreciably enhanced. Early neutron reflectivity work on magnetic multilayers has been reviewed by Endoh [20, 21]. However, sample quality, particularly the failure to maintain a regular bilayer period (which results in a relatively rapid broadening of higher-order reflections), limited initial studies in the detail of the magnetization profile which could be obtained perpendicular to the

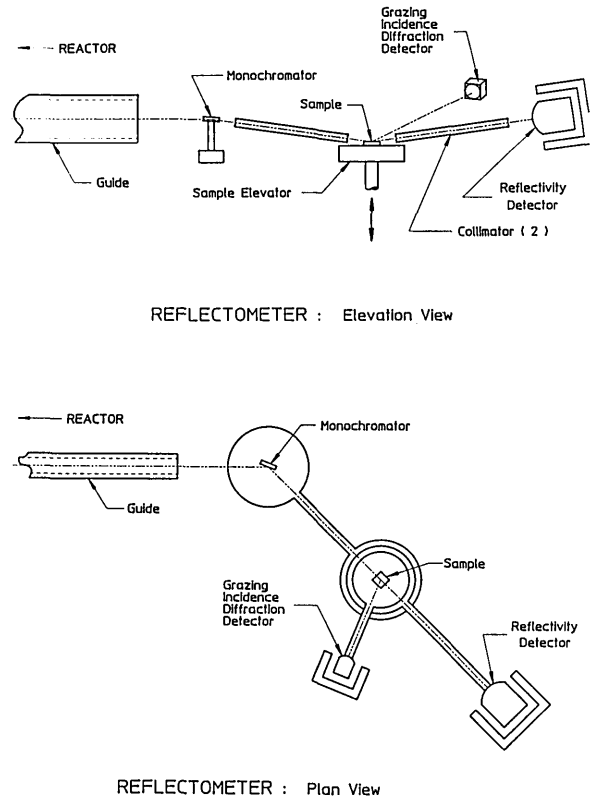

Fig. 3. Elevation and plan views of the cold neutron reflectometer under construction at NIST.

plane of the film. If the bilayer period is well-defined, then a sufficient number of harmonics may be observed to extract a magnetization profile with a resolution of several tenths of a nanometer. In Fig. 4 is shown polarized neutron reflectivity data for an Fe-Ge multilayer [22] with a bilayer spacing D of approximately 10.8 nm. Ignoring slight refraction corrections, multilayer reflections occur at integer multiples of $2\pi/D$. Note that the ratio of the two reflectivities corresponding to the "+" and "−" neutron spin eigenstates is not the same for all harmonics. This immediately implies that the magnetization profile across the ferromagnetic layer is nonuniform. X-ray and neutron diffraction measurements performed at higher values of Q about the Fe(110) peak position have revealed that the central sections of the Fe layers are composed of microcrystallites which have a strong preferred orientation of their close-packed (110) planes parallel to the substrate plane and which are at the same time randomly rotated about the growth direction (the Ge layers were found to be amorphous). Further quantitative analysis of the reflectivity measurements yielded a magnetization

profile with an interfacial region in which the moment was markedly reduced due primarily to interdiffusion.

It is important to note that although it may be possible to obtain an accurate magnetization profile along the growth direction in a given multilayer structure from the neutron reflectivity data, the correct interpretation of this profile requires proper consideration of not only interdiffusion but of interfacial roughness and/or waviness. To distinguish diffusion from roughness, diffraction scans orthogonal to the longitudinal specular reflectivity scans must be done so that a component of Q lies in the plane of the interface. The nonspecular scattering also gives information about possible multiple or simultaneous scattering effects and in-plane composition modulation. An effort is currently being made to extend the methods applied to the treatment of roughness for a single surface [23] to multiple interfaces.

It is also of some interest to point out that ferromagnetic thin film multi-bilayers can be used as efficient neutron polarizers by properly matching *Nb* and *Np* (see, for example Refs. [24] and [25] and references therein).

3.3 Polymer Interfaces

As mentioned in the introduction, neutron scattering amplitudes are isotope dependent. For hydrogen and deuterium the difference in amplitudes is relatively large so that by selective deuteration the scattering density contrast between different polymers or a polymer and solvent, for example, can be greatly enhanced. Neutron reflectivity measurements which yield the refractive index profile normal to the surface have been performed on numerous organic film structures in order to study interdiffusion and mixing as well as the adsorption of surfactants, polymers, and fatty-acids (see Refs. [26–28] and references therein). Langmuir-Blodgett film systems have also been studied by this technique [29–32].

As a specific example, neutron reflectivity can be used to monitor the early stages of interdiffusion of a bilayer heated to a suitable temperature, either taking reflectivity scans short in comparison with the diffusion time or quenching the sample after each anneal. In Fig. 5 is plotted the reflectivity ($\times k_{0z}^4$) of a bilayer of polystyrene of 230,000

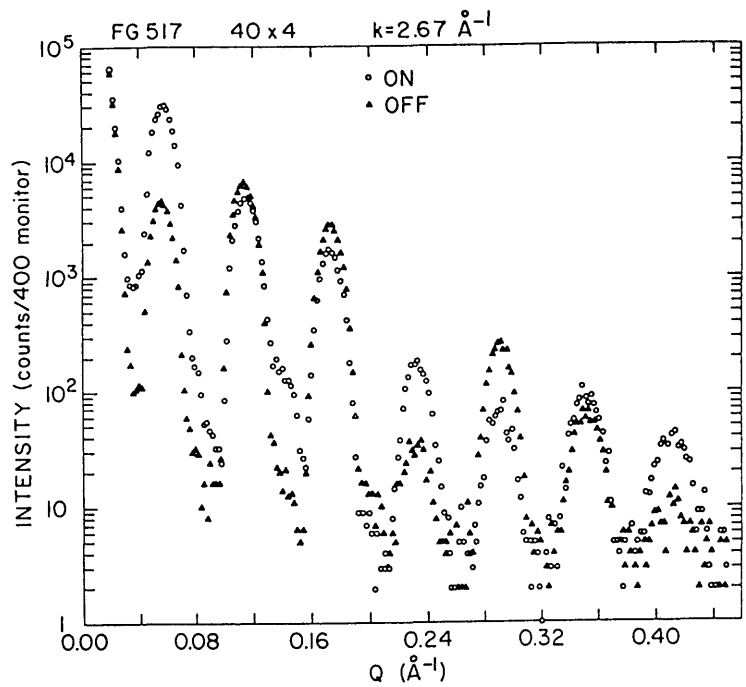

Fig. 4. Polarized neutron diffraction scan with Q perpendicular to the film planes of an Fe-Ge multilayer. Seven multilayer peaks with periodicity $Q = 2\pi m/D$ are shown beginning with $m = 1$. The "ON" ("OFF") data points correspond to incident neutrons in the "+" ("−") spin eigenstate (after Ref. [22]).

molecular weight as cast and after a short time anneal. The contrast between the two layers is obtained by deuterating the bottom layer. The solid lines between data points represent the reflectivities calculated for the layer thicknesses presented in the insert. After the anneal the reflectivity decreases as a result of interdiffusion over a thickness $\langle z^2\rangle^{1/2} = 3.0$ nm.

The interdiffusion of polymers is significantly different from that of simple molecules, where the latter may be represented as unstructured hard balls whose effective motion is completely described by the center of mass. The polymers have instead a characteristic size (radius of gyration) and each molecule is deeply entangled with its neighbors. These entanglements constrain their motion. The segments between the entanglements are relatively free to move, but this does not result in any motion of the center of mass of the molecule. The molecule as a whole may move only by sliding between entanglements with a repetitive motion. According to a theoretical model of polymer diffusion, the diffusion constant D of the molecule (which in conventional diffusion theory is given by $\langle z^2\rangle = 2Dt$) should decrease significantly from the time in which only segmental motion has taken place to the time in which the molecule has moved a full radius of gyration (reptation time) after which the diffusion coefficient should become constant. Figure 6 shows that the neutron

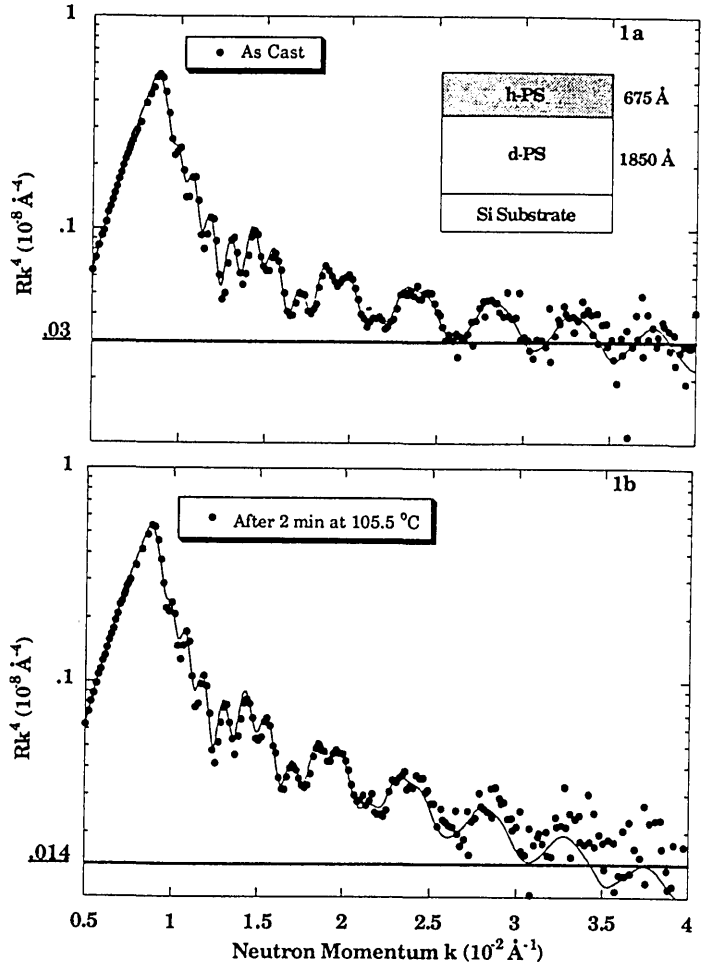

Fig. 5. Neutron reflectivity profile of a bilayer of polystyrene in which one of the layers has been deuterated. The data were collected before and after annealing. The solid lines represent the reflectivities calculated for the layer thicknesses given in the inset. After annealing, the reflectivity decreases as a result of interdiffusion.

reflection experiments are consistent with this picture.

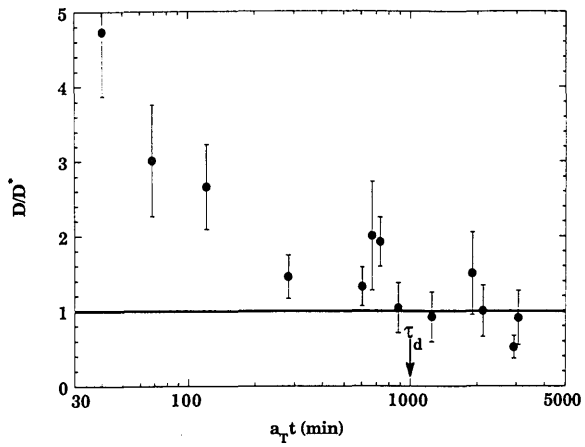

Fig. 6. Results of neutron reflectivity measurements showing that the diffusion constant for polymer systems becomes constant after a molecule has moved to a full radius of gyration.

As another illustration of what can be learned from neutron reflectivity measurements, consider the surface induced ordering of diblock copolymer films. Block copolymers of polystyrene (PS) and polymethylmethacrylate (PMMA) are used as surfactants, compatibilizing agents, and adhesives in biomedical and microelectronics applications. The morphology of these copolymers near surfaces can be significantly affected by the difference in the surface free energy of the two blocks and their affinity for the substrate. Depending on the interaction between the two blocks, the copolymer can be either homogeneously mixed or separated into lamellar microdomains which in the bulk are randomly oriented. However, in properly annealed films, these lamellar microdomains orient parallel to the free surface [33, 34] which is an ideal configuration for determining the compositional profile across the interfacial regions. Other methods such as transmission electron microscopy are limited by the feasibility of staining procedures and/or spatial resolution. These limitations do not apply to neutrons—the reflectivity study performed by Anastasiadis et al. [35] clearly showed that not only does a PS layer preferentially locate at the air-copolymer interface and PMMA at the substrate, but the layer thicknesses at the air and substrate interfaces are half those found in the bulk. Furthermore, an interfacial region was observed and determined to have a width of 5.4 nm to an accuracy of about 0.2 nm. In addition, evidence of surface-induced ordering of these copolymers in the phase-mixed state (above the bulk microphase separation temperature) was found, characterized by an exponentially damped, oscillatory density profile normal to the film surface as recently predicted by mean-field theory [36]. Further neutron reflectivity work on this particular system [37] has demonstrated that the measured reflectivity is also sensitive to the shape of the density profile across the interfacial region as shown in Fig. 7.

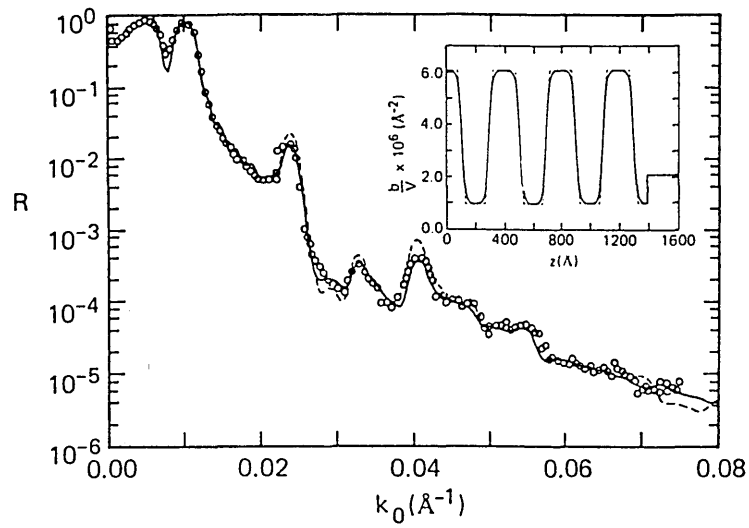

Fig. 7. Comparison of the experimentally measured neutron reflectivity profile and those calculated using a linear (- - -) and hyperbolic tangent (—) function to describe the segment density profile at the interface between the PS and PMMA microdomains for P(d-S-b-MMA) 100 K (after Ref. [37]).

3.4 Reflection at Solid-Solution Interfaces

A distinct advantage in using neutrons for reflectivity measurements is their ability to traverse macroscopic distances in single crystals such as silicon, quartz, or sapphire with relatively little loss. This makes it possible to use one of these crystals not only as a substrate on which a thin film or superlattice can be grown, but also as the incident medium. That is, the neutron beam can enter into one side of the crystal at nearly normal incidence and subsequently reflect at a glancing angle from the crystal-film interface. The opposite side of the film can then be placed in intimate contact with a liquid solution. A similar idea was first used [38] to measure the scattering length of liquid ^{3}He.

A schematic of such a cell, which was recently used to study polymers adsorbed from solution, is shown in Fig. 8. A recent example of the study of polymer brushes at the Si/solution interface [39] is shown in Fig. 9. The polymer used in this case was end-group carboxylated polystyrene (hydrogenated) with deuterated cyclohexane as the solvent. The carboxylated end group of the polymer is strongly adsorbed onto the silicon surface. A well-defined minimum in the reflectivity profile is characteristic of an adsorbed polymer film at the silicon-solution interface. The inset of Fig. 9 shows the concentration profile of this polymer brush at the interface determined by a nonlinear least squares fit of the reflectivity data.

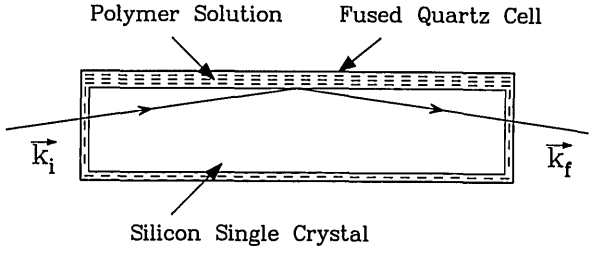

Fig. 8. Schematic (top view) of the cell used for neutron reflectivity measurements at solid-liquid interfaces. A large silicon single crystal is enclosed in a cell made of fused quartz with two 0.5 mm-thick windows for the incident and reflected neutron beams. The volume surrounding the Si crystal contains the polymer and solvent. The most important feature of this cell is that the incident and reflected beams pass through the bulk silicon crystal.

The liquid used in such a cell can even be an aqueous solution which is part of an active electrochemical cell. For example, the diffusion of either hydrogen or deuterium into a metal host film or superlattice can be measured [40] since H and D have scattering lengths which are comparable to those of the much heavier metal atoms. Although the density of hydrogen in thin films or multilayers of metal hydrides can be inferred from an expansion of the host lattice by conventional x-ray diffraction techniques, neutron reflectivity measurements yield the hydrogen density profile directly. By combining neutron reflectivity with higher angle x-ray and neutron diffraction, it is possible in principle to determine the absolute amount of hydrogen soluble in a given metal layer and whether the hydrogen occupies only interstitial sites in the host lattice or resides partly in voids.

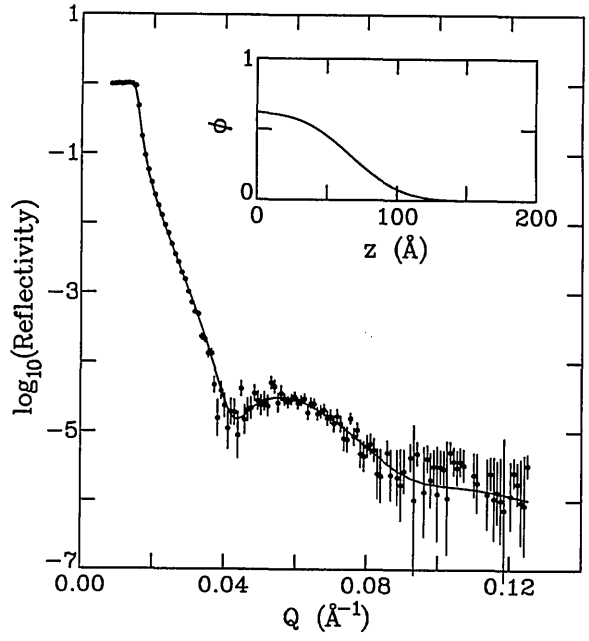

Fig. 9. Open circles show the reflectivity from a silicon surface immersed in pure deuterated cyclohexane (DCH); closed circles show reflectivity from same surface in solution of end-carboxylated polystyrene (PS-COOH) in DCH.

3.5 Epitaxial Superlattices

Advances in molecular beam epitaxy techniques have resulted in the growth of single crystal, magnetic rare earth and transition metal superlattices with well defined periodicities (see, for example, Ref. [19] and references therein). Multilayers such as these are ideal for studying the effects of finite size on the magnetic behavior as discussed earlier. However, in the case of the rare earths the indirect exchange coupling responsible for the magnetic ordering is mediated by the conduction

electrons so that the artificially imposed compositional modulation might in itself be expected to perturb the magnetic state of the superlattice. This is indeed found to occur in a number of superlattices composed of a magnetic rare earth alternating with the nonmagnetic metal yttrium.

Polarized neutron diffraction studies have shown that in Gd-Y superlattices, for certain Y layer thicknesses, the ferromagnetic Gd layers (bulk Gd is a simple ferromagnet) align antiparallel to one another in an antiphase domain structure [41]. The odd integer, SF satellites shown in Fig. 10 occur at positions corresponding to a doubled superlattice spacing and are characteristic of the antiparallel Gd layer alignment. An oscillatory dependence of the Gd layer moment configuration on the intervening Y layer thickness has been interpreted to be a consequence of the coherent propagation of magnetic correlations across the Y via the Ruderman-Kittel-Kasuya-Yosida (RKKY) interaction.

Neutron diffraction studies have also shown that long range magnetic order in the form of spirals and noncollinear structures develops in other rare earth superlattice systems including Dy-Y, Ho-Y,

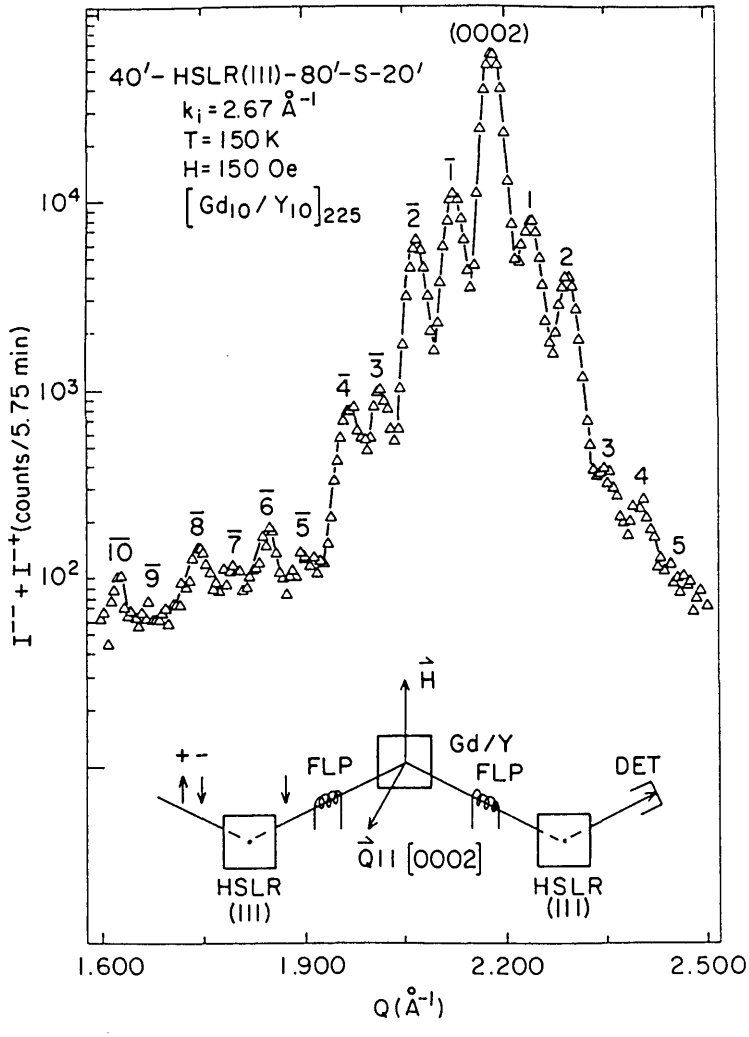

Fig. 10. Polarized neutron diffraction data for a Gd-Y superlattice in which the ferromagnetic Gd slabs or layers are antiferromagnetically coupled across the intervening nonmagnetic Y. The odd-integer superlattice satellite peaks occur at positions which correspond to a doubled chemical superlattice unit cell and are the result of spin-flip scattering only. The lower part of the figure is a schematic of the instrumental configuration where HSLR(111) denotes the reflecting planes of the Cu_2MnAl Heusler polarizing crystals (after Ref. [42]).

Er-Y, and Gd-Dy (for reviews of this work see Refs. [42] and [43]). In addition to the effects of the imposed composition modulation and finite layer thickness, the epitaxial strain due to lattice mismatch at the interface between two dissimilar elements can, through the magnetoelastic energy, play an important role in determining what magnetic order develops [44].

4. Grazing Angle Diffraction

There are a number of methods for studying surface and interfacial phenomena with neutrons and X rays that involve diffraction from ordered crystalline structures (as opposed to the purely refractive effects used in specular reflectivity experiments). Zeilinger and Beatty [45] carried out measurements using asymmetric scattering geometries that yield information about the surface structures of perfect crystals. Al Usta, Dosch, and Peisl [46] have investigated the possibility of measuring the diffuse tails of bulk Bragg peaks ("truncation-rod scattering") with neutrons but find also that low intensity limits the applicability of the method to nearly perfect crystals. The most promising application of crystalline diffraction to surface neutron studies is the grazing-angle diffraction geometry because it possesses the potential to observe imperfect crystals.

Grazing-angle diffraction is an application of specular reflectivity that allows one to study the in-plane structure of near-surface and interfacial layers. The theory of this diffraction geometry, the distorted-wave approximation, has been worked out in a number of papers [47–49]. For grazing-angle diffraction, one uses the amplitude of the evanescent transmitted wave of the specular reflection process as the illuminating field for Bragg diffraction. In Fig. 11, the incident beam k_0 strikes the sample surface near the total reflectivity threshold and excites a specularly reflected beam k_{0s}, with the sample being oriented such that a reciprocal lattice vector G satisfies the Bragg condition with the components of wavevectors k_0 and k_{0G} in the plane of the sample surface: $Q_{\|} = (k_{0G} - k_0)_{\|} = G$. The out-of-plane components control the depth of illumination,

$$Q_{1z} = \sqrt{k_{0z}^2 - 4\pi N_1 b_1} + \sqrt{k_{0Gz}^2 - 4\pi N_1 b_1}\,, \qquad (6)$$

where N_1 is the atomic density of the scatterers in the crystal and b_1 their average scattering length. The characteristic depth probed is simply given by the inverse of the imaginary part of Q_{1z} and typically is of order 5–10 nm at the lowest angles of incidence and exit. Taking into account these refractive corrections, one proceeds with the calculation of the diffracted intensity according to conventional kinematical theory (50). The resulting grazing-angle diffracted intensity is

$$I(Q) = I_0 |t_1(k_{0z})|^2 |t_1(k_{0Gz})|^2 |F_1(Q_{\|})|^2 \left| \frac{e^{iQ_{1z}M_1 a_1} - 1}{e^{iQ_{1z}a_1} - 1} \right|^2 \delta(Q_{\|} - G), \qquad (7)$$

where the exponential terms result from the summation over crystal planes normal to the surface, with M_1 being the number of atomic layers and a_1 their lattice spacing. The delta function expresses the Bragg condition with the in-plane wavevector components and F_1 is the structure factor for the reflection. The terms t are simply the Fresnel transmitted amplitudes of the incident and diffracted waves,

$$t_1(k) = \frac{2k}{k + [k^2 - 4\pi N_1 b_1]^{1/2}}\,. \qquad (8)$$

Just as is the case for reflectivity, the above formulae can be derived for an arbitrary number of diffracting layers [51, 52].

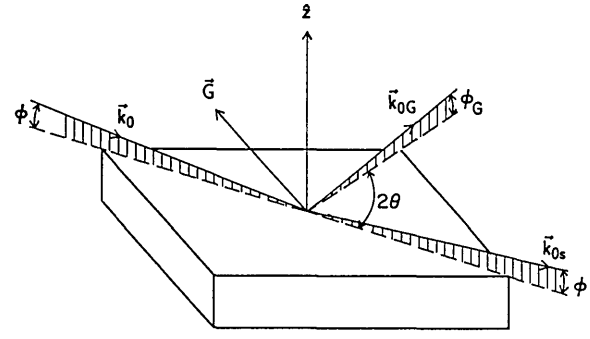

Fig. 11. Grazing-angle diffraction geometry. Simultaneously with the specular reflectivity process (k_{0s}), a sample is oriented such that the components of k_0 and k_{0G} in the surface plane satisfy the Bragg condition with reciprocal lattice vector G.

The primary obstacle to the development and application of grazing-angle neutron diffraction techniques is the relatively low flux of even the most powerful research nuclear reactors currently in existence (compared with x-ray synchrotron sources). Consequently, the first attempts to implement this diffraction scheme included various compromises intended to increase the neutron count rate at the detector [14, 53]. The easiest way to increase the count rate is to relax the collimations of the Bragg

angle θ and the diffracted-beam grazing angle ϕ_G (see Fig. 11). Relaxation of the Bragg angle collimation ($\delta\theta \sim 2°$) degrades the in-plane resolution of the instrument, but presents no problem for isolated Bragg peaks, while Eq. (6) shows that as long as one provides good collimation on the incident beam ($\delta\phi \sim 0.015°$), one can relax the diffracted-beam collimation ($\delta\phi_G \sim 1.5°$) and still retain some depth sensitivity. Figure 12 shows a plot of the first polarized-beam grazing-angle diffraction measurements [51], which were performed using this scheme. The intensity of the reflected-diffracted beam is plotted vs.the incident wavevector component normal to the surface ($k_{0z} = 2\pi \sin\phi/\lambda$) for the $(11\bar{2}0)$ in-plane Bragg reflection of an epitaxially grown film consisting of 15 nm Y(0001) on Gd(0001) measured at $T = 150$ K. As the incident angle increases, the neutrons penetrate through the magnetically dead Y layer into the ferromagnetically ordered Gd which, because of this ordering, has a different structure factor and penetration depth dependence for spin-up and spin-down neutrons. This sensitivity to magnetic order allows one in principle to determine the depth dependence of the magnetization in the sample.

There are a number of improvements which can and have been made to the instrumentation and in the data analysis that should in the near future establish the grazing-angle neutron technique as an important probe in interface science. Al Usta, Dosch, Lied, and Peisl [54] have demonstrated the importance of using a position-sensitive detector to record the data as a function of exit diffraction angle ϕ_G. This angular differentiation is necessary for two reasons: first, one would like to have more precise control of the scattering depth and, second, since the neutron absorption cross section is negligible for most materials there exist a number of spurious refracted beams coming off the sample which must be taken into account before one can see the true surface scattering (this effect is fortuitously not as large in the polarized-beam measurement described above, due to the large absorption cross section of Gd). They have demonstrated that one can obtain adequate intensity with this arrangement, albeit at the cost of greater effort expended in alignment. With the implementation of the appropriate hardware for these measurements comes the need for an adequate formalism to treat the data. The authors have described a formalism for a multi-layer treatment of grazing-angle diffraction [51,52] which is quite similar to the methods used in reflectivity analysis and plan to discuss both reflectivity and grazing-angle modeling in an upcoming paper. With these tools in place, grazing-angle diffraction is poised to become an important new probe of magnetic and hydrogen-bearing materials, substances to which neutrons are uniquely sensitive.

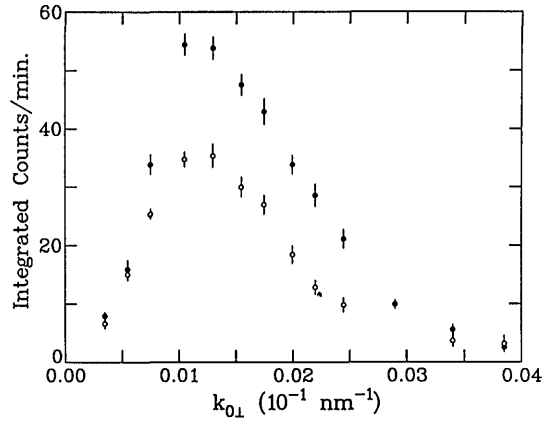

Fig. 12. Polarized neutron grazing-angle diffraction from $(11\bar{2}0)$ reflection of an Y(0001)/Gd(0001) film. The solid circles were measured with neutrons polarized parallel to the sample magnetization and the open circles anti-parallel. The points represent values for fixed incident k_{0z}, integrated over a broad range in k_{0G_z} and over a 2.2 circ width in diffraction angle θ.

5. Summary

The effectively simple description of the scattering of neutrons by condensed matter and the neutron's sensitivity to magnetic moments and light isotopes, particularly hydrogen and deuterium, often outweigh the neutron's relatively weak interaction strength and limited source intensities in probing surfaces and interfaces. There exist numerous examples, several of which have been given in this brief article, of how neutron reflectivity, superlattice diffraction, and grazing angle diffraction methods can be applied to study surface and interfacial phenomena in thin films of magnetic materials, polymers, superconductors, metal hydrides, and electrodes. As thin film and multilayer preparation techniques progress, neutron scattering studies should continue to play an important role in the characterization of the properties of these novel synthetic materials.

6. References

[1] E. Fermi and W. Zinn, Phys. Rev. **70**, 103 (1946).
[2] T. P. Russell, Mater. Sci. Rep. **5**, 171 (1990).
[3] G. P. Felcher, Phys. Rev. B **24**, 1995 (1981).
[4] J. Penfold and R. K. Thomas, J. Phys. C **2**, 1369 (1990).
[5] M. Born and E. Wolf, Principles of Optics, Oxford University Press (1980), pp. 51–70.
[6] V. F. Sears, Neutron Optics, Oxford University Press, (1989).

[7] A. G. Klein and S. A. Werner, Rep. Prog. Phys. **46**, 259 (1983).
[8] B. Farnoux, in Neutron Scattering for Materials Science, S. M. Shapiro, S. C. Moss, and J. D. Jorgensen eds., Mater. Res. Soc. Symp. Proc. 166, Pittsburgh, PA (1990), p. 95.
[9] G. P. Felcher, R. O. Hilleke, R. K. Crawford, J. Haumann, R. Kleb, and G. Ostrowski, Rev. Sci. Instrum. **58**, 609 (1987).
[10] W. G. Williams, Polarized Neutrons, Oxford University Press (1988).
[11] J. Penfold, R. C. Ward, and W. G. Williams, J. Phys. E **20**, 1411 (1987).
[12] Los Alamos Report LA 11301-C (1988).
[13] B. Farnoux, in Neutron Scattering in the Nineties, JAEA, Vienna (1985).
[14] J. F. Ankner, H. Zabel, D. A. Neumann, and C. F. Majkrzak, Phys. Rev. B **40**, 792 (1989).
[15] C. F. Majkrzak and G. P. Felcher, MRS Bull. **15** (11), pp. 65–72.
[16] G. P. Felcher, R. T. Kampwirth, K. E. Gray, and R. Felici, Phys. Rev. Lett. **52**, 1539 (1984).
[17] G. P. Felcher, K. E. Gray, R. T. Kampwirth, and M. B. Brodsky, Physica B **136**, 59 (1986).
[18] J. A. C. Bland, D. Pescia, and R. F. Willis, Phys. Rev. Lett. **58**, 1244 (1987).
[19] L. M. Falicov, D. T. Pierce, S. D. Bader, R. Gronsky, K. B. Hathaway, H. J. Hopster, D. N. Lambeth, S. S. P. Parkin, G. Prinz, M. Salamon, I. K. Schuller, and R. H. Victora, J. Mater. Res. **5**, 1299 (1990).
[20] Y. Endoh, J. Phys. (Paris) **43** (7), 159 (1982).
[21] Y. Endoh, N. Hosoito and T. Shinjo, J. Mag. Mag. Mater. **35**, 93 (1983).
[22] C. F. Majkrzak, J. D. Axe, and P. Böni, J. Appl. Phys. **57**, 3657 (1985).
[23] S. K. Sinha, E. B. Sirota, S. Garoff, and H. B. Stanley, Phys. Rev. B **38**, 2297 (1988).
[24] O. Schaerpf, Physica B **156, 157**, 639 (1989).
[25] F. Mezei, in Thin-Film Neutron Optical Devices, edited by C. F. Majkrzak, ed., SPIE Conf. Proc. 983, Bellingham, WA (1989), p. 10.
[26] J. B. Hayter, R. R. Highfield, B. J. Pulman, R. K. Thomas, A. I. McMullen and J. Penfold, J. Chem. Soc. Faraday Trans. **97**, 1437 (1981).
[27] J. Penfold, in Neutron Scattering for Materials Science, S. M. Shapiro, S. C. Moss, and J. D. Jorgensen, eds., Mater. Res. Soc. Symp. Proc. **166**, Pittsburgh, PA (1990), p. 151.
[28] R. J. Composto, R. S. Stein, G. P. Felcher, A. Mansour, and A. Karim, in Neutron Scattering for Materials Science, S. M. Shapiro, S. C. Moss, and J. D. Jorgensen, eds., Mater. Res. Soc. Symp. Proc. **166**, Pittsburgh, PA (1990), p. 485.
[29] M. Pomerantz, in Molecular Engineering of Ultrathin Polymeric Films, P. Stroeve and E. Frances, eds., Elsevier, Barking, England (1987).
[30] R. M. Nicklow, M. Pomerantz, and A. Q. Segmuller, Phys. Rev. B **23**, 1081 (1981).
[31] R. R. Highfield, R. K. Thomas, P. G. Cummins, D. P. Gregory, J. Mingins, J. B. Hayter, and O. Schaerpf, Thin Solid Films **99**, 165 (1983).
[32] P. Stroeve, J. F. Rabott, R. O. Hilleke, G. P. Felcher, and S. H. Chen, in Neutron Scattering for Materials Science, S. M. Shapiro, S. C. Moss, and J. D. Jorgensen, eds., Mater. Res. Soc. Symp. Proc. **166**, Pittsburgh, PA (1990), p. 103.
[33] H. Hasegawa and T. Hashimoto, Macromolecules **18**, 589 (1985).
[34] C. S. Henkee, E. L. Thomas, and L. J. Fetters, J. Mater. Sci. **23**, 1685 (1988).
[35] S. H. Anastasiadis, T. P. Russell, S. K. Satija, and C. F. Majkrzak, Phys. Rev. Lett. **62**, 1852 (1989).
[36] G. H. Fredrickson, Macromolecules **20**, 2535 (1987).
[37] S. H. Anastasiadis, T. P. Russell, S. K. Satija, and C. F. Majkrzak, J. Chem. Phys. **92**, 5677 (1990).
[38] T. A. Kitchens, T. Oversluizen, L. Passell, and R. I. Schermer, Phys. Rev. Lett. **32**, 791 (1974).
[39] S. K. Satija, J. F. Ankner, C. F. Majkrzak, T. Mansfield, R. Composto, and R. S. Stein (submitted for publication).
[40] C. F. Majkrzak, S. K. Satija, D. A. Neumann, J. J. Rush, D. Lashmore, C. Johnson, J. Bradshaw, L. Passell, and R. DiNardo, in Neutron Scattering for Materials Science, S. M. Shapiro, S. C. Moss, and J. D. Jorgensen, eds., Mater. Res. Soc. Symp. Proc. **166**, Pittsburgh, PA (1990), p. 127.
[41] C. F. Majkrzak, D. Gibbs, P. Boni, A. I. Goldman, J. Kwo, M. Hong, T. C. Hsieh, R. M. Fleming, D. B. McWhan, Y. Yafet, J. W. Cable, J. Bohr, H. Grimm, and C. L. Chien, J. Appl. Phys. **63**, 3447 (1988).
[42] C. F. Majkrzak, J. W. Cable, J. Kwo, M. Hong, D. B. McWhan, Y. Yafet, J. V. Waszczak, and C. Vettier, Phys. Rev. Lett. **56**, 2700 (1986).
[43] J. J. Rhyne, R. W. Erwin, J. Borchers, M. B. Salamon, R. Du, and C. P. Flynn, Physica B **159**, 111 (1989).
[44] R. W. Erwin, J. J. Rhyne, J. Borchers, M. B. Salamon, R. Du, and C. P. Flynn, in Neutron Scattering for Materials Science, S. M. Shapiro, S. C. Moss, and J. D. Jorgensen, eds., Mater. Res. Soc. Symp. Proc. **166**, Pittsburgh, PA (1990), p. 133.
[45] A. Zeilinger and T. J. Beatty, Phys. Rev. B **27**, 7239 (1983).
[46] K. Al Usta, H. Dosch, and J. Peisl, Z. Phys. B **79**, 409 (1990).
[47] G. H. Vineyard, Phys. Rev. B **26**, 4146 (1982).
[48] H. Dosch, B. W. Batterman, and D. C. Wack, Phys. Rev. Lett. **56**, 1144 (1986).
[49] H. Dosch, Phys. Rev. B **35**, 2137 (1987).
[50] B. E. Warren, X-ray Diffraction, Dover, New York, (1990).
[51] J. F. Ankner, C. F. Majkrzak, D. A. Neumann, A. Matheny, and C. P. Flynn, Physica B **173**, 89 (1991).
[52] J. F. Ankner, in Proceedings of the Second International Conference on Surface X-ray and Neutron Scattering, Springer-Verlag, New York (1992), in press.
[53] J. F. Ankner, H. Zabel, D. A. Neumann, C. F. Majkrzak, J. A. Dura, and C. P. Flynn, J. Phys. (Paris) **50** (7), 189–95 (1990).
[54] K. Al Usta, H. Dosch, A. Lied, and J. Peisl, Physica B **173**, 65 (1991).

About the authors: J. F. Ankner, C. F. Majkrzak, and S. K. Satija are research physicists in the Reactor Radiation Division of the NIST Materials Science and Engineering Laboratory. The National Institute of Standards and Technology is an agency of the Technology Administration, U.S. Department of Commerce.

Volume 98, Number 1, January–February 1993
Journal of Research of the National Institute of Standards and Technology

[J. Res. Natl. Inst. Stand. Technol. 98, 59 (1993)]

The Triple Axis and SPINS Spectrometers

Volume 98 Number 1 January–February 1993

S. F. Trevino

ARDEC Picatinny Arsenal,
NJ 07806

and

National Institute of Standards
and Technology,
Gaithersburg, MD 20899

In this paper are described the triple axis and spin polarized inelastic neutron scattering (SPINS) spectrometers which are installed at the NIST Cold Neutron Research Facility (CNRF). The general principle of operation of these two instruments is described in sufficient detail to allow the reader to make an informed decision as to their usefulness for his needs. However, it is the intention of the staff at the CNRF to provide the expert resources for their efficient use in any given situation. Thus, this work is not intended as a user manual but rather as a guide into the range of applicability of the two instruments.

Key words: condensed matter spectroscopy; dispersion curves; hydrogen vibrations and translational diffusion; inelastic neutron scattering; magnetic excitations; neutron spectrometer; physical chemistry spectroscopy; polarized neutrons; rotational diffusion; SPINS spectrometer; solid state tunneling; triple axis spectrometer.

Accepted: July 10, 1992

1. Introduction

The triple axis spectrometer is the most widely used instrument in the study of materials with neutron scattering. No steady state source of neutrons (nuclear reactors) intended for use as a research tool with neutron scattering can be said to be complete without at least one such instrument installed. The concept and initial construction of this type of instrument is due to B. N. Brockhouse [1] who in the early 1950s installed the first model on the reactor located at Chalk River, Canada. This instrument was used to determine in detail for the first time the phonon properties of many different types of simple materials. Its control was primitive compared to that available today with the technology of robotics. Many improvements and expanded capabilities have been incorporated since the first prototype, producing a versatile instrument which has been used in the study of a wide variety of materials. The instrument was intended for the study of elementary excitations in condensed matter. Changes in the energy and momentum of the neutrons upon scattering by the sample are measured in a straight forward manner. These changes are due to the interaction of the neutron with the excitations which are supported by the sample under investigation and constitute a direct measure of the character of the excitations.

The CNRF instruments provide moderate resolution (0.01–1.0 meV) with sufficient intensity for use in a wide range of problems. They are ideally suited for the study of phonon dispersion curves in single crystals, tunneling modes of energies greater than ≈ 0.025 meV, quasielastic scattering studies of rotational and nonlocal diffusion in the time regime of picoseconds, vibrations of surfaces or molecules adsorbed on surfaces and

phonon density of states for that large class of materials which contain hydrogen. Specific mention of the applicability of neutron scattering to the study of hydrogeneous materials should be emphasized here. The hydrogen nucleus has the largest cross section (scattering interaction) for neutron scattering and is predominantly incoherent. Hydrogen vibrations have been detected in samples containing as little as 0.01 mol total hydrogen in the sample. Because the instrument is energy sensitive, it can also be used to measure purely elastic scattering whether it be due to coherent (nuclear or magnetic) or incoherent events. Information on the time-averaged structure of the atomic and molecular constituents of the sample is therefore accessible. Finally, the ability of producing and analyzing polarized neutrons allows more detailed measurement of the magnetic properties of the sample. These magnetic properties can be static, i.e., a structural description of the magnetic moments, or dynamic such as magnons.

The range of energies (0.025-14 meV) of excitations accessible to these instruments is substantially larger (although with poorer resolution) than available with the spin-echo and backscatter spectrometers. Independent control of the momentum (Q) and energy transfer (E) is routine if required as opposed to the time of flight spectrometer in which Q and E are related by the instrumental configuration.

The theory of operation, including considerations such as the factors which determine the resolution, various neutron filters available, and other innovations which enhance the usefulness of the instrument will be described in the next section. That section will include a description of the two instruments installed on neutron guides at the CNRF. The last section presents results of several measurements with a triple axis spectrometer.

2. Fundamentals of the Technique

2.1 The Triple Axis Spectrometer

In Fig. 1 is exhibited a schematic drawing of a triple axis spectrometer. The derivation of the name "Triple Axis Spectrometer" becomes clear from an inspection of this figure. There are three vertical axes about which parts of the machine rotate. The first, labeled monochromator, allows a narrow band of neutron wavelengths to be chosen from the much broader spectrum which is provided by the neutron source. The spectrum of this band is centered at a wavelength λ defined by Bragg's law for the diffraction of radiation by a crystal which is:

$$n\lambda = 2d\sin(\theta) \qquad (1)$$

where d is the lattice spacing of the monochromator crystal, 2θ is the angle through which the neutrons are scattered, and n is a positive integer ($n=1$ is the first order, $n=2$ the second, etc.). This angle is defined by the two collimators located on either side of the monochromator crystal which, along with the mosaic angular spread of the monochromator crystal, determine the width (in wavelength) of the spectrum of neutrons exiting from the second collimator and illuminating the sample. The second axis of rotation passes through the sample and allows for the investigation of the neutron scattering properties of the sample as a function of the scattering angle ϑ. The third axis passes through the analyzer crystal. The function of this latter part of the instrument is to determine the center and width of the band of neutron wavelengths to which the detector will respond. The principle by which this is accomplished is completely analogous to that used in the case of the monochromator. The band width will be determined here by the angular divergence of the last two collimators and the characteristics of the analyzer.

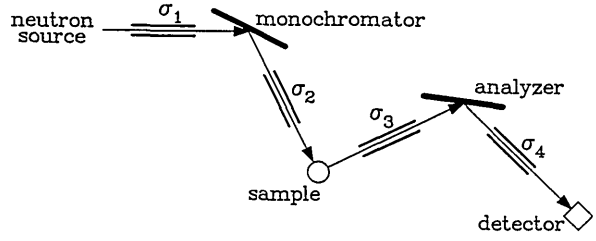

Fig. 1. A schematic diagram of the triple axis spectrometer.

The magnitude of the wave vector $\boldsymbol{k}$ of the neutron (or of any radiation which is characterized by a wavelength λ) is defined as

$$k = 2\pi/\lambda\,, \qquad (2)$$

with the direction of the vector $\boldsymbol{k}$ being that in which the neutron travels. In terms of k the energy of the neutron is

$$E = \hbar^2 k^2/2m\,. \qquad (3)$$

It can be seen that the triple axis spectrometer is capable of defining k_0 (and therefore E_0) of the neutrons incident on the sample, k (and E) of the neutrons scattered by the sample, the wave vector transfer Q

$$Q = k_0 - k \tag{4}$$

whose magnitude is, from the law of cosines

$$Q^2 = k_0^2 + k^2 - 2k_0 k \cos\vartheta\,, \tag{5}$$

and the energy transfer $\hbar\omega$

$$\hbar\omega = E_0 - E\,. \tag{6}$$

The great power of this spectrometer is that it allows choosing arbitrarily these two quantities, Q and $\hbar\omega$ (subject to kinematic constraints), in terms of which the most detailed properties of the scattering law of the sample depend. In turn, the properties of the sample which are reflected in the scattering law will be revealed through its determination [2]. The scattering law of the sample could be dependent on its orientation relative to the wave vector transfer Q. This is certainly true in the case in which the sample consists of a single crystal. Other examples include one dimensional orientation of polymers and two dimensional order produced by epitaxial growth. The instrument is capable of independently producing any desired relative orientation of sample and Q.

2.2 Resolution

The resolution of the instrument will determine its utility for a given measurement. A general rule with this instrument, as with most, is that resolution is purchased at the expense of intensity. This should be kept in mind when configuring the instrument for a given measurement. The parameters which govern the resolution are the angular divergence of the four collimators (σ^1, σ^2, σ^3, σ^4, see Fig. 1), the mosaic divergence η_m and η_a of the monochromator and analyzer crystals, and the Bragg angles θ_m and θ_a of the monochromator and analyzer, respectively. The mosaic divergence of a crystal is usually not available for change since it is a physical characteristic of that crystal. A change of this parameter would require a change of the crystal. Most crystals when first grown have a mosaic which is much too perfect ($\approx$1 min) to be useful as monochromators. The integrated reflectivity is a function of the mosaic of the crystal, being smaller for smaller mosaic. In general, monochromators are used with mosaic divergence of 15-30 min of arc. Techniques for treating virgin crystals to produce such a mosaic have been successfully applied to many different (but not all) crystals including Cu, Si, Zn, and Ge. The value of the divergence of a collimator is determined by the spacing d between the vertical blades and the length l of the blades (to a very good approximation $\sigma = d/l$ rad). It is standard practice to have available several collimators ($\approx$4) varying in values of the divergence from 5–80 min of arc for each of the four positions. The scattering angles from the monochromator and analyzer are continuously variable. The value of each is dictated by the lattice spacing of the crystal and the neutron energy required from it [see Eqs. (1-3)]. The relationship of the resolution to these parameters has been well investigated and the results confirmed experimentally [3]. Computer codes which allow the calculation of both the energy and momentum resolution as functions of all the relevant parameters are available for the efficient planning of any given measurement. Typical values of the energy resolution are a few percent of the energy transfer.

A straightforward differentiation of Eq. (1) leads to the expression

$$\Delta\lambda/\lambda = \cot\theta\,\Delta\theta\,, \tag{7}$$

which relates the effect on the wavelength band width of the scattering angle from both monochromator and detector. A simple method to obtain better resolution would seem to be to increase the monochromator and analyzer scattering angle to as large a value as possible. From Eq. (1), it is seen that this process would produce neutrons of long wavelength (low energy). In order to use this effect productively, there must exist in the spectrum of neutrons incident on the monochromator a sufficient number of low energy (cold) neutrons. Thus the present effort. In Fig. 2 is presented the result of a calculation of the resolution of a triple axis spectrometer as a function of the monochromator scattering angle for the conditions given in the caption. The effect is dramatic.

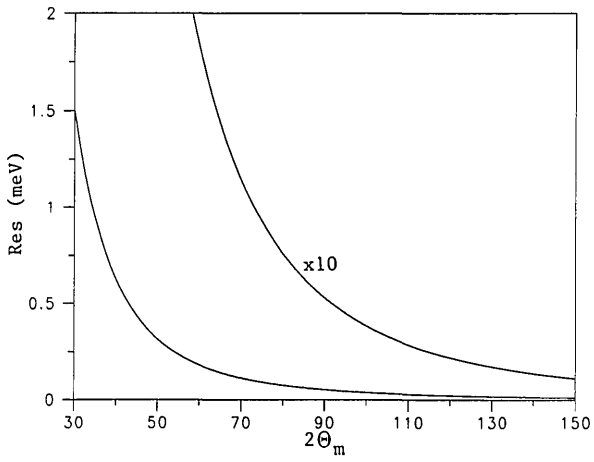

Fig. 2. The calculated resolution of a triple axis spectrometer as a function of the monochromator scattering angle $2\theta_m$. The collimation widths are 40, 20, 20, and 20 min of arc for the collimators before and after the monochromator and before and after the analyzer, respectively. The monochromator and analyzer crystals are both PG (002). The resolution is for elastic scattering ($E = E_0$).

2.3 Filters

Recall from Eq. (1) that a crystal with a given lattice spacing reflects neutrons of several wavelengths, viz. the several orders. The higher order neutrons being of shorter wavelength, viz. $\lambda/2$, $\lambda/3$, etc., are of higher energy, $4E$, $9E$, etc. It is usual to place a filter either in the beam incident on the sample or in that scattered from the sample in order to reduce the "contamination" of these orders so that a clean measurement is possible. Two of the most widely used filter materials for this application are beryllium (Be) and pyrolitic graphite (PG). The mechanisms by which filtering is produced will not be discussed here but only the resulting properties. Polycrystalline Be is an extremely effective low-pass filter. The cutoff energy is ≈ 5 meV. The rejection ratio for neutrons of energies larger than the cutoff to those smaller than the cutoff is a function of the length and temperature of the filter. As an example, for a filter of 100 mm length at a temperature of 78 K (liquid nitrogen), the rejection ratio is 3×10^5 with a transmission of the low energy neutrons of 0.95. More effective rejection can be obtained if required by a particular experiment at a small cost of transmitted low energy neutrons by using a longer cooled filter. There is, unfortunately, no universal filter for energies larger than 5 meV. The most useful filter in this energy region is PG for energies of 13.7, 14.8, 28., 30.5, and 40.3 meV. These are energies for which the transmission of the filter is reasonable (≈ 0.7 for a length of 50 mm) with a rejection of 10^4 for the second order energies. An alternate method of obtaining a "clean" beam is to use a monochromator whose properties are such that the second order reflection, for example, is forbidden. Several planes of Si, which has the diamond structure, satisfy this requirement. The technology for treating virgin Si crystals, which are usually too perfect (having very small mosaic ≈ 1 min of arc resulting in a very small reflectivity), is only now becoming available. It is always true that care must be exercised to ensure that a measured resonance is due to a property of the sample and not some instrumental effect due to a characteristic of the monochromator or analyzer.

2.4 Polarized Neutrons

Because the neutron possess a nuclear magnetic moment, the scattering from a sample which exhibits magnetism will be sensitive to the properties of the sample. The scattering is, of course, still also a function of the nuclear positions and motions. If the resonance produced by the magnetic properties of the sample is well separated from that produced by the nuclear scattering, no further effort is required. If however there is required unambiguous identification of the resonances as arising from a magnetic source, one can increase the sensitivity of the scattering to the magnetic properties, over those which depend only on the position and motions of the nuclei, by using a beam of space polarized neutrons. The scattering law can then be measured as a function of whether the spin of the neutrons is reversed or not in the scattering. Such a spin flip can only be produced by magnetic interactions. This type of measurement is therefore capable of distinguishing that part of the scattering which is due to the magnetic properties of the sample from that which is not. Technologies capable of producing polarized neutrons and effecting their spin flip are required for such measurements.

The production of polarized neutrons has been effected by using magnetic monochromator crystals whose scattering is strongly dependent on the relative orientation of the neutron magnetic moment and a magnetic field (the guide field) extending from the monochromator to the sample (or the sample to the analyzer). The three most widely used materials for this purpose are single crystals of CoFe, Fe^{57}, and Heusler alloy. The first two are

used for neutrons of wavelengths 0.05–0.15 nm (0.5–1.5 Å) and the last for wavelengths of 0.1–0.4 nm (1–4 Å). For neutrons of wavelengths longer than 0.4 nm (4 Å), such as those available at the cold neutron facility, devices constructed of bilayers, a few nanometers (tens of Å) thick, alternately of a magnetic and non-magnetic material, have been constructed with the desired properties (these devices are known as polarizing supermirrors). The efficiency of neutron polarization of these devices is on the order of 98 percent or better. The additional sensitivity to magnetic scattering obtained in this manner is of course not without cost in overall sensitivity in that at most 1/2 of the neutrons incident on the polarizing devices will be scattered by them and available for the measurement. The trade off in most cases is however well worth the effort. In addition to the ability to produce and be sensitive to a particular polarization of the neutron, one must be able to effect a rotation of the polarization of the neutron beam either before or after scattering from the sample. This can be accomplished by passing the neutrons through a magnetic field (the flipping field) directed perpendicular to the plane defined by the neutron wavevector $\boldsymbol{k}$ and the guide field. The mechanism operative in this device is that of matching the Larmor frequency of the neutron in the flipping field to the flight time of the neutron in this field to produce an arbitrary (usually 180°) rotation of the magnetic moment. A second coil is placed between the guide field and the flipping field whose function is to cancel the guide field from the region of space occupied by the flipping field. These devices are well understood and readily available.

2.5 Focusing

In the main, the measured quantities of interest are $\boldsymbol{k}_0$ and $\boldsymbol{k}$ and these depend on the vertical collimation only in second order. This allows the use of devices capable of vertical focusing to increase the signal without unduly affecting the resolution. One such device is a monochromator which consists of several crystals mounted so that each can be rotated about an axis parallel to the scattering surface of the crystals. The crystals are arranged so as to approximate a cylindrical scattering surface with the normal to the surface along the scattered neutron direction and with radius of curvature R. The relation between the neutron wavelength, the curvature radius, and the distance between neutron source-monochromator and monochromator-sample is obtained from simple optical considerations [4]. Such a device is capable of producing an increase in the neutron flux on the sample by a factor of ≈ 2.

2.6 Spin Polarized Inelastic Neutron Scattering (SPINS)

In 1962 G. M. Drabkin [5] proposed a scheme by which a beam of polarized neutrons could be produced whose energy is determined by the state of a magnetic field through which it passes rather than by the angle through which it is scattered from a crystal. This method is in principle capable of modifying one of the characteristics of a conventional triple-axis spectrometer. In the standard spectrometer, the energy resolution and the momentum (wave vector $\boldsymbol{Q}$) resolution, both of which are dictated by the characteristics of the crystals and collimations used, are strongly coupled. In many applications, this is not a particular disadvantage in that a well-defined resolution function is very useful. There would in many instances be an advantage in signal if the momentum resolution could be substantially relaxed with respect to the energy resolution by decoupling the two. Examples of such situations include dispersionless optic modes in crystals and single particle vibrations of hydrogen. The method which Drabkin has proposed produces just such a decoupling.

The device can be understood by consulting Fig. 3. An unpolarized beam with a relatively broad energy bandwidth is first polarized by a supermirror. The beam next traverses a current carrying foil which is folded in such a manner as to produce a small, spatially oscillating magnetic field $\boldsymbol{H}_\perp$ which is normal to both the propagation direction of the beam and to a larger uniform magnetic field H_0 that is superimposed over the full extent of the foil. These two fields are related according to $H_\perp = 2H_0/M$ where "M" is the number of spaces between adjacent current sheets through which the neutrons pass. The resultant magnetic field acts as a velocity or energy selective resonance flipper. Only those neutrons with velocities near $v_0 = a\gamma H_0/\pi$ (where γ is the gyromagnetic ratio of the neutron and "a" is the spacing between adjacent sheets of the foil) will undergo a spin-flip with a high probability. The probability distribution as a function of velocity is centered at velocity v_0 and has a width proportional to $1/M$. Those neutrons which are not flipped are subsequently not reflected by a second supermirror in which the magnetization direction is opposite to that of the first. Thus, the pair of

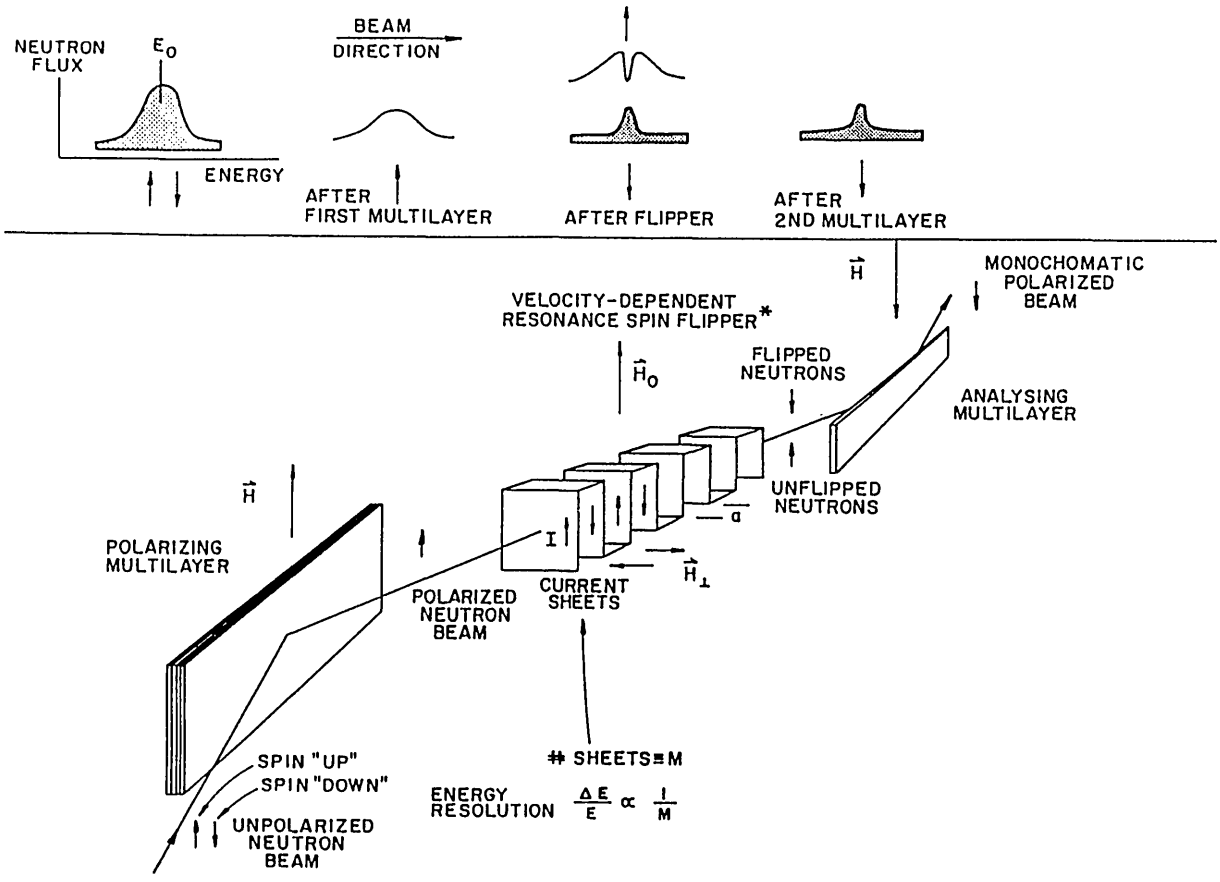

Fig. 3. A schematic diagram of the Drabkin neutron spin-flipper device.

supermirrors and the flipper act as an energy-dependent filter whose characteristics are controlled electrically. Table 1 compares the relative intensity to be expected for a given energy resolution obtained with a spin flip analyzer compared to the conventional triple axis configuration. Note that as the energy resolution is increased, the advantage of the spin flip method is substantial even if the polarized nature of the neutrons is not used.

Table 1. Relative intensity I and energy resolution ΔE obtained with a single spin flipper and 80 min collimation compared with that obtained with a conventional triple-axis spectrometer using PG(002) crystals and various collimations

Spin flipper			Triple-Axis							
			80^4		40^4		20^4		10^4	
M	Rel I	ΔE (meV)	Rel I	ΔE (meV)	Rel I	ΔE (meV)	Rel I	ΔE (meV)	Rel I	ΔE (meV)
50	1	0.320	1	0.308						
100	1/2	0.160			1/10	0.154				
200	1/4	0.080					1/33	0.077		
400	1/8	0.040							1/2000	0.039

A spectrometer can be constructed such that one has the option of using the spin flipper as monochromator or analyzer or both in place of the conventional crystal monochromator. In any case, a vertically bent PG crystal will be used to pre-monochromate the beam. Either a Be or PG filter is used to remove order contamination. The spectrometer will be capable of incident energies from 15 to 2 meV with resolutions from 1 meV to almost 10 μeV with adjustable resolution parameters. It should be noted that although the energy-dependent analyzer makes use of the neutron spin, the sample scattering need not be spin dependent.

3. Applications

3.1 Phonons

The triple-axis spectrometer was originally designed specifically for the purpose of measuring the phonons which a crystalline substance can sustain. A phonon is characterized by a quantized energy $\hbar\omega_s(q)$, momentum $\hbar q$ and eigenvector

$\epsilon_s(q)$. Here s numbers the various normal modes. This quasi-particle is used as a description of vibrations of the atoms and molecules which constitute the crystal. The energy $\hbar\omega_s$ is easily understood as the vibrational energy of the "normal mode," the momentum $\hbar q$, relates the phase of the motions of the atoms whose vibrations constitute the phonon. Two atoms whose spatial position is determined only by the distance $R(h,k,l)$ between the crystalline unit cell in which they exist vibrate temporally with a phase difference of $q_s \cdot R(h,k,l)$, (h,k,l) being the cell indices of one cell with respect to the other. The eigenvector ϵ_s, of dimension $3N$, N being the number of atoms in the unit cell of the crystal, describes in detail the spatial character of the vibrational mode. One consequence of such a description of the mechanical vibrations of the atoms and molecules is that ω_s and ϵ_s are functions of q. The detailed dependence is governed by the interactions between the atoms and molecules of the crystal. An important reason for the experimental determination of the values of $\omega_s(q)$ as functions of q (termed the dispersion curves) is the investigation of these interactions. A neutron when scattered by a substance can interact with these phonons if the requirements of energy and momentum are satisfied. That is, the neutron energy and momentum change must equal the phonon energy and momentum if a scattering resonance is to occur. This requires that

$$E - E_0 = \pm\hbar\omega_{si}(q), \tag{8}$$

and

$$\hbar Q = \hbar(q + \tau), \tag{9}$$

$\hbar\tau$ being a reciprocal lattice vector of the crystal [2]. The fact that these two quantities can be readily controlled by the triple axis spectrometer makes it the obvious choice as the instrument for their determination. Many substances have yielded to such measurements. The more complicated the unit cell (in number of atoms or molecules), the more complicated is the pattern of dispersion curves. An example of a rather complete measurement of the dispersion curves of a moderately complex crystal is presented in Fig. 4. The crystal is of deuterated anthracene [6] ($C_{14}D_{10}$). There are two molecules in the primitive cell giving rise to 12 external modes, 3 translational and 3 rotational for each molecule. There are symmetry-imposed requirements on the properties of the phonons.

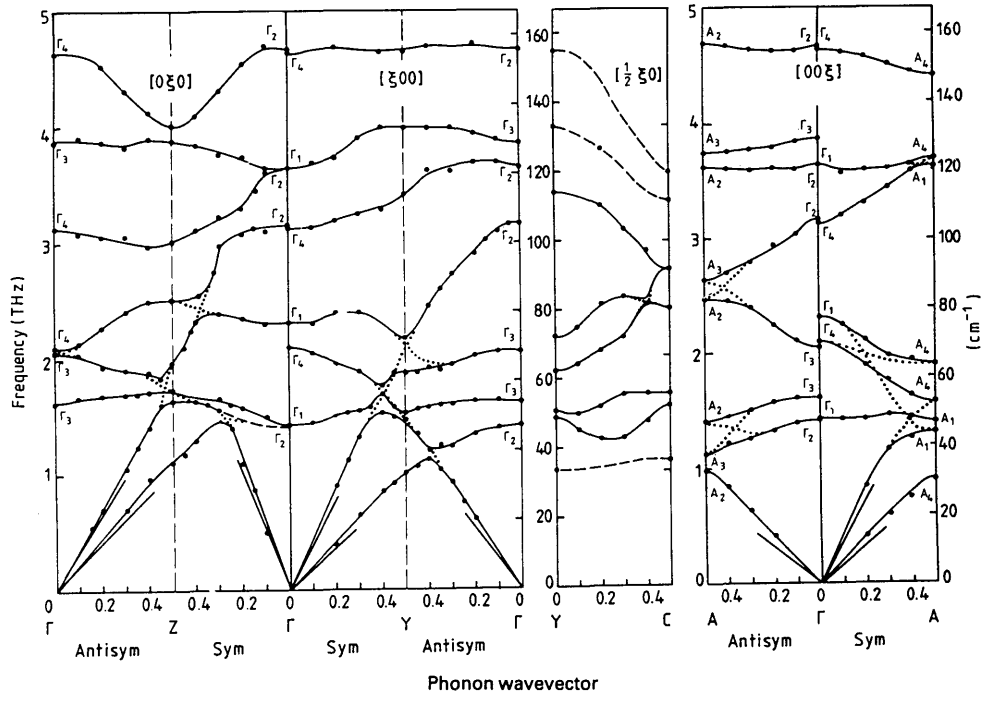

Fig. 4. Measured dispersion curves for the 12 external and the 4 lowest internal modes in anthracne at 12 K for the [ζ00], [0ζ0] and [00ζ] directions. The presentation is given in the extended zone scheme such that branches must not cross. Some dispersion curves in the [0.5, ζ, 0] direction are also shown [6].

For those values of q for which these restrictions are greatest, a consequence is that substantial degeneracy occurs in the values of the eigenfrequencies of several normal modes thus restricting the number of independent oscillators to be measured. This is reflected in the data presented in Fig. 4. Even with these restrictions, there still remain a substantial number of energy levels $\hbar\omega_s(q)$ for each q. In practice an approximate knowledge of the eigenvector $\epsilon_s(q)$ is extremely useful in planning a strategy for the measurement and increasing confidence in the correct identification of the observed resonances. Equation (51) of Berk's [2] article gives the cross-section dependence on these quantities. These eigenvectors are usually obtained from a first approximation of a model describing the crystalline interaction. There are also model independent group theoretical sum rules [7] for the structure factor which have proved very useful in the past [8].

3.2 Rotational Diffusion

Diffusional motion of atoms whether they be local, such as rotational, or non-local, translational, are detectable in neutron scattering through the quasielastic spectrum which they produce. The energy width of the broadened line centered at $\hbar\omega = 0$, and the Q dependence of its intensity with respect to the unbroadened elastic line contain information of both the structural and dynamical character of the motion [2]. The time scale of the motion available in neutron spectroscopy is inversely proportional to the energy resolution of the instrument, hence the motivation for CNRF triple axis spectrometer. The most extensively studied motions are those involving the hydrogen atoms both because it has the largest incoherent scattering cross section for neutrons and because its light mass produces motions of the appropriate time scale. Motions of other light atoms are not excluded and have indeed been investigated. The example used here is that of the rotational dynamics of the ammonia molecule in $Ni(NH_3)_6I_2$ [8]. In the fcc phase of this material, the ammonia molecules are coordinated with the Ni such that the threefold axis of the molecule is directed toward it. This allows for rotation of the molecule about this threefold axis. In Fig. 6 is presented the temperature dependence of the quasielastic scattering spectrum from this substance. Several features are to be noted. The existence of both an elastic and quasielastic component is characteristic of localized diffusional motion. As the temperature increases, the energy width of the quasielastic increases reflecting a shortening of the rotational diffusion time of the molecule. At 5 K, this time is so long that the quasielastic peak is too narrow to be resolved, and at 120 K the time is so short, leading to such a broad quasielastic peak as to be almost unobservable. The temperature and Q dependence of the spectrum yields quantitative results for the structural model, residence times and thermal activation energy of this motion.

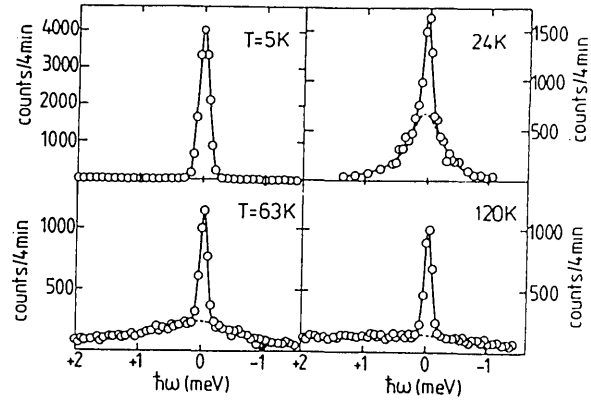

Fig. 5. Temperature dependence of the quasielastic scattering spectrum from $NI(NH_3)_6I_2$ (after Ref. [9]).

3.3 Incoherent Inelastic Scattering

These are studies of motions of hydrogen atoms in materials for reasons of cross section given above. Because of its light mass, hydrogen often finds itself in environments in which measurable quantum mechanical tunneling occurs. Many such situations occur for systems in which hydrogenous molecular groups (CH_3, NH_3, CH_4,...) produce quantum tunneling in the presence of a reorientational potential [10]. We use here an example of H trapped at an interstitial oxygen impurity site in $Nb(OH)_y$ [11]. The tunneling spectrum of H is presented in Fig. 6 as a function of concentration. At very low concentrations there is only one narrow peak suggesting a small number of equivalent sites between which the H tunnels. As the concentration increases, the tunneling peak broadens substantially. This has been interpreted as reflecting interaction between defects, even for these low concentrations, producing a distribution of local potentials. The properties of tunneling modes are extremely sensitive to the environment making their measurement a very useful probe.

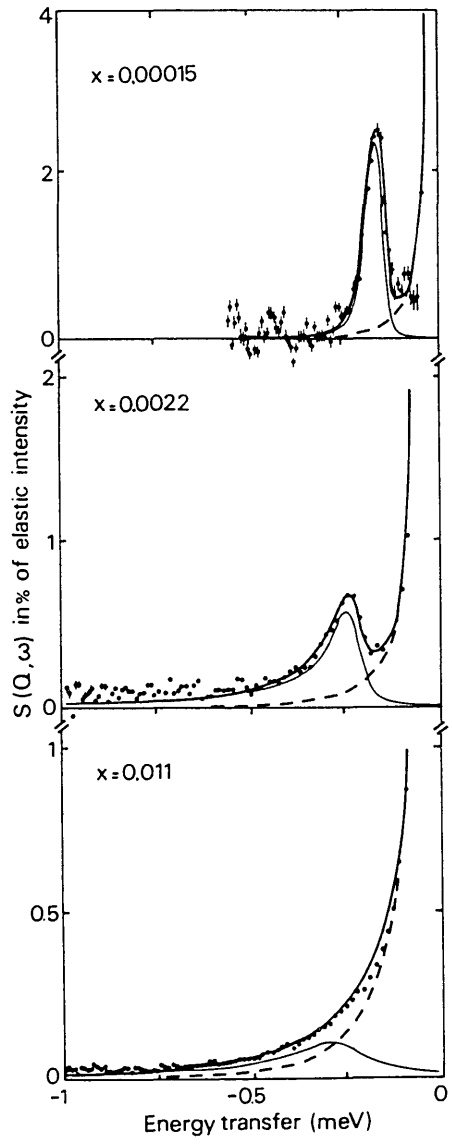

Fig. 6. Tunneling spectrum measured at three concentrations for $Nb(OH)_y$ at 1.5 K (after Ref. [11]).

3.4 Polarized Neutron Scattering

As mentioned above, the use of polarized neutron analysis of the scattering allows the separation of the scattering due to nuclear from that due to magnetic interactions. This powerful method of analysis and the fact that the neutron efficiently couples to the magnetic properties have resulted in very extensive applications of neutron scattering from magnetic materials. A most dramatic demonstration of the usefulness of this technique is represented by its use in detecting spin wave excitations of energy equal to longitudinal fluctuations of the atoms in amorphous ferromagnetic $Fe_{86}B_{14}$ [12]. This material belongs to the Invar system of ferromagnets. Magnets belonging to this system of materials are exceptional as ferromagnets in that they seem not to conform to all the results of linear spin wave theory. An explanation of this behavior requires that there exist non-magnetic fluctuations which couple with the magnetic excitations. These "hidden" fluctuations should exist with very similar energy and form as the magnetic ones. Figure 7 presents a measurement of this effect. The scattering labeled (+ +) is measured with the magnetic fields arranged so that non spin flip neutrons are detected and labeled (− +) so that only those neutrons whose polarization direction is reversed by the scattering are detected. The spin flip is caused by magnetic scattering whereas the non spin flip by non-magnetic scattering by the nuclei. It is clear from these data that there exists excitations of both kinds at very similar energies. The authors strongly suggest this as having demonstrated the source of the "Invar anomaly." It is also clear that only by polarized neutron scattering could such a result have been obtained.

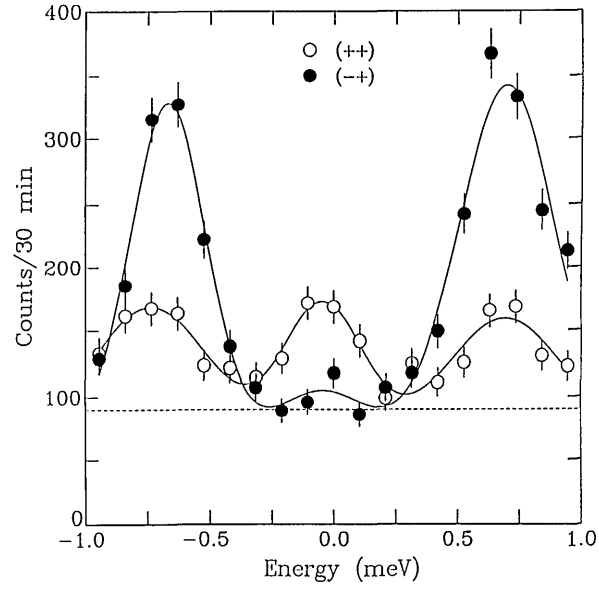

Fig. 7. Observed scattering for $q = 0.009\ nm^{-1}$ ($0.09\ Å^{-1}$) and 465 K in the vertical field configuration ($\hat{P}\,\hat{Q}$). The spin-flip scattering exhibits the usual spin wave excitationns, while the non-spin-flip scattering also reveals longitudinal excitations near the spin wave energies (after Ref. [12]).

4. The CNRF Instruments

Figure 8 presents a schematic diagram of the instruments under construction at NIST for installation on guide tubes at the CNRF. The configuration as presented includes the crystal analyzer which can easily be removed if the Drabkin flipper is used in its place. Both instruments will be constructed from the same design in order to minimize design and construction costs. Their function will depend on easily changed configurations. At present, the monochromator consists of vertically focused PG crystals followed by interchangeable (at the push of a button) PG filter, cooled Be filter, open hole or opaque beam stop. The collimator between monochromator and sample is carried within a movable shield attached to the monochromator to sample arm. This shield is constructed in the form of a "bicycle chain" which continuously covers the gap in the fixed monochromator shield. The position of the sample table is continuously variable along the line to the monochromator on accurate guides with a total travel of 670 mm. This feature allows the placement of polarizers, additional filters or energy-dependent filters before the sample. The analyzer table is also movable along the line to the sample allowing such devices to be placed between the sample and analyzer. The structure which carries the sample and analyzer tables is supported by two steel wheels rolling on flat steel plates. The analyzer and detector are supported on an arm which rotates about the sample and are counter balanced. This configuration was chosen to minimize the floor contact of the spectrometer. The analyzer crystal will consist either of a flat PG crystal or a horizontally focused

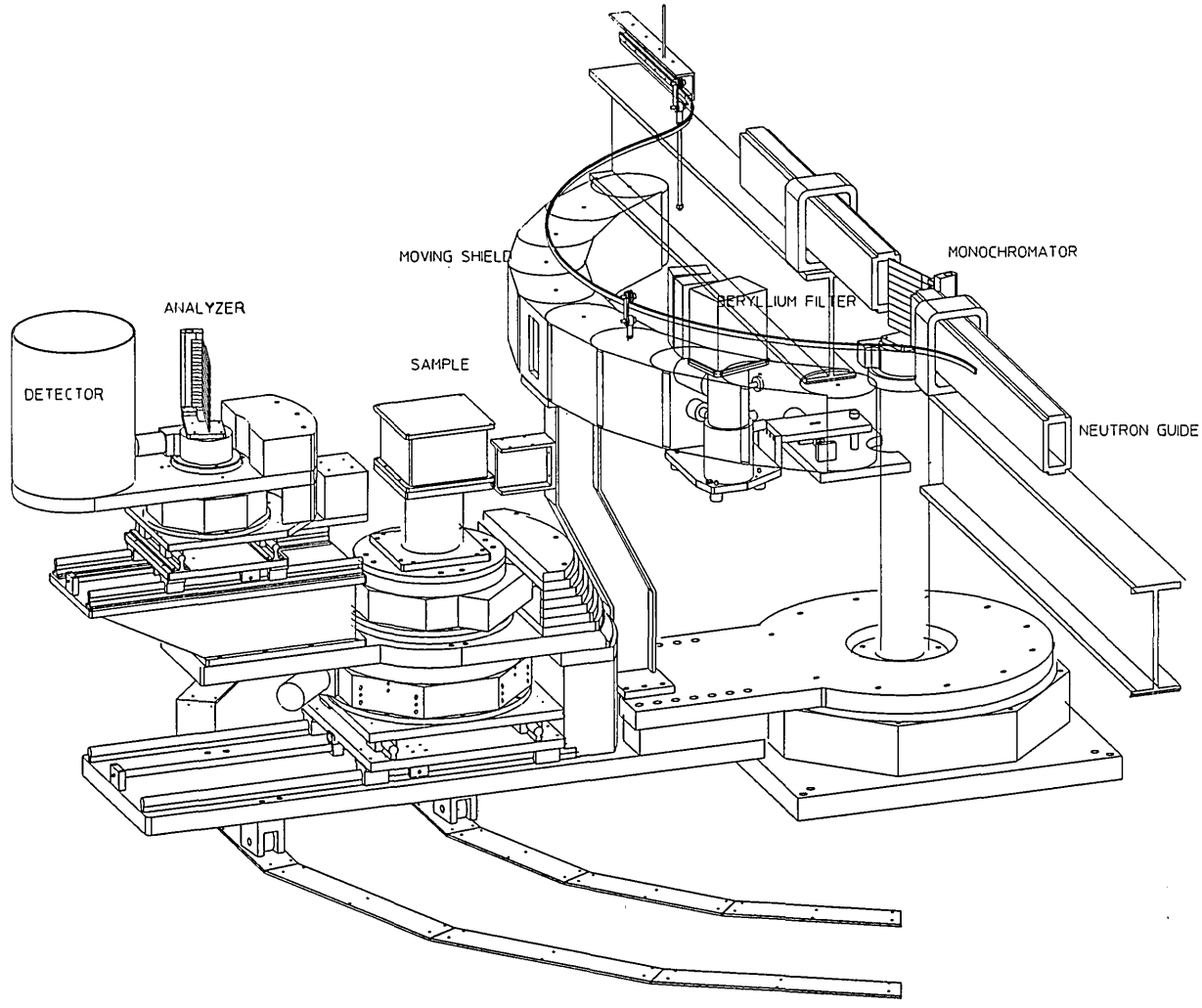

Fig. 8. A schematic diagram of the CNRF triple axis spectrometer. The instrument is shown without the SPINS device.

PG crystal—the two being easily interchanged. The horizontally focused analyzer will provide energy focusing in those situations where the collimators on either side of the analyzer can be removed because of relaxed Q resolution. All of the motions of the spectrometer are produced with stepping motors which are in turn controlled by a computer. A versatile code allows the scheduling of the function of the spectrometer and the storage of the data. The computer which performs the real time control function is connected by a network to a larger, faster multipurpose computer. Data transfers between the two computers are readily accomplished. A substantial package of software exists on the larger computer for use in the analysis and reduction of the raw data.

5. References

[1] B. N. Brockhouse and A. T. Stewart, Phy. Rev. **100**, 756 (1955).
[2] N. F. Berk, J. Res. Natl. Inst. Stand. Technol. **98**, 15 (1993)
[3] M. J. Cooper and R. Nathans, Acta. Cryst. **23**, 357 (1967).
[4] A. C. Nunes and G. Shirane, Nucl. Ins. Meth. **95**, 445 (1971).
[5] G. M. Drabkin, J. Explt. Theoret. Phys. (USSR) **42**, 1107 (1962).
[6] B. Dorner, E. L. Bokhenkov, S. L. Chaplot, J. Kalus, I. Natkaniec, G. S. Pawley, U. Schmelzer, and E. F. Sheka, J. Phys. C, Solid State Phys. **15**, 2363 (1982).
[7] R. S. Casella and S. F. Trevino, S. F., Phys. Rev. B **6**, 4533 (1972).
[8] S. F. Trevino, H. Prask, and R. S. Casella, Phys. Rev. B **10**, 739 (1972). S. F. Trevino, M. K. Farr, P. A. Giguere, and J. L. Arnau, J. Chem. Phys. **68**, 4260 (1978). H. Prask, C. S. Choi, N. L. Chesser, and G. J. Rosasco, J. Chem. Phys. **88**, 5106 (1988).
[9] J. Eckert and W. Press, J. Chem. Phys. **73**, 451 (1980).
[10] W. Press, Single-particle rotations in molecular crystals, Springer Tracts in Modern Physics, **92**, Berlin, Heidelberg, New York (1981); A. Heidemann, A. Magerl, M. Prager, D. Richter, and T. Springer, Quantum aspect of molecular materials, T. Springer Proceedings in Physics **17**, Berlin, Heidelberg, New York, London, Paris, Tokyo (1987).
[11] A. Magrel, H. Wig, K. Neumaier, A. J. Dianouy, and I. S. Anderson, Phys. Rev. Lett. **56**, 159 (1986).
[12] J. W. Lynn, N. Rosov, Q. Lin, and C.-H. Lee, Physica **B** (1992), in press.

About the author: *Samuel F. Trevino is a research physicist for the ARDEC Picatinny Arsenal, New Jersey and the Reactor Radiation Divison of the NIST Materials Science and Engineering Laboratory. The National Institute of Standards and Technology is an agency of the Technology Administration, U.S. Department of Commerce.*

Volume 98, Number 1, January-February 1993
Journal of Research of the National Institute of Standards and Technology

[J. Res. Natl. Inst. Stand. Technol. 98, 71 (1993)]

Neutron Time-of-Flight Spectroscopy

Volume 98 Number 1 January-February 1993

John R. D. Copley and Terrence J. Udovic

National Institute of Standards and Technology,
Gaithersburg, MD 20899

The time-of-flight technique is employed in two of the instruments at the NIST Cold Neutron Research Facility (CNRF). A pulsed monochromatic beam strikes the sample, and the energies of scattered neutrons are determined from their times-of-flight to an array of detectors. The time-of-flight method may be used in a variety of types of experiments such as studies of vibrational and magnetic excitations, tunneling spectroscopy, and quasielastic scattering studies of diffusional behavior; several examples of experiments are discussed. We also present brief descriptions of the CNRF time-of-flight instruments, including their *modi operandi* and some of their more pertinent parameters and performance characteristics.

Key words: diffusion; hydrogen in metals; inelastic scattering; neutron choppers; neutron inelastic scattering; quasielastic neutron scattering; time-of-flight spectroscopy; tunneling spectroscopy; vibrational spectroscopy.

Accepted: July 22, 1992

1. Introduction

The neutron time-of-flight technique has a long and distinguished history. In 1935, only 3 years after the discovery of the neutron, a pair of rotating disks was used to "prove by direct measurement that many of the slow neutrons [from a moderated Rn-Be source] are in the thermal velocity range" [1]. With the advent of the nuclear reactor (in 1942), more difficult measurements became possible, and a very different type of chopper was used by Enrico Fermi and his collaborators to determine the energy dependence of the absorption cross section of boron [2]. By 1960 relatively sophisticated phased chopper machines were being used to measure the scattering properties of materials such as water and polyethylene [3]. Much of the motivation for these experiments reflected the need for "scattering law" data for numerical calculations of the behavior of neutrons within nuclear reactors. Since the mid-sixties the emphasis has steadily shifted to the study of more and more complicated materials, and several kinds of time-of-flight instruments have been developed in order to make possible many different types of experiments [4,5].

The time-of-flight (TOF) method complements the triple-axis spectrometer (TAS) technique which is discussed elsewhere in this volume [6]. The TAS is ideally (but by no means only) suited to the study of excitations in oriented samples at specific points in (Q,ω) phase space. On the other hand TOF instruments may be used to explore rather large regions of phase space because many detectors simultaneously collect neutrons over a wide range of values of the scattered energy. The price paid for the much larger phase space volume is that the intensity on the sample is significantly reduced because the incident beam is pulsed. In another respect the TOF method complements the very high resolution backscattering and neutron spin echo techniques [7].

In Sec. 2 we present the basic principle of a time-of-flight measurement at a reactor-based spectrometer. We then illustrate several uses of the technique, describing a variety of applications in different fields of research. In Secs. 4 and 5 we describe the more important features of the TOF instruments at the CNRF, aspects of their

anticipated performance, the concept of accessible regions in (Q,ω) space, and resolution and intensity considerations. In Appendix A we present important relationships between the wave- and particle-like properties of a thermal neutron. In Appendix B we discuss the functions of the various choppers in a multiple disk chopper TOF spectrometer.

2. The Time-of-Flight Technique

A simple time-of-flight spectrometer is illustrated in Fig. 1. Neutrons from the reactor strike a crystal monochromator which is oriented at angle θ_M to the initial beam direction. Those with wavelength

$$\lambda_0 = 2d_M \sin\theta_M, \quad (1)$$

where d_M is the spacing between reflecting planes in the monochromator, are Bragg reflected in the direction of the sample. The monochromatic beam, characterized by its energy E_0 and wave vector k_0, is then pulsed by a chopper placed at a known distance L_{CS} from the sample. An array of detectors is arranged at a known fixed distance L_{SD} from the sample, and scattered neutrons arrive at the detectors at times determined by their scattered energies E. The time-of-flight of a neutron from the chopper to one of the detectors is simply

$$t_{CD} = t_{CS} + t_{SD} = \tau_0 L_{CS} + \tau L_{SD}. \quad (2)$$

Here t_{CS} and t_{SD} are the times-of-flight of the neutron from chopper to sample and from sample to detector, respectively, and τ_0 and τ are the reciprocal velocities of the neutron before and after scattering, respectively; relationships between λ, τ, k, and E are given in Appendix A. From Eq. (2) it is clear that τ, E, and the energy transfer

$$\hbar\omega = E_0 - E, \quad (3)$$

may be determined from t_{CD} if λ_0 is known. Given the angle between the incident and scattered neutron wave-vectors, i.e., the scattering angle ϕ, the wave-vector transfer

$$Q = k_0 - k \quad (4)$$

is readily calculated. The vast majority of samples studied by TOF spectroscopy have no preferred orientation, so that all that generally matters is the magnitude of Q. We shall ignore the vector character of Q in the remainder of this paper.

The basic quantity which is measured in a TOF experiment is a set of intensities $I(\phi_i,t_j)$ for n_D detectors located at scattering angles $\phi_i (i = 1,2..n_D)$, in n_t time channels centered at times $t_j (j = 1,2,..n_t)$ relative to an appropriate start time. Typically, measurements are made for the sample of interest and an "empty container," and in some cases additional runs must be performed in order to establish calibration constants for the data analysis. The conversion of the raw data to a differential scattering cross section is straightforward, but corrections for instrumental resolution, and for effects [4] such as multiple scattering, sometimes complicate the data reduction procedure. The final result is the scattering function $S(Q,\omega)$ (cf. Ref. [8]) within the region of (Q,ω) phase space accessed in the experiment. The latter concept is discussed in Sec. 5.1.

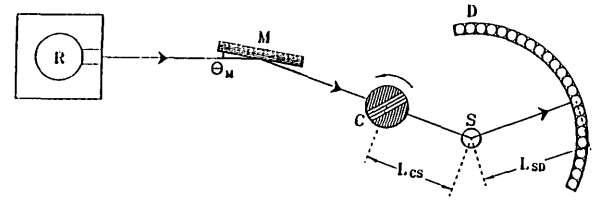

Fig. 1. Schematic plan view of a simple time-of-flight spectrometer. The letters R, M, C, S, and D denote the reactor, monochromator, chopper, sample and detectors, respectively. Important distances are indicated. In practice, the slots in the (Fermi) chopper are curved in order to optimize its transmission.

3. Applications

The utility of TOF spectroscopy stems from its ability to access a region of (Q,ω) phase space which is at the same time important to an understanding of the chemical physics of condensed phase materials, yet difficult to explore by other spectroscopic techniques. Applications of TOF spectroscopy are diverse and numerous (see, e.g., Refs. [4] and [9]). They include investigations of (i) vibrational and magnetic excitations by inelastic scattering, (ii) intermolecular potentials by tunneling spectroscopy, and (iii) translational and reorientational dynamics by quasielastic neutron scattering (QENS). The theoretical framework behind such investigations is summarized elsewhere in this issue [7,8]. The following examples elaborate on these areas and provide a flavor of the benefits of TOF spectroscopy.

3.1 Inelastic Scattering

The TOF technique is useful as a low energy vibrational spectroscopic probe of condensed phase materials, particularly those in which hydrogen motions are important, due to the relatively high incoherent scattering cross section of hydrogen [4,8,10]. The energy range accessible in TOF measurements makes the technique complementary to other vibrational probes which access both higher and lower energy ranges. For example, Fig. 2 shows TOF

spectra for trimethylsilyl [$(CH_3)_3Si$-, TMS] adsorbates bonded to silica via surface oxygens [11]. An energy loss feature at ~2.5 meV at 4 K shows up as both energy loss and energy gain features at 10 K due to increasing population of the 2.5 meV level above the ground state as the temperature is raised. This low energy feature is assigned to the torsional vibration of the entire trimethylsilyl group around the O-Si axis, since the relatively large moment of inertia of this group places the torsional mode in this energy range. The ~2.5 meV vibrational feature is outside the higher energy (15–250 meV) window of a triple-axis/Be-filter spectrometer [10] which was used to measure the other TMS normal-mode vibrational energies.

The complementarity of TOF measurements with other vibrational probes is further illustrated in an investigation of the vibrational dynamics of fractal silica aerogels by neutron TOF, backscattering, and spin-echo techniques in conjunction with Raman spectroscopy [12]. Real fractal solids consist of particles, of typical size a, distributed in fractal fashion up to a correlation length ξ, beyond which the materials are homogeneous. Three régimes can be identified for vibrations of characteristic length ℓ, namely phonons ($\ell > \xi_{ac}$), fractons

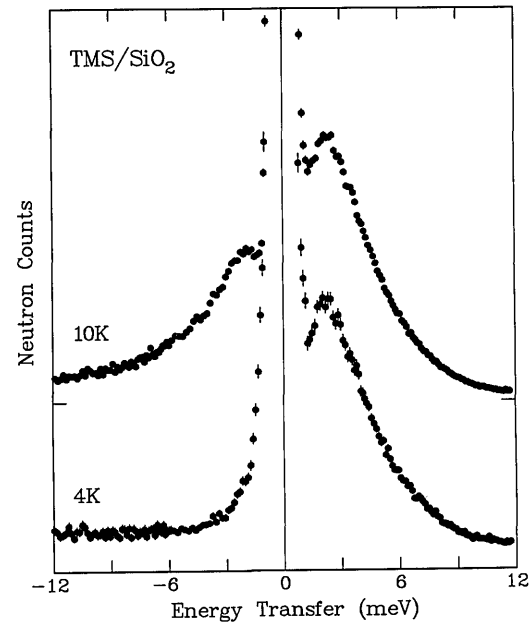

Fig. 2. Low-energy ($E_0 = 13.8$ meV) inelastic TOF spectra for trimethylsilyl adsorbates on silica at 4 and 10 K. Positive energy transfers correspond to neutron energy loss [11].

($\xi_{ac} > \ell > a$), and particle modes ($a > \ell$), where ξ_{ac} is the acoustical correlation length. Figure 3

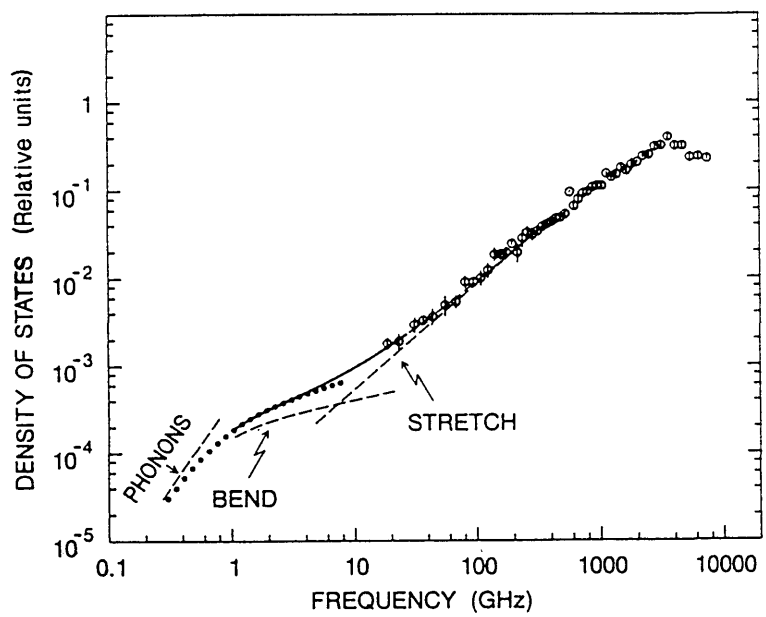

Fig. 3. The density of states (DOS) of a silica aerogel synthesized by hydrolysis of tetramethoxysilane without the addition of ammonia to the reaction water. The open circles are TOF measurements at 160 K using 8 Å incident neutrons. The dotted curve indicates the DOS that fits neutron spin-echo data. The solid line is a fit to neutron backscattering data and is extrapolated as shown by the dashes throughout the high-frequency fracton region. The dashed lines indicate the asymptotic phonon as well as the independent bend and stretch contributions [12].

displays the density of states of a silica aerogel synthesized by hydrolysis of tetramethoxysilane without the addition of ammonia to the reaction water. The TOF data, which cover the high frequency region, were derived from the purely incoherent contribution using the difference between signals measured on two samples: one with protons attached to the silica network and the other with the protons substituted by deuterons. The combination of different neutron scattering measurements illustrates the three régimes (note that 1 GHz=4.1357 μeV): phonons at low frequencies, (<0.7 GHz), fractons at medium frequencies (0.7–250 GHz), and particle modes at higher frequencies (>250 GHz). In addition, the data suggest two distinct elastic régimes in the fracton range as previously predicted [13], associated with bending at smaller scales and stretching at larger scales. Greatly different Debye-Waller factors were found in the two régimes, enabling them to be unambiguously distinguished in the neutron spectra.

Time-of-flight instruments, unlike crystal spectrometers [6], do not readily lend themselves to investigations at constant wave-vector transfer Q. On the other hand the broad Q range available at a given energy transfer, using a multidetector TOF spectrometer, is well-suited to the study of dispersionless phenomena such as crystal-field excitations [14]. This is exemplified in Fig. 4, which illustrates the crystal field transitions (at 3.52 and 6.65 meV at 10 K) of the rare earth ion Ho^{3+} in the cubic Heusler alloy $HoPd_2Sn$. The neutron energy loss intensity for each transition decreases with increasing temperature as expected due to the depopulation of the crystal-field ground state. At elevated temperatures, when the higher energy crystal-field levels become thermally populated (e.g., at $T=23$ and 40 K), an additional transition at -3.5 meV on the neutron energy gain side is also evident. At each temperature, no variation of the excitation energies was observed from detector to detector indicating that the transitions were indeed dispersionless. This permitted an improvement of the statistics by summing many detectors over a broad Q range.

Figure 5 illustrates the dispersionless, first excited level, magnetic-pair scattering energy ($E_{NN}=8.19\pm0.05$ meV) in both energy loss (at 17 K) and energy gain (at 100 K) for nearest-neighbor (NN) Co^{2+} ions in the II–VI diluted magnetic semiconductor $Zn_{0.94}Co_{0.06}S$ [15]. The interaction between the two NN Co^{2+} ions can be treated, to a first approximation, as a Heisenberg-type exchange for a pair of $S_i=S_j=3/2$ spins described by the Hamiltonian $H=2J_{NN}S_i\cdot S_j$. Thus E_{NN} becomes a direct measure of the antiferromagnetic exchange constant J_{NN} (where $E_{NN}=2J_{NN}$), yielding a value of $J_{NN}=4.10\pm0.03$ meV, in good agreement with the result obtained from magnetic susceptibility studies [16]. In this alloy, the magnetic Co^{2+} ions are randomly distributed over a face-centered-cubic cation sublattice. Hence, 48% of the ions are singlets, 24% are members of NN pairs, 4% belong to triads, and the remainder to larger clusters. Since the singlet Co^{2+} ions only possess excited state levels with much higher transition energies outside the

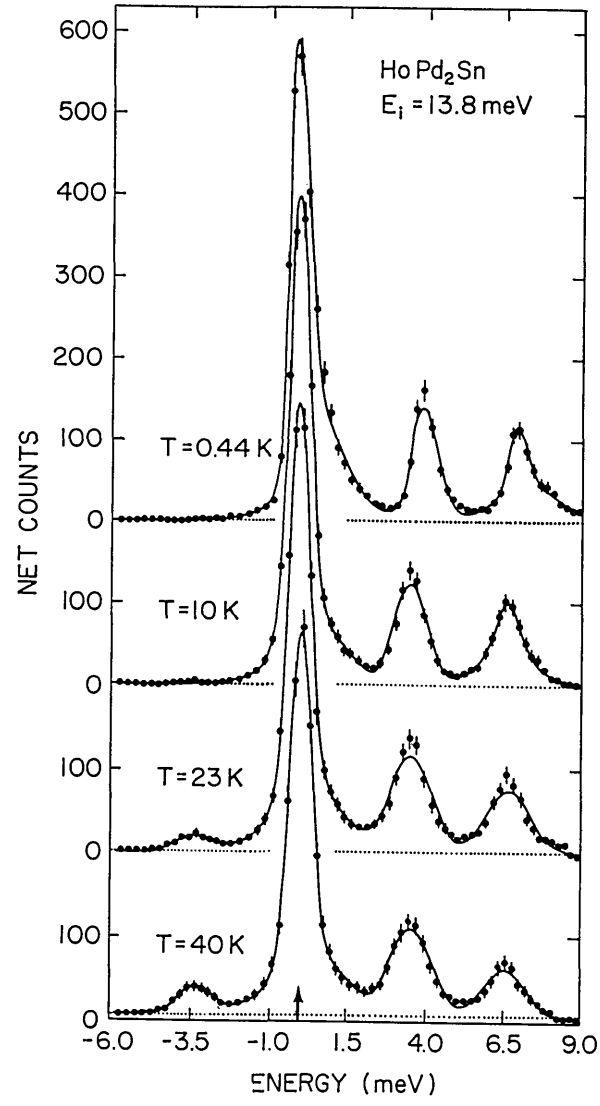

Fig. 4. Elastic and inelastic scattering observed in a powder sample of $HoPd_2Sn$ using the TOF technique with incident energy 13.8 meV. To improve the statistics, the spectra shown were obtained by summing over data acquired in 60 detectors spanning a Q range from 0.48 to 3.85 $Å^{-1}$. At 23 and 40 K, transitions from higher-energy to lower-energy levels are also evident in neutron-energy-gain ($E<0$) [14].

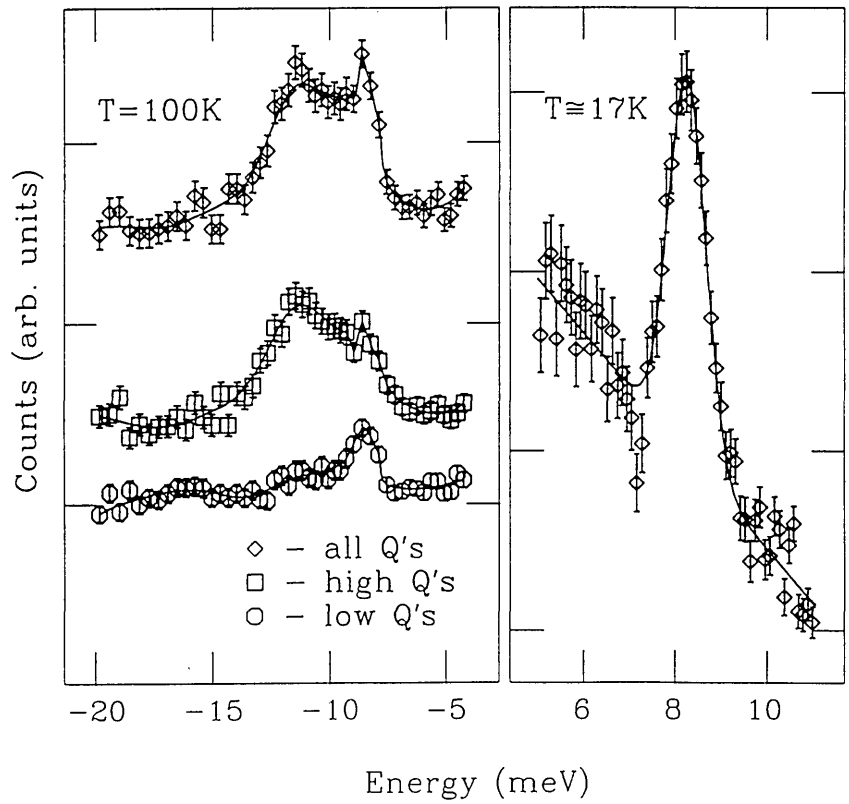

Fig. 5. Examples of inelastic TOF spectra ($E_0 = 13.8$ meV) for $Zn_{0.94}Co_{0.06}S$. The right panel shows the neutron energy-loss side of the spectrum obtained at 17 K with a fitted Gaussian line shape. The left panel shows energy-gain spectra at 100 K obtained by summing the counts from all detectors, from the "high-Q" detectors, and from the "low-Q" detectors. The curves are guides to the eye [15].

relevant measurement range, Co-Co pair scattering is the dominant magnetic inelastic effect in this alloy composition region. Yet its intensity is expected to be relatively weak because the pairs constitute only a small fraction of the total number of atoms in the sample. Since pair scattering energies are dispersionless, the ability to analyze the 100 K TOF spectra as a function of the Q range is useful in order to corroborate evidence that the broad feature at -11 meV is due to Q^2-dependent phonon scattering, rather than to magnetic-pair scattering.

3.2 Tunneling Spectroscopy

Time-of-flight spectroscopy is a useful probe of intermolecular potentials through characterization of tunneling transitions in condensed-phase materials. For example, Fig. 6 is a TOF spectrum illustrating the rotational tunnel splitting of the librational ground state of molecular hydrogen adsorbed in the cavities of partially cobalt-exchanged type A zeolite ($Co_{4.1}Na_{3.8}$-A) [17]. The assignment of the 3.8 meV neutron energy gain and energy loss features to the librational ground-state splitting (i.e., between the $J=0$ (para H_2) and $J=1$ (ortho H_2) rotational states) is unambiguous since the expected intensity ratio between energy gain and energy loss processes would be about 1:40 at 12 K for a translational excitation. This assignment, in conjunction with excitation data at higher energy transfer determined using a triple-axis spectrometer, is in good agreement with a model for the H_2 molecules in a twofold cosine potential with two degrees of rotational freedom. The model implies that the H_2 molecules are bound end-on to the cobalt cations, and perform 180° reorientations with a barrier of 55–68 meV.

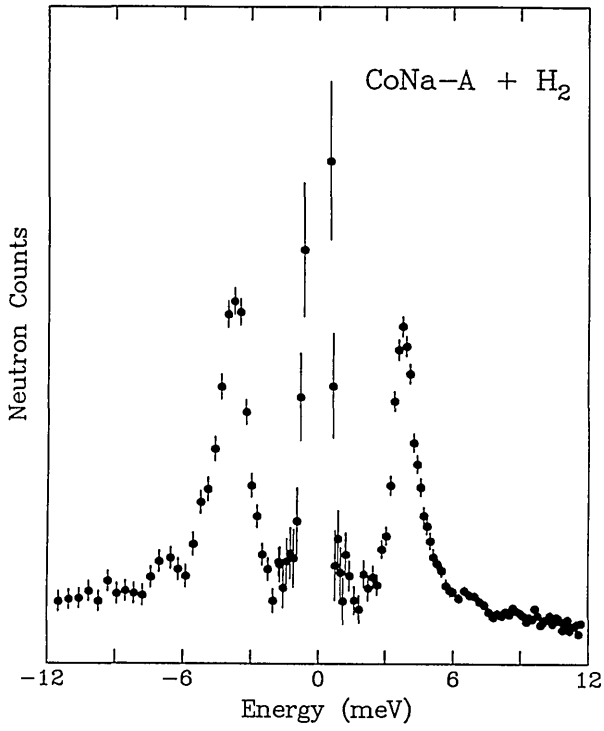

Fig. 6. TOF spectrum ($E_0 = 14.8$ meV) of 0.5 molecules of hydrogen per supercage adsorbed on $Co_{4.1}Na_{3.8}$-A zeolite at 12 K. The spectrum of the dehydrated zeolite has been subtracted from the data. Positive energy represents neutron energy loss [17].

The advent of high resolution TOF (and backscattering [7]) spectrometers, over the past two decades, has provided the ability to measure much lower energy tunneling transitions of condensed molecules and atoms. This is exemplified by the study of quantum states, transitions and interactions in the solid methanes [18]. Figure 7 illustrates TOF tunneling spectra for phase II CH_4 at low temperatures. In this cubic phase (space group *Fm3c*), two of the eight molecules in the unit cell are essentially freely rotating, while the other six molecules are in sites of ($\bar{4}2m$) symmetry, are orientationally ordered, and undergo tunneling. There are three corresponding tunneling states for a tetrahedral molecule or group experiencing a hindering potential in a tetrahedral site symmetry: a singlet ground state (A) and triply and doubly degenerate levels (T and E). Neutron induced transitions from A to E states are not observed since this requires a nuclear spin change from $I = 2$ to $I = 0$, which cannot be caused by a spin 1/2 particle. The 0.2 K spectrum shows an almost complete occupation of the A ground state species, which allows observation of A – T transitions only. As the temperature is raised

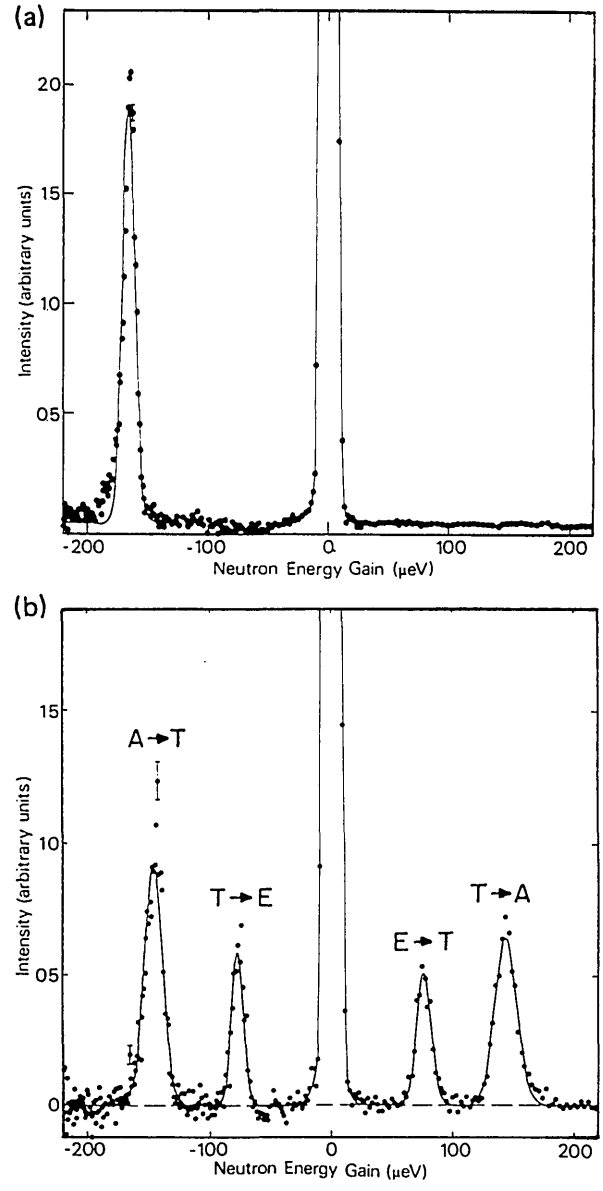

Fig. 7. TOF spectra for 13 Å neutrons scattered by CH_4 (phase II) at sample and spin temperatures of (a) <0.2 K and (b) 5 K. The A–T and E–T transitions are labelled in (b) [18].

both T and E states become populated, allowing observation of A–T and E–T transitions by both neutron energy loss and energy gain scattering. An excellent fit to the observed temperature-dependent widths and energies of these transitions (Fig. 8) assumes a continuously changing local potential, reflecting the changing mixture of spin states with temperature. The highest A–T energy (163.5 μeV) observed at the lowest temperatures (<0.5 K) reflects the potential for A level species surrounded by like species. Decreasing frequencies

(and concomitant increasing linewidths), observed with increasing temperature, indicate an increasing admixture of T and E species, increasing the average barrier height of the ordered CH_4 molecules in the unit cell.

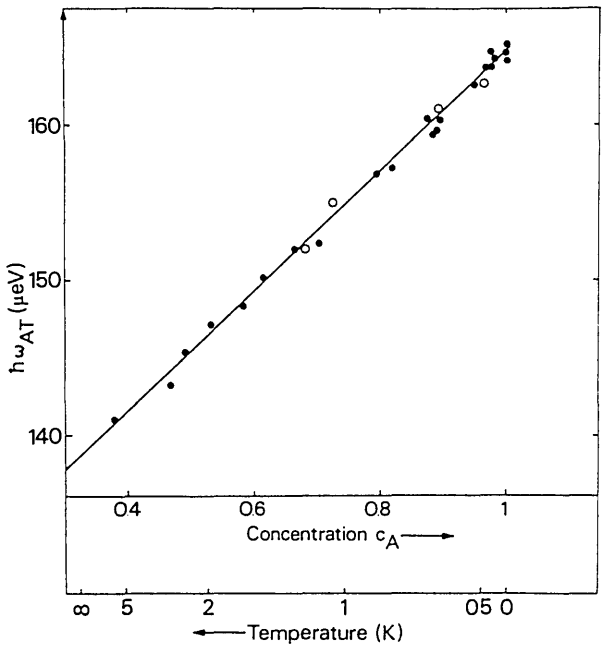

Fig. 8. Energy of the A–T transition peak as a function of the concentration of the A spin species. The straight line represents a fit with the model of inhomogeneous broadening due to a changing mixture of spin states [18].

3.3 Quasielastic Neutron Scattering (QENS)

Time-of-flight spectroscopy is well-suited to probing the translational and reorientational dynamics of atoms and molecules in condensed phase materials, particularly those with important hydrogen motions, via the Q- and T-dependence of the associated quasielastic neutron scattering. For instance, the localized motion of hydrogen in an α-$ScH_{0.16}$ solid solution has been investigated by QENS using TOF techniques [19]. The hydrogen atoms in this system are restricted to pairs of nearest-neighbor tetrahedral (t) sites between metal atoms along the c-axis. All scattering spectra were fit with an empirical two-component function comprising an elastic term described by the resolution function of the spectrometer and a resolution-broadened Lorentzian quasielastic term. Throughout the measurements, the invariance of the quasielastic linewidth Γ with Q corroborated the localized nature of the hopping motions. A hopping distance of 0.10 nm (1 Å) was abstracted from the data on the elastic incoherent structure factor (EISF) as a function of Q, consistent with the known nearest-neighbor t−t distance in this material. Figure 9 illustrates quasielastic scattering spectra for α-$ScH_{0.16}$ at several temperatures; Fig. 10 is a plot of Γ vs T. The data show hydrogen hopping rates between t sites exceeding $\sim 7\times10^{10}$ s^{-1} at all temperatures, indicating very rapid motion compared with the bulk diffusion rate in these systems. The apparent hopping rate increases to 10^{12} s^{-1} at 10 K after passing through a minimum at ~100 K. This remarkable upturn of Γ below the minimum is approximately proportional to T^{-1} in the range shown and is explained in terms of Kondo's [20] prediction of nonadiabatic effects of the coupling of the metal conduction electrons to the protons.

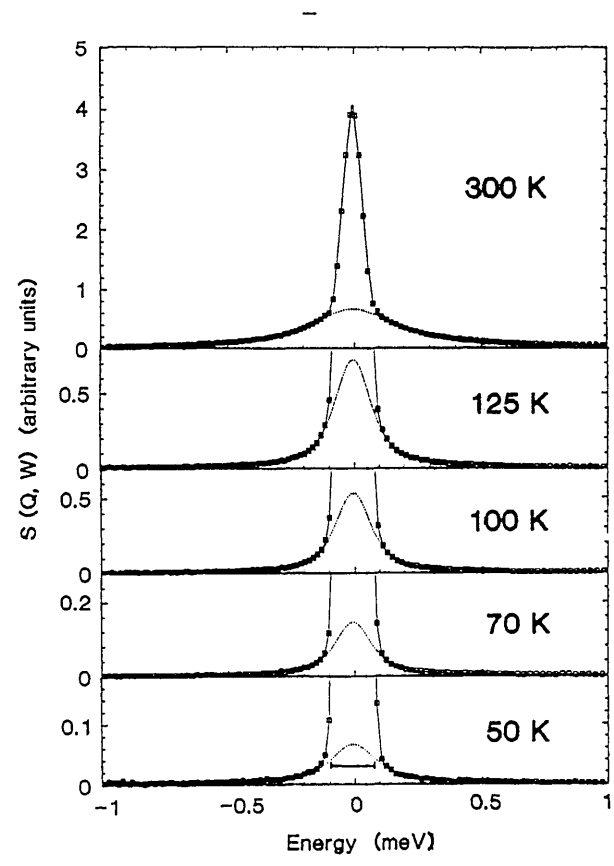

Fig. 9. Quasielastic neutron scattering spectra for α-$ScH_{0.16}$ at several temperatures at 70 μeV FWHM elastic energy resolution. The solid lines are the results of least-squares fits to the data; the dotted lines represent the Lorentzian quasielastic component. The increase in the quasielastic linewidth at low temperature is illustrated in the 50 K spectrum, where the length of the horizontal bar is equal to the width of the 70 K Lorentzian component [19].

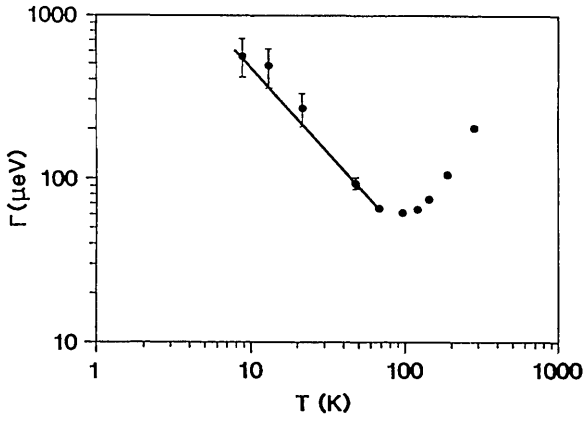

Fig. 10. Fitted Lorentzian linewidths (FWHM) for α-$ScH_{0.16}$. The solid line is the fit to the data below 100 K, assuming electronically induced linewidth broadening with decreasing temperature as described in the text [19].

A similar Kondo effect was observed below ~70 K in the quasielastic scattering from hydrogen trapped by oxygen impurities in Nb (i.e., $Nb(OH)_x$, $1.5\times10^{-4}\leq x\leq 1.1\times10^{-2}$) [21,22]. In particular, the hydrogens are trapped at weakly distorted tetrahedral sites in the body-centered-cubic lattice generated by the presence of oxygen defects at octahedral interstitial sites. Local diffusion of hydrogen occurs between at least two nearest-neighbor tetrahedral trap sites. Above ~70 K, the diffusion is dominated by the interaction with phonons. Below 5 K, well-defined tunneling eigenstates exist due to delocalization of the H between trap sites. Figure 11 shows a narrow inelastic tunneling transition at the lowest measured hydrogen concentration ($x=1.5\times10^{-4}$), which changes into a broad peak at higher concentrations due to increasingly strong interactions between defects.

The ability of TOF techniques to probe molecular dynamics on an atomic scale is further exemplified by QENS investigations of the translational and rotational motions of hydrocarbons adsorbed in zeolites, namely benzene in Na-mordenite [23] and methane in Na-ZSM-5 [24]. Figure 12 compares the EISF data for benzene in Na-mordenite with various theoretical models for the benzene reorientation. The data suggest that the benzene molecules, likely adsorbed by the Na cations via cation interaction with the π-electrons, undergo discrete uniaxial rotational jumps of $2\pi/6$. In contrast, methane in Na-ZSM-5 is found to undergo isotropic rotational diffusion. In this model, methane molecules are assumed to perform continuous small-angle rotations and therefore have no preferred orientation in space. This rotational motion is found to be much slower for methane in the zeolite than in physisorbed layers or in the solid phase.

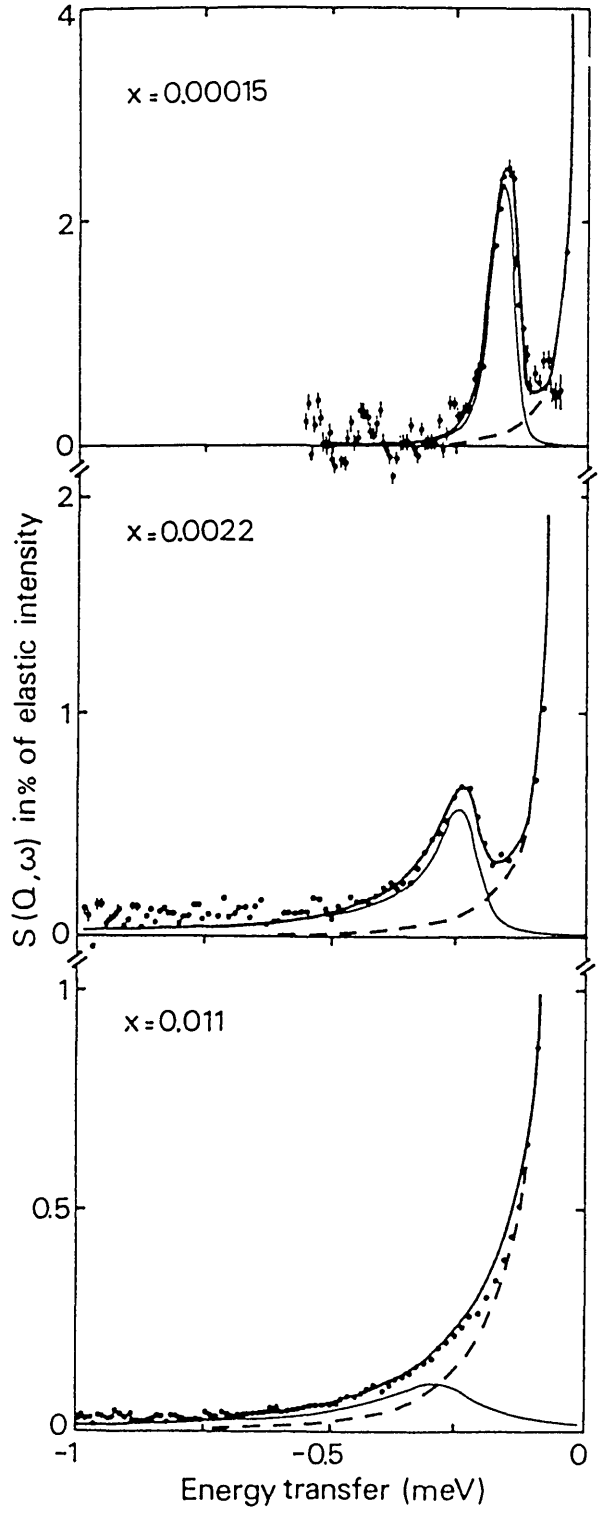

Fig. 11. TOF tunneling spectra measured (in neutron energy loss) at three OH concentrations in $Nb(OH)_x$ at 1.5 K. Elastic energy resolution was 55 μeV FWHM [21].

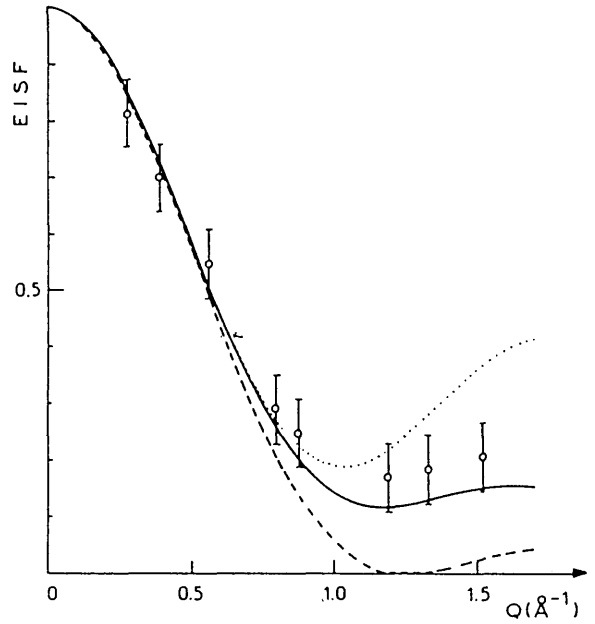

Fig. 12. Elastic incoherent structure factors (EISFs) of benzene adsorbed in Na-mordenite zeolite as a function of scattering vector Q. Open circles represent the experimental data. Theoretical EISFs are shown for rotational diffusion (broken line), for uniaxial rotations of $2\pi/6$ (full line) and for uniaxial rotations of $2\pi/3$ (dotted line) [23].

The translational diffusion behavior also differs between the two hydrocarbon/zeolite systems. For benzene in Na-mordenite, the benzene-Na bonding is weak, and the elastic peak width possesses a Q^2-dependence, implying that the benzene molecules follow Fick's law of continuous translational diffusion, characteristic of diffusion in a liquid, rather than a jump diffusion mechanism. The translational diffusion coefficient was found to be 6.7×10^{-7} cm^2 s^{-1} at 300 K. In contrast, for methane in Na-ZSM-5, the broadening of the elastic peak versus Q^2 deviates from a straight line (see Fig. 13) so that, on an atomic scale, the motion of methane is not simply Fickian. Instead the data agree with a model for translational diffusion which assumes jump diffusion with a Gaussian distribution of jump lengths. The physical interpretation of the model is that methane can perform small jumps inside the zeolite channels, but larger jump distances across the channel intersections are also possible. After a large number of jumps, Fickian diffusion can be observed. The diffusion coefficients for long range translational motion (2.7×10^{-5} and 5.5×10^{-5} cm^2 s^{-1}, at 200 and 250 K, respectively), determined from asymptotic values of the broadening at low Q, do not vary much with methane loading.

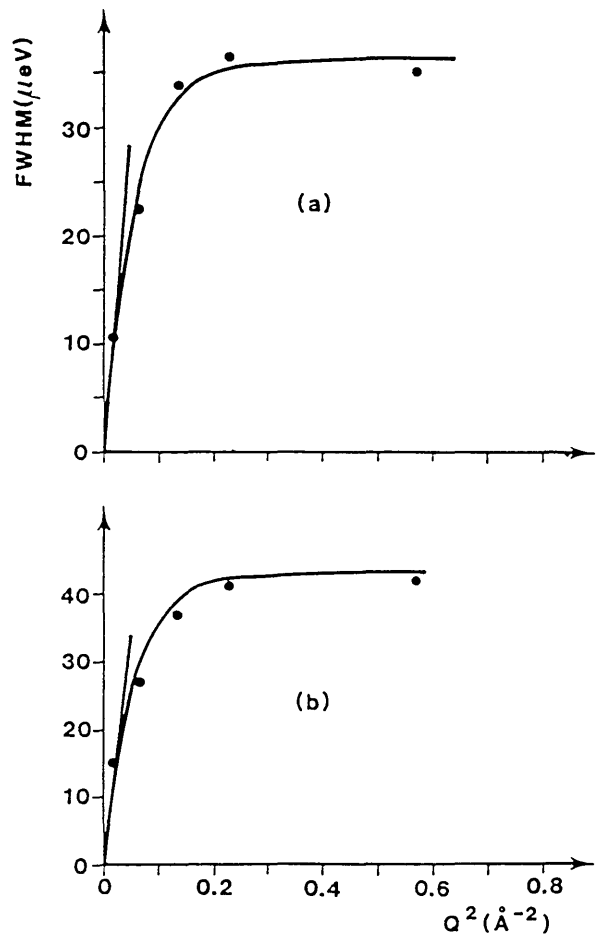

Fig. 13. Broadening of the elastic peak as a function of Q^2 for methane in ZSM-5 zeolite at 250 K: (a) 1.5 molecules and (b) 2.8 molecules per unit cell [24].

4. Time-of-Flight Instruments at the Cold Neutron Research Facility

Two time-of-flight spectrometers are planned for the guide hall of the CNRF. The first of these instruments, which is primarily designed for medium resolution applications, is a modified version of the type of instrument depicted in Fig. 1; it is located on guide NG-6, as shown in Fig. 7 of Ref. [25]. We call it the Fermi Chopper Spectrometer (FCS).

The second instrument, to be located at guide NG-4, uses a number of disk choppers to monochromate and pulse the incident beam; it is intended for high resolution measurements but may also be operated with relaxed resolution when required. We call it the Disk Chopper Spectrometer (DCS).

4.1. The Fermi Chopper Spectrometer

The Fermi Chopper Spectrometer is illustrated schematically in Fig. 14. Detailed specifications are listed in Table 1. The incident beam wavelength (0.23-0.61 nm) is determined using a double monochromator. The principle of this device is similar to that of a single monochromator, but an important advantage is that the selected neutron wavelength can be changed without having to rotate virtually the entire spectrometer about the monochromator axis. This significantly simplifies the design of the instrument. The monochromators are made of individually aligned pyrolytic graphite (PG(002)) crystals. A 60′ Soller collimator is located between the monochromators. The first monochromator is flat, whereas the second monochromator is vertically curved in order to focus intensity at the sample position. Vertical focussing is optimized when the vertical mosaic spread is minimized, yet this same mosaic spread in the horizontal direction would lead to an unnecessarily small wavelength spread and a consequent decreased intensity on the sample. Hence each monochromator is made of two layers of crystals, each layer possessing a 25′ mosaic, but staggered horizontally with 25′ angular offset. This effectively yields a more desirable anisotropic mosaic distribution, 25′ vertically and 50′ horizontally.

The neutron beam leaving the second monochromator is filtered, using pyrolytic graphite or liquid nitrogen-cooled beryllium (see Table 1), in order to remove Bragg (λ/n) (where n is an integer >1) order contamination (cf. [6]), as well as epithermal neutrons. It is then pulsed using a "Fermi chopper" [2]. This is a device which spins about a vertical axis (normal to the direction of the beam), and is fitted with a set of curved slots. The curvature of the slots and the speed of the chopper determine the optimum transmitted wavelength of the chopper [5]. Two slot packages are available, corresponding to optimum transmitted wavelengths of 0.4 and 0.15 nm, respectively, at close to the maximum chopper speed.

The sample chamber can accommodate a wide variety of cryostats and furnaces. An oscillating radial collimator between the sample and the detectors blocks most of the scattering from material components which surround the sample (e.g., heat shields of cryostats). The evacuated sample-to-detector flight path contains an array of ^{3}He neutron detectors covering a scattering range of 5°–140°. Signals from the detectors are amplified, shaped and filtered, and then fed to a time-of-flight encoder and CAMAC-based histogramming memory. The contents of this module are periodically transferred to a microVax computer for subsequent analysis.

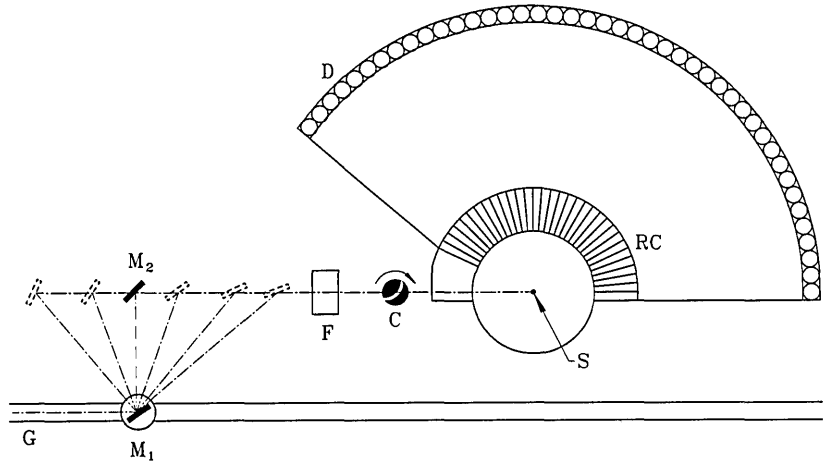

Fig. 14. Simplified plan view of the Fermi chopper spectrometer. The letters G, F, C, S, and D denote the guide, filter, chopper, sample and detectors respectively; M_1 and M_2 are the monochromator crystals and RC is the (oscillating) radial collimator. Incident wavelengths between 0.23 and 0.61 nm are obtained by modifying the Bragg diffraction angle of the double monochromator, as suggested by the dashed lines in the figure. The guide is continued to additional instruments downstream.

Table 1. Specifications and anticipated performance of the Fermi Chopper Spectrometer. Additional details are given in the text

Specifications		
Guide cross section (height × width):	150×60 mm	
Maximum beam size (height × width):	100×25 mm	
Monochromators (double):	Pyrolytic graphite PG(002)	
1st Monochromator (height × width/type):	160×100 mm/flat	
2nd Monochromator (height × width/type):	184×100 mm/vertically focussing	
Monochromator mosaic (vertical/horizontal):	25′/50′	
Intermonochromator collimation:	60′	
Beam filters (thickness/type/temperature):	152 mm/Be/77 K for $\lambda > 0.4$ nm	
	38 mm/PG/296 K for select $\lambda < 0.4$ nm	
Fermi chopper details (2 slit packages)	Package 1	Package 2
Blade curvature radius:	389.0 mm	581.4 mm
Rotor radius:	26.9 mm	25.6 mm
Slot width:	0.635 mm	0.635 mm
Beam window (height × width):	100×25 mm	100×25 mm
Optimum chopper speed:	80.93/λ(nm)Hz	54.15/λ(nm) Hz
Sample–detector distance:	2.286 m	
Scattering angle range:	$5° < \phi < 140°$	
Post-Sample radial collimation (oscillating)		
Blade separation:	3°	
Inner/Outer radius:	203/305 mm	
Detectors (cylindrical, ^{3}He-filled)		
Fill pressure:	0.4 MPa	
Diameter:	25 mm	
Angular separation:	1.273°	
Quantity/Active height:	12/229 mm for $5° < 2\theta < 20°$	
	88/457 mm for $20° < 2\theta < 140°$	
Incident wavelength range:	$0.23 < \lambda_0 < 0.61$ nm (÷2 for PG(004))	
Incident energy range:	$15.5 > E_0 > 2.2$ meV (×4 for PG(004))	
Elastic momentum transfer range:	$1 < Q < 50$ nm^{-1} (×2 for PG(004))	
Anticipated performance		
Fluence rate on sample:	$\sim 1\times10^8$ n/m^2/s at $\lambda = 0.24$ nm	
	$\sim 1.2\times10^8$ n/m^2/s at $\lambda = 0.40$ nm	
Elastic energy resolution:	40 μeV at $\lambda = 0.60$ nm	
	150 μeV at $\lambda = 0.40$ nm	
	600 μeV at $\lambda = 0.24$ nm	
Q Resolution:	$\Delta Q/Q < 3\%$	

4.2 Disk Chopper Spectrometer

The Disk Chopper Spectrometer is illustrated schematically in Fig. 15. The "front end" comprises a novel neutron filter followed by a total of seven disk choppers which collectively produce a clean, usable, pulsed, monochromatic neutron beam at the sample position. The purpose of each of these choppers is explained in Appendix B. The multichopper design (Fig. 16) allows the user a wide and continuous choice of wavelengths, basically constrained by the available spectrum of neutrons in the guide; a change in wavelength is achieved by changing the phase relationship between the disks.

In general the instrumental resolution may be varied (at fixed wavelength) either by changing the speed of the choppers or by changing the width of the beam. It is actually preferable, for reasons discussed in Appendix B, to change the width of the beam keeping the choppers spinning as fast as possible consistent with the desired resolution and with safe operating procedures. To optimize performance this implies changes both in the widths of the slots in the disks and in the width of the guide [26]. The practical realization of this option requires some explanation.

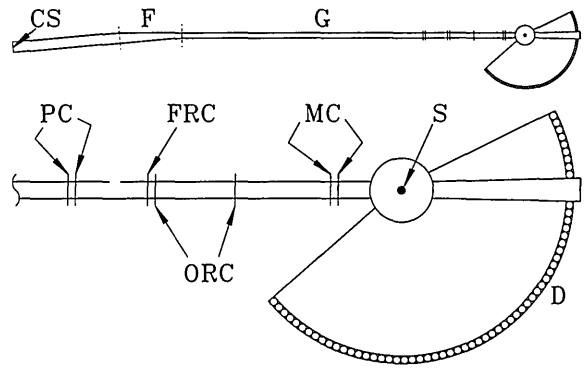

Fig. 15. Simplified plan view of the disk chopper spectrometer. The upper diagram shows the overall setup of the instrument including cold source (CS), filter (F), and guide (G). The lower diagram shows the choppers, the sample position (S), and the detectors (D); PC, ORC, FRC, and MC denote pulsing, order removal, frame removal, and monochromating choppers, respectively. The width of the guide, the separation between closely spaced choppers, and the angle between initial and final guide sections, have been exaggerated for clarity. The filter is a tapered section of guide, ~7 m long, that redirects slow neutrons (through 0.25°) whereas fast neutrons and γ rays are removed from the beam because they are not reflected. It is located within the wall between the reactor confinement building and the guide hall.

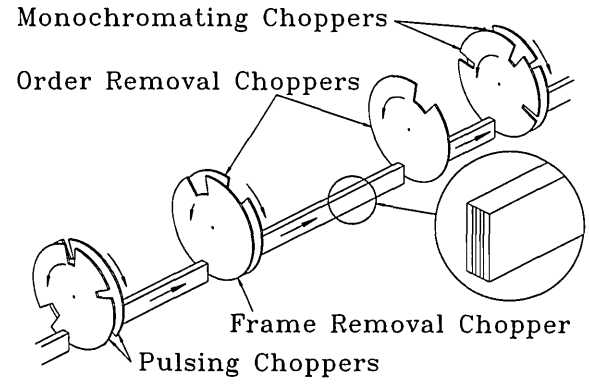

Fig. 16. Simplified view of the choppers and guide for the disk chopper spectrometer. Note that the pulsing and monochromating chopper disks each have three slots (of different sizes for different resolution modes of the instrument) and that the guide is divided into five channels.

Each of the disks in the pulsing and monochromating chopper pairs is equipped with three slots of different width, as shown in Fig. 16. The slots in each counter-rotating pair are located such that the width of the slot presented to the neutron beam can be changed by grossly changing the relative phasing of the disks. The choice of slot positions is complicated because of effects resulting from the small separation between the members of a counter-rotating pair [27,28].

The neutron guide for the DCS is of rectangular cross section, 150 mm high and 60 mm wide, until it reaches the filter; thereafter it is 30 mm wide. After the first chopper it is best described as a channeled guide, fitted with internal reflecting plates as shown in the insets to Figs. 15 and 16. Beam-defining masks limit the number of channels which transmit neutrons, effectively changing the width of the guide. The widths of the channels, and the widths of the slots in the disks, have been chosen to optimize intensity on the sample under each of three distinct resolution conditions at a given wavelength and chopper speed [26]. Typically the overall resolution width doubles, and the intensity on the sample increases by about an order of magnitude, in going from high to medium resolution or from medium to low resolution. The capability to change resolution at fixed wavelength and fixed chopper speed is only possible because we use counter-rotating choppers with multiple slots [29].

After the final chopper the layout of the instrument is not unlike that of the Fermi Chopper Spectrometer, described in the previous subsection. The sample chamber is comparable in size and will be evacuated. On the other hand, the flight path between sample and detector will be filled with an inert gas in order to reduce scattering, and the detectors will be mounted externally. An important difference is that the distance L_{SD} is significantly larger (4000 mm), in order to achieve the desired energy resolution. For the same reason, the detectors will be very thin (~10 mm) in the direction travelled by the neutrons, but relatively wide (~32 mm) in order to capture as many neutrons as possible. They will be rectangular ^{3}He tubes, typically 400 mm long, and there will be three detector banks spanning a wide range of scattering angles. The data acquisition system will be an expanded and somewhat more elaborate version of the system used in the FCS.

Certain specifications of the DCS are listed in Table 2; some of the numbers may be modified as the design progresses. Figures for the anticipated intensity on the sample are somewhat speculative, and the reader is cautioned not to take these intensities at face value. The Q resolution of the instrument will depend on how the detectors are grouped; the best achievable resolution can be estimated from the anticipated resolution in λ_0 (which depends on λ_0 itself, the speed of the choppers, and the resolution mode of the choppers), the divergence of the incident beam (which depends on λ_0), and the angle subtended by a single detector at the sample position.

Table 2. Specifications and anticipated performance of the disk chopper spectrometer. Sets of three quantities within braces refer to the three resolution modes of operation of the instrument, {low, medium, high}, respectively

Specifications	
Beam height at guide exit:	100 mm
Beam width at guide exit:	{30 mm, 15 mm, 5 mm}
Disk chopper details:	
Outside radius:	290 mm
Maximum operating speed:	333 Hz (20,000 rpm)
Maximum tip velocity:	607 m/s
Pulsing chopper slot widths:	{12°, 6.5°, 2.6°}
Monochromating chopper slot widths:	{8°, 3.5°, 1.35°}
Order removal chopper slot widths:	20°, 18°
Frame removal chopper slot width:	20°
Sample-Detector distance:	4 m
Anticipated maximum scattering angle:	140°
Detectors (rectangular cross-section, ^{3}He-filled)	
Fill pressure:	0.6 MPa
Width:	~32 mm
Thickness:	~10 mm
Active length:	400 mm
Arrangement:	3 banks
Approximate incident wavelength range:	$0.2 < \lambda_0 < 1.5$ nm
Approximate incident energy range:	$20 > E_0 > 0.36$ meV
Corresponding elastic Q range:	$0.5 < Q < 60$ nm^{-1}
Anticipated performance	
(assuming a chopper speed of 20,000 rpm)	
Fluence rate on sample ($\lambda_0 = 0.2$ nm):	{45, 10, 2} × 10^6 n/m^2/s
" " " ($\lambda_0 = 0.4$ nm):	{450, 100, 20} × 10^6 n/m^2/s
" " " ($\lambda_0 = 0.6$ nm):	{220, 50, 10} × 10^6 n/m^2/s
" " " ($\lambda_0 = 0.8$ nm):	{100, 20, 5} × 10^6 n/m^2/s
Elastic energy resolution ($\lambda_0 = 0.2$ nm):	{1300, 650, 270} μeV
" " " ($\lambda_0 = 0.4$ nm):	{160, 80, 35} μeV
" " " ($\lambda_0 = 0.6$ nm):	{50, 25, 12} μeV
" " " ($\lambda_0 = 0.8$ nm):	{21, 11, 6} μeV

5. Experimental Considerations

When planning a time-of-flight experiment the interplay of resolution and intensity requirements is an important concern. Generally speaking, instrumental resolution improves dramatically with increasing wavelength; for example the energy width of the elastic scattering approximately varies as the nth power of E_0, where n is about 3. On the other hand the intensity at the sample position tends to decrease as the incident wavelength is increased; for instruments on guide tubes the intensity varies as λ^{-3} at long wavelengths. It is therefore necessary to strike a compromise between the conflicting requirements of high intensity and good resolution.

A further disadvantage of long wavelengths is that an increase in wavelength also reduces the accessible region in (Q,ω) space. Generally speaking the best policy is to use the shortest wavelength consistent with the desired instrumental resolution, in order to be able to access as large a region of (Q,ω) space as possible.

5.1 Accessible Regions in (Q,ω) Space

In TOF experiments the accessible region depends on the choice of incident energy and on the placement of the detectors. The cosine rule, applied to the vectors $\boldsymbol{Q}$, $\boldsymbol{k}_0$ and $\boldsymbol{k}$ [(cf. Eq. (4)], yields the result

$$Q^2 = k_0^2 + k^2 - 2k_0 k\cos(\phi). \quad (5)$$

Converting wave-vectors to energies (see Appendix A), and using Eq. (3), Eq. (5) may be rewritten as follows:

$$\hbar^2 Q^2/2m = 2E_0 - \hbar\omega - 2\sqrt{E_0(E_0-\hbar\omega)}\cos(\phi). \quad (6)$$

In Fig. 17 we show accessible regions for two choices of the incident energy. Detectors are assumed to fill the angular range from 5° to 140°.

The accessible region gets smaller as E_0 is decreased. In particular the accessible range of Q for elastic scattering ($\hbar\omega = 0$) is reduced since in this case Eq. (6) simplifies to the well-known (Bragg) relationship

$$Q = 2k_0 \sin(\phi/2). \quad (7)$$

A decrease in E_0 also means a proportionate reduction in the maximum possible energy transfer in neutron energy loss. The improved resolution that results as E_0 is decreased, i.e., as λ_0 is increased, is a direct consequence of the contraction in accessible (Q,ω) space.

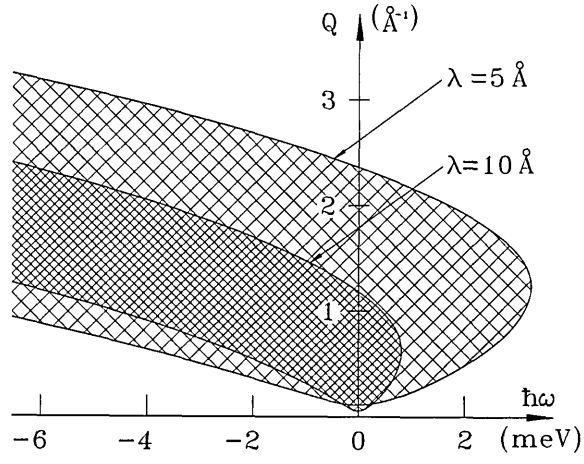

Fig. 17. Plots of the accessible region in (Q,ω) space for neutrons of wavelength 5 and 10 Å (energy 3.272 and 0.818 meV, respectively). The minimum and maximum scattering angles are 5° and 140°. There is no (theoretical) limit to the energy transfer in neutron energy gain.

5.2 Resolution and Intensity

An important contribution to the overall energy resolution of a TOF spectrometer arises from the spread in the time distribution of neutrons in the incident beam.

In the FCS there are two independent sources of incident beam time spread: the monochromator and the chopper. The chopper contribution is independent of distance but the wavelength spread from the monochromator translates into a time spread which increases with distance. The net result is that the width of the time distribution in the unscattered beam, at a point distant x from the chopper, may be written as follows:

$$\sigma^2(x) = \sigma_t^2 + x^2\sigma_\tau^2, \quad (8)$$

where σ_t measures the burst time of the chopper and σ_τ is the spread in the reciprocal velocity distribution of neutrons in the beam.

The time distribution for a two-chopper spectrometer may be similarly written [30]. In this case the time spread is an appropriate average of the burst times σ_1 and σ_2 for the two choppers:

$$\sigma_t^2 = \sigma_1^2\sigma_2^2/(\sigma_1^2 + \sigma_2^2). \quad (9)$$

The reciprocal velocity spread σ_τ is given by

$$\sigma_\tau^2 = (\sigma_1^2 + \sigma_2^2)/L_{12}^2, \quad (10)$$

where L_{12} is the distance between the two choppers, and the distance x is measured from an "effective chopping point" which is located between the choppers at a distance

$$L_{10} = L_{12}\,\sigma_1^2/(\sigma_1^2 + \sigma_2^2) \quad (11)$$

from the first chopper. These expressions may be used to calculate the time distribution in the incident beam of the DCS.

Important additional contributions to the overall energy resolution of a TOF spectrometer stem from flight path uncertainties due to the size of the sample and the geometry of the detectors [5].

The count-rate in a TOF experiment is determined by the intensity of neutrons at the sample position, the scattering properties of the sample, and the detecting efficiency of the array of detectors. To some extent the individual experimenter can select the scattering properties of the sample such as its size and shape, and how it is contained. The efficiency of the detector array can generally be increased, without degrading resolution, simply by purchasing more detectors; thus it largely depends on the available budget. The principal challenge in designing a TOF spectrometer is therefore to optimize the "front end" of the instrument, and indeed considerable efforts have been devoted to this task for both of the CNRF spectrometers.

6. Concluding Remarks

The time-of-flight spectrometers at the CNRF are the only instruments of their type on the North American continent. Once operational, we expect that they will fill a significant gap in the arsenal of neutron inelastic scattering instruments available to the scientific community. We look forward to a variety of collaborations and interactions with scientists wishing to use these instruments.

7. Appendix A

A thermal neutron has energy E, wave-vector k, wavelength λ, velocity v, and reciprocal velocity τ. These quantities are related as follows:

$$E(\text{meV}) = (h^2/8\pi^2 m)k^2 \simeq 0.020721\ [k(\text{nm}^{-1})]^2 \quad \text{(A1)}$$

$$= h^2/2m\lambda^2 \simeq 0.81804/[\lambda(\text{nm})]^2 \quad \text{(A2)}$$

$$= mv^2/2 \simeq 5.2270[v(\text{mm}\ \mu\text{s}^{-1})]^2 \quad \text{(A3)}$$

$$= m/2\tau^2 \simeq 5.2270/[\tau(\mu\text{s mm}^{-1})]^2. \quad \text{(A4)}$$

Furthermore

$$\lambda(\text{nm}) = h/mv \simeq 0.39560/[v(\text{mm}\ \mu\text{s}^{-1})], \quad \text{(A5)}$$

and

$$k(\text{nm}^{-1}) = 2\pi mv/h \simeq 15.8825[v(\text{mm}\ \mu\text{s}^{-1})]. \quad \text{(A6)}$$

In these equations m is the mass of the neutron and h is Planck's constant; values of m and h are taken from Ref. [31].

Useful conversion factors relating different units of energy may also be found in Ref. [31]. Two of the most commonly employed conversions are the following:

$$1\ \text{meV} \simeq 8.0655\ \text{cm}^{-1}$$

$$\simeq 0.2418 \times 10^{12}\ \text{Hz}.$$

8. Appendix B

In the disk chopper spectrometer the functions of pulser and monochromator are assumed by a set of disk choppers which rotate about a common axis parallel to (and some distance above) the direction of the beam. The essential concept can be understood by considering the two chopper arrangement illustrated in Fig. 18(a). The pulsing chopper produces short bursts of neutrons of many different energies. These neutrons have different speeds and therefore arrive at the monochromating chopper at many different times. The phasing of the monochromating chopper is chosen to transmit neutrons of the desired energy. The operation of this system can be represented in a distance-time (x,t) diagram as shown in Fig. 19(a).

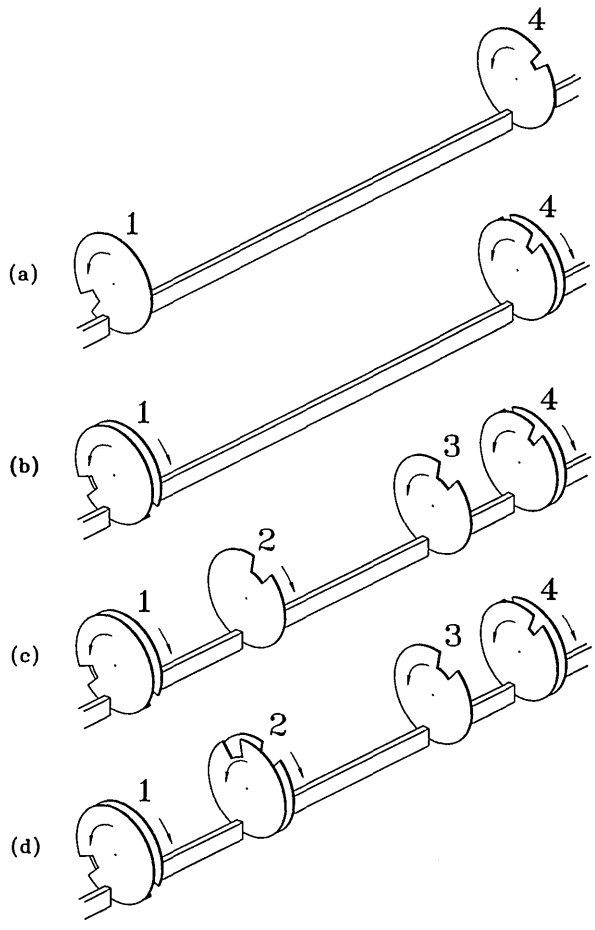

Fig. 18. Various chopper arrangements of increasing complexity. At (a) is shown the bare minimum two chopper arrangement. At (b) is shown a system with two counter-rotating choppers. Order removal choppers have been added at (c), and a slow-moving frame removal chopper is included at (d). The symbols 1, 2, 3, and 4 label choppers and chopper pairs.

Each of the principal choppers in the DCS is actually a counter-rotating pair of disks, as shown in Fig. 18(b). The effective chopping speed for such a device is double that of a single disk which rotates at the same speed as one of the members of the counter-rotating pair [32]. It follows that the intensity per pulse is doubled at constant resolution. This can be understood by considering systems such as the one shown in Fig. 20(a). The burst

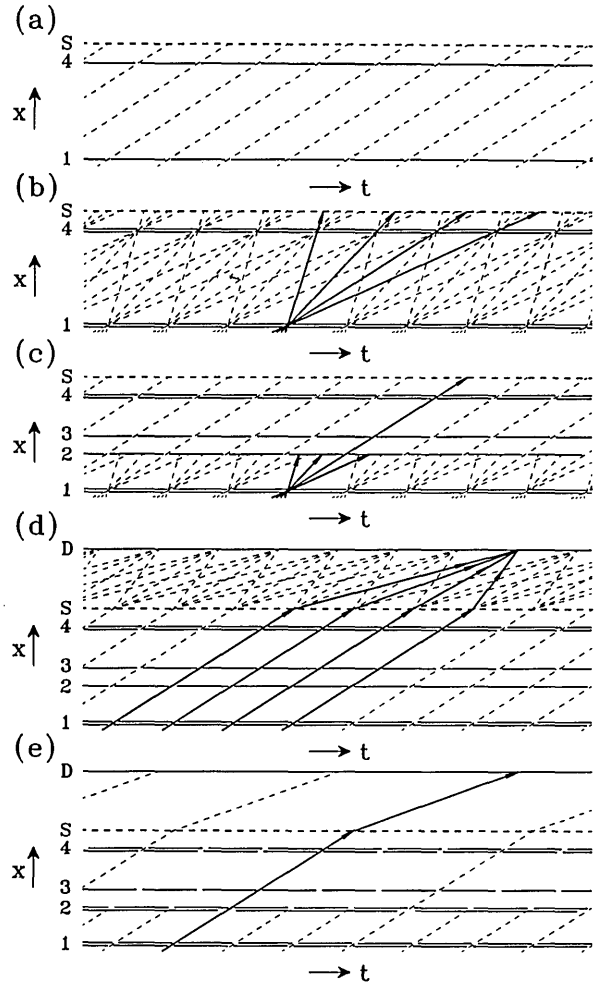

Fig. 19. A series of simplified (x,t) timing diagrams. In each case time is plotted horizontally and distance along the beam direction is plotted vertically; the slope of an inclined line is proportional to the velocity of the corresponding neutrons. The symbols 1, 2, 3, and 4 represent the positions of choppers or chopper pairs; S and D represent the sample position and the detector position, respectively. Breaks in horizontal lines represent time periods when choppers are open to the passage of neutrons. At (a) is shown an idealized timing diagram for a system of two choppers. A more realistic timing diagram for the same system (with counter-rotating choppers) is shown at (b). Several different neutron wavelengths are transmitted and some of those associated with one of the bursts are shown as heavy lines. To stop the unwanted wavelengths order removal choppers are added, as shown at (c). Ambiguities in the analysis of time-of-flight data can arise if the number of bursts at the sample position is too high. This is illustrated at (d); one set of neutrons which arrives at the detector at the same time is shown as heavy lines. A frame removal chopper is used to resolve the problem, as shown at (e); in this example every third burst is transmitted.

time of the illustrated system is simply $\Delta t = (w/u)$ whereas the transmitted intensity per pulse, I_P, is proportional to (w^2/u), where w is the width of the slot and the guide, and u is the chopping speed; the time dependence of the intensity is illustrated in Fig. 20(b). Clearly

$$I_P \propto u(\Delta t)^2 \qquad \text{(B1)}$$

so the intensity per pulse, at constant burst time, is proportional to the chopping speed of the system. A further advantage of the counter-rotating chopper pair concept, the possibility of using slots of different widths to enhance the resolution capabilities of the instrument [29], is discussed in Sec. 4.2. The timing diagram for two counter-rotating chopper pairs is essentially of the type illustrated in Fig. 19(a).

Up to now we have glossed over the fact that neutrons of more than one wavelength can be transmitted by systems such as those shown in Figs. 18(a) and 18(b); this possibility is illustrated in Fig. 19(b). Neutrons of the desired wavelength (λ_0) take a certain time (which is proportional to λ_0) to travel the distance between the choppers. Neutrons which take an integral number of chopper periods longer (or shorter) than this time to travel the same distance stand an equal chance of being transmitted. To suppress such neutrons we have determined

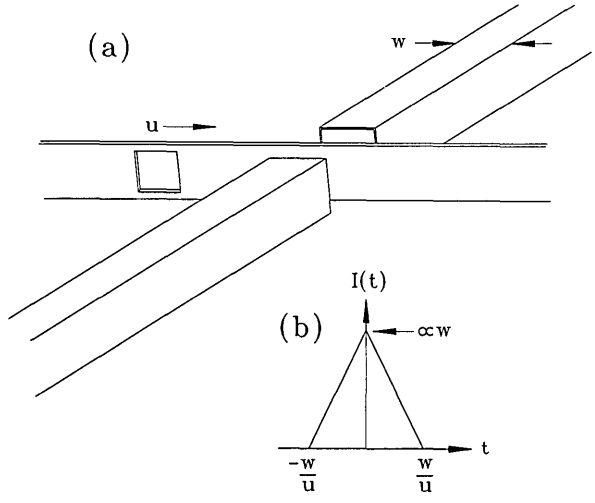

Fig. 20. A linear chopping device is illustrated at (a); the widths of the slot and the guide are both w and the chopping speed is u. The time dependence of the transmitted intensity is shown at (b). The burst time is (w/u) whereas the transmitted intensity is proportional to (w^2/u).

that two additional "order removal" choppers are required. These choppers are placed at intermediate locations between the pulsing and monochromating choppers as shown in Figs. 18(c) and 19(c); their exact positions are critical in order to remove all orders with intensity above background, under all conceivable operating conditions of the instrument.

The six choppers so far described collectively produce sharp bursts of neutrons of a single well defined energy at the sample position, as in Fig. 19(c). From our previous discussion we have seen that these choppers should be operated at the highest acceptable speed in order to achieve the highest possible intensity per pulse, but unfortunately the shortness of the time between pulses can introduce ambiguities into the analysis of a TOF measurement. This is illustrated in Fig. 19(d). We see that neutrons which arrive at the detector at a given time can in general be associated with more than one pulse arrival time at the sample. On physical grounds it is generally possible to rule out all but a few possible energy transfers, but ambiguities may still remain, in which case the appropriate course of action is to reduce the number of pulses at the sample. This is achieved using a chopper which rotates with a period that is an exact multiple of the period of the other choppers. The net effect is illustrated in Fig. 19(e). In the DCS the frame overlap chopper is placed close to the first order removal chopper, as shown in Fig. 18(d), and in Fig. 15.

Acknowledgments

Our thanks to Jack Rush for his advice and encouragement. We are grateful to Al Heald and Lew Robeson for their help in creating several of the figures in this paper, and to David Mildner for a number of comments.

9. References

[1] J. R. Dunning, G. B. Pegram, G. A. Fink, D. P. Mitchell, and E. Segré, Phys. Rev. **48**, 704 (1935). See also G. A. Fink, Phys. Rev. **50**, 738 (1936).
[2] E. Fermi, J. Marshall, and L. Marshall, Phys. Rev. **72**, 193 (1947).
[3] R. M. Brugger, Thermal Neutron Scattering, P. A. Egelstaff, ed., Academic Press, London and New York (1965), p. 53.
[4] M. Bée, Quasielastic Neutron Scattering: Principles and Applications in Solid State Chemistry, Biology and Materials Science, Adam Hilger, Bristol and Philadelphia (1988).
[5] C. G. Windsor, Pulsed Neutron Scattering, Taylor and Francis, London (1981).
[6] S. F. Trevino, J. Res. Natl. Inst. Stand. Technol. **98**, 59 (1993).
[7] D. A. Neumann and B. Hammouda, J. Res. Natl. Inst. Stand. Technol. **98**, 79 (1993).
[8] N. F. Berk, J. Res. Natl. Inst. Stand. Technol. **98**, 15 (1993).
[9] J. J. Rush and J. M. Rowe, Physica **137B**, 169 (1986).
[10] R. R. Cavanagh, J. J. Rush, and R. D. Kelley, in Vibrational Spectroscopy of Molecules on Surfaces, J. T. Yates, Jr., and T. E. Madey, eds., Plenum, New York (1987) p. 183.
[11] T. J. Udovic, D. A. Neumann, J. J. Rush, L. C. Sander, and I. S. Anderson, NIST Technical Note 1272, C. O'Connor, ed., U.S. Government Printing Office, Washington (1989) p. 1.
[12] R. Vacher, E. Courtens, G. Coddens, A. Heidemann, Y. Tsujimi, J. Pelous, and M. Foret, Phys. Rev. Lett. **65**, 1008 (1990).
[13] S. Feng, Phys. Rev. B **32**, 5793 (1985).
[14] W.-H. Li, J. W. Lynn, H. B. Stanley, T. J. Udovic, R. N. Shelton, and P. Klavins, Phys. Rev. B **39**, 4119 (1989).
[15] T. M. Giebultowicz, P. Klosowski, J. J. Rhyne, T. J. Udovic, J. K. Furdyna, and W. Giriat, Phys. Rev. B **41**, 504 (1990).
[16] A. Lewicki, A. I. Schindler, J. K. Furdyna, and W. Giriat, Phys. Rev. B **40**, 2379 (1989).
[17] J. M. Nicol, J. Eckert, and J. Howard, J. Phys. Chem. **92**, 7117 (1988).
[18] A. Heidemann, K. J. Lushington, J. A. Morrison, K. Neumaier, and W. J. Press, Chem. Phys. **81**, 5799 (1984).
[19] I. S. Anderson, N. F. Berk, J. J. Rush, T. J. Udovic, R. G. Barnes, A. Magerl, and D. Richter, Phys. Rev. Lett. **65**, 1439 (1990).
[20] J. Kondo, Physica (Amsterdam) **125B**, 279 (1984); **126B**, 377 (1984); **141B**, 305 (1986).
[21] A. Magerl, A. J. Dianoux, H. Wipf, K. Neumaier, and I. S. Anderson, Phys. Rev. Lett. **56**, 159 (1986).
[22] D. Steinbinder, H. Wipf, A. Magerl, D. Richter, A. J. Dianoux, and K. Neumaier, Europhys. Lett. **6**, 535 (1988).
[23] H. Jobic, M. Bée, and A. Renouprez, Surface Sci. **140**, 307 (1984).
[24] H. Jobic, M. Bée, and G. J. Kearley, Zeolites **9**, 312 (1989).
[25] H. J. Prask, J. M. Rowe, J. J. Rush, and I. G. Schröder, J. Res. Natl. Inst. Stand. Technol. **98**, 1 (1993).
[26] J. R. D. Copley, Nucl. Instr. Meth. A **291**, 519 (1990).
[27] J. R. D. Copley, Nucl. Instr. Meth. A **303**, 332 (1991).
[28] J. R. D. Copley, Physica B **180 & 181**, 914 (1992).
[29] R. E. Lechner, Physica B **180 & 181**, 973 (1992).
[30] R. J. Royston, Nucl. Instr. Meth. **30**, 184 (1964).
[31] E. R. Cohen and B. N. Taylor, J. Res. Natl. Bur. Stand. (U.S.) **92**, 85 (1987).
[32] J. R. D. Copley, Nucl. Instr. Meth. A **273**, 67 (1988).

About the authors: *John R. D. Copley and Terrence J. Udovic are scientists in the Reactor Radiation Division of the NIST Materials Science and Engineering Laboratory. The National Institute of Standards and Technology is an agency of the Technology Administration, U.S. Department of Commerce.*

Volume 98, Number 1, January-February 1993
Journal of Research of the National Institute of Standards and Technology

[J. Res. Natl. Inst. Stand. Technol. 98, 89 (1993)]

Ultra-High Resolution Inelastic Neutron Scattering

Volume 98 Number 1 January-February 1993

D. A. Neumann and B. Hammouda

National Institute of Standards and Technology, Gaithersburg, MD 20899

Two types of ultra high energy resolution neutron scattering instruments, the backscattering spectrometer and the spin echo spectrometer, are described. Examples of the types of research which can be done with these instruments are given and plans for a cold neutron backscattering spectrometer which will be built in the NIST Cold Neutron Research Facility (CNRF) are discussed. It is hoped that this information will be of use to researchers considering neutron scattering experiments at NIST.

Key words: diffusion; inelastic neutron scattering; molecular reorientations, neutron backscattering spectrometers; neutron spin-echo spectrometers; polymer dynamics; rotational tunneling.

Accepted: July 8, 1992

1. Introduction

Neutron scattering has proven to be an extremely valuable tool for studying a wide variety of dynamical processes in solids. This is because the energy of thermal neutrons is comparable to the energies of many elementary excitations in condensed matter while their wavelength is comparable to the interatomic distances. This allows one to simultaneously obtain information on the time scale and the geometry of the dynamical process under study; a feature which is unmatched by any other technique [1–6]. An important time scale for the investigation of dynamical phenomena such as diffusion, molecular reorientations and molecular tunneling is 10^{-7} to 10^{-9} s, the regime of ultrahigh resolution inelastic neutron scattering. The first neutron scattering instrument to operate in this range was a backscattering spectrometer built at the Münich reactor around 1970 which had an energy resolution of 0.425 μeV [7]. In the next section we describe how this excellent energy resolution is obtained and give a schematic description of a backscattering spectrometer. We also describe the spin-echo spectrometer which was first proposed in 1972 [8]. The following section describes the basic theory and gives examples of the use of quasielastic scattering to determine both the time scale and spatial character of diffusion and molecular reorientations. We then go on to discuss rotational tunneling and show how neutron scattering measurements can yield detailed information on the orientational potential felt by molecules in condensed systems. The final section describes the conceptual design of the backscattering spectrometer to be built in the CNRF at NIST and the basic design goals for a spin-echo spectrometer.

2. Fundamentals

2.1 Types of Instruments

2.1.1 Backscattering A neutron backscattering spectrometer is closely related to the triple axis spectrometer [9] shown schematically in Fig. 1. In both types of instruments, a "white" beam of neutrons impinges on a monochromator crystal which

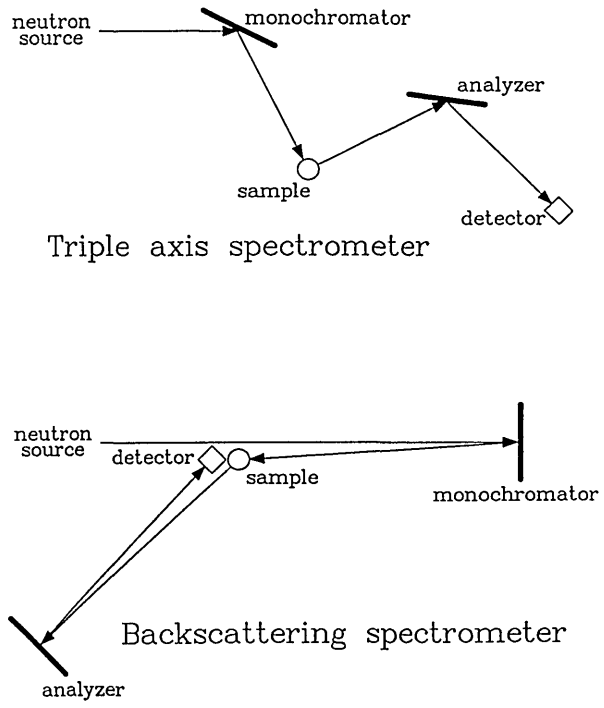

Fig. 1. Schematic diagrams showing the relationship between a triple-axis spectrometer and a backscattering spectrometer. Note that the term "backscattering" refers to the scattering from the monochromator and analyzer crystals and not from the sample.

selects a given neutron wavelength by Bragg diffraction. The resulting monochromatic neutrons then scatter from the sample, possibly gaining or losing energy in the process. The energies of the scattered neutrons are determined by Bragg diffraction from an analyzer crystal. The excellent energy resolution is obtained by taking the triple-axis instrument to its extreme limit, i.e., scattering the neutrons through an angle of 180° at both the monochromator and analyzer crystals. The energy resolution δE for a single Bragg reflection can be found by differentiating Bragg's law. One then obtains

$$\frac{\delta E}{E} = \frac{2\delta d}{d} + 2\cot\theta\,\delta\theta, \qquad (1)$$

where δd and d are the spread and value of the d spacing of the particular lattice planes used for monochromating or analyzing the neutron energy E, θ is 1/2 the scattering angle, and $\delta\theta$ is the angular spread of the neutrons. For a backscattering instrument the second term is zero since θ is 90°. Thus the resolution is determined by $\delta d/d$, which for perfect crystals is given by the Darwin width which is roughly on the order of 10^{-5}. Of course the beam is not perfectly collimated so that the energy resolution in backscattering is actually given by [7]

$$\frac{\delta E}{E} = 2\frac{\delta d}{d} + \frac{1}{4}(\delta\theta)^2. \qquad (2)$$

Thus, using the backscattering geometry for both the monochromator and analyzer, can result in energy resolutions $\lesssim 0.1$ μeV.

There are obvious technical difficulties inherent in the backscattering geometry. For instance one cannot simply scan energy by changing the scattering angle of the monochromator or analyzer since to do so would result in moving away from the backscattering condition. This is overcome by changing the incident energy, E_i, by either Doppler shifting the incident neutrons by rapidly moving the monochromator crystals or by changing the d-spacing of the monochromator crystal as a function of time using thermal expansion. There are several other difficulties including the low intensity and the geometry of the sample detector-area which will be discussed later in this article where the plans for the NIST cold-neutron backscattering instrument are described in detail.

2.1.2 The Neutron Spin Echo The NSE technique [8] uses the Larmor precession of the neutron spin to measure the change in the energy of the neutron upon scattering from some dynamical process in condensed matter. The idea is to make polarized neutrons precess in "very" uniform opposite magnetic fields before and after the sample so that those having slightly different wavelengths end up with the same spin orientation at the analyzer position. This allows the realization of excellent energy resolutions ($\lesssim 1$ μeV) using typical (i.e., broad) neutron wavelength distributions. As indicated in Fig. 2, cold neutrons are first polarized, then made to precess in very uniform magnetic fields in one direction before the sample and in the other direction after the sample and finally their spin orientations are analyzed to obtain the angular shift introduced by the sample on the spin orientation. This angular shift α is proportional to the applied magnetic field H, to the precession length L and to the energy shift during scattering $\hbar\omega = E_f - E_i$:

$$\alpha = [\gamma h^2(\pi/m)^{1/2}]\,\hbar\omega\lambda^3 HL, \qquad (3)$$

where γ, m, h and λ are the gyromagnetic constant, the neutron mass, Planck's constant, and the neutron wavelength, respectively. The analyzer picks up the projection of the magnetic moment along a well defined direction so that the detected neutron

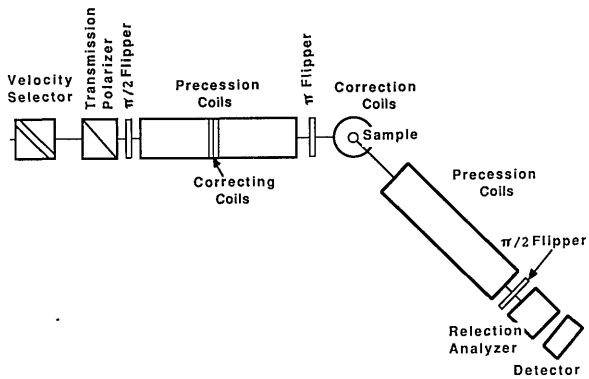

Fig. 2. Schematic diagram of a spin-echo spectrometer.

intensity is proportional to $\cos(\alpha)$ properly weighted over the normal modes distribution $S(Q,\omega)$. The measured intensity is therefore given by the cosine Fourier transform of the dynamic structure factor $S(Q,\omega)$ [6]:

$$I(Q,t)=\int d\omega S(Q,\omega)\cos(\alpha), \tag{4}$$

where the Fourier variable is $t=[\gamma h^3/2(\pi m)^{1/2}]\lambda^3 HL$. In order to scan time, the magnetic field H is varied.

The main components of an NSE instrument [10,11] (see Fig. 2) are the supermirrors to polarize and analyze the neutron spin direction, the coils to create very uniform magnetic fields ($\delta H/H \sim 10^{-5}$) and other conventional neutron scattering components (velocity selector to monochromate, slits to collimate and a detector to count scattered neutrons). Flippers are used to prepare the neutron spin direction before, and after the two precession coils by rotating its direction.

2.2 Quasielastic Neutron Scattering

2.2.1 Basic Theory In this section we first outline basic features of quasielastic neutron scattering and then proceed to illustrate these points with various experimental applications. To date, most quasielastic neutron scattering experiments have been performed using incoherent scattering [6], due to the simpler interpretation in terms of specific microscopic models. This is because the incoherent scattering function $S_{inc}(Q,\omega)$ measured by the backscattering spectrometer is the space and time Fourier transform of the self-correlation function $G_s(r,t)$ which represents the probability that a particle which was at the origin at time $t=0$ is at position r at time t. Thus when devising a model of a diffusional process, it is only necessary to consider the motion of a single atom and not how the motion of that atom is correlated with the motions of other atoms in the system. Another important way of expressing $S_{inc}(Q,\omega)$ is in terms of the intermediate scattering function $I(Q,t)$

$$S_{inc}(Q,\omega)=\int I(Q,t)e^{i\omega t}dt, \tag{5}$$

where $I(Q,t)$ is the space Fourier transform of $G_s(r,t)$ and is the quantity measured by the spin-echo technique.

In order to understand qualitatively how diffusion is manifested in a neutron scattering experiment, we will consider some simple models which display all of the basic features of more complex models. (For a more detailed discussion of the models presented here and for a far wider assortment of models see [5]). First consider simple diffusion which is governed by Fick's law

$$\frac{\partial\rho(r,t)}{\partial t}=D\nabla^2\rho(r,t), \tag{6}$$

where $\rho(r,t)$ is the particle density at position r at time t and D is the diffusion constant. A solution of this equation is given by a self-correlation function of the form

$$G_s(r,t)=\frac{\exp(-r^2/4Dt)}{(4\pi Dt)^{3/2}}, \tag{7}$$

where we have assumed that the times of interest are long enough that the motion is truly diffusive, i.e., much longer than the time between collisions. Then the space Fourier transform of Eq. (6) yields the intermediate scattering function

$$I(Q,t)=\exp(-Q^2Dt) \tag{8}$$

shown in Fig. 3a.

Since this represents an exponential decay in time, the time Fourier transform yields a Lorentzian lineshape

$$S_{inc}(Q,\omega)=\frac{1}{\pi}\frac{DQ^2}{(DQ^2)^2+\omega^2}, \tag{9}$$

which is shown in Fig. 3b. Note that this expression peaks at $\omega=0$ and has an energy width (FWHM) Γ which is given by

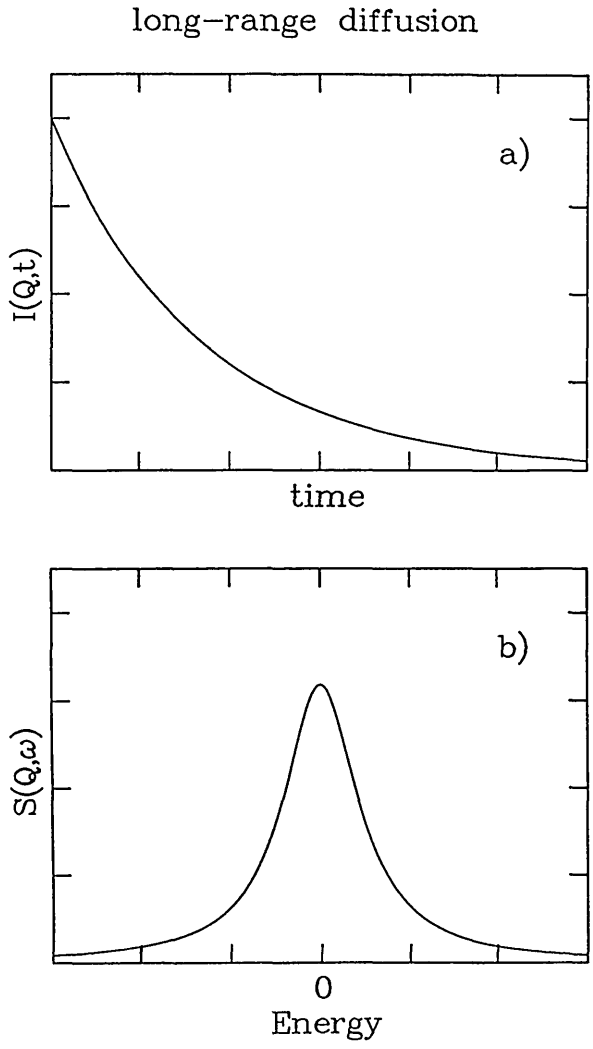

Fig. 3. a) Intermediate scattering function of time at a particular value of the scattering vector Q.b) Scattering function for long-range translational diffusion as a function of energy at a particular Q. This is the Fourier transform of the intermediate scattering function.

$$\Gamma = 2DQ^2. \tag{10}$$

The width of the peak is thus proportional to both the diffusion constant and the square of the scattering vector as shown in Fig. 4.

Chudley and Elliott [12] generalized this picture to describe jump diffusion in solids by assuming that the jump motion is random, that the jumps can be considered instantaneous, and that the available lattice sites form a Bravais lattice. Then the simple rate equation

$$\frac{\partial \rho(r,t)}{\partial t} = \frac{1}{n\tau}\sum_{i=1}^{n}[\rho(r+\ell_i,t)-\rho(r,t)], \tag{11}$$

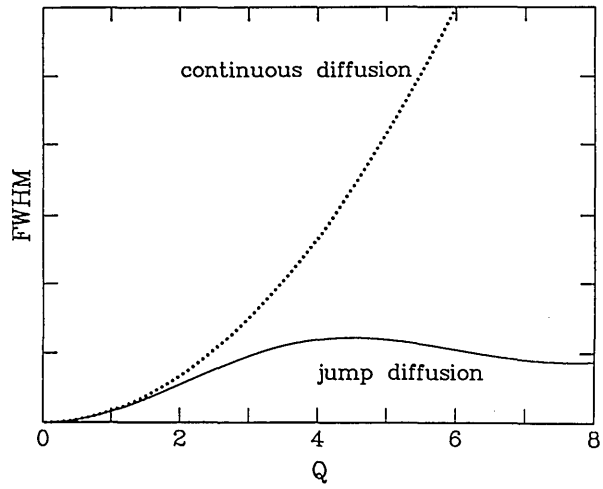

Fig. 4. Full width at half maximum (FWHM) for Fickian (continuous) diffusion (dotted line) and for the Chudley-Elliott model of translational jump diffusion for 1 Å jumps (solid line). Note that they are identical at low Q which means that the macroscopic diffusion constants are identical.

can be used to represent the particle's motion. Here $\rho(r,t)$ is the probability of finding the particle at position r at time, t, τ is the time between jumps and the sum is taken over the nearest neighbor sites at distances ℓ_i. Using the boundary condition $\rho(r,0)=\delta(r)$ makes $\rho(r,t)$ and $G_s(r,t)$ equivalent, and then the Fourier transform of the previous equation yields

$$\frac{\partial I(Q,t)}{\partial t} = \frac{-I(Q,t)}{\tau}\frac{1}{n}\sum_{i=1}^{n}(1-e^{-iQ\cdot\tau_i}). \tag{12}$$

As for the case of pure diffusive motion, this has an exponential solution of the form

$$I_s(Q,t) = \exp\left(-\frac{f(Q)t}{\tau}\right), \tag{13}$$

where

$$f(Q) = \frac{4}{n}\sum_{i=1}^{n/2}\sin^2\left(\frac{Q\cdot\ell_i}{2}\right). \tag{14}$$

Thus the scattering function again has a Lorentzian lineshape given by

$$S_{inc}(Q,\omega) = \frac{1}{\pi}\frac{f(Q)/\tau}{(f(Q)/\tau)^2+\omega^2}, \tag{15}$$

which has an energy width of

$$\Gamma=\frac{2}{\tau}f(Q). \tag{16}$$

The most important thing to note is that Γ oscillates in Q with the periodicity determined by the inverse of the jump vectors ℓ_i. Thus it is possible to determine the microscopic diffusion mechanism via the dependence of the width of the quasielastic scattering on the scattering vector. Another interesting feature is that for small values of Q, $\Gamma \propto Q^2/\tau$. One can then connect this expression to the macroscopic diffusion constant since $D \propto 1/\tau$ and $\Gamma=2DQ^2$ for Fickian diffusion. Fig. 4 compares $\Gamma(Q)$ for a powder averaged Chudley-Elliott model assuming 1 Å jumps with that of Fickian diffusion for identical values of the diffusion constant. The possibility of extracting the macroscopic diffusion constant from the small Q region makes it possible to compare quasielastic neutron scattering results with those obtained using other methods and to discern the activation energy E_0 via the Arrhenius law

$$D=D_0\exp\left(\frac{-E_0}{k_BT}\right). \tag{17}$$

For rotational motions, one is typically concerned with molecules or ions which contain more than one hydrogen atom. Thus it should be reiterated that to describe the motion, only a single atom need be considered for an incoherent scatterer, since the motions of other atoms are irrelevant even if they are coupled to that of the first [6]. The formalism for rotational motions is thus the same as for diffusion in which a single particle is confined to a limited region of space. First let us turn our attention to the case in which an atom undergoes jump diffusion on a limited number of sites which lie on a circle of diameter R. Consider functions $f_i(t)$ which represent the probability that a particular atom is at site i at time t. These functions may be obtained using a rate equation similar to Eq. (10)

$$\frac{df_i(t)}{dt}=\frac{1}{\tau}f_i(t)+\frac{1}{\tau}\sum_{j\neq 1}f_j(t), \tag{18}$$

where τ is the time between jumps and the sum is taken over all orientations from which the molecule can rotate directly to orientation i. For simplicity we will consider the case of two possible equivalent molecular orientations corresponding, for example, to a water molecule undergoing twofold jumps about its C_2 symmetry axis. Then Eq. (17) has the solutions

$$f_1=\frac{1}{2}\left(1+\exp\frac{-2t}{\tau}\right) \tag{19}$$

$$f_2=\frac{1}{2}\left(1-\exp\frac{-2t}{\tau}\right), \tag{20}$$

where use has been made of the relations $f_1(0)=1$, $f_2(0)=0$ and $f_1+f_2=1$. The intermediate scattering function is then given by

$$I(Q,t)=\frac{1}{2}\exp\left(\frac{-2t}{\tau}\right)\times$$

$$[1-\exp(i\boldsymbol{Q}\cdot\boldsymbol{R})]+\frac{1}{2}[1+\exp(i\boldsymbol{Q}\cdot\boldsymbol{R})], \tag{21}$$

where $\boldsymbol{R}$ is the vector between positions 0 and 1. Note that this equation has been divided into two parts. The first decays exponentially in time and thus leads to a Lorentzian component in the quasielastic scattering while the second is independent of time and, therefore, gives a δ-function in energy. This lineshape is displayed in Fig. 5. After performing a three-dimensional powder average and a Fourier transform, one obtains the scattering function

$$S_{inc}(Q,\omega)=\frac{1}{\pi}\left[\frac{1}{2}\left(1+\frac{\sin(QR)}{QR}\right)\delta(\omega)+\left(1-\frac{\sin(QR)}{QR}\right)\frac{2\tau}{(2)^2+(2\omega\tau)^2}\right]. \tag{22}$$

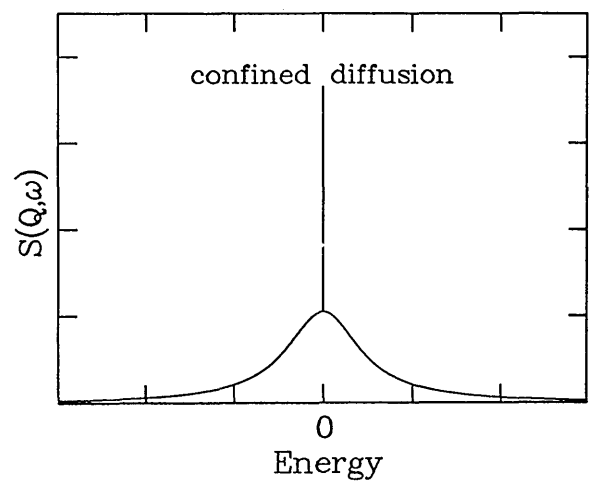

Fig. 5. Scattering function as a function of energy at a particular Q for diffusion confined to a particular region of space (e.g., rotational jump diffusion). Note the narrow component indicative of a process in which the atom has a finite probability of being at its initial position at infinite time.

Note that for rotational jump diffusion, the Lorentzian component has a linewidth which is constant in Q, but that the intensity oscillates with the inverse periodicity of the jump length. The intensity of the δ-function component, termed the elastic incoherent structure factor or EISF, oscillates with the same period but out of phase with respect to the intensity of the Lorentzian component. Thus, characteristic differences exist in the scattering from rotational jump diffusion compared to translational jump diffusion where the lineshape is a single Lorentzian. It is worth pointing out that the δ-function component arises from the fact that at infinite time, the particle has a finite probability of being in its original position. Thus this δ-function component is a characteristic feature of any diffusion process which is confined to a specific region of space.

The microscopic rotational mechanism need not be as well-characterized as it was for this simple example. For instance, if the static potential fluctuates due to phonons, the idea of a single jump frequency needs to be replaced by a distribution of residence times. This situation is called rotational diffusion since the self-correlation function obeys the diffusion equation if the residence time is short. Then for uniaxial rotational diffusion, it can be shown that

$$S_{\text{inc}}(Q,\omega)=J_0^2\left(\frac{QR}{2}\sin\theta\right)\delta(\omega)+$$

$$\frac{2}{\pi}\sum_{i=1}^{\infty}J_i^2\left(\frac{QR}{2}\sin\theta\right)\frac{\Gamma_i}{\Gamma_i^2+\omega^2}, \qquad (23)$$

where R is the diameter of circle on which the diffusion is occurring, θ is the angle between the axis of rotation and Q and $\Gamma_i = i^2 D_R$ with D_R representing the rotational diffusion constant. Thus, the scattering function can still be divided into a completely elastic component and a broadened component. However, in this case, the broadened component is a sum of many different Lorentzians of varying widths. Therefore, the total width of this component may vary somewhat in Q due to the trade-off in intensity between the various Lorentzians. The EISF's of the two models discussed here are displayed in Fig. 6. Note that for the case of twofold jumps, the EISF decays to 1/2 at large values of Q. This is simply a manifestation of the fact that the EISF represents the Fourier transform of the self-correlation function for infinite times. For a two-site model the probability is 0.5 that the particle has its original orientation, therefore the EISF only drops to 1/2, but for the rotational diffusion model the EISF eventually drops to zero since there are infinitely many possible sites on a circle. In principle it is possible to tell if a particle is undergoing rotational jumps or continuous rotational diffusion on this basis alone. In practice one usually cannot reach Q's which are high enough to distinguish continuous diffusion from discrete many-fold jumps.

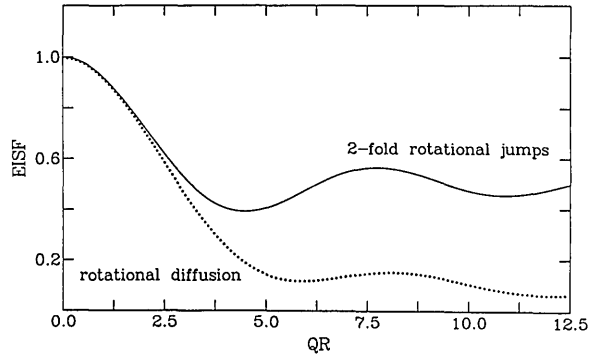

Fig. 6. The elastic incoherent structure factor (EISF) for uniaxial twofold rotational jumps (solid line) and for uniaxial rotational diffusion (dotted line) as a function of QR where R is the diameter of the circle on which the motion occurs.

In polymer research the intermediate scattering function $I(Q,t)$ is often expressed as the density-density correlation between monomers:

$$I(Q,t)=(1/N_P N^2)\sum_{\alpha\beta}^{N_P}\sum_{ij}^{N}$$

$$<\exp[-iQ\cdot(r_{\alpha i}(0)-r_{\beta j}(t))]>, \qquad (24)$$

where $r_{\beta j}(t)$ is the position of monomer j in polymer β at time t, N_p and N are the total number of polymers and the number of monomers per polymer chain respectively. Its initial value is the elastic (also called static) structure factor: $S(Q,0)=I(Q,t=0)$. Fig. 7 shows a typical set of neutron spin echo (NSE) data taken by Ewen [13] from polydimethylsiloxane (PMDS) in a dilute solution of deuterated bromobenzene at the Theta temperature (84 °C). Note that these curves exhibit the simple exponential behaviour displayed schematically in Fig. 3a. Furthermore, Eq. (8) shows that the decay of $I(Q,t)$ increases with Q^2 which is also observed in Fig. 7.

The initial slope of $I(Q,t)$ is called the first cumulant:

$$\Gamma(Q)=\lim_{t\to 0}[\partial I(Q,t)/\partial t]/S(Q,0), \qquad (25)$$

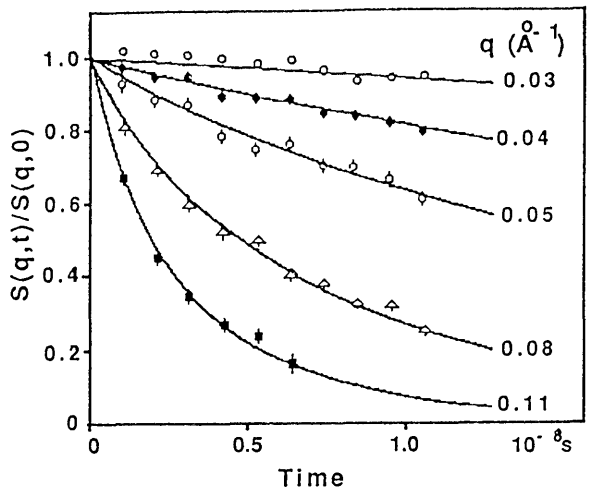

Fig. 7. Neutron spin echo spectra from polydimethylsiloxane in a dilute solution of deuterated bromobenzene at the theta temperature (84 °C) [13].

which is identical to the energy width of $S(Q,\omega)$ and which can readily be modelled for various polymer systems. Many approaches are used: the Kirkwood-Riseman (KR) equation for polymer solutions, the dynamic Random Phase Approximation [14] (RPA) for polymer melts, scaling concepts and renormalization group ideas for both, etc.

The precision of extracting $\Gamma(Q)$ is greatly improved by introducing a shape function [15, 16]

$$f(Q,\tau)=I(Q,t)/S(Q,0), \tag{26}$$

where time is rescaled by defining a dimensionless variable $\tau=\Gamma(Q)t$. This function depends only on QR_g or Qa in the small or high Q regions (where R_g is the radius of gyration and a is the statistical segment length). Moreover, it is independent of Q in the intermediate Q region which means that the scattering function follows a universal shape (the intermediate Q region is defined as $1/R_g<Q<1/a$). An iterative procedure using the shape function $f(Q,\tau)$ yields values for $\Gamma(Q)$ that are more precise than the direct method based on simply extracting $\Gamma(Q)$ as the slope of $I(Q,t)$ at zero time.

Many times a system will display more than one type of diffusive motion; then if the various motions are uncoupled, the intermediate scattering function is given by the product of the individual intermediate scattering functions

$$I(Q,t)=I^{\text{vib}}(Q,t)\prod_j I_j(Q,t), \tag{27}$$

where the product is taken over the various rotational and translational motions and

$$I^{\text{vib}}(Q,t)=\exp(-Q^2<\mu^2>) \tag{28}$$

is simply the Debye-Waller factor. This results in a scattering function which is simply the convolution of the scattering functions of the individual motions. Thus if the motions occur on somewhat different time scales, the various components can often be separated simply because they have different widths (Fig. 8). This is possible because motions which are slow on the scale of the resolution will appear as an elastic component and those which are fast compared to the resolution will appear as an essentially flat background. In order to observe motions occurring on different time scales usually means using different instruments with different dynamical windows or at least adjusting the resolution on a given instrument. Thus it is often important to have a wide dynamical range available in order to completely characterize a diffusional process.

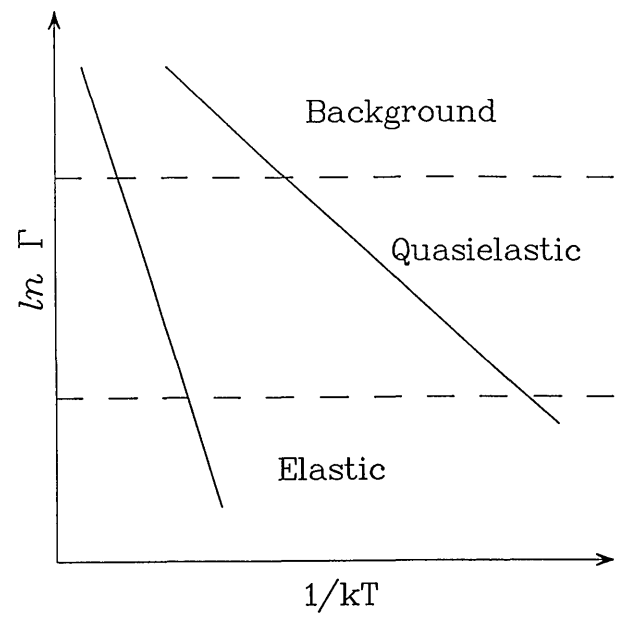

Fig. 8. Schematic Arrhenius plots showing that a motion occurring on a particular time scale can give rise to scattering which appears elastic if the instrumental resolution is too coarse, while it may appear as a flat background if the resolution is too fine. This indicates that motions which occur on different time scales can be separated simply by using instruments having different dynamical ranges or by changing the resolution on a given instrument.

2.2.2 Applications *Li Diffusion in LiC_6.* LiC_6 is a stage 1 graphite intercalation compound in which the Li atoms undergo a transition from an ordered, commensurate $\sqrt{3}\times\sqrt{3}$ R30° phase to a disordered, commensurate lattice gas at a temperature of 715 K [17]. Measurements of the quasielastic scattering due to Li diffusion were made by Magerl, Zabel, and Anderson [18] using a cold neutron backscattering spectrometer below the transition and a time of flight instrument above it. Figure 9 shows the quasielastic widths as a function of Q at 660 and 720 K. These energy widths were determined by fitting the data taken at a particular value of the scattering vector to a Lorenztian convoluted with the instrumental resolution. The solid line in Fig. 9a is a fit to a model which assumes that the diffusion occurs by instantaneous jumps between the nearest Li sites on the ordered sublattice as shown by the vector ℓ_2 in the insert. For the much more rapid Li diffusion in the lattice gas phase, the data can be fit assuming that the jumps occur between the nearest neighbor commensurate sites shown by vector ℓ_1 in the insert. In addition to the diffusional mechanism these fits yield values of the diffusion constant of $1\times10^{-4}\,mm^2/s$ and $24\times10^{-4}\,mm^2/s$ at 660 and 720 K, respectively. From the temperature dependence of the diffusion constant in the ordered phase one obtains an activation energy of (1.0 ± 0.3)eV. These results demonstrate the ability to "tune in" different diffusional processes with different neutron scattering spectrometers which operate in different dynamical ranges.

Self-Diffusion in bcc β-Titanium. When plotted as a function of T_m/T, (where T_m is the melting temperature) self diffusion in the group IVb metals (Ti, Zr, and Hf) is orders of magnitude faster than for other bcc metals. In order to determine the diffusional mechanism Vogl et al. [19,20] have performed an exquisite measurement of the quasielastic scattering due to self diffusion in a single crystal of bcc Ti. A typical spectrum, along with a fit assuming a single Lorentzian convoluted with the experimental resolution is shown in Fig. 10. Figure 11 shows the Q dependence of the widths for two temperatures and several different crystal orientations. The solid lines represent fits to an encounter model of 1/2[111]NN jumps. In a model of this type only the jump vector between the original and final sites is relevant. The details of what happens in between are forgotten. The dashed lines in Fig. 11 represent an encounter model description of [100]NN jumps, while the dotted and dashed lines represent standard descriptions of tetrahedral and octahedral interstitial jumps respectively. Clearly this data reveals that the self diffusion of Ti in β-Ti is dominated by 1/2[111] jumps into nearest neighbor vacancies, however a small additional fraction of jumps into second nearest neighbor positions is also consistent with the data.

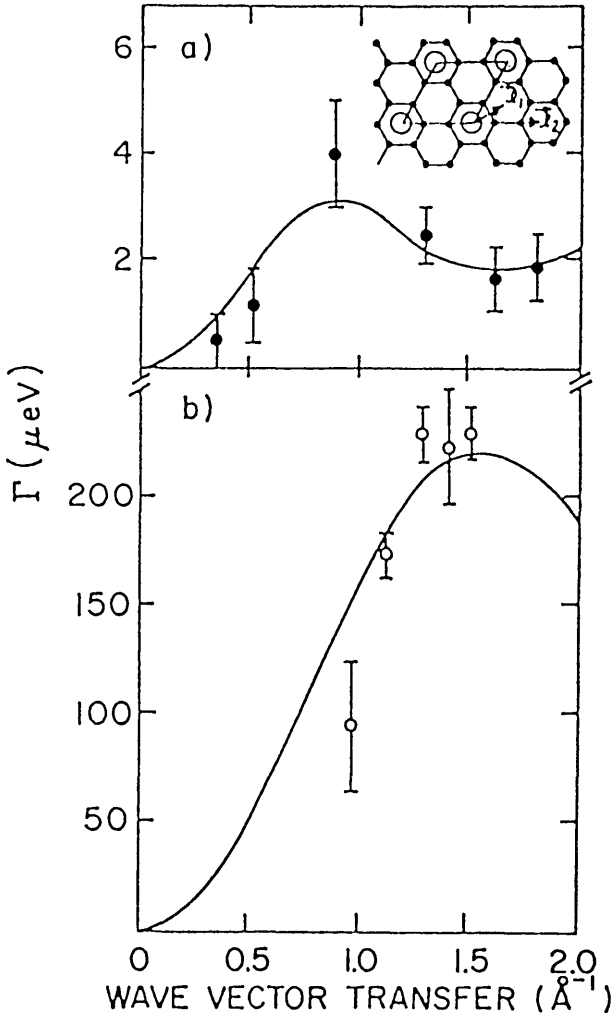

Fig. 9. Linewidths (FWHM) of the quasielastic neutron spectra measured for LiC_6. a) 660 K (below the Li sublattice melting temperature). b) 720 K (above the Li sublattice melting temperature). The inset shows the jump vectors used to calculate the solid lines in both plots. Above the transition, Li jumps to nearest neighbor sites while below jumps occur to sites form the $\sqrt{3}\times\sqrt{3}$ R30° sublattice [18].

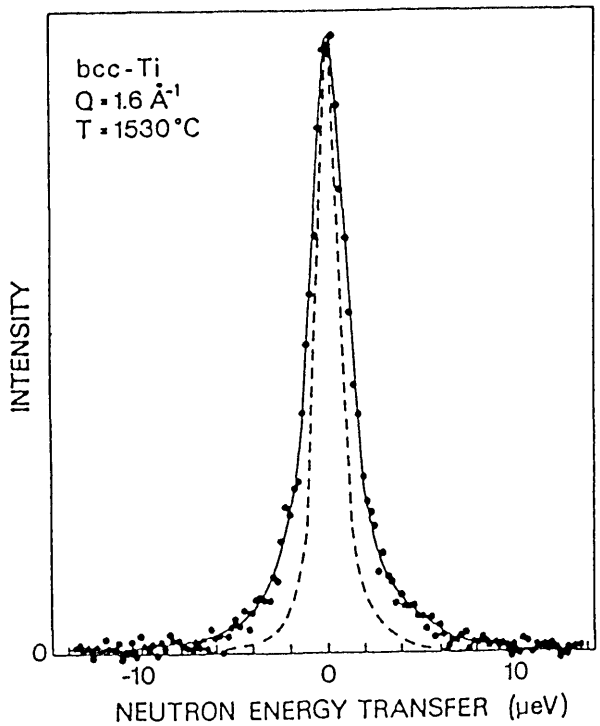

Fig. 10. Quasielastic spectra from bcc Ti at $Q = 1.6$ Å^{-1} and $T = 1530$ °C. The solid line is a fit to a single Lorentzian convoluted with the instrumental resolution. The dashed line represents the measured resolution [19,20].

Reorientations of Benzene. The previous two examples described systems in which the diffusing atoms (Li or Ti) undergo long-range translational motion so that the scattering law consists of a single Lorentzian component. As shown earlier, if the quasielastic scattering is due to rotational jumps, the scattering law is the sum of a δ-function and one or more Lorentzians. An interesting example of this type of system is crystalline benzene which has recently been studied using cold neutron backscattering methods by Fujara et al. [21]. The EISF determined at 210 K by fitting the data to a model of random 60° jumps is shown in Fig. 12. The solid line is a calculation of the EISF assuming sixfold rotational jumps and that the radius of the ring of H atoms is 2.479 Å. The small disagreement at low Q can be attributed to multiple scattering effects. Attempts were also made to fit the data to a model which allowed for 120° and 180° jumps in addition to 60° jumps with equal probabilities. However, the EISF determined using this model was consistently larger than expected for sixfold rotations. Thus, these data show that benzene rotates principally by 60° jumps with a correlation time of approximately 30 ns at 210 K. In addition the temperature dependence of the correlation time was found to be consistent with an activation energy of 182 meV determined using NMR.

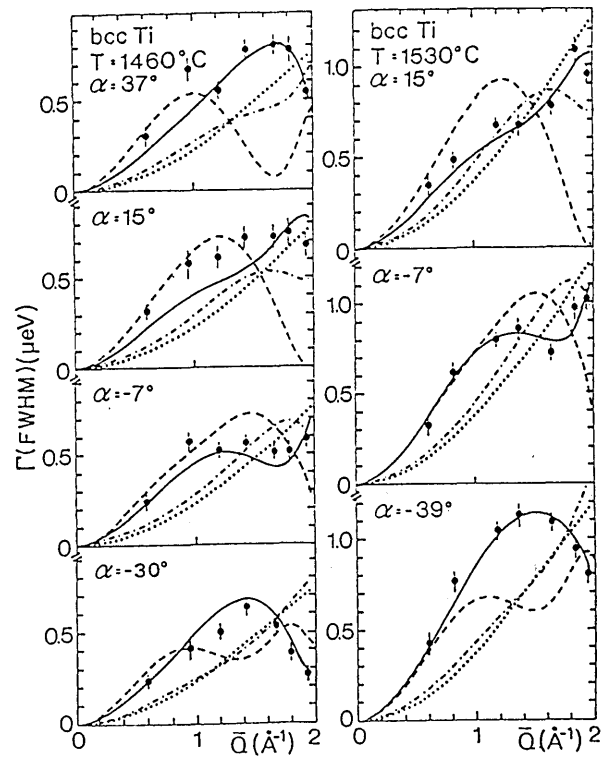

Fig. 11. Linewidths at the quasielastic neutron spectra of bcc Ti at 1460 °C (left) and 1530 °C (right) as a function of Q. Left: scattering plane parallel to the (001) crystal plane. Right: scattering plane parallel to the (012) crystal plane. α denotes a rotation of the sample around an axis perpendicular to the scattering plane and is defined as the angle between the incident neutrons and the <100> crystal direction. The model calculations are: solid line, 1/2[111] nearest neighbor jumps; dashed line, [100] 2nd nearest neighbor jumps; dotted line, tetrahedral interstitial jumps [19,20].

Dilute and Semidilute Polymer Solutions. In dilute (monodisperse) polymer solutions, and at the small Q limit (QELS), $\Gamma(Q)$ shows a characteristic Q^2 dependence seen in Eq. [9]:

$$\lim_{Q\to 0} \Gamma(Q) = Q^2 D, \tag{29}$$

which describes the overall diffusion of the whole polymer chain with a diffusion coefficient D. At intermediate values of Q (where scattering is probing length scales smaller than the chain but larger than the monomer size), a Q^3 dependence of $\Gamma(Q)$ characterizes the Zimm (internal) Brownian diffusive modes [15,22]:

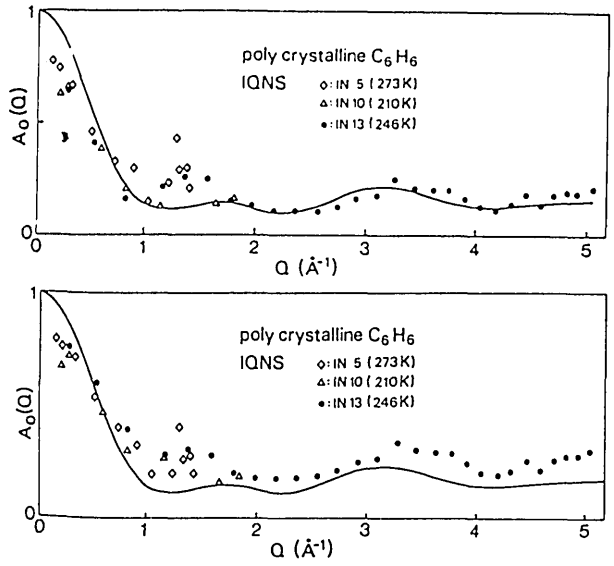

Fig. 12. The elastic incoherent structure factor obtained by a model in which the benzene molecule undergoes rotational jumps of 60° (top) and by a model in which 60°, 120°, and 180° jumps are equally probable (bottom). The neutron scattering data clearly demonstrates that 60° jumps are the predominant rotational mechanism. The disagreement between the data and the model at small Q's is due to multiple scattering effects [21].

$$\Gamma(Q) = C(k_B T/\eta_0)Q^3, \qquad (30)$$

where k_BT is the solution temperature in energy units, η_0 is the solvent viscosity and C is a numerical constant that depends on solvent quality and preaveraging of the hydrodynamic interaction (for Theta solvents, $C = 1/6\pi$ or $C = 1/16$ depending on whether hydrodynamic interactions are preaveraged or not). The Q^2 to Q^3 transition has been observed [16] for polystyrene in various solvents (see Fig. 13). Moreover, at high Q, diffusion of a single monomer dominates and the Q^2 law is recovered again. This last transition (Q^3 to Q^2) involves scattering vectors that can be reached only with NSE [23,24] as shown in Fig. 14.

In semidilute solutions (where individual polymer chains start overlapping each other) hydrodynamic interactions between monomers start being screened so that a Rouse description [25] of polymer dynamics is more appropriate. Moreover, excluded volume effects remain important only between entanglement points so that monomers that are topologically farther apart do not feel each other even if they belong to the same chain. Scaling ideas based on concentration and temperature "blobs" [26] have been successful in describing both static and dynamic properties of polymer solutions. In the case of a three-component polymer system (two polymers and a solvent for example), two characteristic relaxation times are observed [27,28]: a slow mode representing cooperative diffusion and a fast mode representing inter-diffusion.

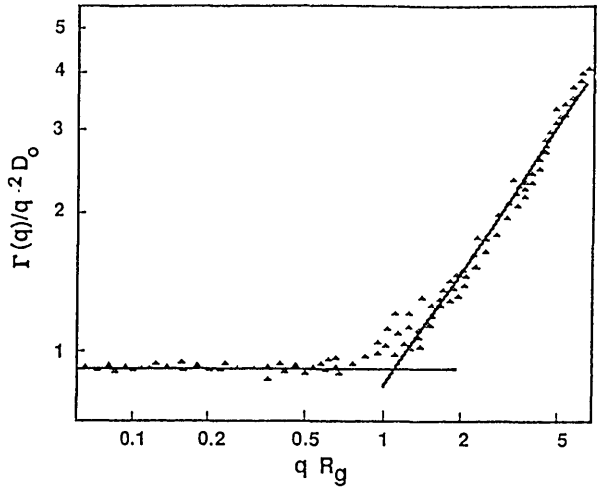

Fig. 13. Quasielastic light scattering from polystyrene in various solvents showing the crossover from the Q^2 to the Q^3 scaling law (small to intermediate Q for the first cumulant) [16.]

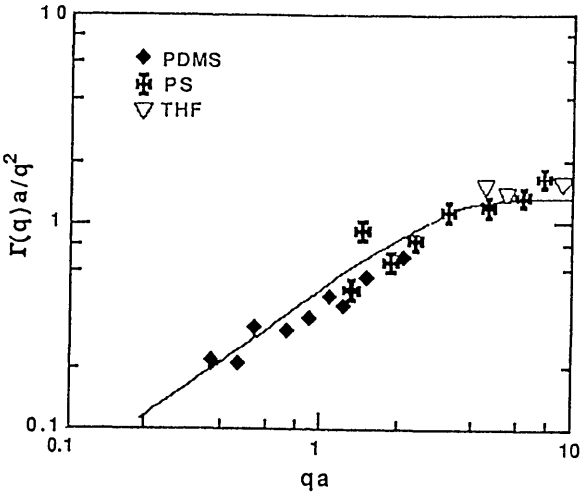

Fig. 14. Neutron spin echo spectra from polystyrene in CS_2 showing the crossover from the Q^3 to the Q^2 scaling law (intermediate to high Q) for the first cumulant.

Concentrated Polymer Solutions and Melts. In contrast to the case of dilute solutions, concentrated polymer solutions and polymer melt dynamics are dominated by interchain correlations. At a length scale smaller than the average distance between two entanglement points, the Rouse model (which neglects hydrodynamic interactions) describes chain dynamics well. The Q^3 power law dependence of $\Gamma(Q)$ in the intermediate Q region becomes a Q^4 dependence [29]. However, at longer

scale lengths, entanglements constrain the chain motion to occur in a "tube" created by surrounding chains. This is the reptation idea [30,31] whereby polymer chains perform a snake like diffusive motion by which they renew their configurations. Reptation corresponds to the slow mode (that was mentioned for semidilute solutions) at high Q. In crosslinked gels, for example, this slow mode disappears so that only fast modes describing local monomer motions remain. Tests of the reptation idea have brought about a better understanding of the viscoelastic behavior of polymer systems.

A dynamic Random Phase Approximation (RPA) approach [32,33] has been used to understand the effect of monomer interactions on the various diffusive normal modes in polymer multicomponent melts. Within this framework, the intermediate scattering function $I(Q,t)$ and its initial slope $\Gamma(Q)$ can be related to their bare (i.e., when no interactions are present) counterparts. This approach has permitted the sorting out of the various diffusion coefficients (self, mutual, inter-, cooperative, etc.) that are measured by various techniques in various experimental (concentration, molecular weight) conditions. Self and mutual diffusion coefficients are measured in dilute polymer solutions and correspond to the diffusion of a single chain and to that of many chains respectively. Inter-diffusion and cooperative diffusion characterize ternary polymer systems comprising, for example, concentrated solutions of two polymers A and B and correspond to the fast and slow modes when taken at the proper limits. The interdiffusion coefficient represents the diffusion of A relative to B while the cooperative diffusion coefficient describes the diffusion of the polymers (both of A and B) in the solvent. Interdiffusion for instance is the dominant mode in phase decomposing blends. It is interesting to note [28] that for the case of a diblock copolymer in solution, the first cumulant for the interdiffusion mode remains finite at the $Q \rightarrow 0$ limit (contrary to the definition of a diffusive mode). This is reminiscent of the "optical mode" in multilayer crystalline solids keeping in mind, of course, that the interdiffusion mode is nonpropagating.

Effects of temperature, concentration, molecular weight and chain stiffness on the dynamics of polymer solutions have been investigated. The molecular weight dependence of the mutual diffusion coefficient changes from $N^{-1/2}$ with hydrodynamic interactions (dilute solutions) to N^{-1} in concentrated solutions of short chains in long chains (Rouse dynamics) to N^{-2} for melts of long chains (where reptation dominates). Recall that N is the number of monomers per polymer chain. The NSE technique is also particularly useful in observing polymer chain stiffness [23,34] and its effects on diffusion at intermediate and high Q values.

Equilibrating Polymer Blends. The previous sections described the dynamics of polymer systems that are in thermal equilibrium. The observed (Zimm, Rouse Reptation) modes are due to Brownian diffusion in solutions and in melts. This section, however, briefly describes "real time" dynamics of polymer systems following gradients in temperature [35] (such as across phase transitions) or in concentrations [36] (two films are superposed face-to-face and allowed to diffuse into each other upon heating). In the first case, the crossing of the phase boundary could be towards equilibration (from two-phase into the miscible region) or towards growth (the other way around). The time scales involved are ideally suited for investigation by quasielastic scattering methods.

The intermediate scattering function $I(Q,t)$ described in the previous sections involves time correlations of the fluctuating density $\rho(Q,t)$ (in Fourier space):

$$I(Q,t) = (1/N_P N^2) < \rho(-Q,0)\rho(Q,t) > . \quad (31)$$

For equilibration/growth processes, what is measured instead is the time evolution of $\rho(Q,t)$:

$$S_t(Q) = (1/N_P N^2) < |\rho(Q,t)|^2 > . \quad (32)$$

The Cahn-Hilliard-Cook theory [37,38] describes small deviations from equilibrium (early stage of spinodal decomposition) and can predict decay rates $R(Q)$ of the time dependent structure factor:

$$S_t(Q) = [S_0(Q) - S_\infty(Q)]\exp[-2R(Q)t] + S_\infty(Q). \quad (33)$$

Here, $S_0(Q)$ and $S_\infty(Q)$ are the initial and final (Virtual) values of the structure factor $S_t(Q)$. When the concentration fluctuations are small, $R(Q)$ can be simply expressed in terms of the mobility M, the interfacial free energy coefficient K and the inter-diffusion coefficient D_{int}:

$$R(Q) = Q^2 D_{int} - 2Q^4 MK. \quad (34)$$

These temperature jump experiments [35] are actually a means to measure D_{int}. Two main theories describe the molecular weight dependence of D_{int}:

a "slow mode" theory [39,40] based on the incompressibility assumption and a "fast mode" theory [41] assuming vacancies present in the relaxing blend. The fast mode theory predicts an additive superposition of the mobilities of each component while the slow mode theory predicts an additivity law for the inverse of the mobilities. This is a new area of research (with ongoing controversies) where quasielastic scattering methods are the main research tools.

2.3 Tunneling Spectroscopy

2.3.1 Basic Theory Perhaps the phenomena most studied using cold neutron backscattering is the rotational tunneling of small molecules and polyatomic ions in solids. In order to understand the origin of this effect consider a molecule in an m-fold potential $V_m(\theta)$ given by

$$V_m(\theta)=\frac{V_0}{2}[1-\cos(m\theta)], \tag{35}$$

where V_0 is the height of the barrier and θ is the rotational angle. The Schrödinger equation is then given by

$$[-B\frac{\partial^2}{\partial\theta^2}+V_m(\theta)]\,\psi_n=E_n\psi_n \tag{36}$$

where $B=\hbar/2I$ (I is the moment of inertia), ψ_n is the wavefunction, and E_n are the energy levels. Figure 15 shows the energy levels which are solutions to this equation as a function of the barrier height V_0 assuming a threefold potential and that the rotating species is a methyl (CH_3) group. Here the solid lines represent singly degenerate levels having A symmetry while the dashed lines correspond to doubly degenerate solutions of E symmetry. Basically there are three regimes. The first is where the barrier is zero which corresponds to free quantum rotors characterized by doubly degenerate levels having energies $E_j \propto j^2$ where j is the rotational quantum number. The second is the limit of large barriers where the molecule or ion undergoes harmonic librations which are characterized by triply degenerate levels with $E_n \propto (n+1/2)$. Here n is the librational quantum number. Perhaps the most interesting region is that between these two extremes which is characterized by the tunnel splitting of the librational ground state and of the excited states resulting from the overlap of the wavefunctions shown schematically in Fig. 16. This splitting is quite sensitive to V_0 since the overlap of the wavefunctions depends exponentially on the barrier. This approximate exponential dependence of the ground state tunnel splitting is shown for both CH_3 and CD_3 in Fig. 17. Thus, tunneling spectroscopy is capable of yielding extremely detailed information on interatomic potentials in solids.

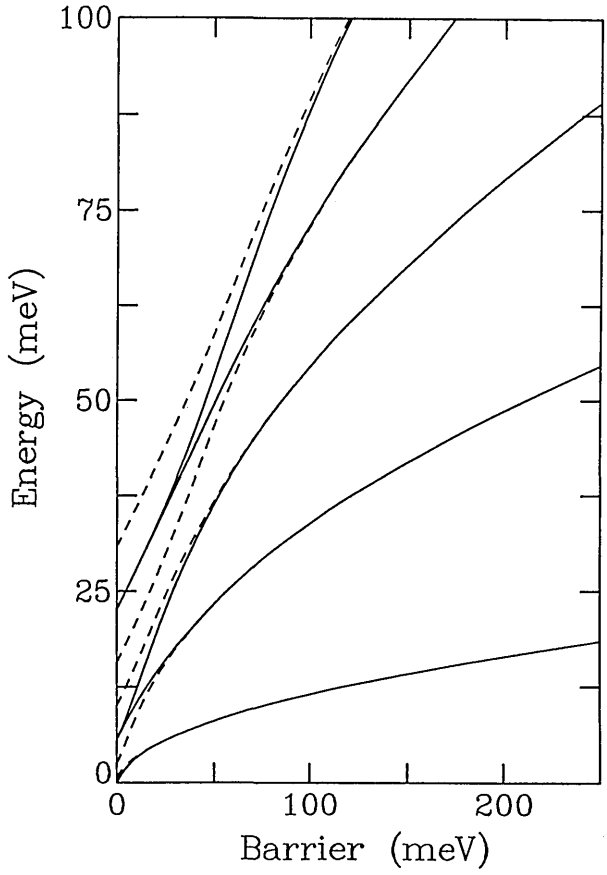

Fig. 15. Energy levels as a function of θ the barrier for methyl groups in a threefold cosine potential. The dashed lines represent singly degenerate states (A symmetry) while the solid lines are doubly degenerate states (E symmetry).

2.3.2 Applications *Nitromethane*. One of the most interesting applications of tunneling spectroscopy is the determination of the rotational potential felt by the methyl group in solid nitromethane (CH_3NO_2). Nitromethane is an ideal candidate for such studies for several reasons. First the internal barrier to rotation is very small. Thus in the solid phase, intermolecular interactions will dominate the rotational potential. In addition, the molecule is a simple one and will display only one-dimensional rotation. Finally, diffraction studies have shown that the space group of the crystalline material is $P2_12_12_1$ which has only one molecule in the asymmetric unit [42]. Therefore, all methyl groups have the same environment and there is only one rotational potential to be determined. Diffraction studies have also demonstrated that no phase transitions occur between 4.2 K and the melting point of 244.7 K [42].

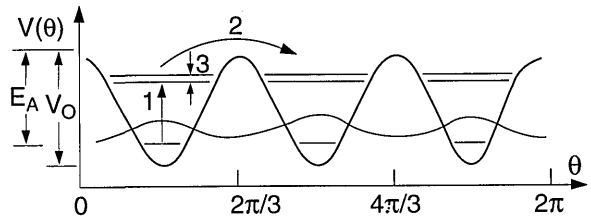

Fig. 16. Schematic diagram of the energy levels in a threefold cosine potential. V_0 is the barrier and E_A is the classical activation energy. Also shown are schematic wavefunctions in the ground state and transitions from the first excited state.

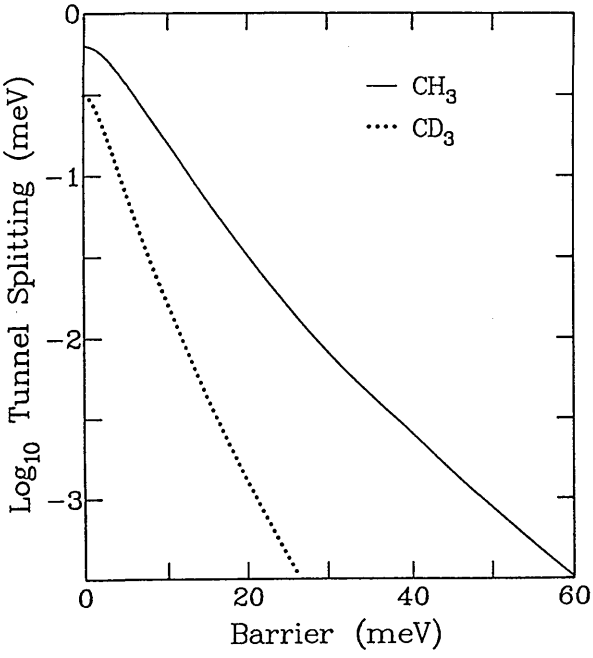

Fig. 17. Semilogarithmic plot of the ground state tunnel splitting of a methyl group in a threefold cosine potential versus the barrier to rotation. The solid line is for a hydrogenated methyl group while the dotted line is for a deuterated one.

The inelastic neutron scattering measurements of the transitions between the ground state and the first excited state obtained by Trevino [43] at 4.2 K are shown for both CH_3NO_2 and CD_3NO_2 in Fig. 18. From these spectra and from the temperature dependence of these spectra, the transition to the first excited state could be assigned to the peaks at 6.7 and 5.3 meV for the hydrogenated and the deuterated compounds respectively. Note that these values do not simply vary as $1/\sqrt{m}$ which indicates that the potential is quite anharmonic. Further measurements also revealed a transition to the second excited state at 17.5 meV for CH_3NO_2 and 10.6 for CD_3NO_2. The most important results for the characterization of the potential are the measurements of the ground state tunnel splittings for both

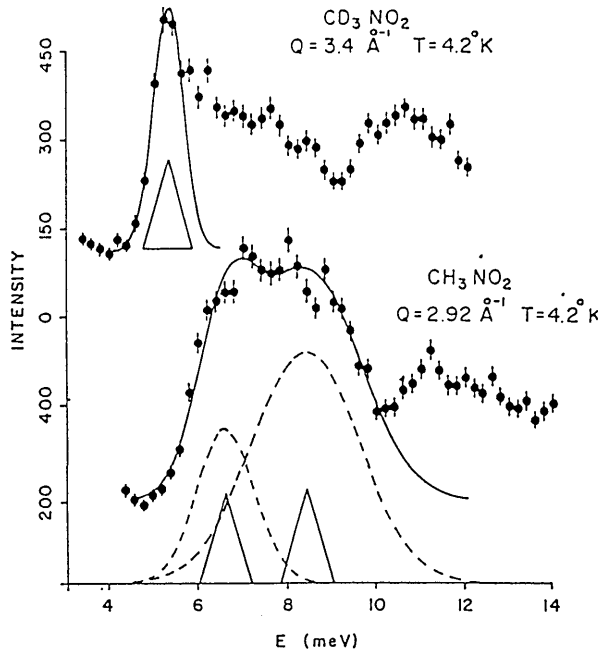

Fig. 18. Inelastic neutron scattering spectra showing the transition from the ground state to the first excited state in CH_3NO_2 (6.7 meV) and CD_3NO_2 (5.3 meV) [43].

samples performed by Trevino and co-workers [44,45] which are shown in Fig. 19. Here one observes clear transitions at 35 and 1.7 μeV for the hydrogenated and deuterated systems, respectively. Taken together these spectroscopic results are inconsistent with a simple threefold potential. However, it was shown by Cavagnat et al. [46] that a potential of the form

$$V(\theta)=V_3[1-\cos(3\theta)]+V_6[1-\cos(6\theta+\delta)] \quad (37)$$

would completely describe all of the spectroscopic results when $V_3=25.5$ meV, $V_6=-15.5$ meV and $\delta=30°$. This potential is shown in Fig. 20 and the calculated energy levels are given in Table 1. In addition, these authors showed that a potential of this form could be obtained by using a simple Lennard-Jones model to describe the interactions between the methyl hydrogens and the surrounding lattice fixed. These calculations indicated that the origin of the sixfold term in the potential is the repulsive H-O interaction and the asymmetric location of the sixfold term with respect to the threefold term is due to the asymmetric distribution of the oxygen atoms with respect to the equilibrium distribution of the methyl groups.

Recently however, Rice and Trevino [47] have pointed out that the potential produced by this H-O interaction does not reproduce the equilibrium orientation of the methyl group. Guided by the

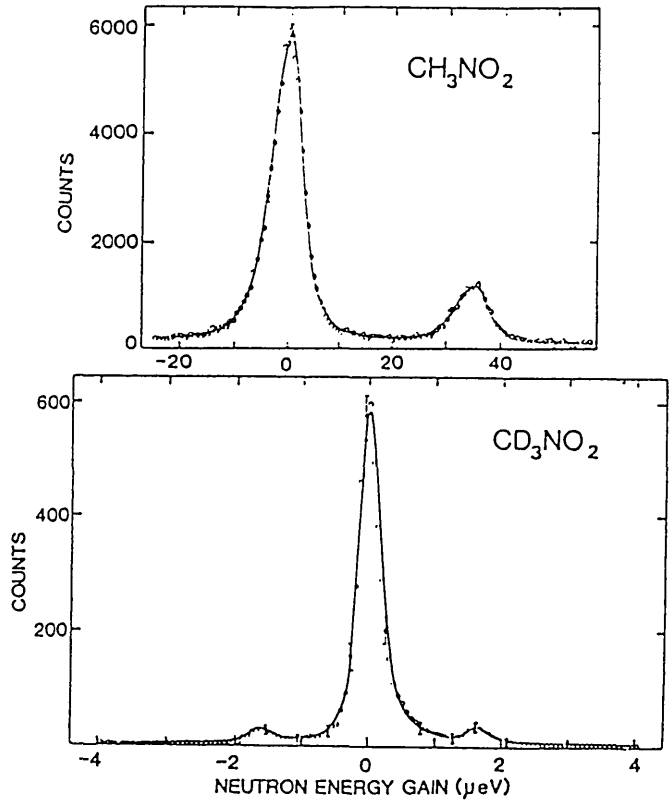

Fig. 19. Measurements of the tunnel splitting for CH_3NO_2 and CD_3NO_2. [45].

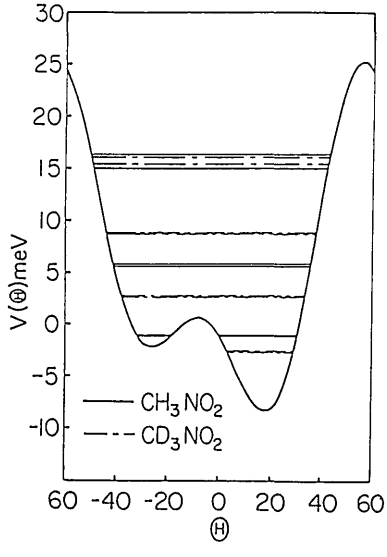

Fig. 20. Potential determined by Cavagnat et al. [46] which is consistent with all of the spectroscopic data. The solid lines are the energy levels for CH_3NO_2.

maximum entropy method they were able to show that by including a small additional wiggle on the Lennard-Jones (Fig. 21) potential all aspects of both the spectroscopy and the structure, could be reproduced. Thus, through the use of a combination of thermal neutron spectroscopy and diffraction and cold-neutron spectroscopy a detailed description of the H-O interaction in nitromethane has been determined.

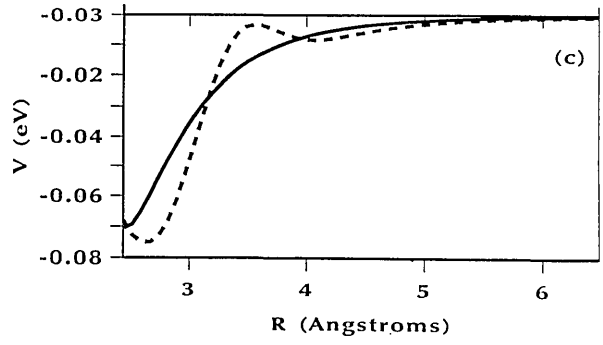

Fig. 21. Lennard-Jones H-O potential used by Cavagnat et al. [47] compared to the Gaussian-corrected Lennard-Jones potential obtained by Rice and Trevino which reproduces both the equilibrium orientation of the methyl group and the spectroscopy results.

Table 1. Characteristics of the backscattering spectrometer being designed for installation in the CNRF

Energy resolution	~0.75 μeV
Maximum energy range	~100 μeV
Neutron energy	2.08 meV
Q-Range	0.1-1.8 $Å^{-1}$
Flux on the sample	~10^5 neutrons/cm^2 s
Maximum sample size	3×3 cm^2
Sample-Monochromator distance	~2 m
Sample-Analyzer distance	~2 m

Methyl Iodide. The pressure dependence of the tunneling transitions in CH_3I is an excellent demonstration of the extreme sensitivity of these excitations to the rotational potential. Like nitromethane, methyl iodide has only one solid phase with only one molecule in the asymmetric unit cell. Therefore, all methyl groups feel the same potential and only one tunneling line will be observed. The spectra obtained using the backscattering technique are shown for several different pressures in Fig. 22a [48,49]. Note that the peaks decrease in energy as the pressure increases indicating an increase in the potential barrier. Fig. 22b shows that the ground state tunnel splitting depends exponentially on the pressure. This is to be contrasted with the results obtained for the energy of the transition to the first excited state shown in Fig. 23. The pressure dependence of this transition is linear and rather weak at that. Prager and coworkers [48,49] also showed that these spectra could be described by a potential of the form

$$V(\theta)=\frac{1}{2}V_3(1+\cos 3\theta)+\frac{1}{2}V_6(1+\cos 6\theta), \quad (38)$$

and that the threefold term accounts for ~92 percent of the total barrier, $V_B=V_3+V_6$. It is worth noting that the value of V_B determined from these measurements increases by <20 percent from ambient pressure to 3 kbar while the tunnel splitting decreases by more than a factor of 2.5 clearly demonstrating the extreme sensitivity of this technique to details of the rotational potential.

3. CNRF Instruments

3.1 NIST Backscattering Spectrometer

The cold neutron backscattering spectrometer (CNBS) which will be located in the CNRF is shown schematically in Fig. 24, (also see Table 1). The guide supplying the neutrons will have a cross sectional area of 6×15 cm^2 and will have

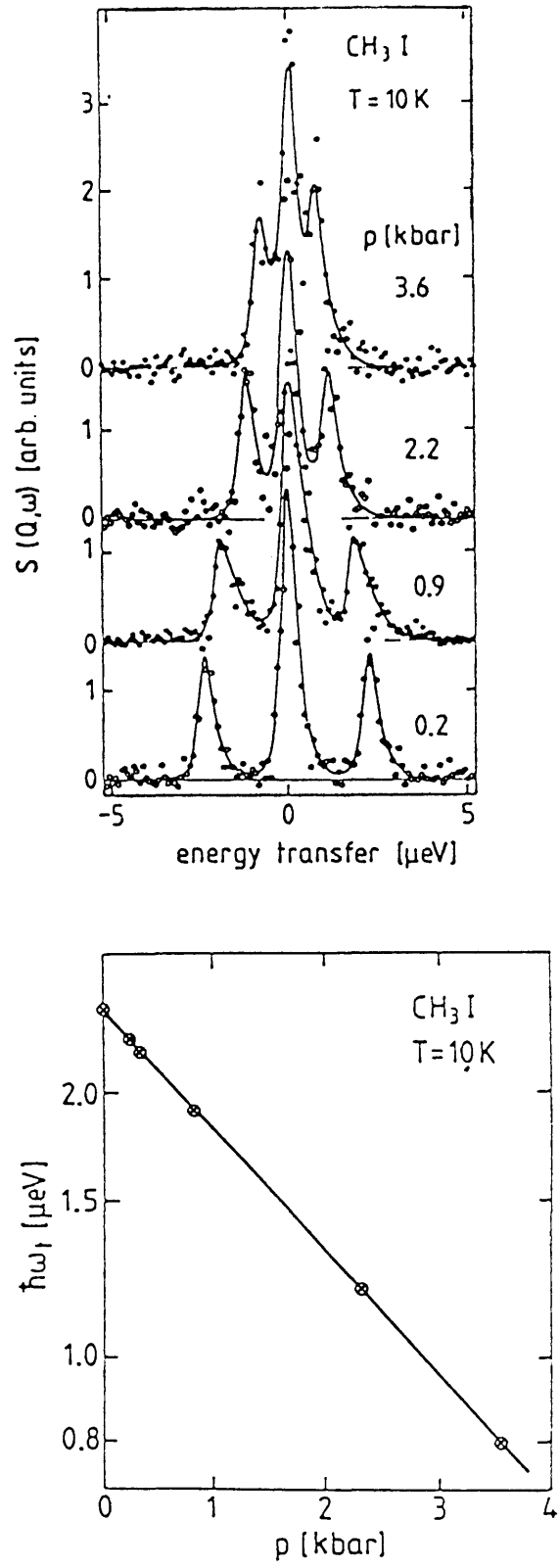

Fig. 22. (a) Tunneling spectra in CH_3I as a function of pressure. (b) Semilogarithmic plot of the tunneling energy as a function of pressure [49].

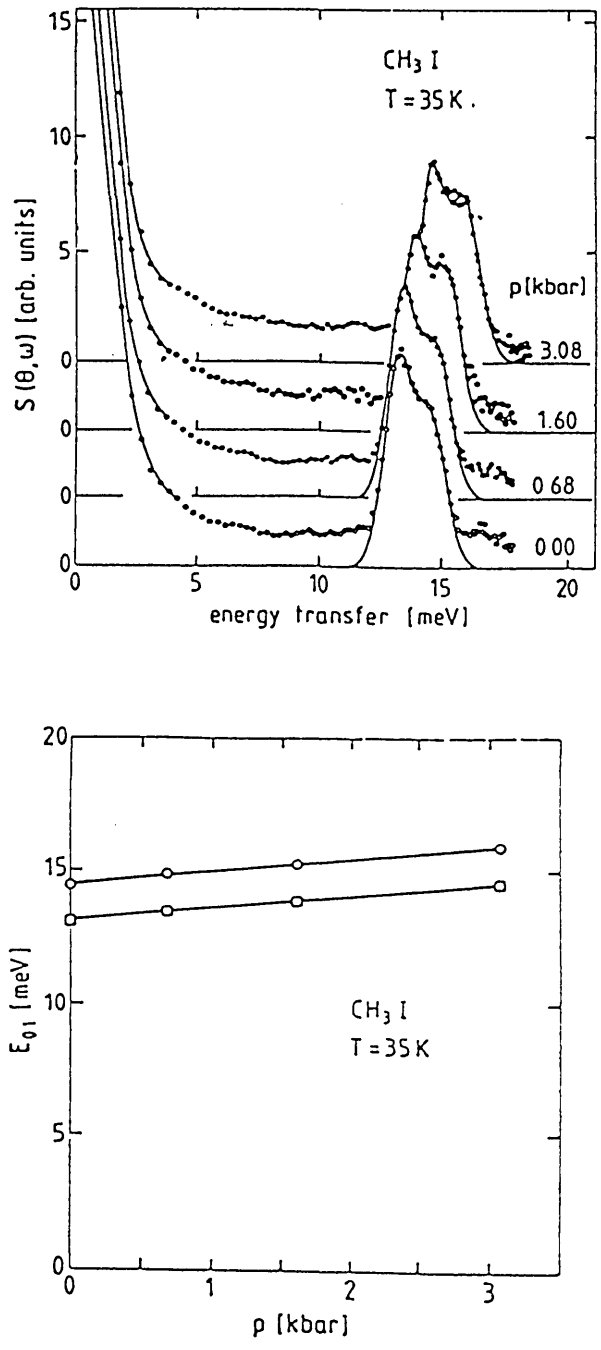

Fig. 23. (a) Inelastic neutron scattering spectra of the transition from the ground state to the first excited state as a function of pressure. (b) Energy of the transition from the ground state to the first torsional level as function of pressure [49].

supermirror coatings on the tops and bottoms while the sides will be coated with ^{58}Ni. The principal design goal has been to maximize the intensity of the instrument while maintaining an energy resolution of <1 μeV. Thus the CNBS will have an energy resolution more than 10 times better than that of any instrument which currently exists in the United States. The first element of the instrument will be a wavelength selection device, the purpose of which is to suppress the background. This will consist of a Be filter, a Bi filter, possibly a velocity selector similar to that used on the small angle scattering and possibly a chopper with a duty cycle of about 1/2 to pulse the beam so that there are no neutrons striking the phase space chopper (which will be described in detail below) when neutrons are being counted in the detector.

The remaining neutrons will then pass through a converging supermirror guide which will compress the beam cross section from 6×15 cm^2 to 3×3 cm^2. It is not presently possible to quantify the length or the angle of convergence of the guide because of uncertainties in supermirror development; however it is hoped that an increase in flux of at least a factor of three will be possible. The neutrons will then impinge on a phase space transformer [50]. This can result in a substantial increase in neutron flux at the sample position because there is typically a substantial mismatch of the angular resolution of the primary and secondary sides of cold neutron backscattering instruments. This occurs because the divergence of the incident beam is limited by the neutron guide on which the instrument is installed, while the angular resolution of the secondary spectrometer is quite low due to the large area analyzing crystals and the detector geometry. Therefore it is possible to increase the flux at the sample position without degrading the energy resolution by increasing the angular divergence of the incident beam. This will be done to some extent through the use of the converging supermirror guide. However, it seems impossible to match the Q resolution of the primary spectrometer to that of the secondary spectrometer with current supermirror technology. To overcome this difficulty Schelten and Alefeld [50] have proposed a neutron phase space transformation which uses moving mosaic crystals to change a well-collimated, white neutron beam into a divergent, nearly monochromatic one. Physically, this occurs because the slower moving neutrons are diffracted at higher angles and therefore, get a "push" from the moving crystal, while the Bragg condition is satisfied at smaller angles for the faster neutrons causing diffraction to occur from crystallites moving away from the incident neutrons thereby reducing their speed.

We have performed Monte Carlo simulations of this device in order to determine the gain expected for parameters relevant to the CNBS at NIST. The beam which emerges from the converging

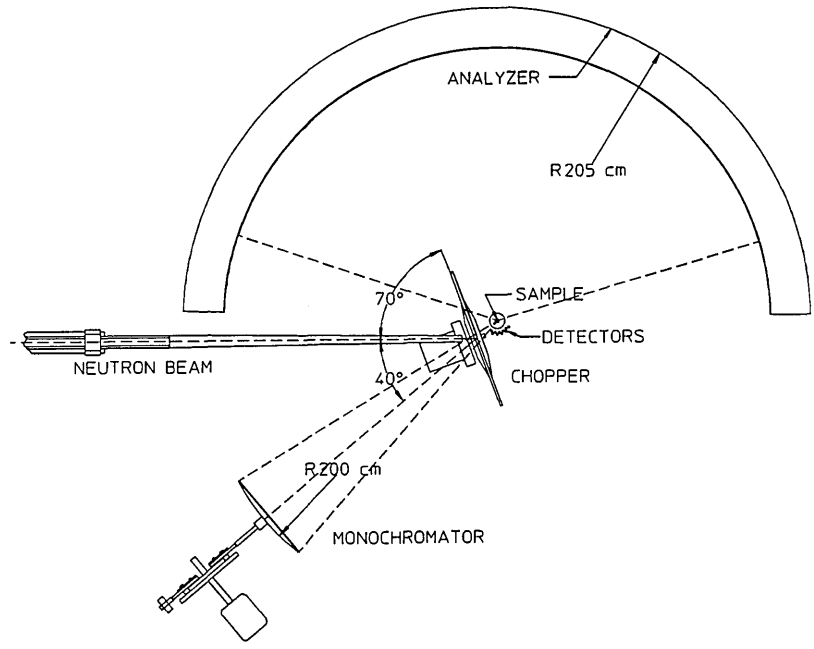

Fig. 24. Schematic diagram of the CNRF backscattering spectrometer.

supermirror guide will have a divergence η approximately twice the critical angle of Ni in the horizontal plane ($\eta_h = 2\theta_c$). For the purposes of this simulation, the phase space crystal was chosen to be pyrolytic graphite ($d = 3.354$ Å and $\theta_0 = 69.181°$) with a thickness of 5 mm. The incident distribution of neutrons was taken to be a 65 K Maxwell-Boltzmann distribution (in accord with measurements of the flux from the cold source) truncated at 4 Å to simulate a Be filter in the incident beam and at 10 Å because wavelengths longer than this have essentially no probability of being diffracted by the moving crystal. This distribution was then multiplied by the square of the incident wavelength in order to account for the fact that θ_c is proportional to the wavelength. The horizontal and vertical mosaics and the velocity of the graphite crystals were included as input parameters. The reflectivity of graphite was accounted for with the Bacon-Lowde equation for diffraction from ideally imperfect crystals [51]. This will overestimate the reflectivity of the deflector crystal resulting in the simulated gains being somewhat larger than what one would actually observe. (Note that the reflectivity is a function of the crystal speed. This has been included.) All of these simulations have been performed using the assumption that Si (111) crystals will be used as the monochromator ($\lambda \approx 6.27$ Å).

Two-dimensional projections of simulated Bragg reflections from a crystal having an isotropic 10° mosaic are shown in Fig. 25 for three different crystal speeds. Here the incident and final k_x and k_y values of the diffracted neutrons are represented by individual dots and the reference values are indicated by the solid lines. Two effects are evident. The first is that the phase space volume increases as the crystal velocity increases. This is because the Bragg reflection takes place at a lower angle in the Doppler frame. The second effect is that the diffracted beam tilts in phase space as the crystal velocity is changed. This tilt can be optimized so that the maximum number of neutrons have the correct energy to be backscattered from a Si (111) crystal. Note that this does not violate Liouville's theorem because the orientation, not the volume, of the final phase space element has been changed.

The most important information from the standpoint of increasing the flux of backscattering instruments is displayed in Fig. 26. Here the peak intensity (relative to that obtained for a crystal velocity of zero) is shown as a function of speed for mosaics of 1°, 3°, 5°, 10°, and 20°. For mosaics of 3° or larger, the relative intensity increases from

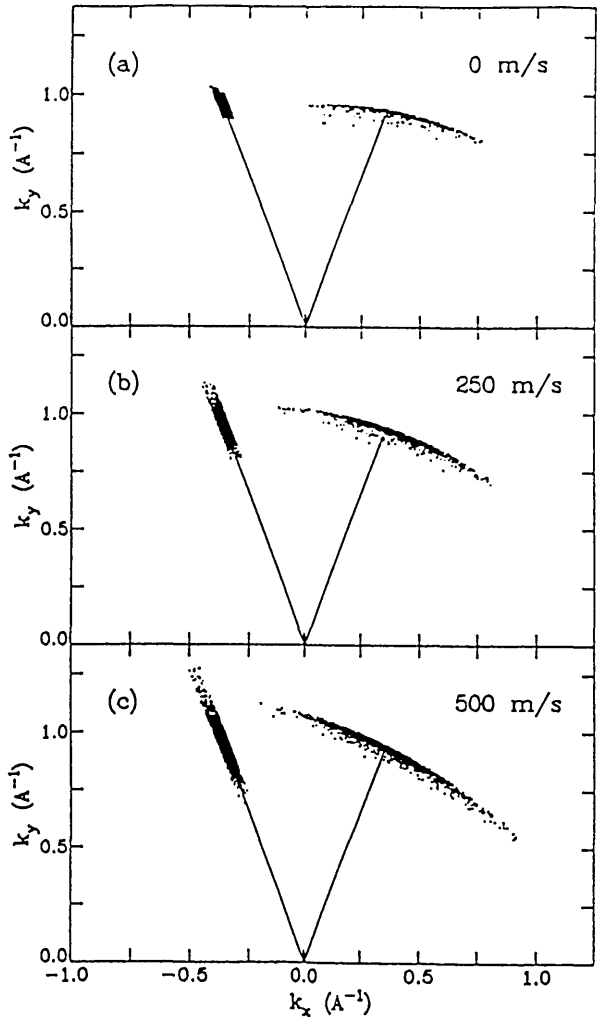

Fig. 25. (a) Projection of a 3-d simulation of Bragg diffraction from a stationary crystal with a mosaic of 10°. The dots represent the initial and final wave vectors of the diffracted neutrons. (b) Same view for a crystal speed of 250 m/s. Note that the initial phase space volume has expanded and the final volume has been "tilted" compared to the results obtained for the stationary crystal. (c) Crystal speed = 500 m/s.

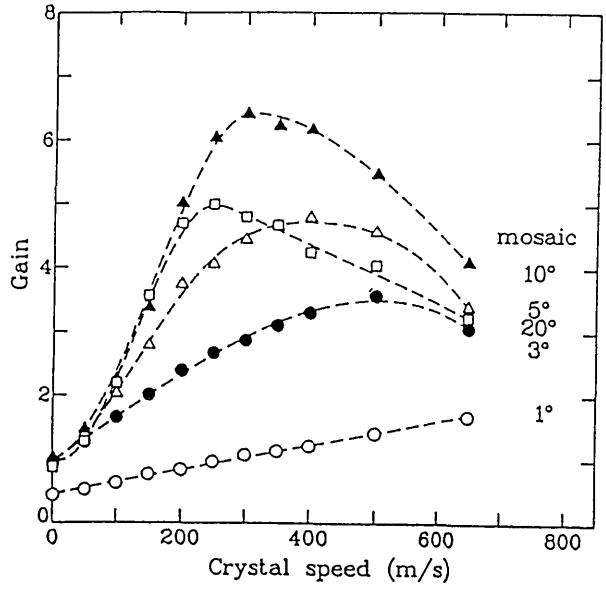

Fig. 26. Peak intensity relative to that obtained for a stationary crystal. For a mosaic of 10°, the phase space transform leads to a gain of 6 for a crystal speed of 300 m/s. The dashed lines are guides to the eye.

about 1 to a broad maximum, before decreasing again. For the parameters chosen here, the maximum gain is about 6 which occurs for crystals with a 10° mosaic moving at about 300 m/s. The results for a 20° crystal show a smaller gain due to the decrease in the reflectivity. The results for a crystal having a mosaic of 1° appear somewhat unique. Here the intensity increases linearly with the crystal speed and has a relative value of only about 1/2 for a speed of 0. This is because a 1° mosaic is too small when compared to the divergence of the incident beam.

After deflecting from the phase space transformer, the neutrons will travel approximately 2 m to the focussing monochromator crystals which will be mounted on a Doppler drive. The Doppler motion is necessary to vary the energy of the neutrons which impinge on the sample. The total range of energies available is determined by the maximum velocity of the Doppler drive. The NIST instrument will have a variable energy range (up to a maximum of ~100 μeV). In order to obtain the maximum flux, the neutrons will be focussed by the monochromator onto the sample. However, Fig. 24 shows that the sample is slightly displaced from the phase space transformer. Thus this results in a small deviation of the backscattering condition. To match this small worsening of the resolution, the monochromator will not be perfect Si, but possibly boron-doped Si. This will result in an increased value of $\Delta d/d$ (see Sec. 2) and therefore increased intensity. A similar result could be achieved by bowing the individual Si crystals, however this results in a more Lorentzian resolution function while the doped crystals result in a more Gaussian lineshape [52]. Note that the level of boron in the sample would not result in significant loss of intensity due to absorption. A $Ge_{0.1}$ $Si_{0.9}$ monochromator which displaces the elastic peak by ~15 μeV will also be available.

After reflecting from the monochromator, the neutrons will pass back through the phase space

transformer. This is possible because only half of the chopper is covered with graphite while the other half is transparent to neutrons. Furthermore, the frequency of the chopper is chosen so that time required for the neutrons to travel from the transformer to the monochromator and return is the same as that for the crystals to move out of the beam.

The neutrons are then scattered from the sample to the large (~ 9 m^2) bank of boron-doped Si analyzer crystals, which focus the neutrons back to the detectors. The focussing and boron doping will be chosen so that the energy resolution of the secondary spectrometer matches that of the primary spectrometer. The detectors are electronically gated so that they are off when neutrons are striking the sample thereby avoiding direct scattering of neutrons from the sample to the detector. The energy transfer is ascertained by measuring the time of arrival of the neutrons at the detector. Since the total distance between the monochromator and sample and the energy of the scattered neutrons are known, the initial energy and therefore the energy transferred by the scattering from the sample can be determined.

Because the detectors are near the incident beam, the most important potential problem with this design is background. If this problem cannot be reduced to acceptable levels by reducing the spread in incident energies, thereby limiting the number of neutrons in the incident beam or by improving the shielding of the detectors, the detectors will have to be moved farther from the guide by placing a deflector in the guide. This will reduce the effectiveness of the phase space transformer so this will only be done as a last resort. However, contingency plans are in place for such an eventuality.

3.2 CNRF Spin Echo Spectrometer

The main components of the CNRF-NSE instrument which is still at a preliminary design stage (Fig. 2) are described here. Neutrons are first monochromated using a velocity selector and then polarized using a supermirror polarizer. Polarization in transmission geometry is preferred for collimation reasons (with reflection polarizers the whole instrument has to be able to rotate around the polarizer axis) although the transmission geometry is hampered by low polarization efficiencies. Next, the neutron spin direction is rotated from the horizontal forward axis to a vertical direction (using a $\pi/2$ flipper) more suitable for use in the first precession coil (solenoid) where the neutron magnetic moment precesses in a vertical plane. After the sample position, another precession coil makes the neutron spin precess in the other direction. In order to flip the spin direction, a π flipper is used between the two coils (just before the sample). Next, another $\pi/2$ flipper is required to rotate the magnetic moment from the radial direction to an axial one before reaching a spin analyzer (array of supermirrors). Finally, neutrons are detected in a position sensitive area detector.

In order for the NSE technique to work, the "field integral" (i.e., the integral of the magnetic field over the neutron path) must remain constant before and after the sample (therefore creating an "echo"). In practice, it is difficult to make exactly identical main coils to be used before and after the sample, so that besides the main coils, other smaller "correcting" coils are also used. Correction coils are added before the sample to optimize the echo and around the sample to correct for the earth magnetic field. No steel or magnetic materials can be used in making the coils or close to the instrument. Moreover, because very stable DC current supplies are required, current stabilities of the order of $dI/I \sim 10^{-5}$ have to be achieved.

The CNRF-NSE spectrometer is in the preliminary design stage; detailed designs are planned to start soon.

4. Summary

We have presented the operating principles of two ultrahigh energy resolution neutron scattering spectrometers, the backscattering spectrometer and the spin echo spectrometer and have described types of measurements which can be done with these instruments at the Cold Neutron Research Facility at NIST. We have also discussed the basic design of the cold neutron backscattering spectrometer to be built in the CNRF. This information will assist researchers who are considering ultrahigh energy resolution neutron scattering experiments at NIST.

5. References

[1] G. E. Bacon, Neutron Diffraction, Clarendon, Oxford (1975).
[2] S. W. Lovesey, Theory of Neutron Scattering from Condensed Matter, Oxford University Press, Oxford (1984).
[3] G. L. Squires, Introduction to the Theory of Thermal Neutron Scattering, Cambridge University Press, Cambridge (1978).

[4] K. Sköld and D. L. Price (Editors), Neutron Scattering, Methods of Experimental Physics Vol. 23, Academic Press, Orlando (1986).
[5] M. Bée, Quasielastic Neutron Scattering, Adam-Hilger, Bristol (1988).
[6] N. F. Berk, J. Res. Natl. Inst. Stand. Technol. 98, 000 (1993).
[7] M. Birr, A. Heidemann, and B. Alefeld, Nucl. Instr. Methods. **95**, 435 (1971).
[8] F. Mezei, Z. Phys. **255**, 146 (1972).
[9] S. F. Trevino, J. Res. Natl. Inst. Stand. Technol. 98, 000 (1993).
[10] P. A. Dagleish, J. B. Hayter, and F. Mezei, in Proceedings of the Workshop on Neutron Spin Echo, ILL-Grenoble (1978).
[11] R. J. Papoular, R. Millet, L. Rosta, and F. Mezei, in Proceedings of the Workshop on Neutron Physics, KFKI-Budapest (1986).
[12] C. T. Chudley and R. J. Elliott, Proc. Phys. Soc. **77**, 353 (1960).
[13] B. Ewen, Pure Appl. Chem. **56**, 1407 (1984).
[14] J. S. Higgins, Physica B & C **136**, 201 (1986).
[15] P. G. de Gennes, Physics **3**, 37 (1967).
[16] C. C. Han and A. Z. Akcasu, Polymer **22**, 1165 (1981).
[17] H. Zabel and S. A. Solin (Editors), Graphite Intercalation Compounds I, Springer-Verlag, Berlin (1990).
[18] A. Magerl, H. Zabel, and I. S. Anderson, Phys. Rev. Lett. **55**, 222 (1985).
[19] W. Petry, T. Flottman, A. Heiming, J. Trampeneau, M. Alba, and G. Vogl, Phys. Rev. Lett. **61**, 722 (1988).
[20] G. Vogl, W. Petry, T. Flottman, and A. Heiming, Phys. Rev. B **39**, 5025 (1989).
[21] F. Fujara, W. Petry, W. Schnauss, and H. Sillescu, J. Chem. Phys. **89**, 1801 (1988).
[22] A. Z. Akcasu and H. Gurol, J. Polym. Sci., Polym. Phys. Ed. **14**, 1 (1976).
[23] L. K. Nicholson, J. S. Higgins, and J. B. Hayter, Macromolecules **14**, 836 (1981).
[24] B. Ewen, D. Richter, J. B. Hayter, and B. Lehner, J. Polym. Sci., Polym. Phys. Ed. **20**, 233 (1982).
[25] P. E. Rouse, J. Chem. Phys. **21**, 1272 (1953).
[26] M. Daoud, These de Doctorat, Paris IV (1977).
[27] A. Z. Akcasu, B. Hammouda, T. P. Lodge, and C. C. Han, Macromolecules **17**, 759 (1984).
[28] R. Borsali, H. Benoit, J. F. Legrand, M. Duval, C. Picot, M. Benmouna, and B. Farago, Macromolecules **22**, 4119 (1989).
[29] J. S. Higgins, L. K. Nicholson, and J. B. Hayter, Polym. Prepr. (ACS) **22**, 86 (1981).
[30] P. G. de Gennes, Scaling Concepts in Polymer Physics, Cornell University Press, New York (1979).
[31] M. Doi and S. F. Edwards, The Theory of Polymer Dynamics, (Clarendon Press, Oxford, 1986).
[32] G. Jannink and P. G. deGennes, J. Chem. Phys. **48**, 2260 (1968).
[33] A. Z. Akcasu, M. Benmouna, and H. Benoit, Polymer **27**, 1935 (1987).
[34] A. Z. Akcasu, B. Hammouda, W. H. Stockmayer, and G. Tanaka, J. Chem. Phys. **85**, 4734 (1986).
[35] T. Sato and C. C. Han, J. Chem. Phys. **88**, 2057 (1988).
[36] R. J. Composto, E. J. Kramer, and D. M. White, Nature **328**, 234 (1987).
[37] J. W. Cahn and J. E. Hilliard, J. Chem. Phys. **28**, 258 (1958).
[38] H. E. Cook, Acta Metall. **18**, 297 (1970).
[39] F. Brochard, J. Jouffroy, and P. Levinson, Macromolecules **16**, 1638 (1983).
[40] K. Binder, J. Chem. Phys. **79**, 6387 (1983).
[41] E. J. Dramer, P. Green, and C. J. Palmstrom, Polymer **25**, 473 (1984).
[42] S. F. Trevino, E. Prince, and C. R. Hubbard, J. Chem. Phys. **73**, 2996 (1980).
[43] S. F. Trevino and W. H. Rymes J. Chem. Phys. **73**, 3001 (1980).
[44] S. F. Trevino, J. Chem. Phys. 71, 1973 (1979).
[45] B. Alefeld, I. S. Anderson, A. Heidemann, A. Magerl, and S. F. Trevino, J. Chem. Phys. **76**, 2758 (1982).
[46] D. Cavagnat, A. Magerl, C. Vettier, I. S. Anderson, and S. F. Trevino, Phys. Rev. Lett. **54**, 193 (1985).
[47] B. M. Rice and S. F. Trevino, J. Chem. Phys. **94**, 7478 (1991).
[48] M. Prager, J. Stanislawski, and W. Häusler, J. Chem. Phys. **86**, 2563 (1987).
[49] M. Prager, C. Vettier, and S. Mahling-Ennanoui, Z. Phys. B. **75**, 217 (1989).
[50] J. Schelten and B. Alefeld, in Proc. Workshop on Neutron Scattering Instrumentation for SNQ, edited by R. Scherm and H. H. Stiller, report Jül-1954 (1984).
[51] G. E. Bacon and R. D. Lowde, Acta Cryst. **1**, 303 (1984).
[52] A. Magerl, private communication.

About the authors: Dan A. Neumann and Boualem Hammouda are research physicists in the Reactor Radiation Division of the NIST Materials Science and Engineering Laboratory. The National Institute of Standards and Technology is an agency of the Technology Administration, U.S. Department of Commerce.

Volume 98, Number 1, January-February 1993
Journal of Research of the National Institute of Standards and Technology

[J. Res. Natl. Inst. Stand. Technol. 98, 109 (1993)]

Neutron Depth Profiling: Overview and Description of NIST Facilities

Volume 98 Number 1 January-February 1993

R. G. Downing, G. P. Lamaze, and J. K. Langland

National Institute of Standards and Technology, Gaithersburg, MD 20899

and

S. T. Hwang

Korea Research Institute for Standards and Science, Taedok Science Town, Taejon, Korea 305-606

The Cold Neutron Depth Profiling (CNDP) instrument at the NIST Cold Neutron Research Facility (CNRF) is now operational. The neutron beam originates from a 16 L D_2O ice cold source and passes through a filter of 135 mm of single crystal sapphire. The neutron energy spectrum may be described by a 65 K Maxwellian distribution. The sample chamber configuration allows for remote controlled scanning of 150 × 150 mm sample areas including the varying of both sample and detector angle. The improved sensitivity over the current thermal depth profiling instrument has permitted the first nondestructive measurements of ^{17}O profiles. This paper describes the CNDP instrument, illustrates the neutron depth profiling (NDP) technique with examples, and gives a separate bibliography of NDP publications.

Key words: boron; cold neutrons; lithium; NDP; neutron depth profiling; nitrogen; oxygen; silicon; surface analysis.

Accepted: August 18, 1992

1. Introduction

The National Institute of Standards and Technology has operated since 1982 a dedicated NDP facility [1] using thermal neutrons at the NIST reactor. This paper describes applications of the NDP technique, presents a new cold neutron depth profiling (CNDP) instrument located on the CNRF at the NIST reactor, and gives in the Appendix an extensive bibliography of NDP publications as of July 1991.

In 1972 Ziegler et al. [2] first reported the development of a near-surface technique which has come to be known as neutron depth profiling (NDP). NDP is an isotope specific, nondestructive technique for the measurement of concentration versus depth distributions in the near-surface region of solids. This technique uses neutron induced reactions to measure the concentration versus depth profiles of a number of the light elements. NDP allows the first few micrometers of nearly any condensed material to be probed nondestructively. Biersack and coworkers [3,4] at the Institut Laue-Langevin facility in Grenoble subsequently advanced the technique to much of its present capabilities.

Since its introduction, over 100 articles have been published (see Appendix) describing the use of NDP to investigate materials and effects directly relating to materials research. The widespread application of NDP has been limited primarily by the number of intense neutron sources available—nuclear research reactors. Besides the NIST facilities, the United States has four other NDP facilities in use or under development: the University of Michigan Ford Nuclear Reactor [5,6], Texas A&M University [7], University of Texas at Austin [8], and North Carolina State University [9]. This activity,

much of it recent, indicates that NDP has significant potential for materials research, and particularly for semiconductor research.

2. Fundamentals of the Technique

2.1 Physics

Lithium, beryllium, boron, sodium, and a number of other elements, have an isotope that, upon capturing a thermal neutron, undergoes an exoergic charged particle reaction. These reactions produce either a proton or an alpha particle, depending upon the isotope, and a recoiling nucleus. Each emitted particle has a specific kinetic energy defined by the Q-value of the reaction which in turn serves to identify the element. For the case of lithium, the reaction proceeds as

$$^{6}\mathrm{Li} + \mathrm{n} \rightarrow {}^{4}\mathrm{He}(2055\ \mathrm{keV}) + {}^{3}\mathrm{H}(2727\ \mathrm{keV}). \quad (1)$$

Four elements, Li, Be, B, and Na, are particularly well suited for the NDP technique since their neutron cross sections are quite large relative to other particle-producing reactions (see Table 1). In principle, there are essentially no interferences and profiling is permissible for all host materials. In practice, however, background contributions arise from energetic electrons and photons when analyzing materials that contain elements with significant (n, γ) cross sections.

To obtain a depth profile, a well-collimated beam of low energy neutrons ($<10^{-2}$ eV) is used to illuminate a sample volume uniformly. While most of the neutrons pass through the sample without interacting, those sites containing reactive atoms capture neutrons in proportion to the capture cross section of the nuclide and act as an isotropic source of monoenergetic charged particles. The particles travel outward in essentially straight paths and lose energy primarily through numerous interactions with the electrons of the matrix. The difference between the well-known initial energy of the particle and its residual energy upon emerging from the surface of the sample is directly related to the depth of origin for the particles (i.e., the site of the parent atom). The target chamber is kept under vacuum so that no additional energy is lost from the emerging particle as it travels between the sample surface and the detector. Because the low-energy neutron carries very little momentum, the reaction center of mass is coincident with the site of the parent atom.

Sample damage due to temperature rise is minimal during the analysis. In the worst case, if an entire 10^{9} n/cm^{2} s beam is stopped by boron reactions in a sample, the temperature would reach a steady-state value of only 0.7 K greater than ambient. This calculation assumes there is no heat removal other than radiative. Such an extreme example would contain the equivalent of a few millimeters thickness of pure ^{10}B. The amount of

Table 1. Summary of the NDP reaction characteristics and example detection sensitivities for the 20 MW NIST reactor

Elem.	Reaction	%Abundance or (atoms/mCi)[a]	Energy of emitted particles (keV)		Cross section (barns)	Detection limit (atoms/cm^2)[b]
He	^{3}He(n,p)^{3}H	0.00014	572	191	5333	1.5×10^{12}
Li	^{6}Li(n,α)^{3}H	7.5	2055	2727	940	9.0×10^{12}
Be[a]	^{7}Be(n,p)^{7}Li	(2.5×10^{14})	1438	207	48000	1.7×10^{11}
B	^{10}B(n,α)^{7}Li	19.9	1472	840	3837	2.1×10^{12}
N	^{14}N(n,p)^{14}C	99.6	584	42	1.83	4.5×10^{15}
O	^{17}O(n,α)^{14}C	0.038	1413	404	0.24	3.5×10^{16}
Na[a]	^{22}Na(n,p)^{22}Ne	(4.4×10^{15})	2247	103	31000	2.3×10^{11}
S	^{33}S(n,α)^{30}Si	0.75	3081	411	0.19	6.0×10^{16}
Cl	^{35}Cl(n,p)^{35}S	75.8	598	17	0.49	1.7×10^{16}
K	^{40}K(n,p)^{40}Ar	0.012	2231	56	4.4	1.9×10^{15}
Ni[a]	^{59}Ni(n,α)^{56}Fe	(1.3×10^{20})	4757	340	12.3	7.0×10^{14}

[a]Radioactive species.
[b]Detection limit based on 0.1 cps, 0.013 Sr detector solid angle, and a neutron intensity of 6×10^{9} s^{-1}.

target nuclide consumed during a typical analysis is only a few tens-of-thousands of atoms. Some damage does occur due to knock-on of the outgoing charged particles with the matrix atoms. Here again the damage is small compared to nearly any other "nondestructive" analytical technique.

The depth corresponding to the determined energy loss for the emitted particle is determined by using the characteristic stopping power of the material, as compiled by Ziegler [10] and others [11] or by estimating the stopping power for compounds using Bragg's law [12] (i.e., the linear addition of the stopping powers of individual elemental constituents). The chemical or electrical state of the target atoms has an inconsequential effect on the measured profile in the NDP technique. Only the concentration of the major elements in the material is needed to establish the depth scale through the relationship of stopping power.

Mathematically, the relationship between depth and residual energy can be expressed as

$$x = \int_{E(x)}^{E_0} \mathrm{d}E/S(E), \qquad (2)$$

where x is the path length traveled by the particle through the matrix material, E_0 is the initial energy of the particle, $E(x)$ is the energy of the emerging particle, and $S(E)$ represents the stopping power of the material. Examples of the relationship between x and $E(x)$ are displayed in Fig. 1 for ^{10}B in silicon and ^{22}Na in silicon.

2.2 Elemental Detection Limits

The detection limit of the NDP method is directly proportional to the total neutron fluence and to the cross section of the reaction of interest. In the low-energy region, these cross sections are inversely proportional to the square root of the neutron energy. The lower the neutron energy, the greater the reaction rate. In a moderating medium, such as water, the neutrons, which start out with a few MeV of energy, are slowed down by successive collisions approaching temperature equilibrium with their surroundings. By lowering the temperature of the moderator, the average energy of the neutrons is also lowered (more commonly referred to as neutrons having a longer wavelength). Figure 2 gives the neutron distribution as a function of neutron wavelength for the NIST cold source; a 65 K Maxwellian distribution of neutrons is given for comparison. By integrating a reaction cross section over this distribution, one can obtain a spectrum-weighted average cross section for this neutron beam. The neutron beam is filtered with highest quality single-crystal sapphire so that epithermal neutrons and gamma radiation are preferentially scattered from the beam [13]. Although this filtering further reduces the cold source moderated neutron fluence rate by about 30 percent, there will be less radiation damage induced in sensitive materials such as polymers used in photoresists or ionic conductors. After taking into account the additional effect of the 135 mm of sapphire filter in the beam, the sensitivity of the CNDP instrument is increased by a factor of 1.7 solely from the effect of having lowered the energy of the neutrons from a thermal average distribution.

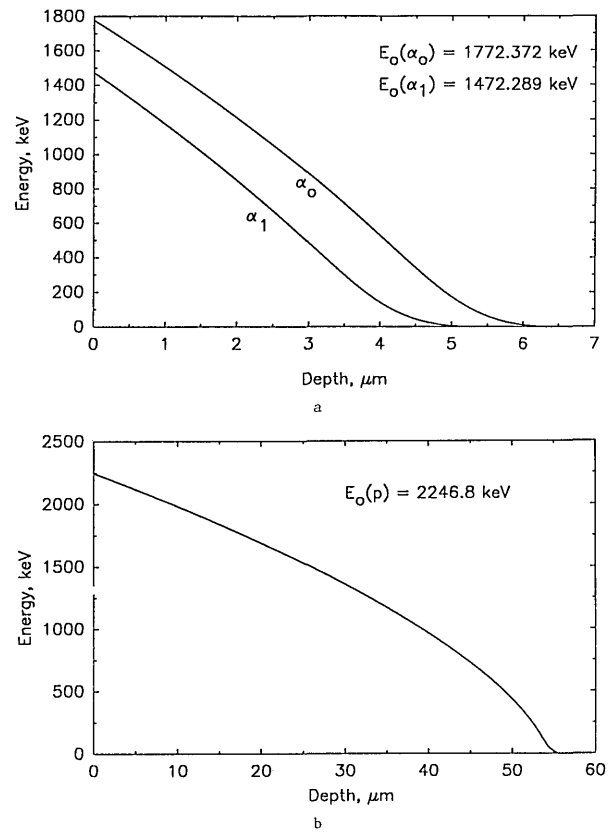

Fig. 1. Plots depicting the relationship between the residual energy of charged particles, and depth of the originating nuclear reaction. Plot (a) gives the residual alpha particle energy versus depth for ^{10}B in silicon, and plot (b) gives the relationship of the residual proton energy versus depth for ^{22}Na in silicon.

The number of charged particle counts collected in a data channel, of energy width $\mathrm{d}E$, is directly proportional to the concentration of target atoms located within that corresponding depth interval. Upon calibrating the facility against an accurate isotopic standard, concentrations can be measured for

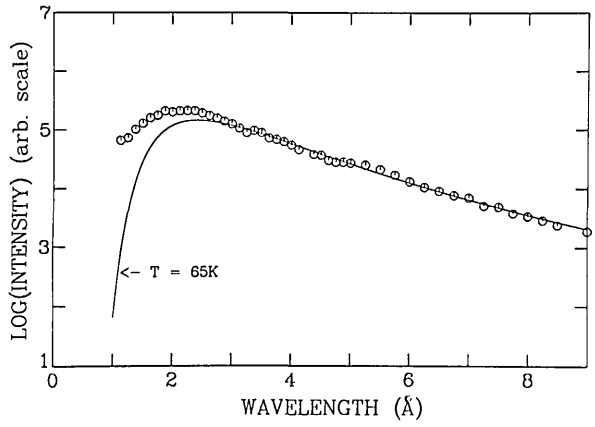

Fig. 2. A corrected wavelength distribution, measured by time-of-flight, for the cold source operating at 30 K with 7.5% H_2O homogeneously mixed in the D_2O. The solid curve is a Maxwellian spectrum for a temperature of 65 K that gave the best fit to the data from 3 to 9 Å.

that isotope (or other similar reactions) in subsequent samples, independent of the matrix, the concentration level, or location (within the depth that induced particles can escape the sample surface and be detected). Table 1 lists several properties for target atoms and the detection limits using the CNDP facility at the NIST reactor. Isotopes with charged particle cross sections of about a barn or greater are given. The conservative detection limits listed were calculated assuming 0.1 cps and a detector acceptance solid angle of 0.1 percent. Assuming a practical profiling depth of 2 μm for the case of boron in silicon, boron concentrations down to the ppm (atom %) level can be accurately measured. The time required for an analysis is a function of the element and the desired accuracy. A boron implant of 1×10^{15} atoms per cm^2 typically takes a few hours to obtain 1 percent precision (counting statistics) at most points along the profile curve. Since the background signal is almost negligible, a sample could be counted for tens of hours to obtain the required definition in the profile shape.

2.3 Reaction Product Energy Spectra

The charged particle energy spectrum is collected using a transmission-type silicon surface barrier detector, electronic amplifiers, an analog-to-digital converter and a multichannel analyzer (see Fig. 3). For the NDP system at NIST, a reference pulse is also fed into the electronics to monitor the stability of the system thus allowing corrections to be made should electronic drift occur during the course of the measurement. Other NDP systems are described more specifically in the references [1,2,4,6,7,14–21]. By using a computer-based data acquisition system, the depth profile can be displayed in real time.

Examples of the detected energy spectra from three boron containing structures are shown in Fig. 4. With boron, 94 percent of the neutron reactions are

$$^{10}B + n \rightarrow {}^4He(1472\ keV) + {}^7Li(840\ keV) + \gamma(478\ keV) \quad (3)$$

and 6 percent of the reactions [22] proceed as

$$^{10}B + n \rightarrow {}^4He(1776\ keV) + {}^7Li(1013\ keV). \quad (4)$$

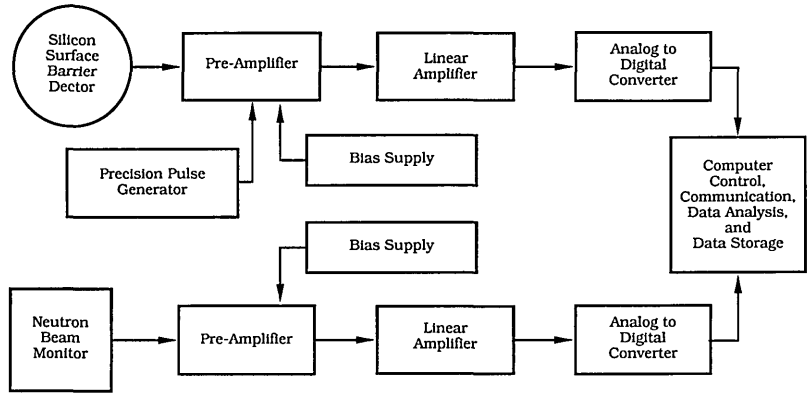

Fig. 3. Basic diagram of the data acquisition, and analysis electronics for either NDP facility. Alterations to the upper half of the scheme are necessary for coincidence detection, and for time of flight detection systems.

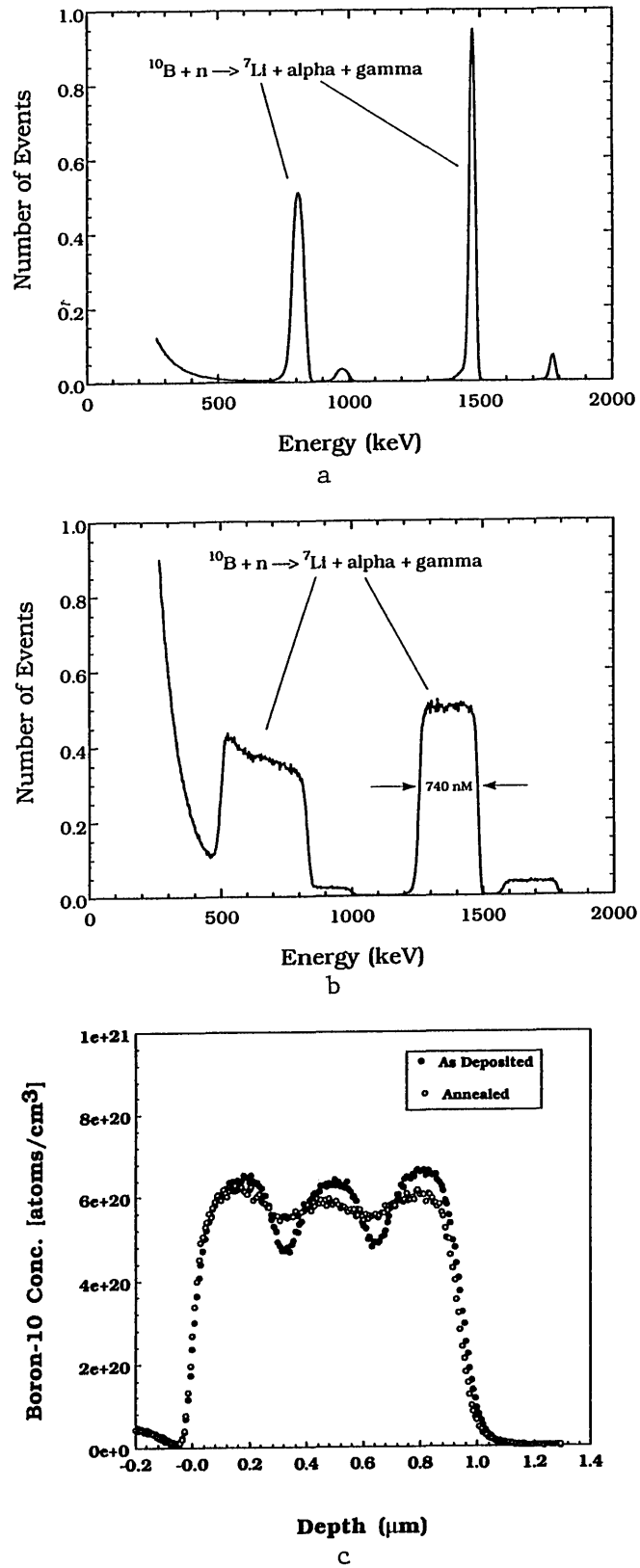

Fig. 4. Energy profiles of particles emitted by the ^{10}B reaction for (a) a 2 nm thick surface deposition, (b) a 740 nm thick borosilicate glass film on Si, and (c) the depth profile using only the 1472 keV alpha particles from a borophosphosilicate glass film, 1.2 μm thick.

Figure 4(a) is the energy spectrum of a 2 nm thick, surface deposit of boron on a nickel substrate. Figure 4(b) shows the energy distribution of particles from a 740 nm thick borosilicate glass (BSG) film on a silicon wafer substrate. Both figures show the fourfold redundancy [see Eqs. (3) and (4)] of depth profiles for a boron containing material. The 1472 keV alpha particle or its 840 keV ^{7}Li recoil particle are typically used for the profile determinations because of their higher intensity, however, the remaining two peaks can serve to confirm the results. Figure 4(c) shows the depth spectrum of the 1472 keV alpha for a borophosphosilicate (BPSG) film with a periodic concentration variation from the surface down to the glass-silicon interface. The total thickness of this film is about 1.2 μm.

2.4 Resolution

The broadening of the signal in Fig. 4(a) is primarily due to the energy resolution of the detector and associated electronics. In addition to the detector and system resolution, other factors that contribute to the depth resolution include: i) small-angle scattering of the charged particles within the sample, ii) energy straggling of the particles, and iii) the nonzero acceptance angle of the detector giving a spread in path lengths for particles from the same depth. These contributions to the resolution are treated by Biersack et al. [23] and by Maki et al. [24]. Item i) above can be seen as a low-energy tail on sharp spectral features appearing some three orders-of-magnitude less in intensity than the main feature.

Each material has a characteristic stopping power and, therefore, the resolution and the depth of profiling will vary in different materials. The lithium particle from the boron reaction has greater charge than its alpha counterpart and loses energy more rapidly allowing greater profile resolution; however, the alpha particles have the greater range and consequently allow deeper profiles to be obtained (typically 1 or 2 μm). The full width at half maximum (FWHM) resolution in the depth profile obtained from the 1472 keV alpha of a boron reaction in silicon is typically a few tens of nanometers. On the other hand, protons from the ^{22}Na(n,p)^{22}Ne reaction give a resolution on the order of a few hundred nanometers, but can be used to profile 30 to 40 μm in depth. Since for thermal or cold neutrons particle emission is isotropic, the detector can be placed at an angle with respect to the normal of the sample surface to view longer particle path lengths from the same sample depth. The depth resolution is improved in this fashion and has been shown to be as well defined as 7 nm (FWHM) for the case of boron in silicon [23,25]. Small concentration variations in the first nanometer of a sample surface can often be identified by comparing differentiated spectra of known homogeneous standards with that of differentiated spectra of unknown samples. Deconvolution algorithms used to unfold the system response function from collected energy spectra [2,24,26–30] have provided improvement in depth resolution by greatly reducing system resolution broadening. With some *a priori* knowledge of the sample, modeling of the spectrum reveals subtle concentration variations.

Improvements to detection limits for NDP require either more intense neutron sources or changes in basic instrumental design. Using larger detectors for greater solid angles are a more efficient use of the existing neutron fluences, however, the energy resolution is degraded. As the energy resolution of charged particle detectors improves there is a corresponding gain in profile resolution. Better algorithms for the deconvolution of system response from the energy spectrum are necessary as well. Fink et al. [16] have described a charged particle energy analyzer for NDP using electromagnetic focusing that should improve the energy resolution, while reducing the photon induced background levels.

Another approach is the use of a coincidence technique [31]. If the sample is thin enough to allow both the light particle and the recoil nucleus to escape from opposing surfaces of the sample, two detectors can be used to detect both particles simultaneously. By requiring a coincidence between the two detectors, background interferences are reduced [32] and the solid angle of collection can be increased by 10 to 100 fold by bringing the detector closer to the sample. The depth resolution is improved because there is no dependency upon solid angle of acceptance to the detector. Mathematically this is made possible by the fact that the sum of the energy loss and the residual energy of the two reaction products must equal the Q-value of the reaction. The major disadvantages are that the sample must be thin enough to permit the escape of both reaction products and that only a few elements are applicable to this method.

Both neutron intensity and gain in spatial resolution will be possible with a neutron focusing device currently being developed at NIST [33]. Long wavelength neutrons are guided to areas of a few mm square providing locally high neutron fluences.

This will permit the development of two- and three-dimensional neutron depth profiling. The use of position sensitive detectors and ion optics can further accelerate progress toward three dimensional nondestructive depth profiling.

3. Applications

The development of the neutron depth profiling technique has been motivated by the importance of light elements in optical, polymer, metal alloy and especially microelectronic materials. Boron is widely used as a p-type dopant in semiconductor device fabrication and in the insulating passivation barriers applied either as an organometallic or a vapor phase deposition of borosilicate glass. NDP has both good sensitivity for boron and good spatial resolution to a depth of a few micrometers. It is used both as a stand alone technique and in a complementary role with a variety of other analytical methods [34–37]. Recently NDP has been used to certify the concentration and confirm the profile of boron in silicon for a NIST Standard Reference Material (SRM 2137) primarily for the use of secondary ion mass spectroscopy (SIMS) calibration.

Applications of NDP are quite diverse as can be seen by the titles of the articles in the appendix. Although an exhaustive discussion of all the uses would be beyond the scope of this paper, a few examples are given to illustrate its strengths.

3.1 Implantation

Ziegler and coworkers [2,18,38,39] introduced NDP by determining the range and shape of boron implantation distributions in doped and intrinsic silicon wafers. With the resultant profiles, they were able to calculate diffusion coefficients for boron in crystalline, amorphous, and arsenic doped silicon. Since little experimental data existed for the case of boron to judge the validity of the current range theories, the shape of the boron profiles from NDP were of great interest. NDP and other techniques have since been able to show that a Pearson IV model rather than a Gaussian profile describes more accurately the implant distribution [24,28,40–42].

In subsequent experiments, Biersack et al. [43] used the boron (n, α) reaction to show the effect of pre- and post-irradiation damage on boron implantation profiles. By post-irradiating a boron implant in silicon with 200 keV H^{2+}, a migration of the boron to the induced damage sites was observed. In the same paper, diffusion and trapping of lithium ions in niobium were reported. Using the lithium (n, α) reaction, irradiation induced crystal defects were mapped through a depth of several micrometers for a variety of sample treatment conditions.

Of significant interest is the fact that determinations by NDP induce negligible damage to most materials. Sample surfaces are neither sputtered, as observed with SIMS, nor is the sample matrix altered. The thermal neutrons carry an insignificant amount of momentum into the material and induced reactions are of such low intensity that radiation damage is usually negligible. This allows precisely the same sample volume to be subjected to different processing conditions and to be examined by NDP at each stage. The sample may thereafter be passed to another analytical method such as SIMS, Rutherford Back Scattering (RBS), Proton Induced X-ray Emission (PIXE), Spreading Resistence Profiling (SRP), or Atomic Emission Spectrometry (AES) to obtain complementary data on the material. Analysis of the same sample by different methods allows extensive experimental testing of possible variability between samples or even across a single sample. As a result, NDP has been used as a reference technique for other methods of analysis [34]. If radioactive nuclides are formed during an analysis, it may not be desirable to place the sample in a sputtering-type instrument, thus avoiding possible contamination of sensitive detectors. This is certainly not the case for silicon wafers and most other electronic materials due to their very small neutron activation cross sections.

Some of the features observed for an NDP profile are illustrated in Fig. 5. Curve 5(a) is an NDP profile for a 70 keV ^{10}B implant in silicon at a total dose of 4×10^{15} atoms per cm^2. To prevent channelling of the boron, the implant was made nominally 7° off normal in silicon cut perpendicular to the $<111>$ surface. Curve 5(b) is the same wafer after being annealed at 1000 °C for 30 min. The diffusion broadening bounded by the surface is clearly apparent. The apparent boron concentration above the surface is an artifact of the detector resolution. Of particular interest is the small peak near the surface. A small unintentional air leak into the nitrogen back-filled annealing furnace allowed a thin film of SiO_2 to grow on the silicon wafer surface. The segregation coefficient of boron between Si and SiO_2 favors movement of the boron in the direction of the SiO_2. Boron, as a consequence, was extracted from the bulk Si wafer into the surface SiO_2. In a similar case Downing et al. [44] have shown that the native oxide (1.0–1.5 nm)

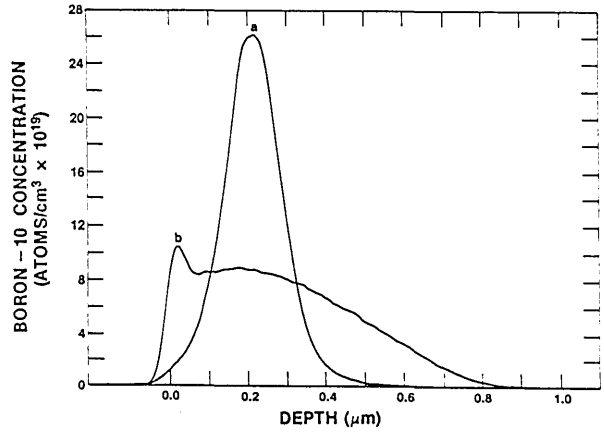

Fig. 5. NDP depth profiles for a 70 keV ^{10}B implant in silicon at a dose of 4×10^{15} atoms per cm^2. Depicted are (a) the as-implanted profile, and (b) after a 30 min anneal at 1000 °C., and indicating air leak during anneal.

that appears on nearly all Si surfaces is contaminated with boron at a level of 10^{12}–10^{13} atoms/cm^2.

Boron profiles by NDP in mercury cadmium telluride, an infrared detector material, have been measured by Ryssel et al. [45], Vodopyanov et al. [46], and Bowman [47]. Cervena et al. [30] have used NDP to study the implantation profiles of ^{10}B in several photoresists used in masking operations and to determine range values for implants in several types of grown or deposited SiO_2 films.

3.2 Interfacial Profiling

Neutron depth profiling is well suited for measurements across interfacial boundaries. Kvitek et al. [27] and others [20,21,28,34] have studied profiles of boron implanted and diffused across the interfacial region of Si/SiO_2. Other NDP experiments [48,49] have been described for interfaces of silicon, silicon dioxide or metal on metal, where diffusion distributions and segregation coefficients were studied.

Knowledge of stopping powers for the major elemental constituents is the primary requirement to establish the depth scale. Figure 6 depicts an NDP profile of boron across an SiO_2 – Si interface. Boron was implanted to a dose of 1×10^{16} atoms per cm^2 at 70 keV into a silicon wafer that had 0.2 μm of thermally grown SiO_2 covering the surface. The ^7Li particle energy spectrum from the $^{10}B(n,\alpha)^7Li$ reaction was used for this profile to increase the depth resolution. Notice the smooth transition of the as-implanted boron concentration across the interfacial region. Although the FWHM depth resolution is on the order of 10–15 nm, it is clear that no discontinuity exists at the interface of the two materials. The same region is shown again after annealing the sample for 30 min at 1000 °C [34]. At the mean depth of the original implant, a residual peak remains. The solid solubility of boron in silicon had been exceeded in the original implant which is suspected [50] to give rise to Si-B compounds. Since the diffusivity of boron is much less in silicon dioxide than in silicon, the boron on the silicon side of interface migrates into the bulk silicon while the boron on the SiO_2 side of the interface remains essentially immobile during the annealing. The segregation coefficient of boron between Si and SiO_2 favors the SiO_2 which accounts for the increase in boron concentration at the interface analogous to the effect seen in Fig. 5(b).

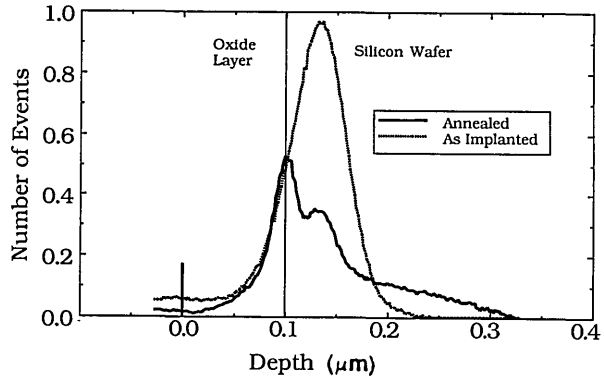

Fig. 6. NDP depth profiles for a 70 keV ^{10}B implant to a dose of 1×10^{16} in an Si wafer that had a 0.2 μm film of thermally grown SiO_2 (a) as deposited, and (b) after a 30 min anneal at 1000 °C.

Matsumura et al. [19,51] discussed the use of the NDP method to investigate the diffusivity of boron in hydrogenated amorphous silicon (a – Si:H), an important material in solar cell production. When using a *p*-type/intrinsic/*n*-type (*p*-i-*n*), layered amorphous silicon structure, the boron from the 60 nm thick *p*-type layer was observed to diffuse into the underlying undoped a – Si:H layer. From these measurements, they were able to calculate the activation energy and diffusion coefficient for boron in a – Si:H (the latter being a dramatic 12 orders of magnitude larger than for crystalline silicon) and estimate the deterioration rate of boron-doped solar cells.

3.3 Channel Blocking

Arrayed-charged particle detectors [40] are used with the NDP technique to determine both the energy and lateral position of emitted particles. Similar to RBS performing channel blocking

experiments, NDP is used to discern between interstitially or lattice located atoms, but only those isotopes which are charged particle emitters. The minor damage incurred from thermal neutron induced reactions is negligible when compared to RBS which bombards the sample with highly energetic charged particles. It therefore seems appropriate that one of the first applications of NDP was to establish the depth and lattice position of dopants in single crystal materials [15,52].

Using NDP, Fink et al. [16] have reported variations in the lattice position of the dopant atoms with respect to the depth and temperature treatment for boron implants in silicon. One example, where a boron implant of 1×10^{16} atoms per cm^2 was made at 120 keV and annealed at 1000 °C for 1 h, showed that two thirds of the boron atoms located near the average range of the implant remained unordered. The remaining one third in that region were shown to be interstitial. The further from the average range of the implanted atoms, both above and below the plane, the more nearly substitutional the boron atoms were in the matrix. The largest component of the total boron implanted in these regions, however, remained randomly located in the lattice.

In the past, researchers [53] have used etchable acetate foils to map the channel blocking pattern, analogous to the nuclear track technique (NTT) method of particle counting. However, quantitative analysis becomes tedious with this method and little depth information is obtained. A review of channel blocking by NDP for boron in silicon is presented by Fink et al. [16]

3.4 Thin Films and Leaching

Materials for optical waveguides and fiber optics depend on uniform composition to prevent changes in the refractive index of the material, which can reduce the intensity of signal transmissions. Similar materials are used in thin, insulating overcoats on electronic devices. The high solubility and mobility of boron and lithium in these technologically important materials make them susceptible to leaching during wet processing, annealing at elevated temperatures, and during the cutting or polishing of surfaces. Riley et al. [54] have studied some of the effects that the processing steps can have on boron in the near surface region of fiber-optic-grade glasses. Using NDP, SIMS, Nuclear Track Technique (NTT), and prompt gamma activation analysis (PGAA) to quantify and map the boron distribution, they were able to show that a significant amount of leaching occurs within the first few micrometers of the samples when a fine grinding cut was made in the presence of an aqueous coolant. The leaching of boron from the near surface is obvious and can be attributed to the action of the water during the cutting step. In their study, Riley et al. demonstrated that leaching could be avoided by substituting a glycol based liquid for the water coolant during the cut.

For a sufficiently thin film, such as a BSG overcoat on a silicon wafer, a single NDP spectrum is capable of revealing the thickness, the boron distribution profile, and the total amount of boron present. Changes in the film can be quantified subsequent to wafer annealing. This processing is designed to drive out trapped reaction products in the CVD process and remove trapped voids from the glass film. Also, the effect of reflowing the glass film on the original boron profile can be shown, including boron loss and diffusion into the substrate [55].

4. The CNDP Instrument

The cold neutron source in the NIST research reactor (called NBSR) is a block of $D_2O - H_2O$ ($7.5\% - H_2O$) ice cooled to ~45 K by recirculating helium gas. The gas is circulated by a compressor through a refrigerator capable of removing 1 kW of heat at 20 K. A lead-bismuth shield removes most of the gamma heating before it reaches the cryostat and cold moderator. Figure 7 indicates the layout of Cold Tube West (CT-W) on which the NDP instrument is located. The neutrons are filtered by 135 mm of single crystal sapphire which has the effect of reducing the slow neutron fluence rate by 1/3, but the fast neutron fluence rate by a factor of about 500. Collimators are located both within the biological shield and in the external-to-the-shield rotating shutter. The shutter is two cylinders, whose beam tubes fully align in the beam open configuration and are nonaligned in the beam closed configuration. The collimator pieces in these shutters can be accessed in the beam closed configuration with the reactor at full power. The diameter and intensity of the neutron beam can then be modified at any time to suit the needs of a particular experiment. The measured neutron fluence rate (capture flux) at the target position with the 16 mm diameter collimator is 1.2×10^9 cm^{-2} s^{-1}. A pancake fission chamber mounted on the entrance port of the NDP chamber provides a run to run monitor.

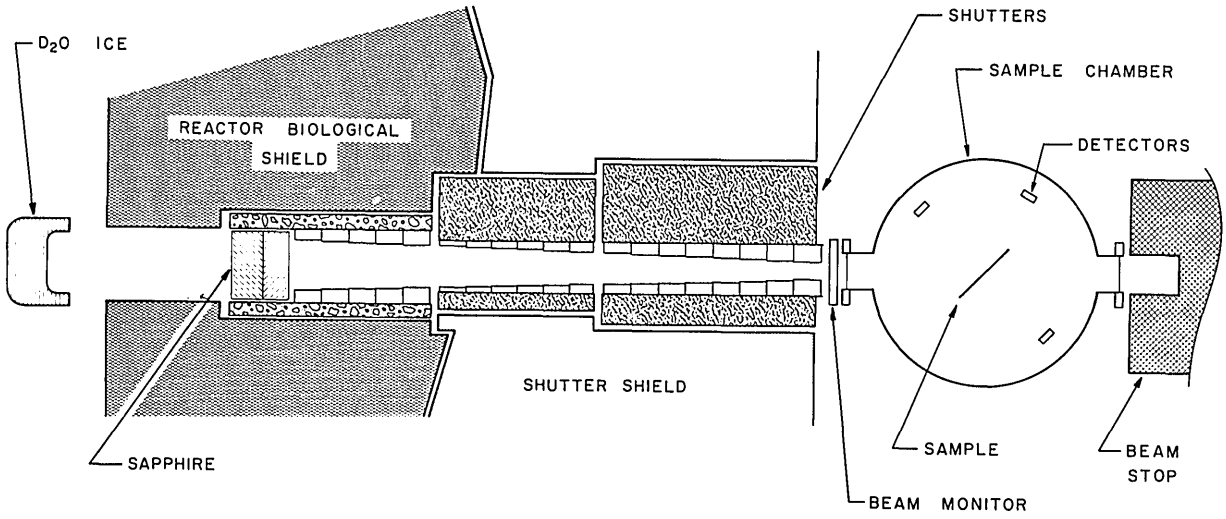

Fig. 7. A schematic layout of Cold Tube-West showing the relative positions of the cold source, sapphire filters, collimators, and the sample chamber.

The target chamber was obtained from a commercial vendor using a design developed at NIST. The entire chamber is stainless steel and uses copper gaskets at all but three sealing surfaces: the beam entrance and exit windows and the opening used for changing samples. This last surface can use either viton O-rings or copper gaskets. In practice, the desire to change samples quickly usually outweighs the need for ultra high vacuum, but that capability is readily accessible. The chamber itself is a 610 mm diameter cylinder with access ports in the top and bottom plates as well as through the side walls. All flanges conform to standard Conflat[1] flange specifications making it possible to add new features to the chamber. Some of these include *in situ* cleaning of samples, time-of-flight measurements, heating and cooling of the sample, and cooling of the surface barrier detectors.

The beam enters and exits through 100 mm diameter ports sealed with thin aluminum windows. These can be replaced with sapphire windows if a metal gasket seal is required. The chamber is evacuated with a 180 L/s magnetic bearing turbo molecular pump. This pump was chosen to reduce microphonic effects on the charged particle detectors. The detectors are transmission-type surface barrier detectors in a ring mount. A rotary base positions the charged particle detectors about the axis of the sample. Detectors can be placed at any angle and detectors can be mounted every 10°. Currently, there exists electronics to operate four detectors simultaneously.

Samples (up to 200 mm in diameter) are mounted on a set of motor driven positioners. A second rotary base selects the angle of the sample with respect to the beam. The ability to rotate the detectors and sample independently allows the detector to be positioned at any angle with respect to the sample without putting the detector in the beam. Mounted on top of the sample rotator are x and y positioners. These have 150 mm of travel each, allowing a full scan of 150×150 mm sample areas. All four positioning devices are controlled by a PC compatible microcomputer. Figure 8 is a photograph of the interior of the CNDP target chamber. A program has been written in BASIC to enable unattended sample scans. The signals from the detectors are processed in a standard fashion and are interfaced with a multiuser minicomputer. This computer can simultaneously process data from both the thermal and cold NDP facilities. Spectra from these computers can then be transferred to a variety of other computers for data reduction, plotting, etc. A comparison of several characteristics of the two NDP facilities at NIST is given in Table 2.

Figure 9 is an $^{17}O(n,\alpha)^{14}C$ profile taken at the CNDP facility. The sample of Cobalt Nickel Oxide (enriched to 50% ^{17}O) was prepared by Eastman Kodak. A surface boron contamination is observed

[1] Certain commercial equipment, instruments, or materials are identified in this paper to specify adequately the experimental procedure. Such identification does not imply recommendation or endorsement by the National Institute of Standards and Technology, nor does it imply that the materials or equipment identified are necessarily the best available for the purpose.

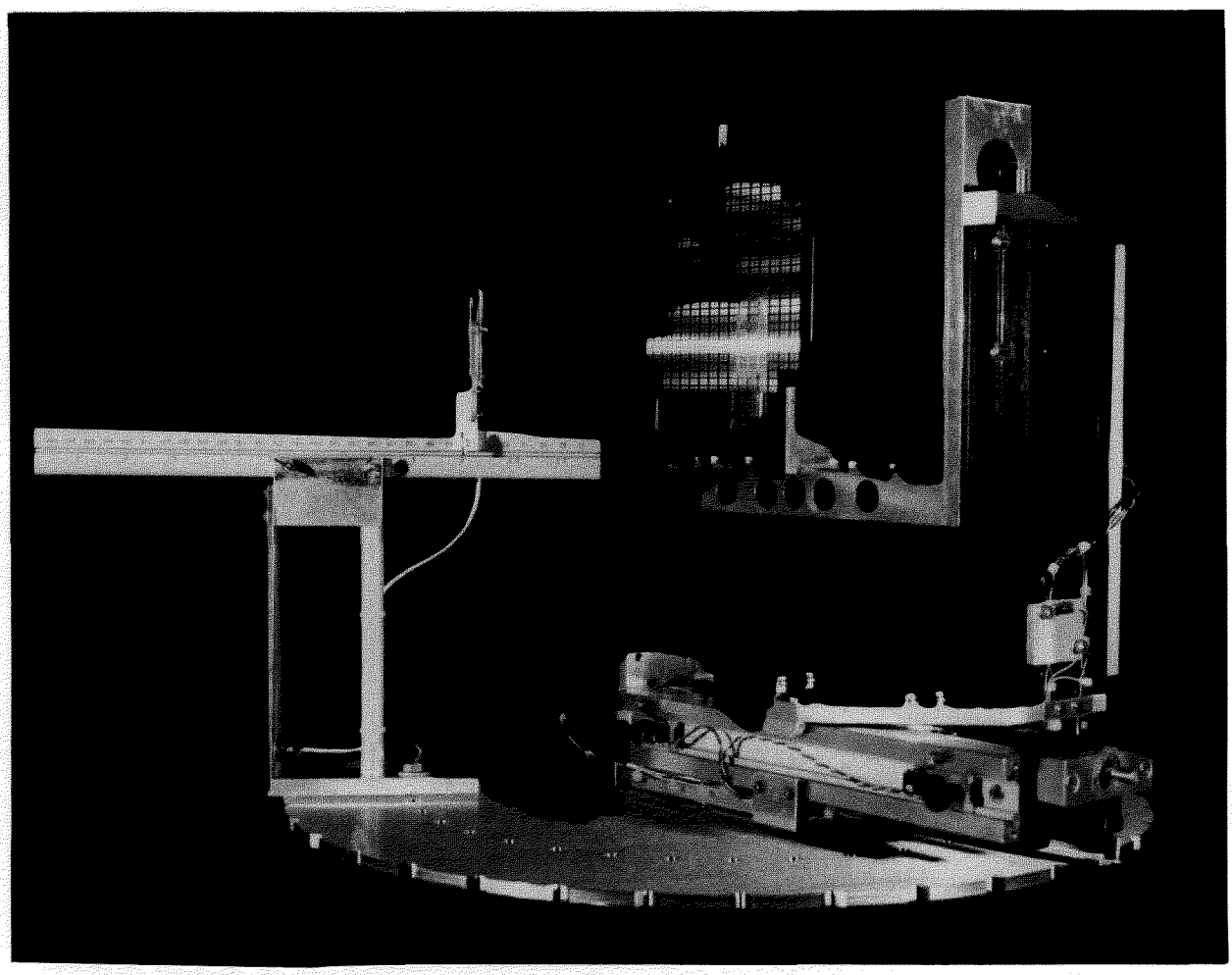

Fig. 8. A photograph of the CNDP sample holder/positioning equipment without the vacuum chamber. A 150 mm silicon wafer is shown in sample position for a sense of dimensions. The sample can be independently translated in two-dimensions and rotated. A transmission-type surface barrier detector is on the right which is mounted on an independently rotatable base.

to the right of the oxygen profile. Because the unattenuated energy of the alpha from the boron reaction is higher in energy (1472 keV) than that of the full energy alpha from the oxygen (1413 keV), the boron profile appears as an artifact peak "above" the surface on the oxygen depth scale. Adjustment of the depth scale will produce a boron concentration profile. To our knowledge, this is the first nondestructive determination of near surface oxygen made by NDP.

5. New Capabilities

Several features are planned for the CNDP instrument in addition to those discussed in the above section on detection limits [22]. This includes cooling of the charged particle detectors which has the effect of reducing the thermal induced electronic noise present in the detector. Ten or more percent improvement in the detector resolution is to be expected by cooling the detector to liquid nitrogen temperatures. Another planned feature of the CNDP system is sputter cleaning by low energy ion beams of sample surfaces in the target chamber. This is important for ultra high vacuum applications, particularly when a time of flight detector is being used. For both UHV and normal applications sputtering can be employed to remove surface layers systematically for profiling deeper into the material. *In situ* heating and cooling of samples for diffusion and annealing studies will also enhance the usefulness of the NDP facility.

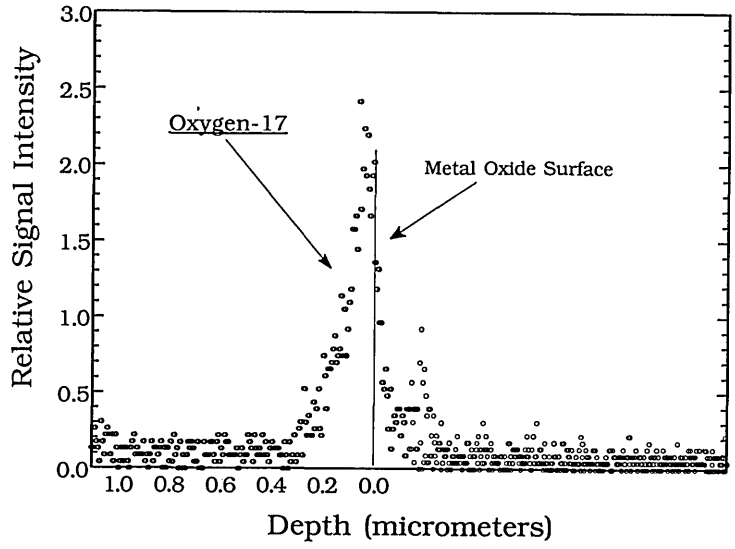

Fig. 9. The profile of oxygen-17 obtained using the cold NDP instrument. The sample was Cobalt-Nickel Oxide enriched with ^{17}O. The small boron peak is due to a contaminant on the surface of the sample. See text for description.

Table 2. Comparison of the two NIST facilities used for NDP. The thermal NDP facility is located at beam tube 3 (BT-3), and has been operational since 1982. The cold NDP facility is a CNRF instrument located at cold tube–west (CT-W), and has been operational since November 1990

	BT-3 (thermal)	CT-W (cold)
Thermal equivalent fluence rate	4×10^{8} cm^{-2} s^{-1}	1.2×10^{9} cm^{-2} s^{-1}
Sapphire filtering	200 mm	135 mm
Peak neutron energy	22.5 meV	≈8 meV
Relative sensitivity	1	3
Gamma dose	400 mR/h	≈400 mR/h
Maximum sample size	100×100 mm	200×200 mm
Typical beam diameter at sample position	13 mm	30 mm
Number of detectors	2	4 (more possible)
Remote sample, and detector rotation	Yes	Yes
Incremental rotational detector movement	0.001°	0.025°
Sample scanning	No	Yes
Incremental rotational sample movement	0.01°	0.025°
Incremental translational sample movement (X–Y)	Hand positioned	3.2 μm
UHV capability	No	Yes

6. Summary

NDP provides an isotope specific, nondestructive technique for the measurement of concentration versus depth distributions in the near-surface region of solids. The simplicity of the method and the interpretation of data have been described. Major points to be made for NDP as an analytical technique include: i) it is nondestructive; ii) isotopic concentrations are determined quantitatively; iii) profiling measurements can be performed in essentially all solid materials with depth resolution and depth of analysis being material dependent; iv) it is capable of profiling across interfacial boundaries; and v) there are few interferences. The profiles are generated in real-time, analyzing depths of up to tens of micrometers. NDP is applied to many areas of materials research, as discussed here and in the references given in the Appendix. With the installation of the CNDP facility the ability to obtain oxygen profiles as well as those for chlorine or sulfur is now possible adding to the elements previously analyzed at NIST: boron, lithium, nitrogen, sodium, beryllium, and helium.

Acknowledgments

The authors would like to thank the many university, government, and industrial collaborators who provided samples and hours of helpful discussion which has lead to the development of these NDP facilities. Appreciation is expressed to Eastman Kodak, Intel Corporation, and Bell Laboratories who have provided outside funding and equipment to the project. We also express our gratitude to the staff of the NIST reactor for their continuing assistance.

About the authors: *R. Greg Downing, a research chemist; George P. Lamaze, a research physicist; and John K. Langland, an engineering technician are with the Inorganic Analytical Research Division of the NIST Chemical Science and Technology Laboratory. Dr. Sun-Tae Hwang is head of the Radiation Laboratory, Division of Quantum Metrology at the Korea Research Institute for Standards and Science. He is visiting NIST on an IAEA fellowship. The National Institute of Standards and Technology is an agency of the Technology Administration, U.S. Department of Commerce.*

7. References

[1] R. G. Downing, R. F. Fleming, J. K. Langland, and D. H. Vincent, Nucl. Instr. Meth. **218**, 47–51 (1983).
[2] J. F. Ziegler, G. W. Cole, and J. E. E. Baglin, J. Appl. Phys. **43**, 3809–3815 (1972).
[3] D. Fink, J. P. Biersack, and H. Liebl, in Ion Implantation: Equipment and Techniques, H. Ryssel and H. Glawischnig, eds., Springer-Verlag, Berlin (1983) pp. 318–326.
[4] D. J. Myers, Range Profiles of Helium in Copper After Thermal Anneals, University of Michigan-Ann Arbor (1979).
[5] D. J. Myers, W. G. Halsey, J. S. King, and D. H. Vincent, Radia. Eff. **51**, 251–252 (1980).
[6] W. G. Halsey, Concentration Dependent Thermal Release of Helium-3 Implantation in Molybdenum, University of Michigan-Ann Arbor (1980).
[7] N. S. Khalil, Design, Installation, and Implementation of a Neutron Depth Profiling Facility at the Texas A&M Nuclear Science Center, Texas A&M University (1989).
[8] K. Ünlü, Private Communication (1990).
[9] N. R. Parikh, W. K. Chu, B. W. Wehring, and G. D. Miller, Boron-10 Distribution in Silicon, $TiSi_2$, and SiO_2 Using Neutron Depth Profiling 1, American Nuclear Society, Los Angeles, CA (1987) pp. 211–212.
[10] J. F. Ziegler, Pergamon Press, New York (1977).
[11] J. F. Janni, Atom. Nucl. Data Tabl. **27**, 147–529 (1982).
[12] D. I. Thwaites, Radia. Research **95**, 495–518 (1983).
[13] H. F. Nieman, D. C. Tennant, and G. Dolling, Rev. Sci. Instr. **51**, 1299 (1980).
[14] J. P. Biersack, D. Fink, J. Lauch, R. Henkelmann, and K. Müller, Nucl. Instr. Meth. **188**, 411–419 (1981).
[15] D. Fink et al., Radia. Eff. **77**, 11–33 (1983).
[16] J. Bogáncs, et al., Radiochem. Radioanal. Lett. **39**, 393–403 (1979).
[17] B. L. Crowder, J. F. Ziegler, and G. W. Cole, in Ion Implantation in Semiconductors, and Other Materials, B. L. Crowder, ed., Plenum Press, New York (1973) pp. 257–266.
[18] H. Matsumura, K. Sakai, M. Maeda, S. Furukawa, and K. J. Horiuchi, Appl. Phys. **54**, 3106–3110 (1983).
[19] K. Müller, R. Henkelmann, J. P. Bierseck, and P. J. Mertens, Radioanal. Chem. **8**, 9–17 (1977).
[20] A. Z. Nagy et al., J. Radioanal. Chem. **38**, 19–27 (1977).
[21] G. P. Lamaze, R. G. Downing, J. K. Langland, and S. T. Hwang, J. Radioanal. Nucl. Chem. **160**, 315–325 (1992).
[22] A. J. Deruytter and P. J. Pelfer, Nucl. Energy **21**, 833–845 (1967).
[23] J. P. Biersack, D. Fink, R. Henkelmann, and K. Müller, Nucl. Instr. Meth. **149**, 93–97 (1978).
[24] J. T. Maki, R. F. Fleming, and D. H. Vincent, Nucl. Instr. Meth. **B17**, 147–155 (1985).
[25] J. Cervená et al., Nucl. Instr. Meth. **188**, 185–189 (1981).
[26] J. Bogáncs et al., Joint Instit. Nucl. Res. **1**, 59–64 (1979).
[27] J. Kvitek, V. Hnatowicz, and P. Kotas, Radiochem. Radioanal. Lett. **24**, 205–213 (1976).
[28] H. Ryssel et al., IEEE Trans. on Elect. Dev. **ED27**, 1484–1492 (1980).
[29] A. Z. Nagy et al., Physica Status Solidi (a) **61**, 689–692 (1980).
[30] J. Cervená et al., Tesla Elect. **14**, 16–20 (1981).
[31] N. R. Parikh et al., Nucl. Instr. Meth. **B45**, 70–74 (1990).
[32] D. Fink et al., Nucl. Instr. Meth. **B15**, 740–743 (1986).
[33] D. F. R. Mildner, Nucl. Instr. Meth. **A299**, 416–419 (1990).
[34] J. R. Ehrstein, R. G. Downing, B. R. Stallard, D. S. Simons, and R. F. Fleming, Comparison of Depth

Profiling B-10 in Silicon Using Spreading Resistance Profiling, Secondary Ion Mass Spectrometry, and Neutron Depth Profiling 1, ASTM, San Jose, CA (1984) pp. 409–425.
[35] D. Fink, Radia. Eff. **106**, 231–264 (1988).
[36] J. N. Cox, R. Hsu, P. J. McGregor, and R. G. Downing, NDP and FTIR Studies of Borophosphosilicate CVD Thin-Film Glasses 1, American Nuclear Society, Los Angeles, CA (1987) pp. 207–209.
[37] D. N. Jamieson, R. C. Bowman Jr., P. M. Adams, J. F. Knudsen, and R. G. Downing, Study of Boron Implantation in CdTe 1, Materials Research Society, Pittsburgh, PA (1988) pp. 299–304.
[38] B. L. Crowder, J. F. Ziegler, F. F. Morehead, and G. W. Cole, in Ion Implantation in Semiconductors, and Other Materials, B. L. Crowder, ed., 267–274, Plenum Press, New York (1973).
[39] J. F. Ziegler, B. L. Crowder, G. W. Cole, J. E. E. Baglin, and B. J. Masters, J. Appl. Phys. **21**, 16–17 (1972).
[40] K. Müller et al., Nucl. Instr. Meth. **170**, 151–155 (1980).
[41] H. Ryssel et al., Appl. Phys. **24**, 39–43 (1981).
[42] H. Geissel et al., Nucl. Instr. Meth. **B2**, 770–773 (1984).
[43] J. P. Biersack and D. Fink in Ion Implantation in Semiconductors, S. Namba, ed., Plenum Press, New York, NY (1975) pp. 211–218.
[44] R. G. Downing, J. P. Lavine, T. Z. Hossain, J. B. Russell, and G. P. Zenner, J. Appl. Phys. **67**, 3652–3654 (1990).
[45] H. Ryssel et al., Physica Status Solidi **57**, 619–624 (1980).
[46] L. K. Vodopyanov and S. P. Kozyrev, Physica Status Solidi **72**, K133–K136 (1982).
[47] R. C. Bowman, Jr., R. E. Robertson, J. F. Knudsen, and R. G. Downing, Studies of Boron Implantations through Photochemically Deposited SiO_2 Films on Hg1-xCdxTe 1, Society of Photo-Optical Instrumentation Engineers, San Diego, CA (1986) pp. 18–25.
[48] F. Jahnel et al., J. Appl. Phys. **53**, 7372–7378 (1982).
[49] L. Pelikan, V. Rybka, P. Krejci, V. Hnatowicz, and J. Kvitek, Physica Status Solidi **72**, 369-373 (1982).
[50] H. Ryssel, K. Müller, K. Haberger, R. Henkelmann, and F. Jahnel, Appl. Phys. **22**, 35–38 (1980).
[51] H. Matsumura, M. Maeda, and S. Furukawa, Japan. J. Appl. Phys. **22**, 771–774 (1983).
[52] J. P. Biersack and D. Fink, in Atomic Collisions in Solids, S. Datz, B. R. Appleton, and C. D. Moak, eds., Plenum Press, New York (1975) pp. 737–747.
[53] J. P. Biersack and D. Fink, Nucl. Instr. Meth. **108**, 397–399 (1973).
[54] J. E. Riley, Jr., et al., Mater. Sci. Forum **2**, 123–132 (1984).
[55] R. G. Downing, J. T. Maki, and R. F. Fleming, in Microelectronics Processing: Inorganic Materials Characterization, L. A. Casper, ed., American Chemical Society, Washington, DC (1986) pp. 163–180.

8. Appendix A. Neutron Depth Profiling Bibliography

Alfassi, Z. B., and Yang, M. H. (1990). Depth Profiling of Silicon by Nuclear Activation Methods. In Activation Analysis, Z. B. Alfassi, ed., Boca Raton, FL, CRC Press, pp. 579–606.

Banerjee, I., Frost, M. R., Davies, P. W., Cox, J. N., and Downing, R. G. (1989). SIMS, and Neutron Depth Profiling Studies of $SiO_2/Si_3N^4/SiO_2/Si$ Structures. In Secondary Ion Mass Spectrometry (SIMS VII), A. Benninghoven, C. A. Evans, K. D. McKeegan, H. A. Storms, and H. W. Werner, eds., Monterey, CA, John Wiley, and Sons, pp. 235–238.

Biersack, J. P. (1983). He Profiles in Various Metals after Implantation, and Thermal Anneals. Radiation Effects **78**, 363.

Biersack, J. P., and Fink, D. (1973). Observation of the Blocking Effect after $^6Li(n,t)^4He$ Reactions with Thermal Neutrons. Nuclear Instruments and Methods **108**, 397-399.

Biersack, J. P., and Fink, D. (1974). Damage, and Range Profiles of Lithium Implanted into Niobium. Journal of Nuclear Materials **53**, 328–331.

Biersack, J. P., and Fink, D. (1975). Channeling, Blocking, and Range Measurements Using Thermal Neutron Induced Reactions. In Atomic Collisions in Solids, S. Datz, B. R. Appleton, and C. D. Moak, eds., New York, Plenum Press, pp. 737–747.

Biersack, J. P., and Fink, D. (1975). Implantation of Boron, and Lithium in Semiconductors, and Metals. In Ion Implantation in Semiconductors, S. Namba, ed., New York, NY, Plenum Press, pp. 211–218.

Biersack, J. P., and Fink, D. (1975). Study of He Distributions in Niobium by Means of (n,p) Reactions. In International Conference on Radiation Effects, and Tritium Technology for Fusion Reactors, CONF-750989, Gatlinburg, TN, USERDA, pp. II362–II371.

Biersack, J. P., Fink, D., Henkelmann, R., and Müller, K. (1978). The Use of Neutron Induced Reactions for Light Element Profiling, and Lattice Localization. Nuclear Instruments and Methods **149**, 93–97.

Biersack, J. P., Fink, D., Henkelmann, R. A., and Müller, K. (1979). Range Profiles, and Thermal Release of Helium Implanted into Various Metals. Journal of Nuclear Materials **85-86**, 1165–1171.

Biersack, J. P., Fink, D., Lauch, J., Henkelmann, R., and Müller, K. (1981). An Instrument for Lattice Location Studies of Light Impurity Atoms by Means of (n, α)-Reactions. Nuclear Instruments and Methods **188**, 411–419.

Biersack, J. P., Fink, D., Mertens, P., Henkelmann, R. A., and Müller, K. (1976). Helium Profiles in Niobium, and Molybdenum. In Plasma Wall Interactions, Oxford, Pergamon Press, pp. 421–430.

Biersack, J. P., Fink, D., Miekeley, W., and Tjan, K. (1986). 1-3 MeV Alpha, and Trition Stopping Powers in LiF, and Li Alloys. Nuclear Instruments and Methods **B15**, 96–100.

Bogáncs, J., Gyulai, J., Hagy, A., Nazarov, V. M., Seres, Z., and Szabó, A. (1979). Use of the Reaction $^{10}B(n, \alpha)^7Li$ to Determine the Distribution of Boron Implanted in Silicon. Joint Institute for Nuclear Research **1**, 59–64.

Bogáncs, J., Szabó, A., Nagy, A. Z., Csoke, A., Pecznik, J., and Krakkai, I. (1979). Nondestructive Nuclear Method for Boron Analysis in Plant Samples. Radiochemical and Radioanalytical Letters **39**(6), 393–403.

Bowman, R. C., Jr., Downing, R. G., and Knudsen, J. F. (1987). NDP Evaluations of Boron Implanted Compound Semiconductors. In American Nuclear Society—Material Characterization Using Neutron Depth Profiling **55**, Los Angeles, CA, American Nuclear Society, pp. 212–214.

Bowman, R. C., Knudsen, J. F., and Downing, R. G. (1990). Neutron Depth Profiling of Boron Implanted Semiconductors. In Materials Research Society **166**, North Holland, pp. 331–336.

Bowman, R. C., Jr., Knudsen, J. F., Downing, R. G., and Kremer, R. E. (1988). Distribution of Boron Atoms in Ion Implanted Compound Semiconductors. In Materials Research Society **126**, pp. 89–92.

Bowman, R. C., Marks, J., Downing, R. G., Knudsen, J. F., and To, G. A. (1987). Effects of Boron Implantation on Silicon Dioxide Passivated HgCdTe. In Materials Research Society **90**, pp. 279–286.

Bowman, R. C., Jr., Robertson, R. E., Knudsen, J. F., and Downing, R. G. (1986). Studies of Boron Implantations through Photochemically Deposited SiO_2 Films on Hg1-xCdxTe. In Infrared Detectors, Sensors, and Focal Plane Arrays **686**, San Diego, CA, Society of Photo-Optical Instrumentation Engineers, pp. 18–25.

Cervená, J., Hnatowicz, V., Hoffmann, J., Kosina, Z., Kvítek, J., and Onheiser, P. (1981). The Use of the Induced Reaction for Boron Profiling in Si. Nuclear Instruments and Methods **188**, 185–189.

Cervená, J., Hnatowicz, V., Hoffmann, J., Kvítek, J., Onheiser, P., and Rybka, V., A. (1981). A Study of Masking properties of SiO2, and Photoresists with Boron Ion Implantation. Tesla Electronics **14**(1), 16–20.

Chu, W. K. (1989). Large Angle Coincidence Spectrometry for Neutron Depth Profiling. Radiation Effects and Defects in Solids **108**, 125–126.

Chu, W. K., and Wu, D. T. (1988). Scattering Recoil Coincidence Spectrometry. Nuclear Instruments and Methods **B35**, 518–521.

Coakley, K. J. (1991). A Cross-Validation Procedure for Stopping the EM Algorithm, and Deconvolution of Neutron Depth Profiling Spectra. IEEE Transactions on Nuclear Science **38**(1), 9–15.

Cox, J. N., Hsu, R., McGregor, P. J., and Downing, R. G. (1987). NDP, and FTIR Studies of Borophosphosilicate CVD Thin-Film Glasses. In American Nuclear Society—Material Characterization Using Neutron Depth Profiling **55**, I. O. Macke, ed., Los Angeles, CA, American Nuclear Society, pp. 207–209.

Crowder, B. L., Ziegler, J. F., and Cole, G. W. (1973). The Influence of the Amorphous Phase on Boron Atom Distributions in Ion Implanted Silicon. In Ion Implantation in Semiconductors, and Other Materials, B. L. Crowder, ed., New York, Plenum Press, pp. 257–266.

Crowder, B. L., Ziegler, J. F., Morehead, F. F., and Cole, G. W. (1973). The Application of Ion Implantation to the study of Diffusion of Boron in Silicon. In Ion Implantation in Semiconductors, and Other Materials, B. L. Crowder, eds., New York, Plenum Press, pp. 267–274.

Deruytter, A. J., and Pelfer, P. (1967). Precise Determination of the Branching Ratio, and Q-Value of the $^{10}B(n,\alpha)^7Li$ Reaction, and of the $^6Li(n,\alpha)^3H$ Reaction. Journal of Nuclear Energy **21**, 833–845.

Downing, R. G. (1988). Neutron Depth Profiling: Current Developments of the Technique in the United States. In Industrial Radiation, and Radioisotope Measurement Applications **56**(3), I. O. Macke, ed., Pinehurst, NC, American Nuclear Society, pp. 15–16.

Downing, R. G., Fleming, R. F., Langland, J. K., and Vincent, D. H. (1983). Neutron Depth Profiling at the National Bureau of Standards. Nuclear Instruments and Methods **218**, 47–51.

Downing, R. G., Fleming, R. F., Maki, J. T., Simons, D. S., and Stallard, B. R. (1984). Near-Surface, and Interfacial Profiling by Neutron Depth Profiling (NDP), and Secondary Ion Mass Spectrometry (SIMS). In Thin Films, and Interfaces II, J. E. E. Baglin, D. R. Campbell, and W. K. Chu, eds., New York, North-Holland, pp. 655–656.

Downing, R. G., Fleming, R. F., Simons, D. S., and Newbury, D. E. (1982). Neutron-Induced Reactions, and Secondary Ion Mass Spectrometry: Complementary Tools for Depth Profiling. In Microbeam Analysis, K. F. J. Heinrich, ed., San Francisco, San Francisco Press, pp. 219–221.

Downing, R. G., Lavine, J. P., Hossain, T. Z., Russell, J. B., and Zenner, G. P. (1990). The Measurement of Boron at Silicon Wafer Surfaces by Neutron Depth Profiling. Journal of Applied Physics **67**(8), 3652–3654.

Downing, R. G., Maki, J. T., and Fleming, R. F. (1986). Application of Neutron Depth Profiling to Microelectronic Materials Processing. In Microelectronics Processing: Inorganic Materials Characterization, L. A. Casper, ed., Washington, DC, American Chemical Society, pp. 163–180.

Downing, R. G., Maki, J. T., and Fleming, R. F. (1987). Analytical Applications of Neutron Depth Profiling. Journal of Radioanalytical and Nuclear Chemistry, Articles **112**(1), 33–46.

Ehrstein, J. R., Downing, R. G., Stallard, B. R., Simons, D. S., and Fleming, R. F. (1984). Comparison of Depth Profiling B-10 in Silicon Using Spreading Resistance Profiling, Secondary Ion Mass Spectrometry, and Neutron Depth Profiling. In Third Symposium on semiconductor processing, ASTM proceedings, 850, San Jose, CA, ASTM, pp. 409–425.

Fink, D. (1983). Li, B, and N in Ancient Materials. Nuclear Instruments and Methods, 218, 456-462. Fink, D. (1988). Helium Implantation, and Thermal Annealing Behaviour. Radiation Effects **106**, 231–264.

Fink, D. (1989). Surface Precipitation of Natural, and Ion-Implanted Lithium, and Boron in Metals. Materials Science and Engineering **A115**, 89–95.

Fink, D., Biersack, J. P., Carstanjen, H. D., Jahnel, F., Müller, K., Ryssel, H., and Osei, A. (1983). Studies on the Lattice Position of Boron in Silicon. Radiation Effects **77**, 11–33.

Fink, D., Biersack, J. P., Grawe, H., Riederer, J., Müller, K., and Henkelmann, R. (1980). Applications of (n,p), and (n,α) Reactions, and a Backscattering Technique to Fusion Reactor Materials, Archeometry, and Nuclear Spectroscopy. Nuclear Instruments and Methods **168**, 453–457.

Fink, D., Biersack, J. P., Jahnel, F., and Henkelmann, R. (1981). Untersuchung von Helium, Lithium, und Bor in Metallen mit Hilfe von (n,p), and (n,α)-reaktionen. In Analysis of Nonmetals in Metals, Berlin, Walter de Gruyter and Co., pp. 163–171.

Fink, D., Biersack, J. P., Kranz, H., De Souza, J., Behar, M., and Zawislak, F. C. (1988). Tilted Angle Ion Implantation. Radiation Effects **106**, 165–181.

Fink, D., Biersack, J. P., and Liebl, H. (1983). Background in (n,p), and (n,α) Spectrometry. In Ion Implantation: Equipment, and Techniques, H. Ryssel, and H. Glawischnig, eds., Berlin, Springer-Verlag, pp. 318–326.

Fink, D., Biersack, J. P., Müller, M., Wang, L. H., Cheng, V. K., Kassing, R., Masseli, K., Weiser, M., and Kalbitzer, S. (1989). Depth Distribution of Megaelectronvolt ^{14}N Implanted into Various Solids at Elevated Fluences. Materials Science and Engineering **B2**, 49–54.

Fink, D., Biersack, J. P., and Städele, M. (1987). Range Profiles of Helium in Solids. Radiation Effects **104**, 1–42.

Fink, D., Biersack, J. P., Städele, M., Tjan, K., Behar, M., Fichtner, P. F. P., Olivieri, C.A., De Souza, J. P., and Zawislak, F. C. (1986). Range Profiles of Ions in Double-Layer Structures. Nuclear Instruments and Methods **B15**, 71–74.

Fink, D., Biersack, J. P., Städele, M., Tjan, K., and Cheng, V. (1983). Nitrogen Depth Profiling Using the $N^{14}(n,p)C^{14}$ Reaction. Nuclear Instruments and Methods **218**, 171–175.

Fink, D., Biersack, J. P., Städele, M., Tjan, K., Haring, R. A., and De Vries, R. A. (1984). Experiments on the Sputtering of Group VI Elements. Nuclear Instruments and Methods **B1**, 275–281.

Fink, D., Biersack, J. P., Stumpff, C., and Schlosser, S. (1986). Background Reduction in Light Element Depth Profiling by a Coincidence Technique. Nuclear Instruments and Methods **B15**, 740–743.

Fink, D., Biersack, J. P., Tjan, K., and Cheng, V. K. (1982). Ranges of He-3, and Li-6 in Various Solids. Nuclear Instruments and Methods **194**, 105–111.

Fink, D., and Fichtner, P. F. P. (1990). Unique Ion Beam Scattering Technique on Depth Profile Determination. Radiation Effects, and Defects in Solids **114**, 337–341.

Fink, D., Müller, M., Stettner, U., Behar, M., Fichtner, P. F. P., Zawislak, F. C., and Koul, S. (1988). Non-Regular Depth Profiles of Light Ions Implanted into Organic Polymer Films. Nuclear Instruments and Methods **B32**, 150–154.

Fink, D., Müller, M., Wang, L., Siegel, J., Vredenberg, A., Martan, J., and Fahrner, W. (1990). Energy, Fluence, and Temperature Dependence of MeV Nitrogen Implantation Profiles in Steel. Radiation Effects and Defects in Solids **115**, 121–134.

Fink, D., and Riederer, J. (1981). Studies of Li, B, and N in Ancient Oriental Pottery, and Modern Ceramic Materials by Means of (n,p), and (n,α) Spectrometry. Nuclear Instruments and Methods **191**, 408–413.

Fink, D., Tjan, K., Biersack, J. P., Wang, L., and Yunru, M. (1989). Lithium Implantation Profiles in Metals, and Semiconductors. Radiation Effects and Defects in Solids **108**, 27–44.

Fink, D., Tjan, K., and Wang, L. (1990). On the Thermal Mobility of Lithium in Metals, and Semiconductors. Radiation Effects and Defects in Solids **114**, 21–50.

Fink, D., and Wang, L. (1990). On the Thermal Annealing Behavior of Boron in Solids. Radiation Effects and Defects in Solids **114**, 343–371.

Fink, D., Wang, L., Biersack, J. P., and Jahnel, F. (1990). 30 keV to 2 MeV Boron Implantation Profiles in Solids. Radiation Effects and Defects in Solids **115**, 93–112.

Geissel, H., Lennard, W. N., Alexander, T. K., Ball, G. C., Forster, J. S., Lone, M. A., Milani, L., and Phillips, D. (1984). Influence of 1.3 MeV He-4 Post-Bombardment of the Depth Profiles of 35 keV He-3 Ions Implanted in Nb, and Au. Nuclear Instruments and Methods **B2**, 770–773.

Grasserbauer, M. (1988). Critical Evaluation of Calibration Procedures for Distributions Analysis of Dopant Elements in Silicon, and Gallium Arsenides. International Union of Pure and Applied Chemistry **60**(3), 437–444.

Guimarães, R. B., Amaral, L., Behar, M., Fichtner, P. F. P., Zawislak, F. C., and Fink, D. (1988). Implanted Boron Depth Profiles in the AZ111 Photoresist. Journal of Applied Physics **63**(6), 2083–2085.

Halsey, W. G. (1976). Measured Range Profile of Helium-3 in Niobium Using the $^3He(n,p)^3H$ Reaction. Masters of Science, University of Michigan-Ann Arbor.

Halsey, W. G. (1980). Concentration Dependent Thermal Release of Helium-3 Implantation in Molybdenum. Ph. D. thesis, University of Michigan-Ann Arbor.

Jahnel, F., Biersack, J., Crowder, B. L., d'Heurle, F. M., Fink, D., Isaac, R. D., Lucchese, C. J., and Petrersson, C. S. (1982). The Behavior of Boron (Also Arsenic) in Bilayers of Polycrystalline Silicon, and Tungsten Disilicide. Journal of Applied Physics **53**(11), 7372–7378.

Jahnel, F., Ryssel, H., Prinke, G., Hoffmann, K., Müller, K., Biersack, J., and Henkelmann, R. (1981). Description of Arsenic, and Boron Profiles Implanted in SiO_2, Si_3N_4, and Si Using Pearson Distributions with Four Moments. Nuclear Instruments and Methods **182-183**, 223–229.

Jamieson, D. N., Bowman, R. C., Jr., Adams, P. M., Knudsen, J. F., and Downing, R. G. (1988). Study of Boron Implantation in CdTe. In Fundamentals of Beam-Solid Interactions, and Transient Thermal Processing **100**, M. J. Aziz, L. E. Rehn, and B. Stritzker, eds., Pittsburgh, PA, Materials Research Society, pp. 299–304.

Khalil, N. S. (1989) Design, Installation, and Implementation of a Neutron Depth Profiling Facility at the Texas A&M Nuclear Science Center. M. S., Texas A&M University.

Knudsen, J. F., Downing, R. G., and Simons, D. S. (1987). NDP, SIMS, and Modeling of Boron Implantation Profiles in Silicon. In American Nuclear Society—Material Characterization Using Neutron Depth Profiling **55**, I. O. Macke, ed., Los Angeles, CA, American Nuclear Society, pp. 210–211.

Kotas, P., Obrusnik, J., Kvitck, J., and Hnatowicz, V. (1976). Study of Diffusion of Impurities in Semiconductor Silicon by Activation Analysis, and Nuclear Reaction Methods. Journal of Radioanalytical Chemistry **30**, 475–488.

Kristiakova, K., Kristiak, J., Kvitek, J., and Cervená, J. (1982). The Surface Boron Concentration of NixFe80-xB20 Samples. Nuclear Instruments and Methods **199**, 371.

Kvitek, J., Hnatowicz, V., and Kotas, P. (1976). Determination of Boron Concentration profiles in Silicon from B-10(n, α)Li-7 Reaction Product Spectra. Radiochemical and Radioanalytical Letters **24**, 205–213.

Lamaze, G. P., Downing, R. G., Langland, J. K., and Hwang, S. T. (1992). The New Cold Neutron Depth Profiling Instrument at NIST. J. Radioanal. Nucl. Chem. **160**, 315–325.

Lee, M. C., Verghese, K., and Gardner, R. P. (1988). A Model for the Detector Response Function in Neutron Depth Profiling. Nuclear Instruments and Methods **B31**, 567–575.

Lennard, W. N., Geissel, H., Alexander, T. K., Hill, R., Jackson, D. P., Lone, M. A., and Phillips, D. (1985). Depth Profiles of 35 keV ^{3}He Ions in Metals. Nuclear Instruments and Methods **B10-11**, 592–595.

Lindhard, J., Scharff, M., and Schiott, H. E. (1963). Range Concepts, and Heavy Ion Ranges. Matematisk-Fysiske Meddelelser udgivet af Det Kongelige Danske Videnskabernes Selskab **33**(14), 1–42.

Losee, D. L., Hossain, T. Z., Lavine, J. P., and Downing, R. G. (1987). Neutron Depth Profiles of Ion-Implanted Boron in Polymeric Films. In American Nuclear Society—Material Characterization Using Neutron Depth Profiling **55**, Los Angeles, CA, American Nuclear Society, pp. 209–210.

Maki, J. T. (1987). Migration, and Release of Helium-3 Implanted in Single Crystal Nickel. Ph. D. thesis, University of Michigan-Ann Arbor.

Maki, J. T., Downing, R. G., and Fleming, R. F. (1985). Nitrogen Concentration Distributions by Neutron Depth Profiling. NBS Technical Note 1207, 114–118.

Maki, J. T., Fleming, R. F., and Vincent, D. H. (1985). Deconvolution of Neutron Depth Profiling Spectra. Nuclear Instruments and Methods **B17**, 147–155.

Maki, J. T., Vincent, D. H., and Fleming, R. F. (1987). Migration, and Release of ^{3}He Implanted in Single-Crystal Nickel. In American Nuclear Society—Material Characterization Using Neutron Depth Profiling **55**, I. O. Macke, ed., Los Angeles, CA, American Nuclear Society, pp. 214.

Matsumura, H., Maeda, M., and Furukawa, S. (1983). Study on Impurity Diffusion in Glow-Discharged Amorphous Silicon. Japanese Journal of Applied Physics **22**(5), 771–774.

Matsumura, H., Sakai, K., Maeda, M., Furukawa, S., and Horiuchi, K. (1983). Measurement of Boron Diffusivity in Hydrogenated Amorphous Silicon by Using Nuclear Reaction $B^{10}(n,\alpha)Li^7$. Journal of Applied Physics **54**(6), 3106–3110.

Mezey, G., Szokefalvi-Nagy, Z., and Badinka, C. S. (1973). Measurement of the Boron Distribution in B-10 Implanted Silicon by the (n,α) Nuclear Reaction. Thin Solid Films **19**, 173–175.

Müller, K., Henkelmann, R., Bierseck, J. P., and Mertens, P. (1977). Determination of Low Dose Concentration Profiles in Solids by Means of (n,p), and (n,α) Reactions. Journal of Radioanalytical Chemistry **38**, 9–17.

Müller, K., Henkelmann, R., and Boroffka, H. (1975). The Determination of Low Dose Boron Implanted Concentration Profiles in Silicon by the (n,α) Reaction. Nuclear Instruments and Methods **129**, 557–559.

Müller, K., Henkelmann, R., Jahnel, F., Ryssel, H., Haberger, K., Fink, D., and Biersack, J. (1980). The Application of (n,α) Method for Boron Depth Profiling, and Channel-Blocking Measurements in Semiconductor Materials. Nuclear Instruments and Methods **170**, 151–155.

Myers, D. J. (1979) Range Profiles of Helium in Copper After Thermal Anneals. Masters, University of Michigan-Ann Arbor.

Myers, D. J., Halsey, W. G., King, J. S., and Vincent, D. H. (1980). He-3 Release from Copper. Radiation Effects **51**, 251–252.

Nagy, A. Z., Bogáncs, J., Gyulai, J., Csoke, A., Nazarov, V., Seres, Z., Szabó, A., and Yazvitsky, Y. (1977). Determination of Boron Range Distribution in Ion-Implanted Silicon by the $B^{10}(n,\alpha)Li^7$ Reaction. Journal of Radioanalytical Chemistry **38**, 19–27.

Nagy, A. Z., Vasvari, B., Duwez, P., Bakos, L., Bogáncs, J., and Nazarov, V. M. (1980). Variation of Boron Concentration in Metallic Glass Ribbons. Physica Status Solidi (a), **61**, 689–692.

Parikh, N. R., Chu, W. K., Wehring, B. W., and Miller, G. D. (1987). Boron-10 Distribution in Silicon, $TiSi_2$, and SiO_2 Using Neutron Depth Profiling. In American Nuclear Society—Material Characterization Using Neutron Depth Profiling **55**, I. O. Macke, ed., Los Angeles, CA, American Nuclear Society, pp. 211–212.

Parikh, N. R., Frey, E. C., Hofsäs, H. C., Swanson, M. L., Downing, R. G., Hossain, T. Z., and Chu, W. K. (1990). Neutron Depth Profiling by Coincidence Spectrometry. Nuclear Instruments and Methods **B45**, 70–74.

Pelikan, L., Rybka, V., Krejci, P., Hnatowicz, V., and Kvitek, J. (1982). Study of Boron Implantation in Ag-Si Layer Structures. Physica Status Solidi **72**, 369–373.

Riley, J. E., Jr. (1987). The Effects of Lithium Isotopic Anomalies on Lithium Niobate. Ferroelectrics **75**, 59–62.

Riley, J. E., Jr., and Downing, R. G. (1987). Quantitative Determination of Boron in Semiconductors Using Neutron Depth Profiling. In American Nuclear Society—Material Characterization Using Neutron Depth Profiling **55**, I. O. Macke, ed., Los Angeles, CA, American Nuclear Society, pp. 207.

Riley, J. E., Jr., Downing, R. G., and Fleming, R. F. (1987). Neutron Depth Profiling of Lithium in Lithium Niobate. In American Nuclear Society—Material Characterization Using Neutron Depth Profiling **55**, Los Angeles, CA, American Nuclear Society, pp. 214–215.

Riley, J. E., Jr., Mitchell, J. W., Downing, R. G., Fleming, R. F., Lindstrom, R. M., and Vincent, D. M. (1984). Material Analysis Using Thermal Neutron Reactions: Applications. Materials Science Forum **2**, 123–132.

Ryssel, H., Haberger, K., Hoffmann, K., Prinke, G., Dumcke, R., and Sachs, A. (1980). Simulation of Doping Processes. IEEE Transactions on Electron Devices IEEE Transactions on Electron Devices **ED27**(8), 1484–1492.

Ryssel, H., Kranz, H., Müller, K., Henkelmann, R. A., and Biersack, J. (1977). Comparison of Range, and Range Straggling of Implanted B-10, and B-11 in Silicon. Applied Physics Letters **30**(8), 399–401.

Ryssel, H., Müller, K., Biersack, J. P., Kruger, W., Lang, G., and Jahnel, F. (1980). Range, and Range Straggling of Ion-Implanted Boron in Cd0.2 Hg0.8 Te. Physica Status Solidi **57**, 619–624.

Ryssel, H., Müller, K., Haberger, K., Henkelmann, R., and Jahnel, F. (1980). High Concentration Effects on Ion Implanted Boron in Silicon. Applied Physics **22**, 35–38.

Ryssel, H., Prinke, G., Haberger, K., Hoffmann, K., Müller, K., and Henkelmann, R. (1981). Range Parameters of Boron Implanted into Silicon. Applied Physics **24**, 39–43.

Thwaites, D. I. (1983). Bragg's Rule of Stopping Power Additivity: A Compilation, and Summary of Results. Radiation Research **95**, 495–518.

Tjan, K., Fink, D., Biersack, J. P., and Städele, M. (1986). Implantation Profiles of Li in Metals. Nuclear Instruments and Methods **B15**, 54–57.

Ünlü, K. (1989). Helium-3 in Nickel Base Amorphous Metals: Surface Features, Subsurface Microstructure, Migration, and Release Upon Annealing. Ph. D. thesis, University of Michigan-Ann Arbor.

Ünlü, K., and Vincent, D. H. (1990). Range Profiles, and Thermal Release of ^{3}He Implanted into Various Nickel-Based Amorphous Alloys. Nuclear Instruments and Methods **A299**, 606–609.

Usmanova, M. M., Zverev, B. P., Simakhin, Y. F., Idrisov, K., and Zhumaev, N. (1984). Analysis of Distribution of Impurities by Using Neutron Beams. Yad. Fiz. Metody Kor. Pol. Mat. Met. 5–13.

Vandervorst, W., Shepherd, F. R., and Downing, R. G. (1985). High Resolution SIMS, and Neutron Depth Profiling of Boron Through Oxide-Silicon Interfaces. Journal of Vacuum Science and Technology **A3**(3), 1318–1321.

Vodopyanov, L. K., and Kozyrev, S. P. (1982). Ion Implantation of B^{+} in n-Hg0.8 Cd0.2 Te. Physica Status Solidi **72**, K133–K136.

Wilson, S. R., Gregory, R. B., Paulson, W. M., Krause, S. J., Gressett, J. D., Hamdi, A. H., McDaniel, F. D., and Downing, R. G. (1985). Properties of Ion-Implanted Polycrystalline Si Layers Subject to Rapid Thermal Annealing. Journal of the Electrochemical Society **132**(4), 922–929.

Zeitzoff, P. M., Hossain, T. Z., Boisvert, D. M., and Downing, R. G. (1990). Measurement, and Control of the Boron, and Phosphorus Concentration in LPCVD Borophosphosilicate Glass. Journal of the Electrochemical Society **137**(12), 3917–3922.

Ziegler, J. F., Cole, G. W., and Baglin, J. E. E. (1972). Techniques for Determining Concentration Profiles of Boron Impurities in Substrates. Journal of Applied Physics **43**(9).

Ziegler, J. F., Crowder, B. L., Cole, G. W., Baglin, J. E. E., and Masters, B. J. (1972). Boron Atom Distributions in Ion-Implanted Silicon by the (n,^{4}He) Nuclear Reaction. Applied Physics Letters **21**, 16–17.

Volume 98, Number 1, January–February 1993
Journal of Research of the National Institute of Standards and Technology

[J. Res. Natl. Inst. Stand. Technol. 98, 127 (1993)]

Prompt-Gamma Activation Analysis

Volume 98 Number 1 January–February 1993

Richard M. Lindstrom

National Institute of Standards and Technology,
Gaithersburg, MD 20899

A permanent, full-time instrument for prompt-gamma activation analysis is nearing completion as part of the Cold Neutron Research Facility (CNRF). The design of the analytical system has been optimized for high gamma detection efficiency and low background, particularly for hydrogen. Because of the purity of the neutron beam, shielding requirements are modest and the scatter-capture background is low. As a result of a compact sample-detector geometry, the sensitivity (counting rate per gram of analyte) is a factor of four better than the existing Maryland-NIST thermal-neutron instrument at this reactor. Hydrogen backgrounds of a few micrograms have already been achieved, which promises to be of value in numerous applications where quantitative nondestructive analysis of small quantities of hydrogen in materials is necessary.

Key words: activation analysis; cold neutron beams; elemental analysis; neutron capture gamma rays; nuclear analytical methods; prompt gamma-rays.

Accepted: August 10, 1992

1. Introduction

The nuclei of some elements of a sample placed in a field of neutrons absorb neutrons and are transformed to an isotope of higher mass number. Conventional neutron activation analysis employs the radiations emitted during the decay of radioactive products for elemental analysis. Some elements do not produce radioactive capture products, but do emit prompt gamma rays at the time of neutron capture. If the sample is placed in an external neutron beam from a reactor and viewed by a high-resolution gamma-ray spectrometer, these gamma rays allow qualitative identification and quantitative analysis of the neutron-capturing elements present in the sample.

As the simplest example, ^{1}H captures a neutron to produce an excited nuclear state of deuterium (Fig. 1). The energy of this state is precisely determined through the Einstein relation by the difference between the masses of the separated neutron and proton and that of the ground state of the deuteron. For a slow neutron this energy is 2224.6 keV. The only available deexcitation mode of this compound nucleus is by the emission of a gamma ray of 2223.23 keV energy, the balance of the reaction energy being carried off as recoil by the deuteron. The presence of a gamma ray of this energy in the spectrum of a specimen during neutron irradiation indicates the presence of hydrogen in the sample, and the intensity of this gamma ray relative to a standard is a quantitative measure of the amount of hydrogen present. This analytical technique has been given a number of names, most often neutron-capture prompt-gamma-ray activation analysis, which we abbreviate as PGAA. Cold neutrons offer substantially improved analytical sensitivity over thermal neutron beams.

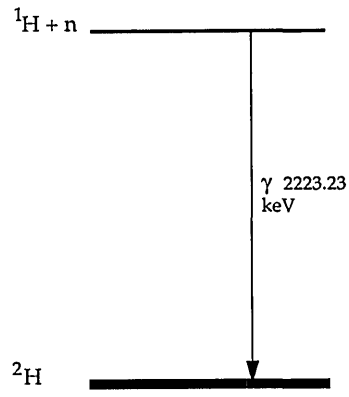

Fig. 1. Energy level diagram of the $A = 2$ system.

2. Principles

2.1 Experimental

The apparatus is conceptually simple (Fig. 2): A collimated beam of neutrons is extracted from the reactor and the sample inserted into the beam. A germanium detector, coupled to a multichannel pulse height analyzer and computer, measures the energy and intensity of the prompt gamma radiation emitted. The apparatus is completed by a beam stop to absorb the neutrons which are not absorbed by the sample, and the shielding necessary to protect the detector and the experimenters from stray gamma rays and neutrons.

2.2 Applicability

The use of neutron-capture gamma rays as a method of elemental analysis was introduced many years ago [1–3]. With the development of large, high-resolution gamma-ray detectors in the past decade, PGAA has taken its place as a complementary technique alongside conventional neutron activation analysis [4,5]. This method is particularly useful for determining nondestructively elements which absorb neutrons but do not produce radioactive products. The PGAA method analyzes the entire sample, including any substrate or container by which it is supported in the beam. The values of the nuclear parameters and the abundances of the

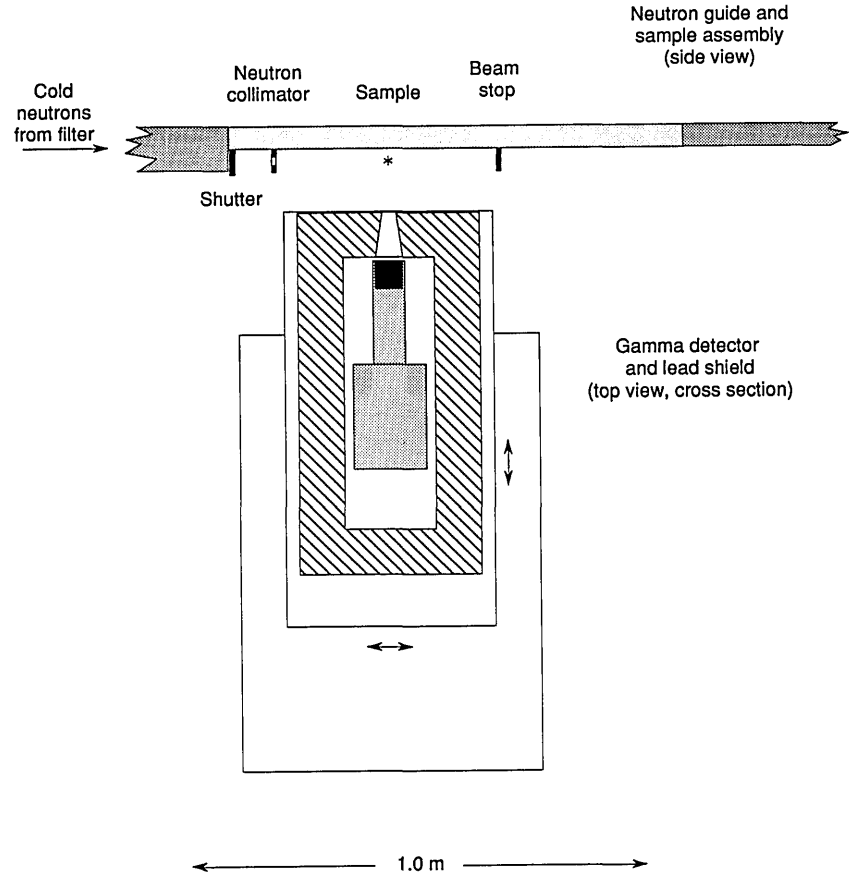

Fig. 2. Schematic of the PGAA apparatus.

elements in common materials are such that PGAA finds its greatest applicability in the determination of nonmetals that form the major and minor elements of geological and biological materials (H, C, N, Si, P, S), or trace elements with high thermal capture cross sections (B, Cd, Gd) that are not readily determinable by other techniques.

PGAA has been used alone to measure up to 21 elements in standard rocks [6,7], and in combination with conventional instrumental neutron activation analysis (INAA) to measure as many as 48 elements in coal without chemical separation [8]. These two complementary techniques have been extensively used in the study of natural and man-made atmospheric aerosols [9]. Two bibliographies of PGAA applications have been compiled [10,11].

Partly because of the need for continuing access to a reactor neutron beam, application of PGAA as a routine method of elemental analysis has been pursued to date at only a few laboratories on a full-time basis (for reviews see [12,13]). Because of lower neutron fluence rate and (usually) lower gamma-ray detection efficiency, the sensitivity of the method for most elements is two to three orders of magnitude worse than INAA, which limits most routine applications to the determination of the above mentioned elements. Irradiation times of at least several hours are required for most multi-element analysis, hence the throughput is low because only one sample can be irradiated and measured at a time.

The sensitivity of PGAA for a given element, expressed in counts·s^{-1}g^{-1}, is given by

$$S = \frac{N_A I \sigma \phi \Gamma \epsilon(E)}{M}, \quad (1)$$

where

S = sensitivity, counts·s^{-1}g^{-1}
N_A = Avogadro's number
I = fractional abundance of the capturing isotope
σ = neutron capture cross section, cm^2
ϕ = neutron fluence rate, cm^{-2}s^{-1}
Γ = gamma ray yield, photons per capture
$\epsilon(E)$ = gamma ray detection efficiency at energy E, counts/photon
M = atomic weight

The useful detection limit in practice is set by the sensitivity, the counting precision required, the blank (signal in the absence of a sample), and the peaked and continuum background caused by all components of the sample.

2.3 Sample Considerations

For a successful PGAA measurement, the sample must be large enough for the analyte to give a usefully strong signal, and small enough that the total capture rate is not too high for the detector and that neutron and gamma-ray scattering and absorption within the sample gives acceptably small errors. For many materials the optimum sample size lies between 0.1 and 10 g. Samples with special geometry such as entire silicon wafers can be accommodated. Ready access to the sample position may make feasible the nondestructive analysis at low temperature of volatile materials such as solid cometary samples [14].

In the analysis of plant and animal tissue, both detection limits and accuracy of PGAA measurements are often determined by the amount of hydrogen in the sample. The strong hydrogen capture gamma ray at 2223.2 keV is accompanied by a high Compton continuum, which makes the detection limits of other elements below 1995 keV poorer than they would otherwise be. Active Compton suppression can reduce this baseline substantially, but not eliminate it. Because of neutron scattering in the sample, a high concentration of hydrogen in the analytical matrix may lead to either larger or smaller signals per gram of the elements of interest [15,16]. This source of bias is minimized for spherical or near-spherical samples [17,18].

3. PGAA at the CNRF

3.1 Cold Neutrons

For chemical analysis, the ideal neutron field has the largest possible number of activating particles (slow neutrons) per second per unit area at the sample, and the smallest possible number of interfering particles (fast neutrons and background gamma rays) at the detector. A narrow beam is desirable so that the gamma-ray detector can be moved near the sample and the size of the shielding may be minimized. The beam need not be parallel, but its intensity should be uniform across the target.

A guided beam of cold neutrons meets these requirements very well [19]. Cold neutrons have been applied to PGAA in only a few laboratories to date [20–23], though several instruments are under

construction or active planning [24–26]. As Maier-Leibnitz pointed out long ago, the reduction in background by use of a high-quality beam is more important for analytical purposes than is an increase in the capture rate [19]. Henkelmann and Born have demonstrated this by collecting spectra with very low continuum background using a curved neutron guide at a cold source [23]. Experience has shown that with purely slow neutrons a neutron collimator and beam stop can be simple, lightweight, and compact; merely thin slabs of metallic ^{6}Li or a ^{6}Li compound without bulky thermalizing material or heavy gamma absorbers [27,21]. In consequence of the low neutron and gamma-ray background, the gamma detector can be placed close to the sample where the detection efficiency is high.

With the high gamma-ray detection efficiency possible with cold neutron beams, a practical limitation on the analytical usefulness of PGAA will be the ability to collect data at high counting rates without distortion. Recent advances in fast amplifier design [28] make it likely that the collection time for electrons in germanium may become the rate-limiting process. With large Ge detectors coupled with compact high-Z gating detectors, Ge-Ge coincidence counting may be done with profit. Multiparameter counting offers a good solution to the problem of interfering lines in a crowded spectrum.

The capture rate is also higher with cold than with thermal beams. Since capture cross sections for most target nuclei are inversely proportional to the neutron velocity, a neutron at 30 K is three times as effective as one at 300 K. Multiple reflections of the neutrons in a straight guide ensure that the intensity of the beam is more uniform across the sample than in most thermal irradiation facilities.

3.2 The CNRF Instrument

In the construction of the PGAA instrument at the CNRF, experience gained with cold neutrons at the German Nuclear Research Center in Jülich [21] and with over a decade's operation of the Maryland-NIST thermal instrument at the NBSR [6] has been incorporated to give high efficiency, low background, and facile operation [23]. The NIST instrument is installed on neutron guide NG-7 in the CNRF hall (see Fig. 7 of Prask et al., p. 11 this issue). A filter of 152 mm of single-crystal Bi and 127 mm of Be, both at liquid nitrogen temperature, is installed in the guide 3.1 m upstream from the PGAA sample position.

The apparatus is shown in Fig. 2. The lower 50×45 mm of the 50×110 mm NG-7 guide is extracted into air through a window of magnesium 0.25 mm thick. (The upper 50×50 mm beam continues past the PGAA station another 2 m to the velocity selector of the 30 m SANS instrument.) A translating shutter of ^{6}Li glass [30] 15 mm thick just behind the window admits the neutrons to the sample. The 10 mm thick glass slab which forms the bottom of the continuing guide is capped with 15 mm of ^{6}Li glass to avoid background from neutron scattering and capture. The neutron fluence rate was measured with 25 μm Au to be 1.5×10^8 $cm^{-2}s^{-1}$ (thermal equivalent: using $\sigma=\sigma_{th}=98.65$ b) at a reactor power of 20 MW.

The 1 m section of neutron guide adjacent to the PGAA station is made of boron-free silicate glass in order to avoid generating large amounts of ^{10}B capture gamma radiation from neutron leakage due to imperfections and misalignment of the guide. To reduce the neutron background, the outside of this guide section is covered with a ^{6}LiF-graphite paint [31]. A plate of fused $^6Li_2CO_3$ [32] with a 20 mm aperture, placed just behind the shutter, collimates the neutron beam to a size not much larger than a typical sample. A beam stop of ^{6}Li glass is placed behind the sample. Secondary fast neutrons generated in the collimator and beam stop by reactions of the fast tritons from ^{6}Li(n,α)^{3}H [33] have not yet been troublesome. Hydrogen-containing materials have been avoided to the maximum extent possible in the vicinity of the sample and detector. Samples are held in the beam in envelopes of 25 μm Teflon[1] FEP held by taut strings of 200 μm Teflon PFA between the prongs of a supporting fork. The volume between the neutron collimator and the beam stop assembly can be flooded with He at atmospheric pressure in a Teflon tent to reduce air scatter and reduce the hydrogen and nitrogen background.

A Ge gamma-ray detector (27% relative efficiency, 1.7 keV resolution) views the sample through a ^{6}Li-glass window along an axis at right angles to the neutron beam. The field of view of the detector is collimated so as to view chiefly the

[1] Certain commercial equipment, instruments, or materials are identified in this paper to specify adequately the experimental procedure. Such identification does not imply recommendation or endorsement by the National Institute of Standards and Technology, nor does it imply that the materials or equipment identified are necessarily the best available for the purpose.

sample. Environmental gamma radiation is reduced by shielding the detector with at least 100 mm of lead in all directions. The lead in turn is shielded from stray neutrons (which produce 7 MeV Pb capture gamma rays) with sheets of Boral. The shielded detector is carried on a table, the top of which is adjustable vertically and parallel to the beam with leadscrews. The table rolls on a track perpendicular to the beam to adjust the counting distance, which can be as close as 200 mm from the sample to the front face of the detector. Experiments are continually under way to optimize the shielding in the vicinity of the sample-detector assembly.

Gamma-ray spectra are acquired with a 16384-channel analog-digital converter (Canberra Nuclear Data ND581 ADC) coupled to a multichannel pulse height analyzer (ND556 AIM). The AIM is controlled over Ethernet by Nuclear Data acquisition and display software on a VAX-station 3100, which in turn communicates for data analysis with a MicroVAX 3400 and numerous other computers and terminals on the building-wide Ethernet [34].

3.3 Applications

Several measurements have been made in the short time that this cold-neutron instrument has been in operation [23]. Sensitivities of a number of elements were compared with those of the Maryland-NIST thermal PGAA instrument. At the same reactor power, sensitivities for most elements are a factor of four to six better with the cold-neutron apparatus. Expected detection limits with the CNRF instrument are given in Table 1, which are extrapolated from measured detection limits in biological and geological materials with the existing thermal PGAA instrument at NIST [13].

The first measurement with cold neutron PGAA in the CNRF was the determination of hydrogen in a sample of C_{60} fullerene "buckyballs" intended for neutron scattering studies. Cold-neutron PGAA found a hydrogen concentration of 0.92 ± 0.09 wt%, which is too high for satisfactory scattering measurements. After repurification of the material, hydrogen was measured again. A 600 mg sample, contained in the aluminum sample holder intended for the scattering measurements, was irradiated in the PGAA beam for 100 min live time while surrounded with a flowing atmosphere of He contained in a Teflon tent. A clear H peak was visible at more than ten times the intensity of a blank sample of spectroscopic grade graphite. The sample was found to contain 0.077 ± 0.014 wt % H, which was adequately low for the neutron scattering measurements. Numerous samples of pure and substituted fullerenes have been analyzed (e.g., [35]).

In other work, hydrogen was measured in a Pr_2CuO_4 superconductor analog; a 1 h irradiation gave a concentration of $[H] = 0.017 \pm 0.010$ wt %. Hydrogen was sought in a 50 nm borophosphosilicate glass film on a quarter of a 10 cm silicon wafer; an upper limit of 2 $\mu g/cm^2$ was found.

Table 1. Expected interference-free detection limits for neutron-capture prompt gamma-ray activation analysis[a]

Element	Det. limit, μg	E_γ, keV
Hydrogen	2	2223
Boron	0.003	478
Carbon	4000	1262, 4945
Nitrogen	400	1885, 5298
Fluorine	500	583, 1634(D)[b]
Sodium	7	472, 869
Magnesium	200	585, 1809
Aluminum	50	1779(D), 7724
Phosphorus	200	637, 1072
Sulfur	30	840, 2379
Chlorine	1	517, 786
Potassium	10	770, 7771
Calcium	60	519, 1943
Titanium	4	342, 1381
Vanadium	4	1434(D)
Chromium	15	749, 834
Manganese	3	847(D), 1811(D)
Iron	30	352, 7631
Cobalt	1	230, 556
Nickel	20	283, 465
Copper	1	159, 278
Zinc	70	115, 1077
Arsenic	10	164
Selenium	4	239
Bromine	10	195, 244
Strontium	40	898, 1836
Molydenum	15	720,778
Silver	3	192, 236
Cadmium	0.01	559, 651
Indium	0.5	162, 186
Barium	10	627, 818
Neodymium	1	619, 697
Samarium	0.003	333, 439
Gadolinium	0.002	182, 1186
Gold	3	215
Mercury	0.15	368
Lead	4000	7368

[a] Assumptions: 24 h irradiation with NBSR at 20 MW.
[b] (D) signifies a decay gamma ray, not prompt.

4. Future Plans

Future enhancements to the counting system will include a redesigned sample positioning and shield-

ing assembly, a Compton suppressor, an automatic sample changer, and a second detector system which will permit γ-γ coincidence measurements. A new cold source under design is predicted to increase the neutron fluence rate by a factor of about five. The difficulties associated with working adjacent to the upper guide—restricted space and Si capture background—may be ameliorated in the future by deflecting the PGAA beam away from the guide. Additional improvement in sensitivity is possible since neutron optics may be used to focus cold neutrons onto a small area. Gains of an order of magnitude in fluence rate may be obtainable by these techniques [36–38].

Acknowledgments

I thank D. L. Anderson, R. R. Greenberg, E. A. Mackey, C. A. Stone, D. H. Vincent, and R. Zeisler for numerous contributions to this work. I also thank W. A. Bowman and J. K. Langland for mechanical design and construction, and R. L. Cappelletti, J. N. Cox, and J. W. Lynn for supplying samples.

5. References

[1] W. G. Lussie and J. L. Brownlee, Jr., in Proc. Conf. Modern Trends in Activation Analysis, College Station, TX (1965), p. 194.
[2] T. L. Isenhour and G. H. Morrison, Anal. Chem. **38**, 162 (1966).
[3] T. L. Isenhour and G. H. Morrison, Anal. Chem. **38**, 167 (1966).
[4] M. P. Failey, D. L. Anderson, W. H. Zoller, G. E. Gordon, and R. M. Lindstrom, Anal. Chem. **51**, 2209 (1979).
[5] A. G. Hanna, R. M. Brugger, and M. D. Glascock, Nucl. Inst. Methods **188**, 619 (1981).
[6] D. L. Anderson, Y. Sun, M. P. Failey, and W. H. Zoller, Geostand. Newslett. **9**, 219 (1985).
[7] S. A. Kerr, R. A. Oliver, P. Vittoz, G. Vivier, F. Hoyler, T. D. MacMahon, and N. I. Ward, J. Radioanal. Nucl. Chem. **113**, 249 (1987).
[8] M. S. Germani, I. Gokmen, A. C. Sigleo, G. S. Kowalczyk, I. Olmez, A. M. Small, D. L. Anderson, M. P. Failey, M. C. Gulovali, C. E. Choquette, E. A. Lepel, G. E. Gordon, and W. H. Zoller, Anal. Chem. **52**, 240 (1980).
[9] M. E. Kitto and D. L. Anderson, in The Chemistry of Acid Rain (Symp. Ser. 349), R. W. Johnson, and G. E. Gordon, eds., Am. Chem. Soc., Washington (1987) p. 84.
[10] E. S. Gladney, A Literature Survey of Chemical Analysis by Thermal Neutron-Induced Capture Gamma-Ray Spectroscopy, Los Alamos Sci. Lab. Report LA-8028-MS (1979).
[11] M. D. Glascock, A Literature Survey of Elemental Analysis by Neutron-Induced Prompt Gamma-Ray Spectroscopy and Related Topics, University of Missouri, Columbia, (unpublished, 1984).
[12] R. E. Chrien, in Neutron Radiative Capture, B. J. Allen, I. Bergqvist, R. E. Chrien, and D. Gardner. eds., Pergamon, Oxford, (1984) p. 187.
[13] R. M. Lindstrom and D. L. Anderson, in Capture Gamma-Ray Spectroscopy and Related Topics–1984, S. Raman, ed., Am. Inst. Physics, New York (1985), p. 810.
[14] D. J. Lindstrom, in Proc. NASA Workshop on Analysis of Returned Comet Nucleus Samples, unpublished (1989).
[15] J. R. D. Copley and C. A. Stone, Nucl. Inst. Methods **A281**, 593–604 (1989).
[16] E. A. Mackey, G. E. Gordon, R. M. Lindstrom, and D. L. Anderson, Anal. Chem. **63**, 288 (1991).
[17] J. R. D. Copley, Nucl. Inst. Methods **A307**, 389 (1991).
[18] E. A. Mackey, G. E. Gordon, R. M. Lindstrom, and D. L. Anderson, Anal. Chem. **64**, 2366–2371 (1992).
[19] H. Maier-Leibnitz and T. Springer, Reactor Sci. and Tech. **17**, 217 (1963).
[20] R. Henkelmann and H. J. Born, J. Radioanal. Chem. **16**, 473–481 (1973).
[21] R. M. Lindstrom, R. Zeisler, and M. Rossbach, J. Radioanal. Nucl. Chem. **112**, 321–330 (1987).
[22] M. Rossbach, R. Zeisler, and R. M. Lindstrom, In Multipurpose Research Reactors (IAEA-SM-300/16), IAEA, Vienna (1988), p. 475.
[23] R. M. Lindstrom, R. Zeisler, D. H. Vincent, R. R. Greenberg, C. A. Stone, D. L. Anderson, D. D. Clark, and E. A. Mackey, proc. 8th Internat. Conf. Modern Trends in Activ. Anal. (Vienna, 1991), to be published in J. Radioanal. Chem.
[24] D. D. Clark, T. Emoto, C. G. Oullet, E. Pekrul, and J. S. Berg, (1989), in J. W. Behrens and A. D. Carlson, eds., 50 Years With Nuclear Fission, Am. Nucl. Soc. (1989), p. 855.
[25] G. Molnár, Z. Révay, A. Veres, A. Simonits, and H. Rausch, proc. 8th Internat. Conf. Modern Trends in Activ. Anal. (Vienna, 1991), to be published in J. Radioanal. Chem.
[26] C. Yonezawa, A. K. H. Wood, M. Hoshi, Y. Ito, and E. Tachikawa, Nucl. Inst. Methods A, in press (1993).
[27] T. Kobayashi and K. Kanda, Nucl. Inst. Methods **204**, 525 (1983).
[28] G. P. Westphal, Nucl. Inst. Methods **A299**, 261 (1990).
[29] D. L. Anderson, M. P. Failey, W. H. Zoller, W. B. Walters, G. E. Gordon, and R. M. Lindstrom, J. Radioanal. Chem. **63**, 97 (1981).
[30] C. A. Stone, R. Zeisler, D. H. Blackburn, D. A. Kauffmann, and D. C. Cranmer, in C. O'Connor, ed., NIST Tech. Note 1285 (1990), p. 116.
[31] J. E. Nelson, Argonne National Laboratory, personal communication (1989).
[32] B. M. Rustad, C. J. Christensen, and B. Skytte Jensen, Nucl. Inst. Methods **33**, 155 (1965).
[33] M. A. Lone, D. C. Santry, and W. M. Inglis, Nucl. Inst. Meth. **174**, 521 (1980).
[34] M. Blaauw and R. M. Lindstrom, proc. 8th Internat. Conf. Modern Trends in Activ. Anal. (Vienna, 1991), to be published in J. Radioanal. Chem.
[35] D. A. Neumann, J. R. D. Copley, R. L. Cappelletti, W. L. Kamitakahara, R. M. Lindstrom, K. M. Creegan, D. M. Cox, W. J. Romanow, N. Coustel, J. P. Jr. McCauley, N. C. Maliszewskyj, J. E. Fischer, and A. B. III Smith, Phys. Rev. Lett. **67**, 3808–3811 (1991).
[36] D. F. R. Mildner, Nucl. Inst. Methods **A299**, 416 (1990).
[37] M. A. Kumakhov, V. A. Sharov, Nature **357**, 390 (1992).
[38] H. Chen, R. G. Downing, D. F. R. Mildner, W. M. Gibson, M. A. Kumakhov, I. Yu. Ponomarev, and M. V. Gubarev, Nature **357**, 391 (1992).

About the author: *Richard M. Lindstrom is a research chemist with the Nuclear Methods Group, Inorganic Analytical Research Division of the NIST Chemical Science and Technology Laboratory. The National Institute of Standards and Technology is an agency of the Technology Administration, U.S. Department of Commerce.*

Volume 98, Number 1, January–February 1993
Journal of Research of the National Institute of Standards and Technology

[J. Res. Natl. Inst. Stand. Technol. 98, 135 (1993)]

Facilities for Fundamental Neutron Physics Research at the NIST Cold Neutron Research Facility

Volume 98 | Number 1 | January–February 1993

M. Arif, M. S. Dewey, G. L. Greene, and W. M. Snow

National Institute of Standards and Technology, Gaithersburg, MD 20899

The features of two fundamental neutron physics research stations at the NIST cold neutron research facility are described in some detail. A list of proposed initial experimental programs for these two stations is also given.

Key words: beta decay; neutron decay; neutron interferometry; neutron lifetime, neutron wave; vibration isolation.

Accepted: July 8, 1992

1. Introduction

In most of the experimental facilities at the CNRF, neutrons are used as probes to study structures and excitations in condensed matter. By contrast, the two research stations described in this article are devoted to the study of the neutron itself and its interactions. This area of research has come to be referred to as "fundamental" neutron physics.

The properties of cold neutron beams at guide halls are well-suited to fundamental neutron physics experiments. The slower average speed and consequent higher density of the neutrons in a cold beam (as compared to thermal and epithermal beams) result in improved accuracy in many measurements due to the longer interaction times with matter and external fields and the higher neutron decay activity per unit length. The relative ease with which cold neutron beams can be polarized and manipulated is very important for a number of experiments: in particular, it is crucial for experiments which search for effects due to parity and time reversal violation. Finally, the relatively quiet environment of a cold neutron guide hall (as compared to a reactor building) can lead to enhanced sensitivity in delicate experimental techniques such as neutron interferometry.

The fundamental neutron physics program at the NIST cold neutron research facility has two separate positions: A) A fixed neutron interferometer position, and B) an end guide position where appropriate instruments will be placed as needed to carry out various fundamental neutron physics experiments. We will first focus our attention on a general description of the neutron interferometry technique. A more detailed description of this technique can be found in references [1]–[7].

2. Neutron Interferometry

2.1 Background

A neutron interferometer is topologically analogous to the Mach-Zehnder interferometer of classical optics and operates on the basis of coherent splitting and recombination of the incident wave amplitude of a neutron wave through Bragg reflection in perfect crystals. Various arrangements

have been realized to obtain interference effects between spatially separated coherent neutron beams. One of the most commonly used schemes is shown in Fig. 1a. The device consists of three very flat identical "ears" cut from a monolithic piece of silicon perfect single crystal leaving the three ears attached to a common base. The ears are usually cut perpendicular to strongly reflecting (220) lattice planes. Such a device is typically 50 to 100 mm in length and ears are typically 1 to 3 mm thick, 30 to 100 mm wide and 10 to 30 mm high.

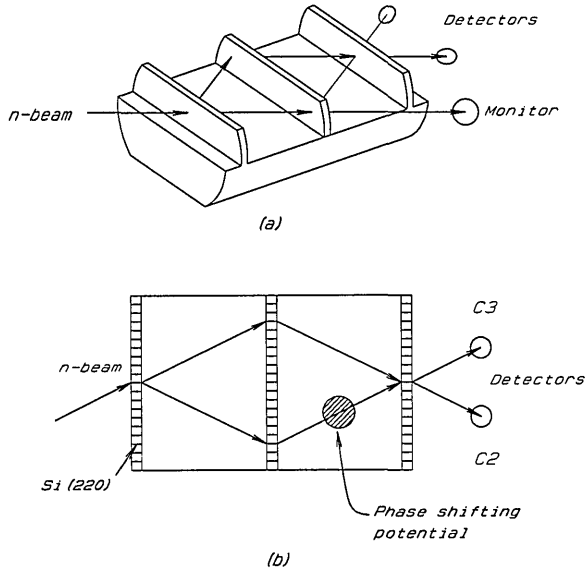

Fig. 1. Schematic of ILL type neutron interferometer. Such a device was first tested by Rauch, Treimer, and Bonse in 1974.

In a neutron interferometry experiment the *phase* of a neutron wave becomes directly accessible. In this sense it is very different from other neutron experimental techniques where only the *intensity* of a neutron wave is accessible. In a simple manner the operating principle of such an interferometer can be understood from Fig. 1b. A nominally monoenergetic incident beam is coherently split by Bragg reflection in the first crystal ear (splitter). These two coherent beams are again split by the second ear (mirror) and finally two of the beams from the second ear overlap at the third ear (analyzer). If one of these interfering beams is phase shifted by an amount β with respect to the other beam due to interaction of some perturbing potential it can be shown that the expected intensities in the two detectors C2 and C3 are of the form,

$$I(\mathrm{C2}) = A - B\cos\beta \qquad (1)$$

$$I(\mathrm{C3}) = B\,(1+\cos\beta)\,, \qquad (2)$$

where A and B are constants depending on the properties of interferometer crystal and incident beam flux. The above equations predict that the sum of the intensities of the outgoing interfering beams is a constant. As a result the intensity is "swapped" back and forth between C2 and C3 and as evident from the above equations shows sinusoidal patterns. Relevant information about the interaction between the neutron wave function and the perturbing potential may be extracted from the phase, amplitude, and period of the intensity oscillation pattern.

The transit time of thermal neutrons through such a device is rather long (typically 30 to 100 μs) and there are perhaps 10^9 quantum wavelengths in each path. To maintain the Bragg condition for a given wavelength of the neutron beam, the three ears must remain aligned within better than 10^{-6} rad. As a result neutron interferometry experiments are very easily adversely affected by environmental disturbances. Consequently, very stringent thermal, vibrational, acoustic, and geometric tolerances are required for successful operation of a neutron interferometer.

Research in neutron interferometry is primarily focused on three broad areas: the measurement of fundamental properties and interactions of neutrons, tests of fundamental propositions of quantum mechanics, and development of new measurement techniques. Since the first neutron interferometry experiment carried out by Rauch, Triemer, and Bonse in 1974, a large number of beautiful experiments have been performed to probe certain aspects of quantum mechanics which were previously either untested or indirectly inferred. The verification of the principle of equivalence in the quantum limit, the spinoral nature of fermions, and the Aharonov-Casher effect are some examples. A list of important neutron interferometry experiments in the last decade and a half is listed in Table 1. A list of proposed initial experiments for the CNRF interferometer is given in Table 2.

Table 1. Neutron Interferometry (1974–1990)

1. First test of Si-crystal interferometer.
   Vienna (1974).
2. Sign change of fermion wave function during 2π precession.
   ILL,[a] MURR[b] (1975, 1976).
3. Gravitationally induced quantum interference.
   Ann Arbor, MURR (1975, 1980, 1985, 1986).
4. Neutron Sagnac effect.
   Earth's rotation. MURR (1979).
   Turntable MIT[c] (1984).
5. Neutron Fizeau effect.
   Moving boundaries. ILL (1981, 1985).
   Stationary boundaries, MURR (1985, 1988).
6. Search for non-linear terms in the Schrödinger equation.
   LL interferometer. MIT (1981).
   Long wavelength fresnel diffraction. ILL (1981).
7. Search for Aharonov-Bohm effect for neutrons.
   MIT (1981).
8. Measurement of neutron longitudinal coherence length.
   MURR (1983).
9. Coherent superposition of spin states.
   ("Wigner phenomena") ILL (1983).
10. Search for quaternions in quantum mechanics.
    MURR (1984).
11. Quantum interference in accelerated frames.
    ILL (1983).
12. Search for new gauge fields.
    MIT (1983).
13. Precision measurement of scattering lengths.
    ^{149}Sm, ^{235}U, ^{3}He, ^{3}H (four body nuclear reaction).
    ILL, MURR (1975-1985).
14. Observation of the Aharonov-Casher effect.
    MURR (1989).
15. Stochastic vs. deterministic attenuation of neutrons.
    ILL (1987).
16. Neutron spin-pendellosung resonance.
    MIT (1988).

[b] MURR—Unversity of Missouri Research Reactor.
[c] MIT —Massachusetts Institute of Technology.
[a] ILL —Institut Laue-Langevin.

Table 2. Initial scientific programs

End position	Interferometer position
1. Determination of neutron lifetime.	1. Michelson-Morley experiment.
2. Time reversal in neutron-decay.	2. Wheeler delayed choice experiment.
3. Parity violation in neutron-nuclear scattering.	3. Precision Aharonov-Casher experiment.
4. Measurement of fundamental constants of neutron.	4. Search for Mahshoon effect.
5. Determination of neutron-decay coefficient.	5. Large-scale interferometer development: Cavendish experiment.
6. Studies of polarized neutron interaction with polarized nuclei.	

2.2 The NIST Interferometer

2.2.1 Interferometer Position This position is situated in neutron guide number 7 (NG-7). The neutron interferometer experimental facility will consist of two major parts: (1) a double crystal monochromator assembly for extracting neutrons from the neutron guide, and (2) an environmentally controlled enclosure for experiments. These are discussed in the next few sections. In addition, a special interferometer mounting, neutron detection, and beam manipulation and analyzing setup will be built. A complementary x-ray setup will also be constructed for experiments and crystal diagnostics.

2.2.2 Monochromator System A variable-energy, monochromatic beam is provided by a double-crystal monochromator assembly. A schematic drawing of the overall layout of the interferometer station is shown in Fig. 2; a diagram of the double-crystal monochromator is shown in Fig. 3. This double-crystal arrangement allows the neutron beam to remain unidirectional at all attainable wavelengths. The range of 2θ angles is 40° to 90°, providing neutrons with energy range of 15.6 to 3.64 meV from pyrolytic graphite (002) and 47.7 to 11.2 meV from pressed silicon (220) monochromator crystals. The reflectivity of pyrolytic graphite (002) crystals in the range of wavelengths specified is 80% to 90%, while for pressed Si(220) it is expected to be 60% to 70%. Higher-order beam contaminants may be filtered-out with pyrolytic graphite or Be. The beam paths are necessarily rather long in this assembly. Therefore, to reduce attenuation due to air scattering and divergence, He-filled guide tubes will be employed. Each monochromator crystal is mounted on small high-precision rotary tables and positioned in angle, translation, and tilt by computer-driven stepping motors. This entire monochromator assembly is situated up-stream from the enclosure housing the interferometer vibration isolation platform discussed in the next section. The first monochromator crystal is mounted inside the neutron guide. This provides a significant reduction in background as the primary neutron beam does not pass through any windows or suffer air scattering between the primary guide sections. A novel monochromator support has been devised (Fig. 4) which allows manipulation of the horizontal tilt as well as the axial position of the crystal within the guide. The monochromator inside the guide has been installed recently. All its components have been tested and work well. A preliminary measur-

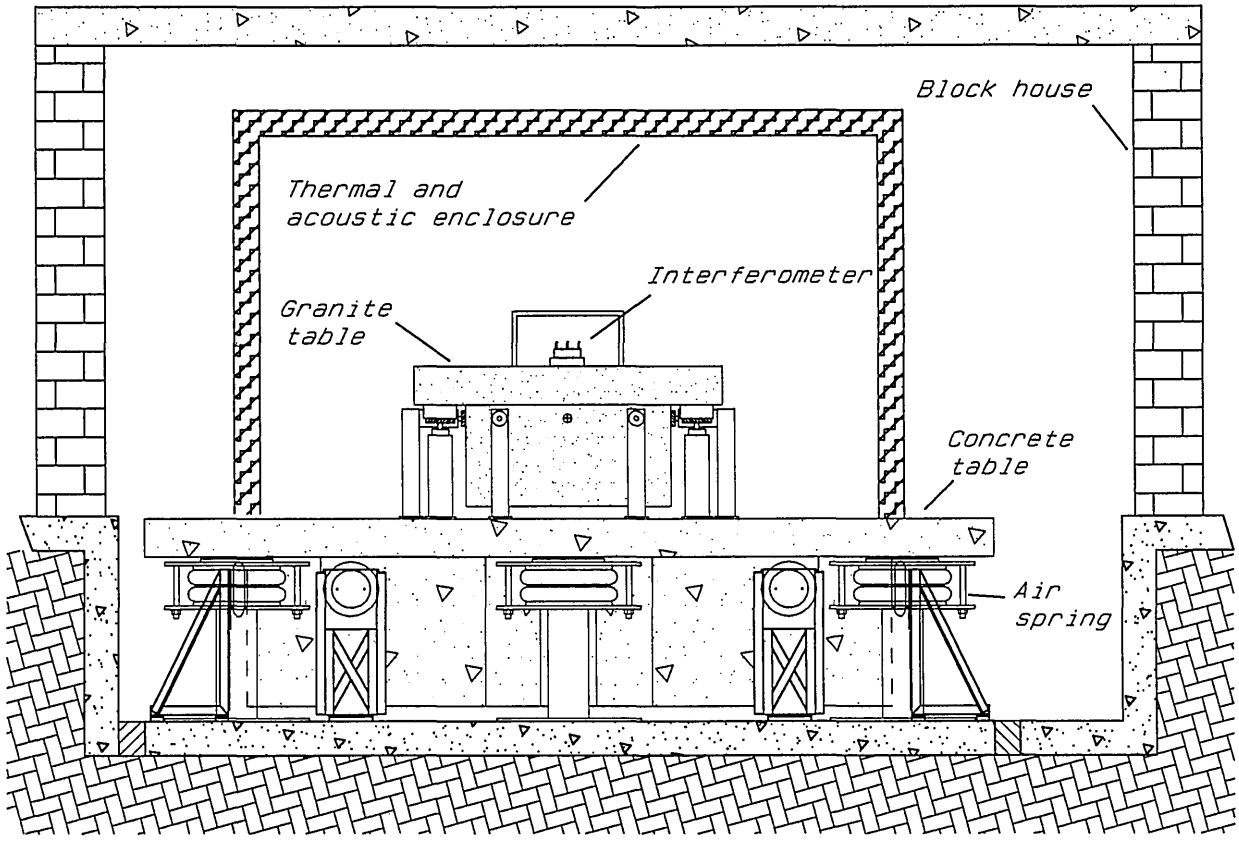

Fig. 2. Schematic of the NIST interferometer setup.

ment shows a neutron flux of $\sim 1.0 \times 10^6$ neutron $\cdot$ cm$^{-2} \cdot$ s^{-1} at nominal 14.8 meV neutron energy. To the best of our knowledge this is the first and only monochromator operating inside a neutron guide.

2.2.3 Environmental Control Perfect crystal neutron interferometers are extraordinarily sensitive to environmental perturbations. Temperature gradients of millidegrees, displacements of fractions of an nm, velocities of μm/s, rotational velocities of μrad/s, and vibrational amplitudes of nm are sufficient to seriously interfere with experiments. Obviously, these problems are more severe for the large, split-component (two or more pieces) interferometers. The major design goal for the interferometer station is to attain the best practical level of thermal, vibrational, acoustic, and seismic isolation. In the following we describe the environmental system designed to minimize environmental noise. The philosophy of the overall environmental system is based on the notion of "nested" isolation sub-systems. Experience has shown that it is difficult to obtain suitable isolation in a single "step". An implementation of this philosophy is outlined in Fig. 2.

2.2.4 Thermal Isolation At least three levels of thermal control are envisioned. In each, a temperature control servo will be used to stabilize the ambient temperature: the first environment will consist of a large ($\sim 6 \times 8 \times 3$ m) concrete block house. The temperature of this large house will be thermostatically controlled by adjusting the flow of chilled water through radiators mounted on the interior house walls. Within this larger enclosure there is a smaller, acoustically isolated, quasi-hermetic room containing a monolithic granite surface plate with mass of ~3000 kg. This enclosure has been designed and built. The temperature of this plate will be controlled by a heater fed back through an autotuning PID controller. By judicious selection of time constants, it will be possible to avoid coupled instabilities between these two nested servo loops. The third sub-environment will consist of a relatively small isothermal Aluminum Box whose temperature will also be controlled by a PID controlled Peltier heater/cooler.

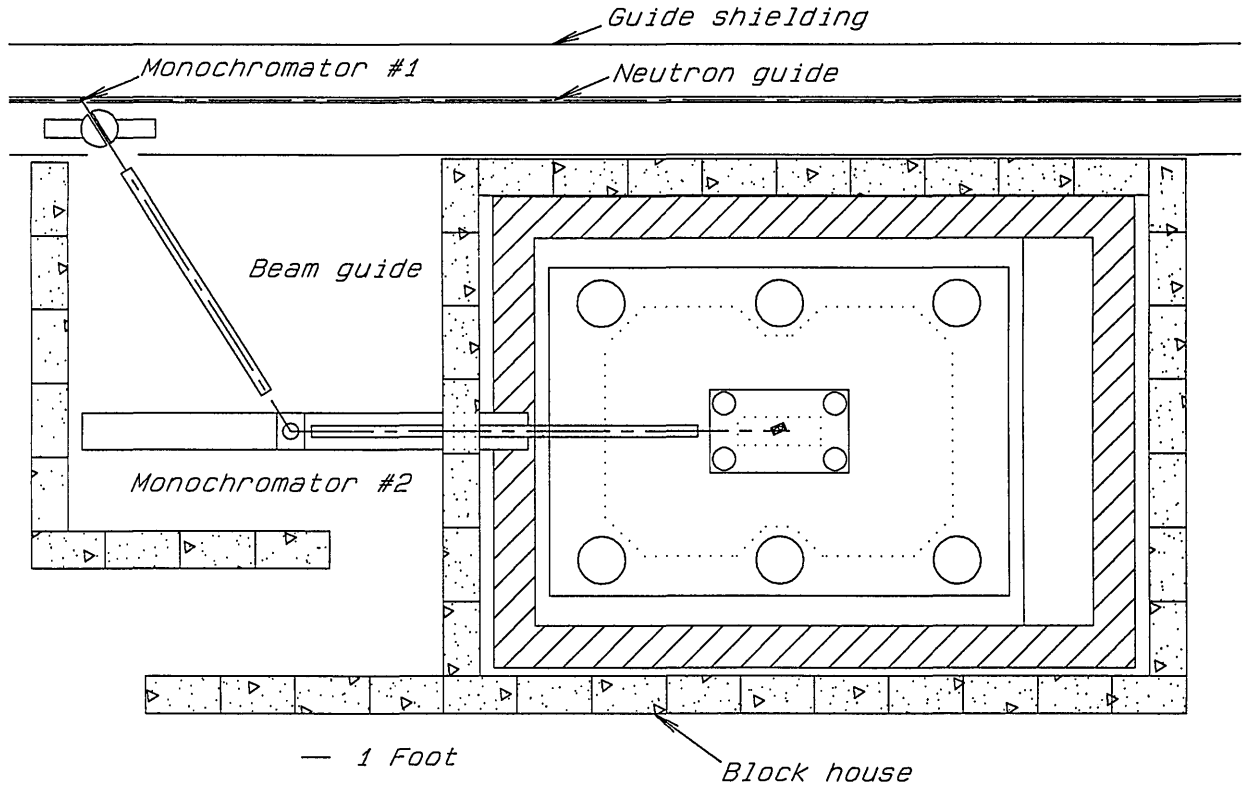

Fig. 3. Diagram showing the double crystal monochromator layout for the NIST interferometer setup. The design of this monochromator system provides a unidirectional beam for the interferometer at all accessible incident neutron energies.

2.2.5 Vibrational and Seismic Isolation If the interferometer were rigidly attached to the floor of the guide hall, it would be subjected to very significant accelerations (even micro "*g*" accelerations are significant). Therefore, major steps must be taken to decouple the interferometer from floor-born disturbances. Once again a system of nested isolation techniques has been employed. The first stage of isolation has already been provided for in the design of the guide hall building. The interferometer position is located on an independent foundation which is coupled to the rest of the building only through compliant joints (Fig. 2). Thus, the very significant amount of vibration associated with a reactor based experimental environment, which would normally be conducted along the path provided by continuous reinforced concrete, has been eliminated. It should be noted that no neutron interferometry experiments carried out thus far have had the benefit of such an independent foundation slab. In all other installations the interferometer position was located on a common foundation with reactor pumps, cranes, and heavy equipment. This feature of the proposed facility promises a very significant improvement over all previous installations. The second stage of vibration isolation is a pneumatically supported reinforced concrete slab of dimensions $\sim 5 \times 4 \times 1$ m. This slab, with a mass of approximately ~ 37000 kg rests on commercial pneumatic airspring supports. Such mass/spring systems can be conveniently modeled as damped harmonic oscillators. In this case the resonant frequency will be about 2 Hz. The response of such resonant systems to external driving forces at frequencies above the resonant frequency decreases logarithmically at about 6 dB/octave. Thus, such a system acts as a "low pass" filter for vibrational noise. High frequency vibrations will therefore be significantly reduced. In such a system it is important to insure that any internal resonances of the isolated mass have frequencies far higher than the characteristic mass/spring resonance of the isolator. If these criteria are not met, there may be significant coupling between the internal modes of the isolated mass and the "rigid body" excitations. The internal modes of the primary mass were estimated using dynamic finite element analysis. It has been

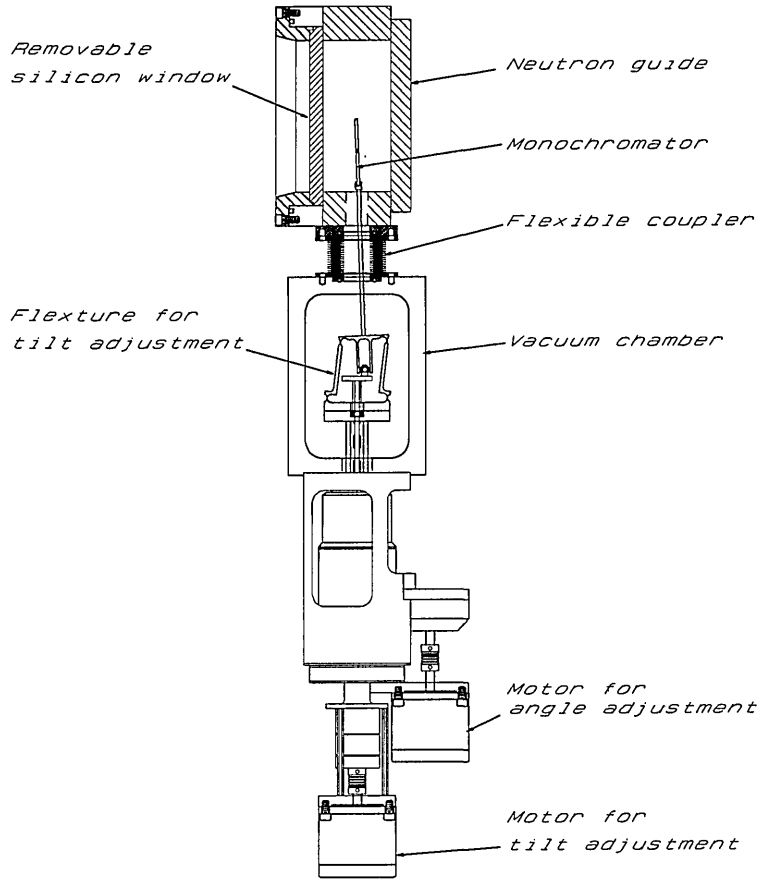

Fig. 4. Diagram of the monochromator assembly which would allow rotation as well as tilting of a monochromator inside the guide.

determined that the lowest modes of the concrete slab lie in the range 80-100 Hz which is safely above the 2 Hz rigid body frequency. This second stage of vibration isolation has been installed recently. All its components and control system have been tested and this stage of vibration isolation has become operational. To further reduce vibration coupling to the interferometer, a second pneumatically supported granite table will be placed on top of the floating floor slab. This table has a mass of about 3000 kg and will be supported with a resonant frequency of about 0.5 Hz in the vertical and about 0.1 Hz in the horizontal directions. Because both the frequency and mass of this second suspended object are an order of magnitude less than the floating floor slab, coupled motions between the two coupled resonators will be small. In such a regime the overall isolation above the resonances will be multiplicative. Thus about 12 dB/octave roll-off in the high frequency regime can be expected. A practical problem associated with all pneumatic isolators arises from the intrinsic long term "softness" of such supports. A platform mounted on totally passive isolators (i.e., ones that are sealed) will exhibit long term positional drifts due to changes in ambient temperature, barometric pressure, or due to isolator leaks. Using a long time-constant electro-pneumatic servo mechanism (Ref. [7]), long-term positional stability of <10 μrad will be maintained.

2.2.6 Acoustical Isolation Unwanted instrumental vibrations can result not only from floor-born seismic noise, but also from airborne acoustic noise. To minimize coupling, both enclosures have been designed with careful attention to acoustic isolation. In addition they are lined with highly absorbing anechoic foam panels. Such panels are very effective in reducing reverberation times.

3. Fundamental Neutron Physics End-Guide Station

3.1 General

The end position on the NG-6 beam line at the CNRF is devoted to experiments in the field of fundamental neutron physics. The unique properties of the neutron which make it an ideal probe for a broad range of scattering experiments also make it an ideal system with which to address a number of important questions in nuclear physics, particle physics, and astrophysics. Typical experiments in the field include measurements of the static properties of the neutron, tests of fundamental symmetry principles, and investigations of neutron beta decay. The reader is referred to the proceedings of a recent conference in Ref. [5] to get a fuller view of the field.

In contrast to the neutron interferometry facility described in this paper, there is no permanently installed instrumentation or specific technique to be described. The properties of the beam must be matched to the requirements of each experiment individually. Aside from the beam shutter and a beam stop, the only other permanent equipment on the beamline is a filter cryostat to remove fast neutrons and gamma rays. A variety of collimators, polarizers, spin flippers, and transport tubes can be made available for individual experiments. The capture flux at the end of the 15×6 cm NG-6 guide has been measured to be about $4.0 \times 10^{+8}$ neutrons/(cm^{2}s), which is about a factor of nine lower than the 3×5 cm SN-7 guide at the ILL. This flux will increase significantly after the installation of the hydrogen cold source.

A measurement of the lifetime of the neutron is currently underway at NG-6. Testing of a prototype detector and polarizer system designed to search for time reversal invariance violation in neutron beta decay has been performed at NG-6. Other experiments in the near future may include searches for parity violation in neutron-nucleus scattering and studies of polarized neutron interactions with polarized nuclei.

3.1.1 The Neutron Lifetime Measurement We will describe the neutron lifetime experiment in some detail. This experiment developed from an earlier collaboration between NIST, the University of Sussex, and the Scottish Universities Research and Reactor Center, with related work on advanced methods of neutron flux measurements performed by NIST, the Central Bureau for Nuclear Measurements, the Scottish Universities Research and Reactor Center, Harvard University, and Los Alamos National Laboratory. A more detailed description than that given here can be found in Ref. [5].

A free neutron decays into a proton, an electron, and an electron antineutrino with a lifetime on the order of 900 s. There are a number of areas of physics for which a more accurate value for the neutron lifetime, τ_n, is important. Within the context of the V-A theory of weak interactions a more accurate value for τ_n, in combination with neutron decay asymmetry measurements, can provide accurate values for the weak vector and axial vector coupling constants g_A and g_V. In an astrophysical context, the rate of energy generation in the sun is proportional to g_A^2, and a reduction in the accepted value of the neutron lifetime could contribute to an understanding of the solar neutrino problem. The neutron lifetime also has an important effect on the rate of helium production in the early universe (an important test of big bang nucleosynthesis) and on nucleosynthesis-derived limits on the number of light neutrino species, which constrain the number of generations in the present-day Standard Model of particle physics. The importance of these issues, coupled with the well-known inconsistencies in many earlier measurements, provide strong motivation for more accurate measurements of τ_n.

The strategy of our experiment is to measure the neutron decay rate N_{decay} and the mean number of neutrons N_n within a well-defined volume traversed by a cold neutron beam. The decay rate is related to these quantities by the differential form of the exponential decay law $N_{decay} = N_n \tau_n^{-1}$. Figure 5 shows a schematic outline of the method. N_{decay} is measured in our experiment by trapping the protons produced in the decay with a Penning trap and counting the trapped protons. N_n is measured by requiring the neutrons leaving the decay volume to pass through an accurately calibrated neutron monitor.

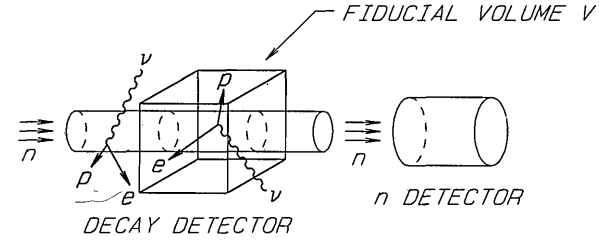

$$\dot{N}_{decay} = \rho_n V \tau^{-1}$$

$$N_{decay} = \frac{\dot{N}}{\bar{V}} V \tau^{-1}$$

Fig. 5. Illustration of the idea for the neutron lifetime measurement.

The response of the neutron monitor is proportional to the beam flux weighted by the reciprocal of the velocity, in the absence of low energy resonances, the absorption cross section for neutrons is proportional to $1/v$. Since N_n is simply the beam flux integrated over the decay volume weighted by the reciprocal of the velocity (slower neutrons spend more time in the decay volume), the response of the beam monitor is proportional to N_n. No detailed knowledge of the velocity distribution of the beam is necessary: however, it is necessary to measure the efficiency ϵ_0 of the neutron monitor at a single neutron velocity v_0. In terms of experimental quantities, the expression for the neutron lifetime becomes

$$\tau_n = \frac{N_\alpha L \epsilon_p}{N_p \epsilon_0 V_0}, \tag{3}$$

where N_α is the count rate of the alpha particles produced by neutron absorption in the monitor, L is the length of the decay volume, and N_p and ϵ_p are, respectively, the count rate and the efficiency for the detection of the decay protons.

Figure 6 illustrates our realization of the strategy described above. The collimated neutron beam passes into the vacuum region and through the Penning trap, which is coaxial with the beam. The Penning trap consists of an axial magnetic field of approximately 5 T produced by a superconducting magnet along with an electrostatic potential well approximately 1 kV deep produced by a set of 16 isolated electrodes. The segmented electrode structure allows the decay volume to be varied electronically so that the ratio N_p/L can be measured precisely: this procedure eliminates uncertainties in the size of the trapping volume due to unknown electric field end effects. Protons produced in the trap from neutron decay are confined radially in cyclotron orbits around the magnetic field lines. Since the maximum kinetic energy of the recoiling protons is 750.7 eV, the 1 kV electrode potentials confine the protons in the axial direction.

In order to count the protons, one end of the trap is opened by reducing the potential on an end electrode and producing a ramp in the potential with the middle electrodes. The protons then exit the trap and are guided along the magnetic field lines. A gentle 9° bend in the field lines guides the protons out of the neutron beam and toward a surface barrier detector held at a high negative potential (15-40 kV). The energy of the protons striking the surface barrier detector is high enough to produce a signal which is well separated from the electronic noise. The signal to noise ratio is further increased by gating the proton detector only while the trap is open.

The neutrons which pass through the trap strike the neutron monitor. The monitor consists of a thin silicon wafer with a thin deposit of ^{10}B. Neutrons absorbed in the boron produce alpha particles which are detected by four surface barrier detectors.

The first experiment using this apparatus, performed at the ILL, measured a neutron lifetime of 893.6 s with a 1σ error of 5.3 s. This result is in excellent agreement with other recent direct measurements of the neutron lifetime using completely different techniques. In the next experiment, to be conducted at the NIST CNRF, we hope to reduce the 1σ error to 1.5 s. Table 3 shows the error budget

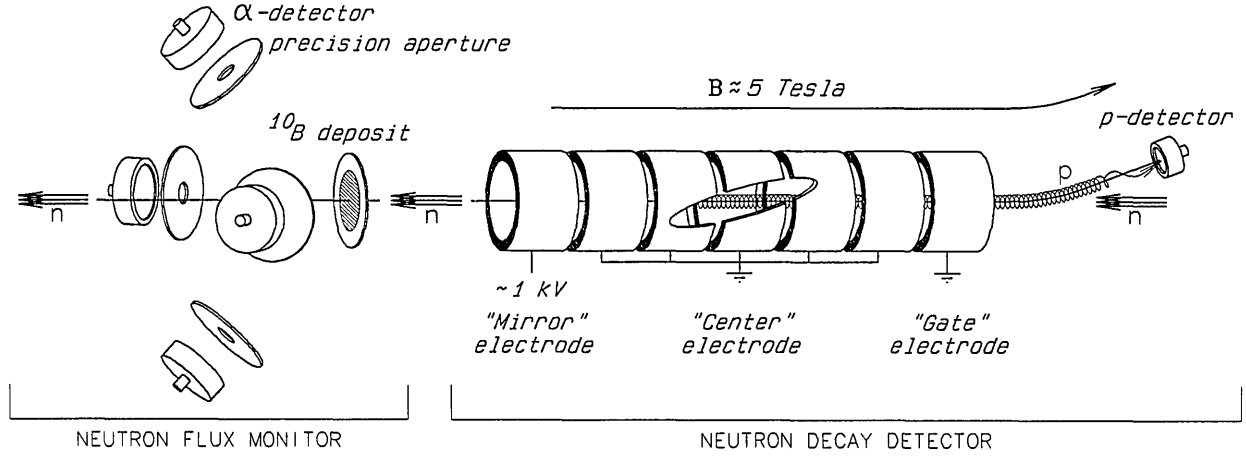

Fig. 6. Schematic diagram of the neutron lifetime apparatus.

for the ILL experiment (phase 1) and the anticipated error budget for the NIST CNRF experiment (phase 2). Most of the improvement in the anticipated error comes from better counting statistics and improvements in the calibration of the neutron monitor detector efficiency.

Table 3. Error estimation

Source of Error	Phase 1 (s)	Phase 2 (s)
Statistics of decay detection	3.8	<10
^{10}B-foil mean mass per unit area (IDMS)	2.8	NA
^{10}B cross section	1.4	NA
^{10}B-foil central shape correction	0.4	NA
^{10}B-foil central shape x beam profile	0.4	<0.1
^{10}B-foil absorption	0.7	0.1
Si-backing absorption	0.2	0.1
Si-backing incoherent scattering	0.5	0.2
α-detector solid angle Ω	1.0	NA
α-detector $\sigma\Omega$ due to beam profile	0.3	0.1
p backscattering from Au	1.0	0.2
Near normal forward scattering of protons	0.1	0.1
Si-p backscattering	0.5	0.2
Trap length 20 °C	0.5	0.2
Timing of mirror electrode	0.5	0.3
Trapable background	<0.1	<0.1
Trap thermal contraction	<0.1	<0.1
Si-backing Bragg Scattering	<0.1	<0.1
Ω (B) modification of trajectory	<0.1	<0.1
Neutron trajectory in trap	<0.1	<0.1
Trap alignment	<0.1	<0.1
Diffusion loss of protons	<0.1	<0.1
Neutron beam centroid misalignment	<0.1	<0.1
Trap end effect and beam divergence	<0.1	<0.1
Calibration of neutron monitor	NA[a]	≈1.0
Total error	5.3	≈1.5

[a] Not Applicable.

In the ILL experiment, the neutron monitor efficiency was calculated using measurements of the detector solid angle, the cross section for neutron absorption in ^{10}B, and the mass per unit area of the boron deposit. For the NIST measurement, we intend to determine ϵ_0 by calibrating the monitor in a monochromatic beam with accurately known velocity v_0 against two totally absorbing ("black") neutron detectors. One of the black detectors is a cryogenically cooled neutron calorimeter which can determine the neutron flux by measuring the heat produced by neutron capture in a totally absorbing ^{6}LiPb target. The other instrument is a totally absorbing capture gamma detector, whose efficiency is determined directly by alpha-gamma coincidence counting and indirectly by comparison with standard alpha sources. Each of the methods has a potential accuracy at the 0.1% level. If the uncertainty in ϵ_0 can be reduced by calibration with the black detectors, the neutron lifetime measurement at the NIST CNRF may turn out to be the most accurate measurement of the neutron lifetime.

3.1.2 Time Reversal Symmetry Violation in Neutron Decay A prototype detector and polarizer system designed to search for time reversal violation in neutron decay was tested in spring 1992. The prototype has been constructed as a collaborative effort by Los Alamos National Laboratory, Harvard University, Argonne National Laboratory, the University of Michigan, the University of California, and NIST. The goal of the measurement is to improve by an order of magnitude the sensitivity to T violation in neutron decay through a possible term in the decay probability which is proportional, in the nonrelativistic limit, to the triple correlation $\sigma_n \cdot [p_e \times p_\nu]$. This possible time reversal violating term in neutron decay is known as the D coefficient.

The only experimental evidence for time reversal violation found to date lies in the dynamics of the neutral K-meson system. Although the standard model of particle physics with three generations of quarks and leptons can accommodate the possibility of time reversal violation in the K-meson system, it is still not known whether or not theory and experiment are in quantitative agreement. The observation of time reversal violation in any other system would be a result of fundamental importance. The observation of a non-zero value for D in the 10^{-3}-10^{-4} range, which should be within the sensitivity of this experiment, would almost certainly indicate the presence of physics beyond the standard model.

The actual T violation measurement concerns the correlation between the neutron spin (σ_n) and the decay proton and electron momenta (p_p,p_e). The triple correlation involving the neutrino momentum p_ν can be inferred from this measurement. The experimental apparatus consists of two major components: a neutron polarizer to fix σ_n and a coincidence detector capable of simultaneously determining p_p and p_e.

The experiment will employ a novel method of neutron polarization based on transmission of neutrons through spin polarized ^{3}He. The neutron cross section for ^{3}He is very spin dependent: for thermal neutrons the cross sections are 5327 b for

antiparallel spins and only a few b for parallel spins. The ^{3}He will be polarized by spin exchange with optically pumped rubidium in a vapor cell. Such a polarizer is ideally suited for polarized neutron decay experiments. It will produce much less background due to absorption in the "wrong" spin state than more conventional polarizers and therefore a much lower rate of false coincidences in the decay detector. In addition, such a ^{3}He polarizer will not significantly increase the divergence of the neutron beam, in contrast to conventional magnetic mirror devices.

The coincidence detector will consist of alternating electron and proton detector panels arranged in an octagonal array surrounding the neutron beam. The electron detectors will be plastic scintillators. The proton detector panels will consist of an array of silicon detectors biased at 30-40 kV with electrostatic lenses for focusing. The proton detector will provide directional information only: from extensive Monte Carlo simulations it has been determined that the absence of proton tracking only minimally reduces the sensitivity of the experiment. This detector arrangement was successfully tested in spring 1992.

4. Conclusions

The NIST CNRF will provide new opportunity to researchers in traditional areas of materials, structural, and dynamic applications. However, the spectrum of research will not be limited only to these areas, but will also expand to experimental inquiry in which low energy neutrons will be used for the investigation of fundamental interactions. The proper development of these fundamental physics research stations will be vitally important for the growth and successful continuation of the programs in this field. We envision that when fully developed, the experimental facilities provided by these two stations will be comparable or better than similar facilities elsewhere. It is hoped that the research facilities at these two positions will enhance and stimulate further research work in topics of fundamental interest such as parity and time reversal symmetry violation, baryon nonconservation, weak interactions, fundamental constants, charge conservation, and various other quantum mechanical phenomena. Results of these works will have important implications in particle and nuclear physics, astrophysics and cosmology, and fundamental quantum theory.

The end position has recently become operational and as mentioned earlier a measurement of the neutron life time is already underway. The major design works of the neutron interferometer station have been completed or are nearing completion. It is expected that a preliminary neutron interferometer setup will become operational in 1993.

About the authors: M. Arif, M. S. Dewey, G. L. Greene, and W. M. Snow are physicists in the Ionizing Radiation Division of the NIST Physics Laboratory. The National Institute of Standards and Technology is an agency of the Technology Administration, U.S. Department of Commerce.

5. References

[1] S. A. Werner, Physics Today, December, 1980.
[2] U. Bonse and H. Rauch, eds., Neutron Interferometry, Oxford Press, Oxford, U. K. (1979).
[3] B. Desplangues, F. Gonnenwein, W. Mampe, eds., Workshop on Reactor Based Fundamental Physics, Journal de Physique Colloque C3, supplement No. 3 (1984).
[4] G. L. Greene ed., The Investigation of Fundamental Interactions with Cold Neutrons, Natl. Bur. Stand. (U.S.) Special Publication 711 (1986).
[5] M. Arif, R. D. Deslattes, M. S. Dewey, G. L. Greene, and I. G. Schroder, Nuclr. Instr. Meth., **A284** (1) 216 (1989).
[6] G. Badurek, H. Rauch, and A. Zeilinger, eds. Proceedings of the International Workshop on Matter Wave Interferometry, Vienna, Austria, 14-16 September 1987 North-Holland, Amsterdam, Netherlands.
[7] G. L. Greene, Rev. Sci. Instr. **58**, 1303 (1987).

Volume 98, Number 1, January–February 1993
Journal of Research of the National Institute of Standards and Technology

News Briefs

General Developments

Inquiries about News Briefs, where no contact person is identified, should be referred to the Managing Editor, Journal of Research, National Institute of Standards and Technology, Administration Building, A635, Gaithersburg, MD 20899; telephone: 301/975-3572.

PRESIDENT HONORS BALDRIGE WINNERS

President George Bush presented five U.S. companies with the Malcolm Baldrige National Quality Award during a ceremony on Dec. 14, 1992, at the Department of Commerce in Washington, DC. The 1992 recipients are: AT&T Network Systems Group/Transmission Systems Business Unit (Morristown, NJ) and Texas Instruments Inc. Defense Systems & Electronics Group (Dallas, TX) in the manufacturing category; AT&T Universal Card Services (Jacksonville, FL) and The Ritz-Carlton Hotel Co. (Atlanta, GA) in the service category; and Granite Rock Co. (Watsonville, CA) in the small business category. The ceremony was held in the Commerce Department's Malcolm Baldrige Great Hall.

FAA ASKS NIST TO MEASURE HIGH-FLYING EMFS

NIST has received an 18 month contract from the Federal Aviation Administration to determine the best techniques for measuring electromagnetic fields within aircraft. The FAA award was made at the urging of the General Aviation Manufacturers Association. As the aircraft industry adopts more and more electronic control systems, the FAA is interested in knowing the electromagnetic environment within the airframe. These fields come from radar pulses beamed toward a plane, entering via windows and other apertures. Electromagnetic susceptibility is now part of the FAA certification process for all new electronic aviation systems and aircraft. NIST will perform theoretical, modeling and field studies for the FAA to determine the best ways to measure radiation properties outside and within an aircraft frame, as well as analyzing the shielding effectiveness of the airframe. Measurements will be made over the frequency range of 400 MHz to 18 GHz. The field study will utilize a general aviation airframe on a turntable at a U.S. Army facility at Fort Huachua, AZ. For more information, contact Moto Kanda, Div. 818.03, NIST, Boulder, CO 80303-3328, (303) 497-5320

CERTIFICATION PLAN ASSESSES ANTENNA PERFORMANCE

Companies and agencies planning to construct near-field ranges to measure the performance of phased-array antennas will be interested in a new NIST publication outlining a certification plan that tests such facilities for various parameters. Titled A Certification Plan for a Planar Near-Field Range Used for High-Performance Phased-Array Testing (NISTIR 3991), the document discusses policy issues, measurement requirements, and various test required to characterize errors associated with measurements. Tests include those for alignment accuracy, errors caused by the instrumentation, and errors caused by radio-frequency energy traveling undesired paths. NISTIR 3991 is available from the National Technical Information Service, Springfield, VA 22161, (703) 487-4650 for $17 (print) or $9 (microfiche). Order by PB 92-213305.

MICROWAVE USERS: NEW NOISE STANDARDS AVAILABLE

Three new thermal noise measurements are being offered by NIST that can benefit manufacturers and users of microwave equipment. The first of these services measures noise standards at discrete frequencies of 12.4, 13.5, 14, 15, 16, 16.5, 17, and 18 GHz using type N and 3.5 mm connectors in coaxial cable. The second service measures noise standards from 18 to 26 GHz in WR42 waveguide, while the third measures noise from 18 to 26 GHz using 3.5 mm connectors in coaxial cable. There are specific requirements for reflection coefficient, temperature, and excess noise ratio. For additional details on these new services, contact J. Wayde Allen, Div. 813.01, NIST, Boulder, CO, 80303-3328, (303) 497-5871.

NIST/INDUSTRY TO WORK ON SUPERCONDUCTING MATERIALS

A private company and NIST will cooperate in the development of materials for practical superconducting devices. Under a cooperative research and development agreement, the company will provide samples of high-temperature superconductors for the testing of various magnetic characteristics. NIST will test these materials with the Institute's equipment and computer programs. Tests such as onset temperature for superconductivity, sharpness of the superconducting transition, and flux pinning characteristics revealed through hysteresis loops will be carried out. NIST and the private company will exchange technical expertise concerning testing and results, and will develop new suggestions for processing the material. For information on the 3-year program, contact Lawrence H. Bennett, B152 Materials Building, NIST, Gaithersburg, MD 20899-0001, (301) 975-5966.

ISDN DEMO DUBBED A "MILESTONE"

At a Nov. 17, 1992, demonstration that helped usher in the "information highway" known as the Integrated Services Digital Network, it was stated that the technology "can revolutionize the communications market in the same way the personal computer promoted a new computing [ideal]." This statement was made at NIST as part of the week-long Transcontinental ISDN Project '92. This event, for the first time, bridged over 150 American and foreign sites, inaugurating the network that soon will be available nationwide to businesses, schools and the general public. ISDN allows voice, data and images to be sent simultaneously in digital form over one telephone line. On display at NIST was a sneak preview showing 20 ISDN applications. Attendees could, for example, talk to someone in England while watching that person on a PC screen and simultaneously exchange data. Another demonstration showed how ISDN users could access medical images such as pathology specimens, x rays and cardiology studies sent from hospitals. Also on view were futuristic tax filing, desktop conferencing, and high-resolution facsimiles.

ASSESSORS WANTED FOR FASTENER ACCREDITATION

Mechanical engineers, metallurgist, chemists, physical scientists, and technical experts in industry, universities, and government with experience in evaluating the performance of materials are needed by NIST to conduct on-site assessments of laboratories that perform testing and inspection of metals and fasteners. The assessors are required for a new National Voluntary Laboratory Accreditation Program to meet the requirements of the Fastener Quality Act of 1990. NVLAP will accredit laboratories to test and inspect metals and fasteners using techniques in mechanical and physical testing, chemical analysis, dimensional inspection, metallographic analysis, and non-destructive inspection. Individuals with a background in the testing and inspection of metals and fasteners, and with experience in laboratory management and operations, are invited to send a resume to S. Wayne Stiefel, Fastener Program Manager, NVLAP, Rm. A162, Building 411, NIST, Gaithersburg, MD 20899-0001, (301) 975-4016, fax: (301) 926-2882.

AWARD TO ADVANCE DIAMOND FILM TECHNOLOGY

The NIST Advanced Technology Program (ATP) has announced support for a joint research project to develop an efficient, high-volume commercial production technology for diamond films. The award to private companies, could total $2.4 million over the 3 years of the project. Diamond is the hardest known substance, has the highest thermal conductivity of any known material, is extremely transparent from infrared wavelengths into the far ultraviolet, has high electrical resistivity, is an excellent electrical barrier, is corrosion resistant, has a low coefficient of friction, and even has some useful semiconductor properties. The project's target application is coatings that would substantially extend

the life of solid carbide tooling. The private companies will study the problem of scaling up the promising—but experimental—arc plasma chemical vapor carbide tooling. The private companies will study the problem of scaling up the promising "but experimental" arc plasma chemical vapor deposition process to levels high enough to demonstrate commercial potential. Project managers estimate that a successful scale-up would ultimately cut the cost of thin-film diamond coatings from today's level of about $150 per gram to less than $25 per gram, giving U.S. industry an important lead toward capturing a significant share of the emerging diamond film market.

NVLAP TEST PROGRAM ADDS WOOD-BASED PRODUCTS

The commercial products program of NIST's National Voluntary Laboratory Accreditation Program recently added the testing of wood-based products. This was done at the request of the American Plywood Association and with support by the National Particleboard Association and concurrence by the Department of Housing and Urban Development. The commercial products program was established by NIST in 1984 at the request of the International Coalition for Procurement Standards, an association of more than 100 federal, state and local purchasing officials. The program offers buyers a list of laboratories that can test products important to the purchasing community. Currently, the commercial products testing program includes paint, paper, plastics, plumbing, and seals and sealants. For information, contact Lawrence Knab, (301) 975-6712, or Lawrence S. Galowin, (301) 975-4016, fax: (301) 926-2884, NVLAP, A124 Building 411, NIST, Gaithersburg, MD 20899-0001.

FIELD STRENGTH COMPARISON STATUS UPDATED

In 1991, NIST initiated an international intercomparison of measurements of electric field strengths for the International Bureau of Weights and Measures. The goal: to ensure electromagnetic compatibility among products traded internationally. To accomplish this, NIST supplies each participating country with five electric field sensors to be tested at a minimum of four frequencies. The results are analyzed by NIST. To date, an intercomparison has been completed with two government and several industrial laboratories in Japan. In 1993 and 1994, NIST plans to perform intercomparisons with the United Kingdom, Germany, France, Italy, Poland, Austria and Korea. Switzerland, Russia and China also are expected to participate at a later date. The entire intercomparison project, which should take another 4 or 5 years to complete, is needed to show traceability among national standards laboratories. This traceability will become important in 1995 when the 12 nation European Economic Community requires imports to meet standards for electromagnetic compatibility. For information, contact Motohisa Kanda, Div. 813.03, NIST, Boulder, CO 80303-3328, (303) 497-5320.

ELEVEN INVENTIONS READY FOR LICENSING

NIST recently announced that the following 11 government-owned inventions are now available for licensing:

- High-T_c Superconducting Unit Having Low Contact Surface Resistivity and Method of Making (Docket No. 87-028);
- High-T_c Superconducting Unit Having Low Contact Surface Resistivity (Docket Nos. 87-029 and 88-040);
- High-T_c Superconductor Contact Unit Having Low Interface Resistivity (Docket No. 88-041);
- A System for Detecting Transition and Rare Earth Elements in a Matrix (Docket No. 88-038);
- Process for Forming Alloys in situ in Absence of Liquid-Phase Sintering (Docket No. 91-018);
- Intermetallic Thermocouples (Docket No. 92-001);
- Apparatus for Detecting Transition and Rare Earth Elements in a Matrix (Docket No. 92-003);
- Bi-Flow Expansion Device (Docket No. 92-006);
- Method and Apparatus for Detecting Guided Leaky Waves in Acoustic Microscopy (Docket No. 92-030); and
- Liposome Immunoanalysis (Docket No. 92-054).

For technical and licensing information on these inventions, contact Bruce E. Mattson, B256 Physics Building, NIST, Gaithersburg, MD 20899-0001, (301) 975-3084.

TWENTY-ONE GRANTS ANNOUNCED FOR ATP'S THIRD YEAR

The Department of Commerce announced on Dec. 17 the third set of grants under the Department's Advanced Technology Program. The NIST-administered grants to private industry are designed to stimulate research and development of cutting-edge, generic technologies with significant commercial promise. Twenty-one new programs were selected for funding under the ATP, including proposals in technology areas such as machine tools, biotechnology, electronics, optics, materials engineering, lighting technology, and refrigeration. Two-thirds of the awards are to projects led by small businesses, and three are from newly formed joint ventures. The awards will help finance the multiyear R&D projects with a projected total cost of more than $94 million, of which some $48 million will be funded by the ATP.

WEIGHTS AND MEASURES HANDBOOKS UPDATED FOR 1993

Two NIST handbooks have been revised and a supplement to a third one has been issued to reflect changes adopted at the July 1992 Annual Meeting of the National Conference on Weights and Measures. Established in 1905, NCWM is an organization of state, county and city weights and measures enforcement officials and associated federal, business and consumer representatives. NCWM is sponsored by NIST, a non-regulatory agency, and receives technical support through the institute's Office of Weights and Measures.

NIST Handbook 44-1993, Specifications, Tolerances, and Other Technical Requirements for Weighing and Measuring Devices. A major change in the new edition is the incorporation of the modernized metric system, the International System of Units (known as SI), into most of the codes. In addition, the Scales Code was revised to specify a new minimum load requirement for vehicle scales used to weigh scrap material for recycling and to include a definition, specifications and test notes for vehicle on-board weighing systems. The liquid-measuring devices codes now include a separate tolerance for electronic temperature-compensating systems. Repeatability tolerances have been added to several different codes for liquid meters. Additionally, effective Jan. 1, 1994, liquefied petroleum gas meters must be equipped with ticket printers and a copy of the delivery ticket must be left with the customer following bulk deliveries of LP gas through vehicle-mounted meters.

Handbook 130-1993, Uniform Laws and Regulations. A labeling exception for decorative wallcovering borders has been added to the Uniform Packaging and Labeling Regulation. Requirements for standard sizes of bread loaves were deleted from the Uniform Method of Sale of Commodities Regulation; however, bread is still required to be sold by mass. Another change to the UMSCR was the addition of a new section on Home Food Service Plan Sales. This section establishes contract and disclosure requirements for home food service plans and provides guidelines for advertising. Method of sale requirements for baler twine and potpourri were also added to the uniform regulation.

Supplement 3, 1993, to Handbook 133-Third Edition, 1988, Checking the Net Contents of Packaged Goods, now includes moisture loss requirements for dry pet foods. In addition, the supplement contains test procedures and a worksheet for use in checking the net contents of packages of baler twine.

Copies of the handbooks are available from the Superintendent of Documents, U.S. Government Printing Office, Washington, DC 20402. Order NIST Handbook 44-1993 by stock No. 003-003-03185-2, $14 prepaid; NIST Handbook 130-1993 by stock No. 003-003-03184-4, $13 prepaid; and Supplement 3, 1993, to NIST Handbook 133-Third Edition, 1988, by stock no. 003-003-03183-6, $2.75 prepaid. For information on NIST Handbook 133-Third Edition, 1988, and supplements 1 and 2, contact the Office of Weights and Measures, A617 Administration Building, NIST, Gaithersburg, MD 20899-0001, (301) 975-4004.

FUTURISTIC WAVEGUIDES DETECT CHEMICALS WITH LIGHT

Researchers at NIST and a private company are combining cutting-edge technologies from physics and biology to create new biosensors based on optical computer technology. Their aim is to develop highly sensitive and specific biosensors for measuring chemicals in medical and environmental samples. Called optical waveguides, these futuristic devices direct a laser beam through a film on the surface of a silicon or glass chip of 4 μm thickness. The wave-guide is coated with an antibody, a protein that binds only to specific chemicals. When a sample containing one of these chemicals is placed in contact with the waveguide, the molecules interact, and some of the light passing through the wave-guide is altered. Interference of this light with

an unaltered reference beam can measure drugs, chemicals such as hormones, or viruses in the sample. NIST and the private company recently signed a cooperative research and development agreement for this work.

EXPORT WORKSHOP ANNOUNCED ON ADVANCED MATERIALS

Exploring the international marketplace will be the focus of an industry workshop, "Advanced Materials—The International Trade Dimension," on May 10, 1993, at NIST in Gaithersburg, MD. Cosponsored by NIST, the Federation of Materials Societies, and the Department of Commerce's International Trade Administration, the workshop will focus on how DoC can help U.S. firms to become more competitive overseas. The program is designed for large, medium-sized, and small producers and suppliers of advanced ceramics, polymers, composites, and metal materials. Topics will include U.S. policy on the advanced materials industry, export controls, financing, and DoC services to industry. The day after the meeting, participants will have an opportunity to visit research facilities at NIST and have meetings with officials at the Small Business Administration, the Export-Import Bank and others at the Commerce Department. For information, contact Daniel B. Butrymowicz, B309 Materials Building, NIST, Gaithersburg, MD 20899-0001, (301) 975-5656, fax: (301) 926-8349.

U.S. JOINS JAPAN'S REAL WORLD COMPUTING PROGRAM

The White House Office of Science and Technology Policy has announced that the U.S. and Japanese governments have agreed "to undertake a joint prototyping project to further the design and development of advanced computing technologies that combine lightwave and electronic components." Part of Japan's Real World Computing program "a 10 year, $500 million initiative to develop next-generation information processing technologies" the new optoelectronics project will involve researchers and processing facilities in both nations. The hybrid systems to be worked on would serve as a bridge between today's electronic computers and the fully optical, parallel-processing machines that are envisioned for the future. A 10-member joint management committee, composed of five representatives from each nation, will guide the project. A NIST scientist chairs the U.S. portion of the committee. For more information, contact OSTP, Old Executive Office Building, Rm. 428, Washington, D.C. 20500, (202) 456-7710.

ILAC 92 MEETING

During Oct. 12–16, 1992 over 150 attendees from 33 countries, including 21 from the United States, participated in ILAC 92, the 15th meeting of the International Laboratory Accreditation Conference (ILAC). This biennial conference provides an opportunity for those interested in their national programs to share information and experience with one another. Topics receiving attention were uncertainty estimates in test reports, traceability of measurements, reference materials, proficiency testing, surveillance and monitoring activities, assessor qualifications, and some issues concerning the use of ISO/IEC Guide 25 on requirements for the acceptance of calibration and testing laboratories. ILAC will produce a guidance document on the relationship between Guide 25 and the ISO 9000 Quality Standards Series, and a second guidance document for interpretive guides to be used in conjunction with the application of Guide 25 to specific areas of testing. The first of these documents is needed to eliminate user confusion over whether a laboratory should be accredited or 9000-registered; the latter will deal with the anticipated proliferation of documents in specialized fields of application, e.g., information technology. A detailed report on the meeting is available.

NASA PRAISES NIST WORK SUPPORTING ADVANCED COMMUNICATIONS TECHNOLOGY SATELLITE

The Flight Segment Office of the National Aeronautics and Space Administration's Lewis Research Center has acknowledged the "outstanding contribution" made by NIST scientists in support of the Advanced Communications Technology Satellite (ACTS), scheduled to be launched next June. The scientists investigated possible sources of error arising from measurements of the ACTS multibeam antenna (MBA), a pair of offset Cassegrain antennas with 50 transmit and 50 receive beams. The MBA was measured on a newly constructed antenna near-field spherical-scanning range by a NASA contractor. In addition to work at NIST, both researchers took part in numerous meetings with the contractor and NASA Lewis. The scientists are credited with identifying a subtle error in the contractor's version of the program for trans-

forming measured near-field data to computed far-field performance (broadly based on NIST original principles and NIST developments for near-field scanning). They also provided suggestions for improving the measurement techniques. The result was "good agreement between predicted and measured antenna performance and ... antenna measurements in which we have confidence." The MBA measurement program now has been completed.

NIST CARRIES OUT FIRST DEMONSTRATION OF INTEGRATED-OPTIC WAVEGUIDE LASER FABRICATED IN LITHIUM TANTALATE

NIST scientists have carried out the world's first demonstration of an integrated-optic waveguide laser fabricated in ferroelectric lithium tantalate; the results were published in the journal *Optics Letters*. The device is optically pumped near 750 nm and lases near 1090 nm. These results are the first step to obtaining visible light from the waveguide laser, and experiments are now under way to force the laser to self-double the 1090 nm emission and to parametrically mix the laser output and the pump input. The result should be a waveguide laser that simultaneously can produce infrared, green, and blue light. The team expects the new laser to have significant impact in application areas such as optical recording, optical computing, medical diagnostics, and chemical sensing.

SENSOR TO DETECT AND CLASSIFY SUB-MICROMETER PARTICLES NOW AVAILABLE FOR LICENSING FROM NIST

NIST recently received a Notice of Allowance from the U.S. Patent and Trademark Office for the solid-state sensor capable of detecting particles having dimensions down to 0.1 μm; the next step is the formal issuance of a patent. This invention is now available for licensing from NIST, and NIST's Office of Technology Commercialization is currently seeking one or more commercial companies with which to collaboratively develop and evaluate the sensor for specific industrial applications and to which to grant an exclusive license for manufacture and marketing. The target application is for detecting particles in the ultra-clean environment required for the manufacture of integrated circuits. Present methods using anomalous scattering of laser light beams also are able to detect 0.1 μm particles, but the proposed sensor is expected to offer advantages in terms of cost, compactness, and in some applications, safety.

Companies presently being contacted are informed that the potential applications extend beyond integrated circuit manufacturing and that the sensor could be configured for use in gas, liquid, vacuum, or plasma environments confined within small vessels or fluid feed lines. As conceived, the sensor consists of a dime-sized "monolithic" array of individually addressable, photosensitive pixel cells connected to a hardware/software electronic subsystem. The array is activated by illumination with an electronically alterable spectrum of electromagnetic radiation. When a particle of opacity at some wavelength comes to rest on the sensor surface, a degraded video signal from the underlying pixel or pixels indicates the presence of the particle. A key claim of the patent application is an opaque screen patterned with apertures of different sizes and geometries designed to facilitate the extraction of the incident particle size distributions using neural network algorithms.

NIST DEVELOPS METHOD FOR PRODUCING MICROMACHINED GAS SENSOR ARRAY BY CMOS POST-FABRICATION PROCESS

NIST researchers have developed a method for fabricating micromachined gas sensors that takes advantage of a commercial complementary metal oxide-semiconductor (CMOS) process. Arrays of thin-film gas sensors hold great promise for improving the selectivity and reliability of commercial gas sensing devices. An optimized array element would include a heater, a thermometer, and a gas-sensitive film; previously, such structures have been fabricated only by specialized micromachining processes in research laboratories using expensive lithographic equipment.

The NIST team has built a device that has demonstrated sensitivity to hydrogen. The results have importance for the commercial development of micromachined devices, improved and low-cost gas sensors, and applications requiring processing of materials on a microscopic scale. Three patent disclosures relating to this work have been filed. The team specified the layout of the devices as instructions to a CMOS foundry which fabricates application-specific integrated-circuit chips. The team treated chips received from the foundry with an anisotropic silicon etch which produces thermally isolated microbridges. Each microbridge contained a polysilicon heater, an aluminum hotplate (which also was used to measure temperature),

and aluminum contact pads. The team completed the sensor structure by depositing gas-sensitive tin oxide over the aluminum pads. The team also was able to enhance sensor performance through temperature control of array elements during tin oxide deposition and device operation.

METHOD DEVELOPED FOR ELECTRICAL CHARACTERIZATION OF MULTICARRIER SEMICONDUCTORS

NIST scientists have developed an improved method for determining the carrier density and mobility of each carrier component in multicarrier semiconductor systems. The method can be applied to gallium arsenide-based layered structures, such as high-electron-mobility transistors used for high-speed integrated circuits, and to structures fabricated from other compound semiconductors, such as mercury cadmium telluride used for infrared detectors. The electrical conduction process in these materials is often associated with more than one type of carrier, each component having a distinct mobility and density, resulting in a multicarrier system. By contrast, in silicon electric current is carried primarily by one type of carrier, either electrons or holes, and the carrier density and mobility can be determined by measuring conductivity and Hall effect at a fixed magnetic field. However, this conventional method becomes ineffective and the results often misleading for multicarrier systems. The team's method involves measuring both the parallel and transverse components of the conductivity tensor as a function of magnetic field and fitting the measurements to a multicarrier model to extract the density and mobility of each carrier component. The work includes the development of software to normalize the data and iterate the fitting parameter. The method is easy to implement and is expected to provide a better understanding and characterization of a range of compound semiconductors.

PRODUCT DATA HYPERMEDIA OVERVIEW

NIST scientists have produced Version 2 of a brief hypermedia introduction to the who, what, how, and why of STEP (Standard for the Exchange of Product Model Data). The hypermedia document, STEPing into the 21st Century-Product Data for a Changing World, presents a broad, non-technical overview of STEP for a wide audience.

The program runs under Windows 3.1 using a run-time version of Toolbook, the multimedia authoring system used to create the presentation. Because technology transfer is vital to the success of STEP, it is important to meet the varying information needs of managers, engineers, and others involved in the development and implementation of STEP.

ASME Y14.5.1 STANDARD NEARS COMPLETION

ASME Working Group Y14.5.1 on Mathematical Definition of Dimensioning and Tolerancing Principles is nearing completion of a standard for establishing mathematically precise definitions of dimensional tolerances that appear on mechanical part drawings. The working group met during October and resolved all outstanding technical issues for the standard. A NIST scientist is overseeing the process of assembling the components of a document into a complete draft. When the new standard is issued by ASME sometime this year, it will be a companion to the existing Y14.5 Standard on Dimensioning and Tolerancing.

The Y14.5 standard, in use since 1966, is intended for use in traditional drafting practice. In recent years, computer software has become much more important in manufacturing. Software engineers have had to interpret Y14.5 when developing computer-aided design, analysis, inspection, and more recently, product data exchange systems. Because these new users of Y14.5 are from a different culture than the traditional users of Y14.5, ambiguities in Y14.5 have led to conflicting interpretations, and systems do not work well together. The new Y14.5.1 standard is expected to resolve these problems. It is scheduled for release for public comment early in 1993. The standard will also be submitted as a Committee Draft Standard within ISO/TC10 and will form the basis of the Shape Tolerance Model for STEP within ISO/TC184/SC4.

NIST RESEARCHERS ESTABLISH ENVIRONMENTAL PROPERTIES OF MTBE, POPULAR OXYGENATE FUEL ADDITIVE

Starting Nov. 1, 1992 federal law required that automobile fuels in about 40 urban areas of the United States must contain added "oxygenates" during the winter months. These new regulations are for those areas where air quality standards for carbon monoxide emission are exceeded.

An oxygenate is a liquid fuel component such as an ether or alcohol that contains oxygen. Oxygenate additives also increase the octane rating of the gasoline. Most of the fuel in use in the Washington-Baltimore area will contain the oxygenate MTBE "methyl tertiary-butyl ether" a compound whose atmospheric chemistry was established by research carried out at NIST.

Four years ago, NIST scientists reported the first temperature-dependent absolute value for the rate constant for the reaction of MTBE with the hydroxyl radical. The major tropospheric loss process for organic compounds released to the atmosphere is the reaction with hydroxyl radicals. The results of this study established that the atmospheric lifetime of MTBE is about 4 days, indicating that MTBE is not highly reactive and, therefore, does not contribute significantly to photochemical air pollution in urban areas.

MOLECULAR BEAMS AND DIODE LASERS PROBE ATMOSPHERIC DIMER MOLECULES

The oxides of nitrogen, NO_2, N_2O_3, N_2O_4, NO_3, N_2O_5, play an important role in atmospheric chemistry, with NO_2, NO_3, and N_2O_5 having been detected in the stratosphere with spectroscopic techniques. For chemical systems rich in NO_x species, the concentrations of these species are all interrelated. Because of this inter-relationship, it is important to have remote sensing techniques to measure the spatial and temporal concentrations of the various nitrogen oxides simultaneously. Infrared spectroscopy using satellite or ground-based spectrometers is a non-intrusive technique that allows accurate measurements of these species concentrations in the atmosphere. To use these capabilities requires measurement and interpretation of the infrared spectra of the relevant molecules.

NIST recently has examined the infrared spectra of two important NO_x species, the dimer of NO_2 (N_2O_4) and the mixed dimer of NO and NO_2 (N_2O_3). Spectra were recorded using a newly constructed diode-laser molecular-beam spectrometer, in which the dimers are formed by co-expanding NO and NO_2 gas mixtures with argon through a 10 cm long by 25 m wide slit nozzle. In the resulting molecular beam the molecules are rotationally and vibrationally cold, with a measured rotational temperature of approximately 20 K. The molecular beam is interrogated with a frequency-tunable diode laser. The cold molecular beam conditions dramatically simplify the spectra, making analysis possible while still yielding a high signal-to-noise ratio. The spectra have been analyzed to obtain accurate spectroscopic constants and structural information. For example, for N_2O_4 we find a N–N bond length of 1.753 Å, which is intermediate between a van der Waals separation and a covalent bond. Future efforts will include measurement of the strong infrared bands of N_2O_5.

MEASUREMENTS WITH NIST GAMMA-RAY SPECTROMETER FEATURED IN INTERNATIONAL WORKSHOP

On Oct. 5-7, a Workshop on Applications of High-Resolution Gamma Spectroscopy in Studies of Atomic Collisions and Nuclear Lifetimes was held at the Institut Laue-Langevin (ILL), Grenoble, France. An international collection of 61 scientists gathered to hear invited presentations on precision gamma-ray spectroscopy, nuclear lifetimes, and atomic collisions. A NIST scientist served as external chairman of this workshop and helped to introduce the workshop by lecturing on "The History of High Resolution Gamma Spectroscopy."

The workshop emphasized precision measurements of Doppler-broadened gamma-ray profiles and the use of these profiles to determine nuclear lifetimes and atomic collision parameters. The recent interest in Doppler-broadened gamma-ray profiles stems from the fact that the small broadening resulting from nuclear recoil can be measured precisely with the NIST high-resolution double flat crystal spectrometer. Originally the NIST spectrometer was installed at the ILL to measure high-energy gamma-ray wavelengths because the ILL high-flux reactor is the only facility in the world which provides intense gamma-ray beams and specialized source changing facilities.

The features of the NIST spectrometer that make it a uniquely suited instrument for Doppler-broadened profile measurements are the very high resolution (10^5 to 10^6) and the very well-characterized instrument function. More than 20 non-NIST scientists have been associated with the Doppler-broadened profile measurements, and during the past 2 years, 75 percent of the available gamma-ray beam time at the ILL has been scheduled on the NIST spectrometer. Another NIST scientist described the NIST spectrometer and its performance in detail and conducted tours of the NIST/ILL gamma-ray facility.

NIST DEDICATES NEW HIGH-DOSE COBALT-60 FACILITY FOR RADIATION PROCESSING APPLICATIONS

In October, NIST installed a new, cobalt-60, GammaCell 220 source as the main 1.2 MeV gamma-ray irradiator in a new user facility for research and calibrations. The self-shielded irradiator contains 24000 curies of the cobalt-60 radionuclide, which decays with a half life of 5.27 years. This very strong gamma-ray source gives NIST the capability of irradiating samples with a dose rate of 5 Gy/s. The facility also includes two other cobalt-60 irradiators with dose rates of 1.5 Gy/s and 0.5 Gy/s. Total doses for typical industrial radiation processing applications are in the range 100 to 10000 Gy.

The GammaCell irradiators are used to administer accurate gamma-ray doses to transfer and reference standard dosimeters such as radiochromic films and alanine, which are used in the NIST high-dose calibration services. The main users are in the areas of industrial radiation processing and medical device sterilization. These irradiators are also used by other NIST laboratories for radiation-hardness testing of electronics, polymers research, radiation chemistry, and the study of radiation-induced changes in biomolecules. The new facility at NIST is equipped with modern spectrophotometers, laser scanning densitometers, and associated computers for reading irradiated radiochromic films. Provisions can be made for proprietary use by industrial investigators.

NIST PROVIDES RADON STANDARDS TO UNITED KINGDOM AND ITALY

In the past year, NIST, at the request of two other national metrological laboratories, the National Physical Laboratory and the Ente per le Nuove Technologie L'Energia e L'Ambiente, provided the necessary radium-226 transfer standards that will serve as the national radon standards for the United Kingdom and Italy, respectively. NIST is the only national metrological laboratory in the world that disseminates radium and radon standards that have continuous calibration links to the international primary radium mass standards prepared by Marie Curie in 1911 and Otto Hönigschmid in 1934. Despite the passage of so many intervening years, these links to artifact standards are still of great significance. Unlike the calibration of many other radionuclides, there is no currently available activity standard for radium-226. Radium-226 is the progenitor of radon-222, and much of its continuing importance is due to widespread concern for the potential health hazards of naturally occurring indoor radon levels. The radioactivity group serves in many ways as the primary reference laboratory and "keeper" of international radium solution and radon gas standards.

COUNCIL ON IONIZING RADIATION MEASUREMENTS AND STANDARDS (CIRMS) MEETS AT NIST

The Council on Ionizing Radiation Measurements and Standards conducted its first meeting at NIST Oct. 22–23, 1992. The organization represents tens of thousands of users engaged in industrial radiation processing and sterilization, medical radiation therapy and diagnostics, nuclear power radiation programs, and radiation worker protection programs. CIRMS provides a forum for discussing ionizing radiation measurements and standards issues, defining and prioritizing needed work, disseminating information on standards, and organizing workshops and meetings to advance ionizing radiation technology. Sixty-two participants attended the meeting. Invited lectures were given on the status and needs for radiation technology in nuclear medicine, radiation oncology, diagnostic radiology, industrial processing, industrial radiography, radioactivity monitoring at nuclear power stations, nuclear power materials dosimetry, environmental radioactivity assessments, and radon measurements. Needs from other agencies such as DOD, DOE, and USDA were also presented. A workshop on Measurement Quality Assurance for Ionizing Radiation will be sponsored by CIRMS and other interested organizations in March 1993.

NIST QUANTIFIES OXIDES ON INTERMETALLICS COMPOUNDS FORMED AT ELECTRONIC INTERCONNECTS

The oxides that form on Sn-based intermetallics can determine the solderability of electronic components and the reliability of electronic interconnects. NIST researchers working with the Naval Research Laboratory combined the electrochemical techniques of cyclic voltammetry, impedance spectroscopy, and chrono-coulometry with the surface chemical analysis techniques of Auger electron spectroscopy and x-ray photoelectron spectroscopy to study the oxides that form on Cu_3Sn, Cu_6Sn_5 and Ni_3Sn_4 intermetallics under different exposure conditions. Combining these techniques allows for the identification of the oxide phases and quantification of the thickness of the phases that form for different exposures. The

results of this work were presented at the Corrosion and Reliability of Electronic Materials and Devices Symposium at the 182nd meeting of the Electrochemical Society in Toronto, Canada.

CALCULATIONS SUGGEST STRAIN REDUCES STERIC HINDRANCE IN ENVIRONMENTALLY ENHANCED FRACTURE OF SILICA AND SILICON

The presence of active environmental molecules, e.g., water, has long been known to cause bond rupture in ceramics at applied stresses well below the theoretical strength of the material. In this process, the presence of both stress and environment are necessary. It has been thought that stress causes polarization of the crack tip bonds which attracts the environmental molecule, leading to bond rupture. However, molecular orbital calculations made on silica and silicon systems at NIST suggest that an equally important aspect of the applied stress is the removal of steric hindrances which prevent environmental molecules from reaching the crack tip bonds in the absence of stress. Calculations indicate that these hindrances are caused by the presence of the atoms neighboring the crack tip which prevent the passage of the environmental molecule. Application of stress widens the crack, thereby reducing the blockages caused by these atoms.

NIST-ACC COLLABORATION ON ENVIRONMENTAL DEGRADATION IN GLASS-FIBER-BASED COMPOSITES

A NIST report on environmental degradation in glass-fiber-reinforced composites has been distributed to the U.S. Automotive Composites Consortium (ACC). The report identifies the most important technical and scientific issues in this area and will be used to formulate a joint NIST-ACC experimental program to address the key concerns.

The ACC was formed by the automatic industry to develop the generic technology necessary to use polymer matrix composites in structural applications. Requirements for mechanical performance and cost dictate the use of glass fibers in the majority of composites used in the automotive industry. Environmental stability of glass-fiber-reinforced composites is critical to increased use of these lightweight materials.

The report identifies degradation of the glass/polymer interface to be a critical concern. To deal with this problem, NIST has initiated studies of the effects of glass-fiber surface treatments on strength of the interface and how the strength degrades upon exposure to moisture. Facilities to measure interface strength are available at NIST and, in fact, were used by research scientists from one automobile manufacturer to quantify the effects of processing and surface treatments on interface strength.

NIST WORKS TO IMPROVE U.S. PASSPORT SECURITY

NIST and the State Department hosted a meeting of industry and government experts to discuss test methods for evaluating the durability and security of the U.S. passport. Each passport has a plastic laminate that covers the personal data and photograph and protects this information from wear, dirt, moisture, discoloration, and tampering. A series of nine tests was developed by the State Department and NIST to evaluate potential laminate systems and determine which best serves the needs of the government.

The meeting, attended by representatives from all potential suppliers of security laminates, provided an opportunity for industry to get a detailed description of the tests and make suggestions for improvements. Overall, the tests were viewed by industry as appropriate, but several important modifications were suggested. As a result of the meeting, better test methods are now available, information on testing gained by the companies will assist them in making better products, and representatives from several other government agencies with security concerns learned of the latest developments.

NIST COMPLETES STUDY ON FUNDAMENTAL BOILING MECHANISMS OF OZONE-SAFE REFRIGERANT/LUBRICANT MIXTURES

A NIST scientist completed a NIST/DOE project that investigated the fundamental parameters of nucleate flow boiling of refrigerant R11 and its temporary replacement R123, with and without the addition of oil. The bubble frequency, the bubble diameter, the site density, the contact angle, and the heat transfer coefficient for these fluids were measured for boiling inside a horizontal tube. The heat transfer effectiveness of the replacement R123 was up to 8 percent better than that of R11 under some operating conditions and was enhanced 20 percent with the addition of 0.5 percent alkylbenzene oil, which is typically used in refrigeration applications. The purpose of the study was to establish the ground work for a generic boiling model that can be used to predict the heat transfer

coefficient based on known parameters. A general boiling model will enable refrigeration companies to accurately design efficient evaporators for the ozone-safe refrigerants. A reliable model will reduce the number of hours spent on heat exchanger research and development. This work is presented in NISTIR 4948, Simultaneous Visual and Calorimetric Measurements of R11, R123 and R123/Alkylbenzene Nucleate Flow Boiling.

ACOUSTIC EMISSION OF STRUCTURAL MATERIALS EXPOSED TO OPEN FLAMES

Recent experiments by NIST scientists have shown that acoustic emission (AE) can be used as an early indicator of hidden structural fires. By mounting piezoelectric transducers directly on beams of materials such as wood, plastic, and gypsum board, the ultrasonic events that result from the relief of stress created by changing temperatures can be measured. The number of AE events in a minute and the cumulative energy released when the material is exposed to a flame provide a good measure of the overheated state of many materials well before a temperature increase is registered at the same location. Wood is particularly susceptible to acoustic emission, producing more than 1000 events/min in a solid fir board and 30/min in 13 mm thick plywood when exposed to a 1.0 kW flame. Gypsum board produces about half as many events per minute, which is still 50 times greater than the background activity.

The advantages of this new technique for sensing a fire are that a deep-seated fire may be detected quickly and obscuration by dust and smoke would not degrade performance. Critical issues that remain to be investigated are the signal-noise-ratio in a field installation, the extent of coverage possible with a single transducer, and the economics of installation and maintenance.

FIRST TEXT RETRIEVAL CONFERENCE (TREC) HELD

On Nov. 4–6, 1992 NIST and the Defense Advanced Research Projects Agency co-sponsored the first conference to examine text retrieval methodologies. Participants represented government, industry, and academia with 28 text retrieval systems evaluated. The goal of the conference was to encourage research in text retrieval from large document collections by providing a large test collection, uniform scoring procedures, and a forum for organizations interested in comparing their results. NIST will publish the conference proceedings this year.

The test collection, which will be made available for further research, was based on over 740000 documents (about 2 gigabytes of data) from newspapers, wire services, and other standard text, and 100 topics were used as test topics. Results from each system were passed by human assessors for correctness, and tables showing individual system performance were compiled. Participants gave presentations on their systems and attended workshops on areas of common interest among the systems. A major strength of the conference was the wide range of methods used for retrieval. NIST will co-sponsor a second TREC conference next year and anticipates that the conference series will continue for several years.

NIST PUBLISHES RESULTS OF FIRST OPTICAL CHARACTER RECOGNITION SYSTEMS CONFERENCE

NISTIR 4912, The First Census Optical Character Recognition Systems Conference, discusses the results and conclusions of this conference held at NIST in May 1992.

Following the 1990 Census, NIST and the Bureau of the Census joined forces to sponsor a scientific experiment and conference to determine the state of the art in the optical character recognition industry. Twenty-nine groups from North America and Europe participated in the experiment, which involved a comparison of image data bases. NIST scored the results and the conference convened to discuss findings and share ideas on the ongoing research into machine recognition of handprint, specifically the machine recognition of individual or segmented characters without context.

NIST COLLABORATES WITH THE DEPARTMENT OF THE ARMY ON THREATS TO COMPUTER SYSTEMS

As a participant in the U.S. Army Computer Vulnerability/Survivability Study Team, NIST was asked to assess the threats to computer systems that use commercially available hardware and software. NISTIR 4939, Threat Assessment of Malicious Code and External Attacks, provides an assessment of the threats from malicious code (viruses and worms) and human threats (hackers). The report gives the history of each type of threat, describes current protection methods, and projects future threats.

PROGRAMS FOR NEURAL NETWORK CALCULATIONS

Software developed by NIST will enhance the efficiency, and thus the feasibility, of industrially important systems based on neural network computations. Neural networks are an active area of research and development for numerous applications, particularly for automatic character recognition systems. For example, at least a dozen U.S. companies, several companies in Europe, and other research groups are developing optical character recognition systems for deciphering handwritten characters. The time-consuming task of "training" the neural networks has for some years been done by a method known as backpropagation. Mathematically, "training" corresponds to minimizing an error function. Backpropagation is known to be a slow method, and better methods (such as conjugate gradient methods) have been known for years, but backpropagation continues to be used.

A NIST scientist has written an easy-to-use training program using conjugate gradients, which runs from 10 to 100 times faster than backpropagation. He has made the program available to users via electronic mail. To date, over 50 copies have been distributed to users in universities, government, and industry in the United States and 11 foreign countries.

NIST scientists have used his training program as part of a state-of-the-art recognition system that correctly recognizes over 96 percent of handwritten digits.

Standard Reference Materials

STANDARD REFERENCE MATERIALS 2709–2711 SOIL SAMPLES

EPA has been monitoring a number of toxic metals in the environment for a number of years under the Resource Conservation and Reclamation Act and the Superfund clean-up programs. To ensure accurate detection and quantitation of toxic metals of interest, and to know the reliability and comparability of data across regions and local sampling sites, accurate standards are needed.

The Standard Reference Materials Program announces the availability of three soil Standard Reference Materials (SRMs) specifically designed to meet these needs. The first, SRM 2709, is a San Joaquin Valley soil having the toxic metals at concentrations which generally reflect their occurrence in uncontaminated environments. The soils, SRM 2710 and SRM 2711, collected in Montana, were selected to reflect soils heavily contaminated and moderately contaminated, respectively, with toxic metals. For example, lead occurs at 18.9 mg/kg in SRM 2709, at 5532 mg/kg in SRM 2710, and at 1162 mg/kg in SRM 2711. Antimony, arsenic, cadmium, copper, manganese, mercury, molybdenum, silver, and zinc also occur at unusually high levels in SRMs 2710 and 2711. However, other environmentally important metals like chromium, nickel, and selenium are at similar levels in all three materials.

In addition to being certified for the environmentally significant trace elements, the soils are also certified for the major constituents. Each of the soil SRMs is issued in 50 g units of powdered material.

STANDARD REFERENCE MATERIALS 458–460 BERYLLIUM-COPPER ALLOYS

The explosive growth in the computer and electronics industries has created a greatly increased demand for beryllium copper. This electronic material is found in essentially all electronic systems, as a spring material in contacts and connectors linking electronic components together. The quality of these devices depends on the metallurgy and chemistry of the beryllium copper alloys. Accurate standards are needed to help producers of these materials control the quality of their products.

The Standard Reference Materials Program announces the availability of three new Standard Reference Materials to help meet these needs. SRMs 458–460 are intended for use in chemical analysis of beryllium-copper alloys. In all three, the copper concentration exceeds 97 percent and is reported as an information value. The analytical effort is focused on establishing the present best estimate of "true" concentration of 11 constituents occurring at concentrations below 2 percent. The SRM is issued in units of 50 g of chips sized between 0.50 mm and 1.18 mm sieve openings.

Volume 98, Number 1, January–February 1993
Journal of Research of the National Institute of Standards and Technology

Standard Reference Data

DATA ON CHEMICAL REACTIONS IN SOLUTIONS AVAILABLE

Research chemists, environmental scientists, pharmacologists and others in the health care field now have rapid access to information on the reactions of more than 6400 chemicals in water and other solvents via the NIST Solution Kinetics Database for personal computers. It holds information on the rates of 7800 free radical reactions derived from more than 10300 experimental determinations. The PC database was compiled from the available printed literature through 1990 by the Radiation Chemistry Data Center. The NIST Solution Kinetics Database, Standard Reference Database 40, is available for $190 from the Standard Reference Data Program, A320 Physics Building NIST, Gaithersburg, MD 20899-0001, (301) 975-2208, fax: (301) 926-0416. Yearly updates are planned.

NEW PC DATABASE CALIBRATES INFRARED SPECTROMETERS

High-accuracy data files are now available for the calibration of infrared spectrometers used in chemical research and environmental monitoring. NIST Wavenumber Calibration Tables, Standard Reference Database 39, for personal computers, is a supplement to NIST Special Publication 821, Wavenumber Calibration Tables from Heterodyne Frequency Measurements, an atlas of spectral maps and tables. In preparing the tables, far more transitions were calculated than could possibly be published. The PC database includes ASCII files for the separate molecules listing wavenumber, uncertainty, lower-state energy level, intensity, descriptive quantum numbers, and band identification. The primary calibration molecules are the linear triatomic carbonyl sulfide and nitrous oxide that cover portions of the infrared spectrum ranging from 488 to 3120 wavenumbers. Gaps in the coverage are covered by nitric oxide, carbon monoxide and carbon disulfide. The text of SP 821, as printed in the NIST Journal of Research, is included in the database package. NIST Standard Reference Database 39 is available for $165 from the Standard Reference Data Program, A320 Physics Building, NIST, Gaithersburg, MD 20899-0001, (301) 975-2208, fax: (301) 926-0416.